

WESTFÄLISCHE  
WILHELMS-UNIVERSITÄT  
MÜNSTER

# > A coupled bulk-surface reaction-diffusion- advection model for cell polarization

Dissertation

Natalie Emken  
- 2016 -





Fach: Mathematik

# **A coupled bulk-surface reaction-diffusion-advection model for cell polarization**

**Inaugural-Dissertation  
zur Erlangung des Doktorgrades der Naturwissenschaften  
– Dr. rer. nat. –  
im Fachbereich Mathematik und Informatik der  
Mathematisch-Naturwissenschaftlichen Fakultät der  
Westfälischen Wilhelms-Universität Münster**

eingereicht von

Natalie Emken

aus Wittmund

– 2016 –

---

**Dekan:**

Prof. Dr. Martin Stein

**Erstgutachter:**

Prof. Dr. Christian Engwer

**Zweitgutachter:**

Prof. Dr. Martin Burger

**Tag der mündlichen Prüfung:**

07.11.2016

**Tag der Promotion:**

---

## Acknowledgements

I would like to take the chance to express my gratitude to all the people who supported me while I was writing this thesis.

First of all, I would like to thank Prof. Dr. Christian Engwer for giving me the opportunity to work on this interesting topic and for his comprehensive encouragement during my work. By the successful cooperation marked by many effective discussions, I have always enjoyed the work in his research group. Particularly, I would like to thank Sebastian Westerheide who is concerned with a related topic and often helped me with the DUNE software libraries.

Not to be forgotten are my thesis committee members. Prof. Dr. Martin Burger, who supported me during my diploma thesis, gave me the idea to do my PhD. He informed me about this fellowship that made this work possible in the first place. Relating to biological questions, Prof. Dr. Roland-Wedlich Söldner was the perfect point of contact for this project. He helped me to understand complex biological processes and gave me the opportunity to get my own idea of performing experiments. While doing so, his post-doc Christian Schuberth always supported me why I also would like to thank him.

Further thanks go to the coordinators of the CiM-IMPRS Graduate School, Sylvia Krüger and Martin Wild, who provided help with organizational questions. At this point, I also wish to give thanks to the CiM-IMPRS Graduate School for funding my research.

Moreover, I would like to express my gratitude to my proof readers Heike Emken, Carolin Roßmanith and especially to Gareth Finn who has volunteered to read this thesis, although we barely know each other.

Another thanks go to all of my friends and colleagues who not only encouraged and supported me during the last three years but also helped me to achieve a good work-life-balance.

And last but not least, I must thank my parents, and the rest of my family, for their unconditional support, love, and encouragement. Especially my husband An has always stood by my side during the years of my work.

This thesis was supported by the CiM-IMPRS Graduate School:

CiM Graduate School and  
International Max Planck Research School – Molecular Biomedicine

Schlossplatz 5  
48149 Münster  
Germany



## Abstract

The yeast cell *Saccharomyces cerevisiae* provides an excellent model system to study the underlying mechanisms of cell polarity, a process fundamental to the function of many cell types. Two positive feedback loops are thought to contribute to the local polarization of the most important polarity regulator Cdc42, one actin-dependent and one actin-independent mechanism.

A common model explains polarity by a Turing-type reaction-diffusion mechanism that can concentrate Cdc42 by a Bem1-mediated recruitment [32]. Since biological experiments have shown that cell polarity occurs even in the absence of Bem1, recent models emphasize the GDI-mediated exchange between the cytosol and the plasma membrane and the associated different diffusion rates [48, 84]. However, these reaction-diffusion Turing-type models do not take into account the suggested actin-mediated feedback loop. Cdc42 orients actin cables, which in turn deliver secretory vesicles containing Cdc42. Vesicle trafficking models based on stochastic equations have demonstrated that this mechanism can either reinforce [28, 98] or perturb polarization [52, 76].

Following the approach proposed by [32] and [48], we present a minimal mathematical model based on reaction-diffusion-advection equations that, in addition to the diffusive transport, explicitly includes an advective term to simulate the actin-mediated vesicle transport. Vesicles move along actin cables, thus we additionally consider actin polymerization and depolymerization and incorporate exocytosis and endocytosis of Cdc42. Since we consider multiple substances, either cytosolic, membrane-bound, or vesicle-bound, and model the full geometry we have a coupled bulk-surface problem. Thereby, our model does not rely on a Turing-type mechanism as it includes the actin-dependent advection of molecules and distinguishes between a cytosolic and membrane domain. Unlike [28] or [47] we further describe vesicle transport in a continuous model, which allows a deeper analysis.

We present numerical results in 2D and 3D and compare those to experimental data. Thus, we show that the model is able to reproduce experimentally observed pathological cases and demonstrate how vesicle trafficking could reinforce polarization.

Based on this specific model, we develop a general system of three membrane reaction-diffusion equations coupled to two diffusion equations inside the cell. Following the approach proposed in [72], we perform a linear stability analysis and derive conditions for a transport-mediated instability which are confirmed numerically. In order to conclude this work, we finally compare the continuous approach for actin cable movement to a stochastic model.





## Zusammenfassung

Die Hefe Zelle *Saccharomyces cerevisiae* bietet ein exzellentes Modellsystem zur Forschung der grundlegenden Mechanismen der Zellpolarität, ein fundamentaler Prozess für viele Funktionen in verschiedenen Zelltypen. Es wird vermutet, dass zwei positive Rückkopplungsschleifen zur lokalen Polarisierung des wichtigsten Proteins Cdc42 beitragen, ein Aktin-abhängiger und ein Aktin-unabhängiger Prozess.

Ein bekanntes Modell erklärt Polarität durch einen Turing-basierten Reaktions-Diffusions-Prozess [32]. Hierbei führt eine Bem1-vermittelte Rekrutierung zur Konzentration von Cdc42. Da biologische Experimente allerdings gezeigt haben, dass Zellpolarität auch ohne Bem1 erreicht werden kann, heben jüngste Forschungen den GDI-vermittelten Austausch zwischen dem Zytosol und der Plasmamembran und die damit verbundenen unterschiedlichen Diffusionsraten hervor [48, 84]. Doch Turing-artige Reaktions-Diffusions-Modelle berücksichtigen keinen Aktin-basierten Feedback. Die Richtung der Aktinkabel, welche in der Lage sind sekretorische Vesikel mit Cdc42 zu transportieren, hängt von der lokalen Cdc42-Konzentration ab. Vesikelmodelle, die auf stochastischen Gleichungen basieren, haben gezeigt, dass dieser Mechanismus die Polarität entweder verstärken [28, 98] oder aber auch stören kann [52, 76].

In Anlehnung an die Modelle von [32] und [48] präsentieren wir hier ein minimales Modell, das auf Reaktions-Diffusions-Advektions-Gleichungen basiert. Zuzüglich zum diffusiven Transport schließt dieses Modell einen advektiven Term ein, um den Aktin-basierten Transport zu simulieren. Da sich Vesikel entlang Aktikabel bewegen, berücksichtigen wir außerdem Aktin-Polymerisation und Depolymerisation sowie Exozytose und Endozytose von Cdc42. Das Modell simuliert mehrere Substanzen, die entweder im Zytosol, an der Membran oder vesikelgebunden vorzufinden sind. Dabei modelliert es die gesamte Geometrie der Zelle, so dass ein gekoppeltes System zwischen dem Volumen und der Oberfläche entsteht. Durch die Unterscheidung von Zytosol und Membran sowie die Berücksichtigung der advektiven Bewegung von Molekülen, basiert das Modell nicht nur auf einem Turing-artigen Mechanismus. Anders als [28] oder [47] nutzen wir ein kontinuierliches Modell, um den Vesikeltransport zu simulieren, wodurch eine ausführlichere Analysis möglich ist.

Wir präsentieren numerische Ergebnisse in 2D und 3D und vergleichen diese mit experimentellen Daten. Wir zeigen, dass das Modell experimentell beobachtete pathologische Fälle reproduzieren kann und veranschaulichen, wie Vesikeltransport die Polarität verstärken kann.

Basierend auf diesem speziellen Modell entwickeln wir ein allgemeines System von drei auf der Membran definierten Reaktions-Diffusions-Gleichungen, gekoppelt an zwei in der Zelle definierten Diffusions-Gleichungen. Dem Ansatz aus [72] folgend, führen wir eine lineare Stabilitätsanalyse durch und leiten Bedingungen für eine transportgetriebene Instabilität her, welche wir numerisch untermauern. Um die Arbeit abzuschließen, vergleichen wir schließlich den kontinuierlichen Ansatz zur Modellierung der Aktinkabelbewegung mit einem stochastischen Modell.

# Contents

<b>1. Introduction</b>	<b>1</b>
1.1. Motivation . . . . .	1
1.2. Objective . . . . .	2
1.3. Outline . . . . .	3
<b>2. Biological preliminaries</b>	<b>5</b>
2.1. The mechanism of cell polarity . . . . .	5
2.2. The role of the cytoskeleton . . . . .	7
2.3. The Rho GTPases as key regulators in cell polarity . . . . .	8
2.4. Yeast as a model system for cell polarity . . . . .	9
2.4.1. Yeast polarity pathways and Cdc42 as key regulator . . . . .	11
2.4.2. Models for yeast cell polarity . . . . .	19
<b>3. Mathematical preliminaries</b>	<b>29</b>
3.1. Mathematics of reaction-diffusion-advection equations . . . . .	29
3.1.1. Conservation principles . . . . .	31
3.1.2. Diffusion and advection . . . . .	32
3.1.3. Initial and boundary conditions . . . . .	34
3.1.4. Systems of reaction-diffusion-advection equations . . . . .	36
3.2. Stability analysis . . . . .	37
3.2.1. Stability of linear systems . . . . .	39
3.2.2. Principle of linearized stability . . . . .	42
3.3. Turing instability and pattern formation . . . . .	43
3.4. Traveling waves in reaction-diffusion equations . . . . .	49
3.5. Sobolev spaces and the weak formulations . . . . .	51
3.6. Coupled bulk-surface PDEs . . . . .	56
<b>4. Numerical methods</b>	<b>61</b>
4.1. Triangulations and ansatz spaces . . . . .	61

## Contents

4.2. Finite Elements and the Galerkin method . . . . .	63
4.3. Finite volume methods . . . . .	65
4.3.1. Dual box-grids . . . . .	65
4.3.2. Upwind stabilization . . . . .	67
4.4. Time discretization . . . . .	69
<b>5. Computational implementation</b>	<b>71</b>
5.1. The DUNE framework . . . . .	71
5.1.1. DUNE core modules . . . . .	72
5.1.2. Dune-multidomain and dune-multidomaingrid . . . . .	73
5.2. Numerical treatment of coupled bulk-surface problems . . . . .	75
5.3. Dual grid assembly . . . . .	77
5.4. The implementation of test problems . . . . .	79
5.4.1. A coupled-bulk-surface test problem . . . . .	79
5.4.2. An advection-dominated test problem . . . . .	83
5.5. Discussion . . . . .	85
<b>6. A continuous reaction-diffusion-advection model for yeast cell polariza- tion</b>	<b>87</b>
6.1. The reaction-diffusion system . . . . .	87
6.2. The reaction-diffusion-advection system . . . . .	91
6.2.1. Transport from and to internal membranes . . . . .	92
6.2.2. Transport through a domain . . . . .	97
6.3. Numerical simulations . . . . .	99
6.3.1. Polarization in the absence of actin-mediated transport . . . . .	103
6.3.2. Enhanced polarization by actin-mediated transport . . . . .	105
6.3.3. Actin-mediated transport in the absence of Bem1 . . . . .	109
6.3.4. Actin-mediated transport in the absence of GDI . . . . .	116
6.4. Model comparison . . . . .	119
6.5. Discussion . . . . .	120
<b>7. Derivation of a generic bulk-surface reaction-diffusion-advection system</b>	<b>123</b>
7.1. Model reduction . . . . .	123
7.2. Non-dimensionalization . . . . .	125
7.3. The generic coupled bulk-surface reaction-diffusion-advection system	128
7.3.1. Numerical results . . . . .	129
7.3.2. Applications of models from the literature . . . . .	143

7.4. Linear stability analysis . . . . .	152
7.4.1. Numerical results . . . . .	170
7.5. Discussion . . . . .	173
<b>8. A stochastic approach to vesicular trafficking-mediated cell polarity</b>	<b>177</b>
8.1. Brownian motion on a surface . . . . .	177
8.1.1. The two-dimensional case . . . . .	178
8.1.2. The three-dimensional case . . . . .	178
8.2. Derivation of the stochastic model . . . . .	180
8.3. Numerical results . . . . .	182
8.4. Discussion . . . . .	184
<b>9. Summary and outlook</b>	<b>187</b>
<b>A. Chemical reactions</b>	<b>191</b>
<b>B. Spherical harmonics</b>	<b>193</b>
<b>C. Glossary</b>	<b>195</b>
<b>D. Notation and symbols</b>	<b>199</b>
<b>Bibliography</b>	<b>201</b>



# List of Figures

1.1. The emergence of human existence . . . . .	2
2.1. Types of cell polarity . . . . .	6
2.2. Scheme of the GTPase cycle . . . . .	8
2.3. Scheme of polarization in budding yeast . . . . .	10
2.4. Model of actin-mediated transport . . . . .	12
2.5. Signaling pathways of GTPases in budding yeast . . . . .	13
2.6. Schemes of molecular mechanisms underlying polarity in budding yeast	14
2.7. Polarized budding yeast cells . . . . .	17
2.8. Schematic representation of the pathological cases observed by bio- logical experiments . . . . .	18
2.9. Overview of mathematical models for transport-mediated yeast cell polarity . . . . .	26
2.10. Overview of reaction-diffusion models for yeast cell polarity without consideration of active transport . . . . .	27
2.11. Overview of coupled reaction-diffusion-transport-models for yeast cell polarity under consideration of active transport . . . . .	28
3.1. Scheme of a control volume . . . . .	31
3.2. Illustration of diffusion in a domain . . . . .	32
3.3. Illustration of advective transport through a domain . . . . .	33
3.4. Illustration of stability of an equilibrium . . . . .	39
3.5. Plot of functions determining a Turing-type instability . . . . .	48
3.6. Illustration of a Turing-type pattern . . . . .	49
3.7. Plot of a traveling wave solution for the Fisher equation . . . . .	51
3.8. Numerical solution of the <i>Wave-Pinning</i> system . . . . .	59
4.1. Basis functions for a finite element space in 1D . . . . .	63
4.2. Visualization of the dual grid for a 2D or 3D simplex . . . . .	66
4.3. Basis functions for a finite volume space in 1D . . . . .	69

## List of Figures

5.1. Illustration of the numerical approach to solve a coupled bulk-surface problem with dune-multidomaingrid and dune-multidomain . . . . .	75
5.2. Dual nodes and edges in a 2D reference element . . . . .	77
5.3. Analytical solution of the coupled bulk-surface test problem . . . . .	80
5.4. Plot of relative errors computed with the test problem . . . . .	83
5.5. Comparison of the Galerkin method and the vertex-centered finite volume upwind scheme . . . . .	84
6.1. Reaction scheme of the model system . . . . .	89
6.2. Model geometry for the reaction-diffusion system . . . . .	90
6.3. Model geometry for the reaction-diffusion-advection system . . . . .	93
6.4. Illustration of the vesicular trafficking machinery . . . . .	98
6.5. Comparison of stimuli induced polarity for cells treated with latrunculin A . . . . .	106
6.6. Effect of parameter changes on polarization . . . . .	107
6.7. Cdc42-GTP cluster formation considering transport through a defined domain . . . . .	108
6.8. Effect of transport related parameter changes on actin-mediated polarization in distinct phenotypes . . . . .	110
6.9. Effect of the endocytic control rate on the shape of the polar cluster	110
6.10. Effect of parameter changes on transport-mediated polarization . . . . .	111
6.11. Numerical simulations of the pathological cases . . . . .	112
6.12. Predicted dynamics in Bem1 mutant cells exhibiting a homogeneous but high GEF activation . . . . .	114
6.13. Cdc42-GTP cluster height for changing molecule numbers . . . . .	115
6.14. Computational results showing two transient peaks . . . . .	117
6.15. Cdc42-GTP cluster formation considering transport from and to internal membranes . . . . .	118
6.16. Comparison of polarization in different mutant cells . . . . .	119
7.1. Illustration of a cell that fails to polarize due to transport . . . . .	132
7.2. Numerical simulations of the generic system using distinct kinetic functions applied to a sphere . . . . .	134
7.3. Numerical simulations of the generic system using distinct kinetic functions applied to an ellipse . . . . .	135
7.4. Numerical simulations of the generic system using distinct kinetic functions applied to a rod-shaped cell . . . . .	136



7.5. Numerical simulations of the generic system using distinct kinetic functions applied to a cell with a protrusion . . . . .	137
7.6. Comparison of the impact of transport on cell polarity in a rod-shaped cell . . . . .	138
7.7. Computational results showing the influence of non-uniform membrane diffusion on trafficking-mediated cell polarity . . . . .	139
7.8. Illustration of the influence of internal barriers on cell polarization .	141
7.9. Comparison of the influence of organelles as well as the cell shape on diffusion- and transport-mediated polarization . . . . .	142
7.10. Numerical simulations of the WP system applied to a sphere . . . . .	144
7.11. Investigation of the influence of internal barriers on diffusion- and transport-mediated polarization calculated with the WP system . .	145
7.12. Investigation of the influence of internal barriers and the cell shape on diffusion- and transport-mediated polarization calculated with the WP system . . . . .	146
7.13. Computational results of the GOR and WP system using distinct rates of endocytosis . . . . .	148
7.14. Computational results of the GOR system applied to a sphere . . .	149
7.15. Simulations of the GOR system considering distinct diffusion barriers	150
7.16. Investigation of the GOR system for the influence of internal barriers and cell shape on polarization . . . . .	151
7.17. Computational results demonstrating the influence of the diffusion constant for actin cable movement on the polarization process . . .	170
7.18. Numerical simulations of the generic system showing distinct cases of instability . . . . .	171
7.19. Numerical simulations of the generic system showing capacity-driven instability . . . . .	171
7.20. Numerical simulations of the RR model showing distinct cases of instability . . . . .	172
7.21. Numerical simulations of the RR model showing capacity-driven instability for equal membrane and cytosolic diffusion constants . .	172
8.1. Schematic representation of the calculation procedure for standard Brownian motion on a surface . . . . .	179
8.2. Computational results of the stochastic approach in 2D . . . . .	183
8.3. Computational results of the three-dimensional stochastic approach	184



# List of Tables

5.1. Overview over bulk $L^2$ errors and EOCs calculated for the test problem	81
5.2. Overview over bulk $H^1$ errors and EOCs calculated for the test problem	81
5.3. Overview over surface $L^2$ errors and EOCs calculated for the test problem . . . . .	82
5.4. Overview over surface $H^1$ errors and EOCs calculated for the test problem . . . . .	82
6.1. Reaction rate constants and parameter estimates used to solve the reaction-diffusion system . . . . .	103
6.2. Parameter sensitivity of the system with and without transport . .	113
6.3. Reaction rate constants and parameter estimates used to simulate active transport . . . . .	113
7.1. Overview over parameters used for computations of the generic system	133
7.2. Parameters used for numerical simulations of the WP and GOR system	147
8.1. Parameters used to simulate the stochastic approach. . . . .	184



# 1 | Introduction

In the course of this thesis, we will introduce a novel mathematical approach for transport-mediated cell polarization. It is derived from a complex model proposed for symmetry breaking in budding yeast. However, because of its flexibility, it can be applied to a variety of cell types. Before going into the details, we first motivate our principal topic.

## 1.1. Motivation

Look at the picture 1.1. For an embryo to become a living organism, the formation of certain cell and tissue types is not enough. They must emerge at the correct time and in a proper direction. Ever wonder why the nose is in the middle of the face and the ears are on each side of the head? Or asked differently: What are the mechanisms behind this development? How do the cells know how to develop? How do they know the right direction?

The determination of the underlying mechanisms, which lead to this development and thereby define top and down or front and back, is a challenging problem. The study of cell polarity mainly addresses this issue. However, to solve this problem you have to start at the first-line level of cells which are themselves profoundly polarized. It is not without reason that the cell is called the fundamental unit of life. Cells have to provide many different functions, particularly they reproduce by division. Without cell division any other living thing would not continue to live. For example, without the replacement of red blood cells each human would have a very short life expectancy, corresponding to that of red blood cells. To accomplish these special various and famous functions in living organisms, cell polarization is an essential process. Only by this important mechanism is the cell able to divide asymmetrically. Conversely, the lack of polarization can have fatal consequences, e.g. cells may develop abnormally. Concerning the human organism, this can cause the development of diseases or mutations. Studies currently examine if infections or cancer may emerge due to a failure to polarize [94].



**Figure 1.1.: The emergence of human existence.** Image of an embryo which grows and develops into an infant [99,102].

However, dependent on the increasing complexity in the course of ever smaller systems, biological experiments become more and more difficult. Meanwhile, mathematical models and simulations play an important role in supporting biological research. Besides theory and experiment, computational simulations can give insights into these complex systems.

## 1.2. Objective

The main goal of this work is the derivation of a mathematical model for cell polarization as well as its numerical and analytical study. The model contributes to the understanding of underlying processes involved in symmetry breaking. Based on the signaling pathways of budding yeast, a first rather complex model simulates distinct experimentally observed pathological cases. Taking account of the full cell geometry, its investigation by numerical simulations helps to make predictions which can be proved by biological experiments. For example, the sensitivity analysis of this system yields statements about the system behavior due to parameter changes.

Since the analytical study of such complex models is very difficult, another aim of this thesis is to derive a generic and more flexible system. It serves as an exemplary model for transport-mediated cell polarization that can not only be analyzed analytically but also be studied in terms of different structure forming systems. Considering distinct kinetic functions, it allows the investigation of pattern formation in different cell types. In doing so, it is possible to determine how the cell shape influences transport-mediated polarity.

In order to demonstrate how delivery mechanisms can induce a sustained cluster, the linear stability analysis of the generic system is a further goal of this work. This analysis serves to derive stability and instability conditions which allow determination of when a small initial perturbation of the homogeneous state leads to a spatial pattern, even under unusual circumstances.

## 1.3. Outline

This thesis consists of nine chapters. After this introduction, Chapter 2 will provide the biological background needed to understand the process of cell polarization. Starting with a general explanation of cell polarity, this work mainly focuses on the yeast cell as a convenient model organism. How this process occurs in budding yeast is explained. Furthermore, the main signaling pathways relevant for the model derivation and its simulations are presented.

This basic part is followed by a chapter that provides the mathematical preliminaries required for the formulation and analysis of a model problem as discussed in this work.

Chapter 4 and 5 address implementation issues. These parts are concerned with the numerical realization of the model problems, including numerical schemes. The simulations are computed with the DUNE framework, especially using the `dune-multidomaingrid` and `dune-multidomain` modules. Its main concepts and how they serve to simulate the equations presented in this thesis are briefly explained. For a test problem, the stability and the convergence of the employed numerical approach is shown.

Chapter 6 is central to this work. It derives the continuous model for transport-mediated cell polarization which is the basis of the numerical simulations presented in this thesis. It is a new approach to the modeling of vesicular trafficking-mediated cell polarization in yeast cells. Different results are discussed and compared to previous ones.

The following chapter deals with the non-dimensionalization and reduction of this complex system to a generic approach. This has the advantage that it can be applied to different cell types and hence cell geometries. By means of a stability analysis, conditions for a transport-driven instability resulting in polarization are deduced. The theoretical results are then compared to numerical simulations.

As we will see later on, the continuous approach to the transport feedback performed here is a simplification of a discrete biological process. In order to ascertain whether this simple approach qualitatively affects the results, Chapter 8 deals with a stochastic approach to this mechanism.

A summary and outlook of this work follows in Chapter 9. The subsequent appendix provides short introductions into further mathematical tools and concepts used for the model derivation, implementation, and its stability analysis. It further supplies a glossary with biological terms as well as a list of abbreviations, notations, and mathematical symbols.





## 2 | Biological preliminaries

To develop a mathematical model that simulates a specific biological phenomenon, it is important to figure out its fundamental mechanisms. Therefore, this chapter is concerned with the underlying pathways leading to the process of cell polarity. Since Rho GTPases are often assumed to play an important role in symmetry breaking, the significance of Rho GTPases and their features are subsequently presented. One function of Rho GTPases is the regulation of the cytoskeletal system. Since the organization of the cytoskeleton is another important aspect in cell polarization, the ensuing section covers this topic. Depending on the cell type, different cell polarities can occur. However, in this thesis we are mainly interested in the modeling of budding yeast cell polarization. Therefore, we further focus on the determining signaling pathways important for symmetry breaking in this model organism.

### 2.1. The mechanism of cell polarity

Cell polarity is a crucial process during cell development in both single-celled and multicellular organisms. It describes the formation of specific molecules in certain regions of the cell which leads to the definition and maintenance of a spatial arrangement. Through this symmetry breaking event the cell generates an internal functional, structural, and molecular difference which is important for many cellular processes. For instance, the process of cell polarity determines the growth of different eukaryotic cells. As a result of intrinsic or extrinsic cues, an asymmetric distribution and/or activation of downstream effectors enables the cell to generate different shapes. In addition to its role in cell growth and morphogenesis, symmetry breaking is essential for cell migration, signal transmission or cell differentiation and proliferation. Consequently, the ordered, asymmetric distribution of proteins and membrane components in the cell is the basis to specifically and efficiently realize fundamental cellular functions.

Depending on cell types, different specific cell polarities can be distinguished. To emphasize the multiplicity of polarization aspects, Figure 2.1 shows a few examples of

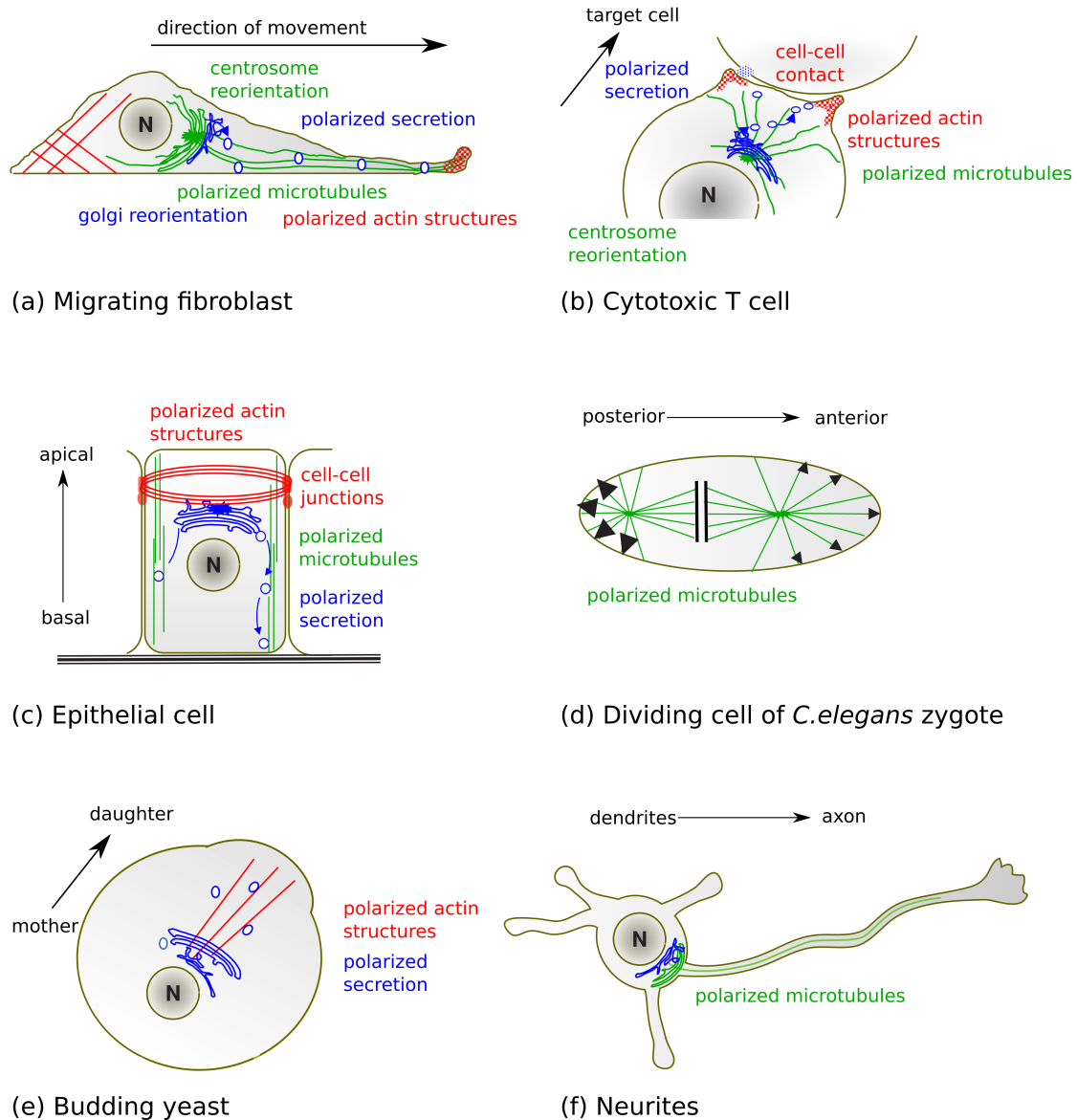


**Figure 2.1.: Illustration of different polarized cells.** A few examples of polarized cells are shown to demonstrate the importance of cell polarity and its different aspects. (a) Migrating fibroblasts form actin-rich extensions at the leading edge to drive protrusions of the membrane and its associated cell movement. (b) Polarized cytoskeletal assemblies and secretion characterize polarization of cytotoxic T cells. (c) Epithelial cells show polarized actin structures and secretion. These polarized orientation promotes the formation of an apical and basal domain. (d) Dividing cells of *C. elegans* zygote form a posterior and anterior domain characterized by polarized microtubules and the location of specific polarity regulators. (e) Budding yeast cells require polarized actin structures and secretion to generate the daughter cell. (f) Neurites polarize to form a long thick axon and multiple dendrites. Thereby, actin and microtubules act in parallel to reinforce neuronal asymmetry (modified on [24, 25]).

polarized cells. For instance, in migrating cells like yeast cells or filopodia polarization refers to a so-called front-rear polarity. The front determines the part closest to the migration direction and the rear its opposite side. In this case, a molecular and functional difference between these two parts provides the force and defines the direction of cell movement [73].

Contrarily, epithelial cells which constitute the assignment to the exterior milieu feature an apical-basal polarity. Like in the case of a front-rear polarity, polarization in these cells describes the functional and structural difference of specific cell regions, also referred to as domains. According to this, the apical domain which faces the external environment separates from a basolateral domain which is in contact with the interstitial space. These domains are kept apart by tight junctions that act as a fence at the boundary between them. In epithelial cells, cell-cell or cell-substrate adhesion initially generates polarity. Subsequently, intracellular polarity complexes and a polarized membrane transport regulate the arrangement of proteins. It is assumed that these complexes give essential cues that control a polarized organization of epithelial cells [65,90].

The establishment of an axon out of multiple neurites provides a further example for the importance of cell polarization. During the development of the nervous system neurons polarize to generate a single long axon and multiple dendrites [89].

An example for polarization on the level of a variety of cells is planar cell polarity (PCP). This process applies to cells with diverse morphologies and is mainly based on the so-called PCP signaling pathway. It regulates the collective array and behavior of cells across the tissue plane. Since PCP is a global property of multicellular tissues, it requires the establishment of asymmetry within cells and the alignment of these asymmetries in cells located dozens or hundreds of cells apart [106].

## 2.2. The role of the cytoskeleton

Filamental structures cross eukaryotic cells and entirely form the cytoskeleton which is crucial for many cellular processes. Composed of protein filaments, it constitutes a complex, flexible, and dynamic meshwork in the cytoplasm. The most important types of protein structures are actin filaments and microtubules [19,69]. The cytoskeleton causes a multiplicity of essential biological functions in all eukaryotic cells [36]. For instance, it contributes to cell motility, development and maintenance of cellular morphogenesis, intracellular transport, contractility, and the interaction with the extracellular matrix [19]. The cytoskeleton also has an important role in the establishment of cell polarity. Polarization establishment affects different

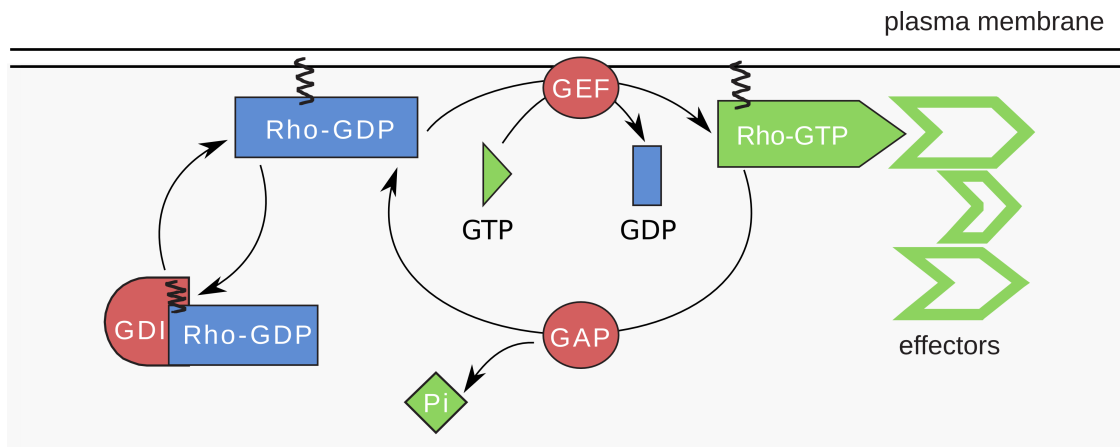


**Figure 2.2.: Scheme of the GTPase cycle.** GTPases switch between an inactive, GDP-bound and an active, GTP-bound state. While the GDI-bound GTPase diffuses in the cytosol, the inactive GTPase is recruited to the plasma membrane. There GEFs catalyze the exchange of GDP to GTP and hence achieve its activation (modified on [25]).

cellular processes and by association causes changes in the cytoskeleton. Thus, the rapid assembly and disassembly may be a fundamental property of eukaryotic actin cytoskeletons [6, 7]. Furthermore, cells require a dynamic actin cytoskeleton to achieve polarization. For instance, the actin filaments within the growth cone of the future axon of a neuron are highly dynamic in contrast to those within other minor neurites. Furthermore, during elongation of neurites the actin filaments show rigorous deformations [3, 104].

### 2.3. The Rho GTPases as key regulators in cell polarity

A special protein family, the Rho GTPases (*guanosine triphosphatases*), mainly regulates signaling pathways which are critical for the establishment of cell polarity. Rho GTPases feature many different cellular functions. They affect numerous proteins downstream which in turn control different signaling pathways. In this way they regulate the organization and the modification of the actin cytoskeleton, cell adhesion, migration, cell polarity, cell differentiation, endocytosis, vesicle trafficking, and oncogenesis (development of cancer). For this reason, Rho GTPases are key integrators of environmental signals which are essential for the establishment of cell polarity [25, 67].

Rho GTPases are members of the super family of small guanosine triphosphate

(GTP)-bound proteins (G-Proteins). They function as molecular switches between their active, GTP-bound form and their inactive, guanosine diphosphate (GDP)-bound form. The inactive form is achieved by hydrolysis of GTP to GDP [25,88]. Certain exchange factors regulate this cycle. The so-called guanine nucleotide exchange factors (GEFs) and GTPase activating proteins (GAPs) as well as GTPase dissociation inhibitors (GDIs) affect the activity of GTPases. GEFs catalyze GDP/GTP exchange and GAPs inactivate GTPases. Via binding to GTPases GDIs prevent membrane association and thereby GTP activation (see Figure 2.2) [25, 50, 88].

## 2.4. Yeast as a model system for cell polarity

The investigation of model organisms provides a promising approach to study molecular mechanisms that underlay and maintain cell polarity. Model organisms are well documented non-human species used to understand specific biological processes. Using simple but effective culture conditions it is expected that discoveries made in the organism model will give an insight into the functions of other organisms. Therefore, the choice of a model organism particularly depends on the biological issue.

To investigate the constitutive mechanisms of cell polarity the eukaryote of budding yeast (*Saccharomyces cerevisiae*) provides an exemplary model organism. The budding yeast is a single-cell organism in which cell differentiation and morphogenesis directly depend on cell polarity. It is essential to division and mating. Furthermore, these cells polarize at different times during cell division. More importantly, the culturing of yeast cells is simple and the genetics are comprehensively studied. However, polarization of yeast cells shares many features with symmetry breaking in more complex cells with regard to the internal cell structure [17, 42].

Three major stages characterize the yeast life cycle: Cell division by budding, mating and sporulation. During budding and mating, cells are highly polarized whereby sporulating cells remain unpolarized [17].

In this thesis we will focus on the polarization during budding. Figure 2.3 illustrates the formation of an axis of polarization in budding yeast cells. This process is spatially as well as temporally controlled: The bud develops at a distinct site of the cell cortex and to a certain time in the cell cycle. At first the growth of cells proceeds isotropically until it reaches a critical size and retracts a bud. The development of this bud can normally be separated into two consecutive stages. During the short initial stage a cluster of active Cdc42, a small GTPase of the Rho family which is the key regulator of polarity in yeast, establishes at the inner face of the plasma membrane.

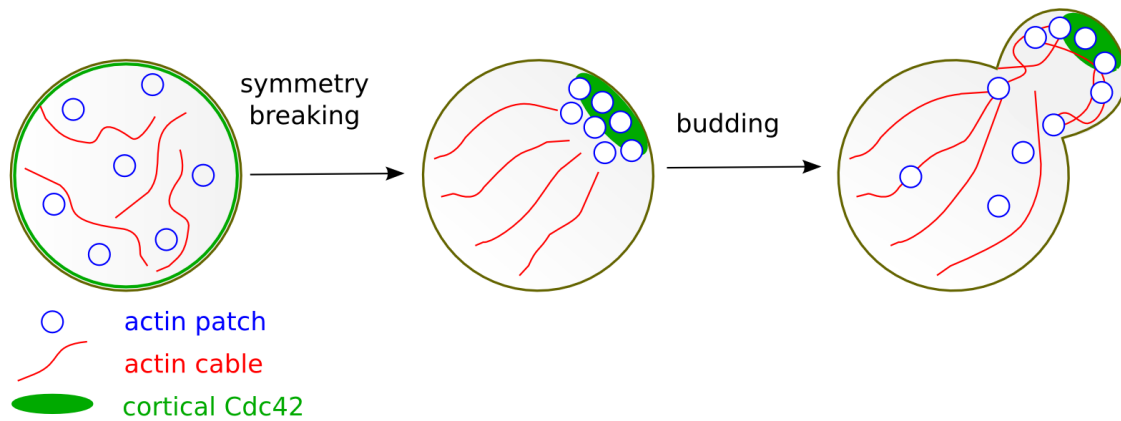


**Figure 2.3.: Polarization in budding yeast.** Initially the distribution of Cdc42 is uniform at the plasma membrane. In response to extracellular guidance cues or spontaneously the cell becomes polarized. This leads to a cluster of activated Cdc42 at the bud-site and hence polarized growth (modified on [82]).

Thereby, specific so-called landmark proteins determine the site of polarized growth. Among others, the Ras family GTPase Rsr1/Bud1 and its regulators have been identified to play a key role in this selection step. They determine a specific site for polarized growth. In newborn cells this is naturally the position around the bud scar remaining from the previous cell division (1. Choosing a direction for polarization). This step is followed by an adjacent recruitment of components essential for bud formation at the chosen site. Its assembly, which needs the activation of the Rho family GTPase Cdc42 and its effectors, is required for bud growth at the polar site. The interaction of Cdc42 with various proteins causes downstream processes and leads to the formation of actin cables as well as a concentric septin ring that defines the bud neck (2. Building an axis). In the ensuing phase of growth and elongation the actin cables serve as tracks for polarized exocytosis of vesicles. These vesicles eventually provide material for the bud growth. This polarized patch remains focused at the bud tip at the early phase of bud growth but becomes broader and disperses as the bud extends [17, 42, 67, 97, 98].

Although it is difficult to separate between them, it is reasonable to distinguish the establishment of Cdc42 polarization from the maintenance of its polarization. In wild type cells internal and external spatial cues like a pheromone gradient or the bud scar control polarity establishment. However, yeast cells are also able to polarize spontaneously. Spontaneous polarization means that the cell is able to polarize correctly without any directional cue. In this case, the cells exhibit no defects in polarity establishment and maintenance or cell morphology. Only polar cluster formation and the subsequent bud growth proceeds in a random direction [85, 97].

### 2.4.1. Yeast polarity pathways and Cdc42 as key regulator

Yeast cell polarity is a complex process that requires the activation of different signaling pathways coordinating multiple cellular activities. The most prominent feature in the process of budding is the organization of the polarized actin cytoskeleton which guides secretion towards the bud-site, resulting in polarized cell growth. While in higher eukaryotes microtubules as well as actin are important for polarization, only actin is essential in yeast cells [7, 43]. The importance of an intact actin cytoskeleton could be shown by studies using drugs that cause the disassembly of filamentous actin. In that regard, its depolarization resulted in an isotropic growth of the mother cells [6, 70].

The polarized actin cytoskeleton consists of filamentous actin structures such as actin patches and actin cables. Actin patches which accumulate at the polarized site for bud growth and actin cables which are polarized towards this site have different properties. Whereas patches may serve as docking sites for vesicles or as endocytosis sites for recycling of membrane, cables may serve as tracks for directed transport of organelles and secretory vesicles to the bud-site. In this way actin is required to localize secretory vesicles. This transport is achieved by cortical type V myosin Myo2 which functions as a cargo motor using actin cables as tracks (see Figure 2.4) [33, 46, 71]. Due to this, actin cables are necessary for several events important for cell polarization like polarized delivery, transport of late Golgi elements into the bud, and asymmetric transport of mRNA [17, 67].

In addition to cables and patches as structures of the actin cytoskeleton, it consists of an contractile septin ring. By regulation of septin dynamics throughout the budding process, actin rings help to constrict the bud neck and to accurately coordinate morphogenesis [18].

The dynamics of actin filaments is determined by balanced activities of stabilizing and destabilizing proteins. It involves nucleation by formins, stabilization by tropomyosins, and cross-linking or bundling by actin-binding proteins (ABPs) [100]. This is why actin assembly and organization of the cytoskeleton changes rapidly during cell polarity [7]. Two different actin nucleators, the Arp2/3 complex and formins, regulate this rearrangement. While the formins Bni1 and Bnr1 are important for actin cables, actin patches are nucleated through the Arp2/3 complex [26, 75, 101]. Since Myo2 contributes to actin dynamics and thereby actin remodeling as well, a recent study suggests that the cargo motor Myo2 may also function as a motor for translational cable movement at the cell cortex [105].

In Sections 2.2 and 2.3 we already discussed the role of GTPases in the process of cell polarization and especially its impact on the cytoskeleton. In yeast cells Rho

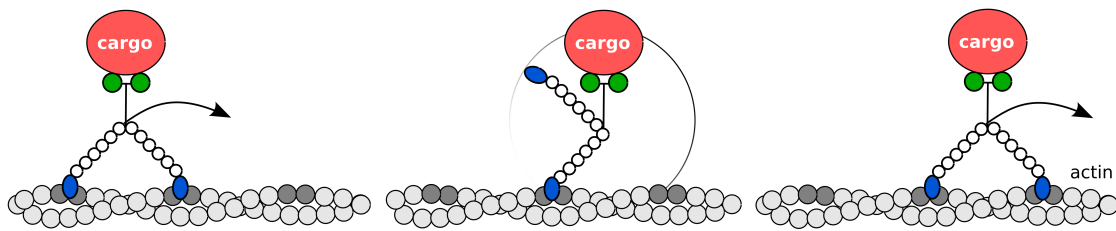


**Figure 2.4.: Model of actin-mediated transport.** During its ATPase cycle, conformational changes in the actin-binding domain lead to the rotation of the lever arm. Thus, the movement of a myosin-V dimer along actin is a result of repeated binding sites (highlighted in gray) (modified on [78]).

GTPases are involved in the step of bud-site selection and bud-site assembly. In the latter step of budding GTPases regulate the activity of stabilizing and destabilizing proteins [36, 67]. Through this, Rho GTPases regulate the polarized organization of the actin cytoskeleton and cell wall biogenesis [67, 98].

These GTPases include Rho1 and Rho2, Rho3, and Rho4, and the Rab family GTPase Sec4. For instance, Rho1 and Rho2 are supposed to maintain polarization of the actin cytoskeleton and cell wall biosynthetic activities [17]. Rho GTPases also regulate the directed movement of secretory vesicles. Biological experiments have demonstrated that Rho1, Rho3, and Cdc42 regulate the so-called exocyst, a multiprotein complex that is involved in this process. ROBINSON ET AL. [74] showed that Rho3, which plays an essential role in the control of bud growth, acts upstream to Exo7, a component of the exocyst [74]. On the other hand Rho1 and Cdc42 control the Sec3 component of the exocyst [87].

Because of this, members of the Rho family of small GTPases turned out to be essential for the assembly of the actin cytoskeleton. But Rho3 does not only affect Exo7. It has also the ability to bind Myo2. As previously mentioned, Myo2 is an essential myosin that regulates transport of secretory vesicles and may control the cytoskeletal assembly. Thus, Rho3 further contributes to the delivery of exocytic vesicles. Furthermore, since Rho3 and Rho1 interact with Bni1, they are assumed to induce changes in the actin cytoskeleton [74, 75]. The activators Sec4 finally regulate secretion or exocytosis from the Golgi apparatus to the plasma membrane, a mechanism important for the emergence and growth of the bud [67] (see Figure 2.5 (b)).

As mentioned before, the localization of the GTPase Cdc42 to a single discrete site on the plasma membrane is a crucial event essential for the achievement of symmetry breaking and bud-site establishment in haploid yeast cells [67]. Genetic studies indicate that Cdc42 effectors act together with Cdc24 and Cdc42 GAPs like Bem2, Bem3, Rga1/Dbm1, and Rga2 to establish polarity (see Figure 2.5 (a)).



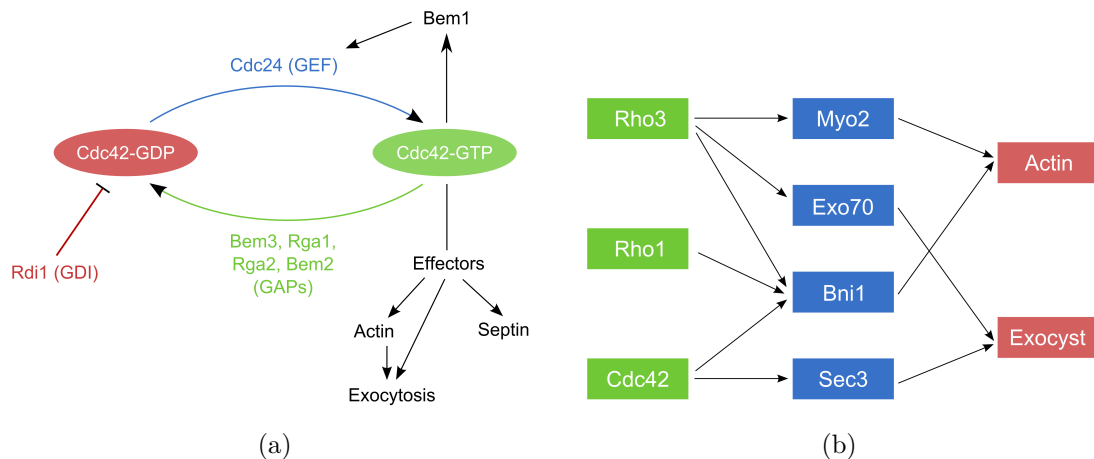


**Figure 2.5.: Signaling pathways of Rho GTPases in budding yeast.** (a) The activity of the GTPase Cdc42 is controlled by three types of regulators: the GEF Cdc24, the GAPs Bem3, Rga1, Rga2 and Bem2 as well as the GDI Rdi1. In its active form Cdc42 influences the assembly of the actin cytoskeleton and the septins. Furthermore, it is involved in the process of exocytosis (on [17]). (b) The exocytosis is regulated by three Rho GTPases that directly interact with a component of the exocyst: Rho3, Rho1 and Cdc42 (modified on [87]).

Among this the Rho family GTPase Cdc42 and its GEF Cdc24 are essential for the assembly of the polarized area and septin ring as well as for the polarization of actin cables [42, 67]. Cdc42 appears to function in two different modes: First, to turn on signaling pathways in its GTP-bound state and second, to assemble a macromolecular structure such as the septin ring [67]. Because of this, the GTPase Cdc42 is pointed out to be a key player in polarity establishment. In other words, it appears to be the central factor in polarizing the cell and is the convergence point for polarization machinery during budding [17]. This thesis focuses on the initial establishment of a polar Cdc42 cluster. This is why the signaling pathways leading to Cdc42 polarity are subsequently explained in more detail.

### Bem1-mediated polarity

We already mentioned that although *in vivo* the Cdc42 cluster is predetermined by landmark proteins including Rsr1, yeast cells can polarize even in the absence of any spacial cues. This random symmetry breaking process led to the hypothesis that an intrinsic ability to break symmetry exists. In this case, the initial asymmetric signal only affords the orientation for the pattern with respect to an internal or external cue [97]. Thus, one of the key issues concerning the role of Cdc42 in polarity development is to understand how Cdc42 itself becomes polarized and how its polarization state is maintained during the cell cycle [67].

Feedback loops have been linked to the fundamental process of pattern development

and gained in importance by describing the mechanisms underlying cell polarization [30,59]. Recent studies investigating the establishment of cell polarity in different cell types have shown that positive and negative feedback loops are important for the emergence of spontaneous polarization [54,66].

In budding yeast cells it has been proposed that the ability of Cdc42 to cycle between its active GTP-bound and inactive GDP-bound state is essential for actin-independent polarization. Together with the scaffold protein Bem1, this exchange generates a positive feedback mechanism. Bem1 builds a complex with active Cdc42, its GEF Cdc24, and its effector Cla4 to support the accumulation of Cdc42-GTP at the site of polarized growth. The localization of Bem1 at the emerging bud requires activated Cdc42. The expression of Cdc42-GTP is in turn sufficient to enrich Bem1 at the plasma membrane. Through the binding of Cdc24 to Bem1, Bem1 stabilizes Cdc24 at the polarized site so that its local accumulation may then result in a higher concentration of Cdc42-GTP and Cdc24 at the polar site. Thus, the Bem1-mediated complex formation generates a positive feedback loop (see Figure 2.6 (a)) [13,16]. Interestingly, this feedback loop is sufficient to achieve spontaneous polarization in the absence of landmark proteins. For instance, biological experiments using knock-out mutant cells have shown that whereas  $\Delta rsr1$  cells polarize in a random direction,  $\Delta rsr1 \Delta bem1$  double mutants fail to form a polarized cap [49].

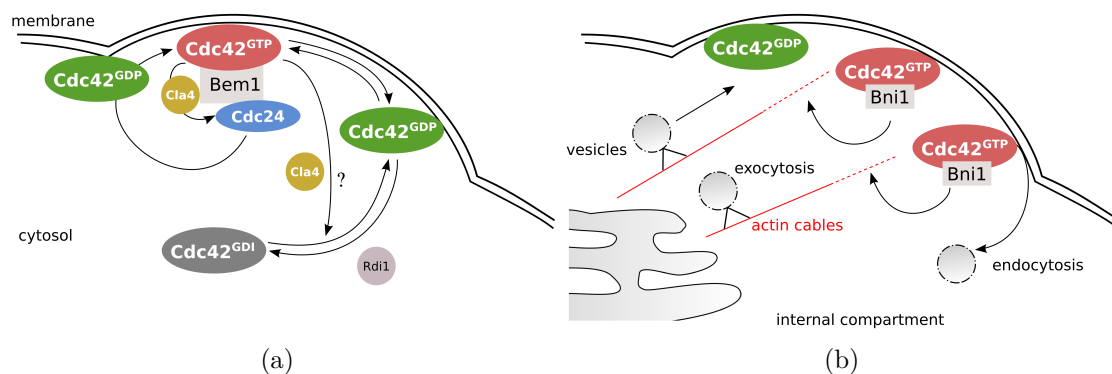


**Figure 2.6.: Schemes of molecular mechanisms that underlay the establishment and maintenance of spontaneous polarization in budding yeast cells.** (a) It is supposed that Cdc42 in its GTP-bound form clusters spontaneously and temporarily at the site of polarized growth. This becomes stabilized through the coupling with Bem1, Cdc24, and Cla4. The Bem1-based complex then leads to the phosphorylation of Cdc24 by Cla4 and thus to further recruitment of activated Cdc42 at the polarized site. (b) Simultaneously, Cdc42 in its GDP-bound and GTP-bound form is transported to this site. The transport is achieved by the type V myosin Myo2 that uses the actin cables as tracks to deliver secretory vesicles that carry Cdc42. At the growth site the inactive Cdc42 is disposed to activation by the GEF Cdc24. After its activation Cdc42 is able to bind to the formin Bni1, which nucleates actin. Since this leads to the assembly of further actin cables and hence an increased transport of Cdc42, this mechanism generates a positive feedback loop.

But not only the interaction between Bem1, Cdc24 and Cdc42 plays an important role in this feedback loop. The binding of Cla4 to Bem1 could also essentially contribute to this mechanism. It has been shown that, when bound to the same Bem1 molecule, Cla4 phosphorylates Cdc24 *in vivo* and *in vitro* [13, 16, 35, 51, 93]. But there are various opinions about the role of Cla4 within this complex so that the significance of Cdc24 phosphorylation still remains questionable. On the one hand, it has been suggested that phosphorylation of Cdc24 by Cla4 could contribute to the positive feedback by promoting polarized growth [13]. On the other hand, Cdc24 phosphorylation could negatively affect the feedback loop. In this case it is assumed that Cdc24 phosphorylation triggers the dissociation of Cdc24 from Bem1 [35]. Contrarily, the results of another study have suggested that Cdc24 phosphorylation provides a negative feedback by inhibiting GEF activity [51]. Thus, it is still unclear whether the initial Cdc42 activation involves phosphorylation of the GEF Cdc24.

### **GDI-mediated polarity**

Although the Bem1-mediated feedback loop and its associated cycling of Cdc42 between its GDP and GTP states is able to explain spontaneous polarization, this mechanism alone is not sufficient to guarantee robust cluster formation. As long as Rsr1 is present and locally activates Cdc42, even  $\Delta bem1$  cells still have the ability to polarize [41, 84]. These results implicate that other mechanisms are required for the generation of a robust and unique polarized patch. One of them belongs to the actin independent pathway which refers to the mechanisms that control the GTPase cycle. Besides Bem1, the Cdc42 cycle involves Rdi1, the sole GDI of budding yeast. Whereas Bem1 mediates a positive feedback mechanism, Rdi1 controls Cdc42-GDP recruitment. Rdi1 interacts with Cdc42 as it extracts Cdc42-GDP from the plasma membrane and then forms a Rdi1-bound complex. This complex diffuses in the cytosol and forms the cytosolic pool which is not only required to maintain but also to establish Cdc42 polarity under certain conditions. For instance,  $\Delta rdi1$  cells which also lack the below specified actin pathway fail to polarize [28, 84]. These results have shown that targeting of Cdc42 from the cytosolic Rdi1-bound pool is just as essential for Cdc42 cluster formation in the absence of actin-mediated vesicle transport as the feedback mechanism controlled by Bem1. In the absence of actin, polarity is only possible when both, Bem1 and Rdi1, ensure an intact GTPase cycle. However, the underlying molecular mechanisms triggering cytosolic targeting remain unclear. One possibility is that Cla4 may be involved in Cdc42 membrane recruitment and its subsequent activation. Biological research has shown that Cla4 disrupts Rdi1-Cdc42 complexes. Thus, Cla4 could negatively regulate the binding to Rdi1 either

by inhibition of the formation of a Rho GTPase-Rdi1 complex or, on the other hand, by disruption of an already existing complex [91] (see Figure 2.6 (a)). An alternative explanation could be a GEF-mediated displacement of Cdc42 from its GDI Rdi1 and a competition between GEF and GDI [48]. Nevertheless, the pathways involved in GDI-mediated polarity are still unknown and require further research.

### **Actin-mediated polarity**

In budding yeast cells different independent parallel acting feedback mechanisms are proposed to achieve and maintain symmetry breaking. Besides the mentioned actin-independent pathways, an actin-mediated feedback loop is hypothesized to contribute to polarization in budding yeast cells, or rather it is supposed to be required for the generation of robust cell polarity [96].

As mentioned before, actin cables serve as tracks to deliver secretory vesicles to the polarized site. Thereby, two forms of cables nucleated by Bni1 and Bnr1 can be distinguished. Whereas Bni1 nucleates cables which are localized to the bud tip, Bnr1 nucleates those localized to the bud neck. Since Cdc42 directly interacts with Bni1, it regulates the polarization of actin cables and hence generates a positive feedback loop [15]. In fact, it has been shown that a stochastic increase in the local concentration of activated Cdc42 on the plasma membrane enhances the probability of actin polymerization. An increased number of nucleated actin cables in turn leads to a higher probability of further Cdc42 accumulation at that site [96,98] (see Figure 2.6 (b)). Furthermore, it has been shown that inhibition of actin-based transport resulted in unstable Cdc42 clusters [98].

These mechanisms prove the importance of an intact actin cytoskeleton and hence polarized secretion.

But the actin cytoskeleton may also be involved in the process of endocytosis. Endocytosis describes the internalization of molecules, plasma membrane components, and extracellular material into cytoplasmic vesicles and its subsequent transport to internal compartments. Thus, it acts as opposing intracellular membrane trafficking process towards exocytotic secretion. Since the accumulation and stabilization of active Cdc42 require the balance of exocytosis and endocytosis, this internalization process also plays an important role in yeast cell polarity [47,56,79]. It is assumed that proteins are internalized from the cell surface to early endosomes via endocytosis. The vesicles then transit from the early endosome to the trans-Golgi network before they return to the plasma membrane via exocytic secretion. That the latter process requires an intact actin cytoskeleton has been outlined above. Considerable evidence indicates that endocytosis and actin regulation are also closely linked processes. For

instance, cortical actin patches, which show a dynamic but characteristic distribution throughout the cell cycle, are often disrupted in endocytosis mutants [79]. Furthermore, disturbance of actin filament dynamics demonstrated that endocytosis requires an intact actin cytoskeleton [6].

In order to further illustrate the mentioned processes, Figure 2.7 finally shows microscopic images of budding yeast cells characterized by polarized Cdc42 and actin cables.

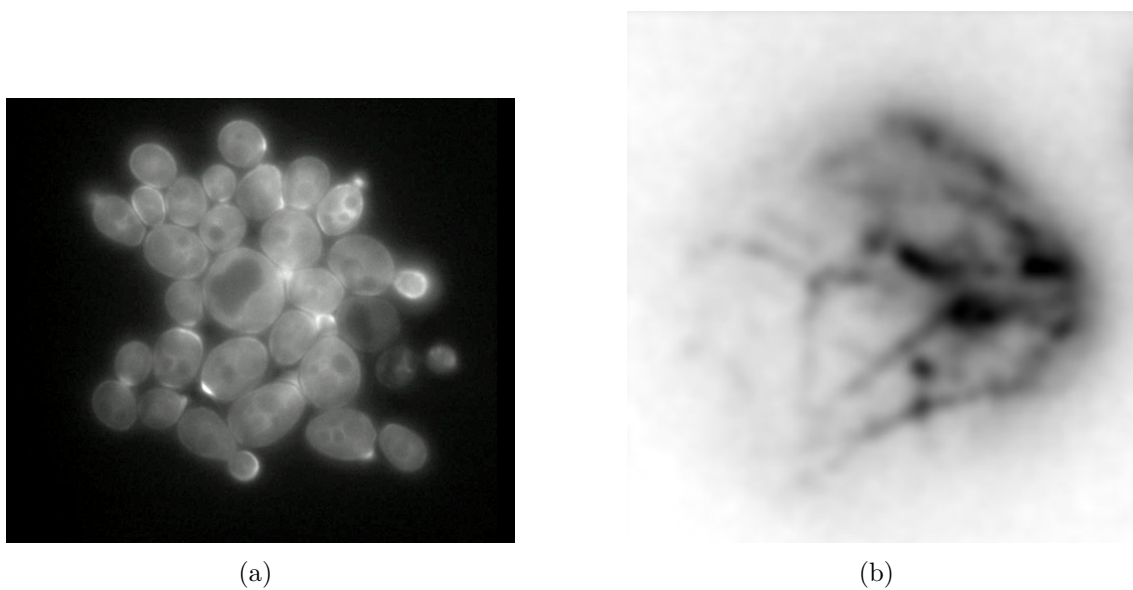


**Figure 2.7.: Polarized budding yeast cells obtained from computer assisted microscopy.** (a) Polarized Cdc42-GFP. (b) Polarized actin cables (R. Wedlich-Söldner, Institute of Cell Dynamics and Imaging Münster).

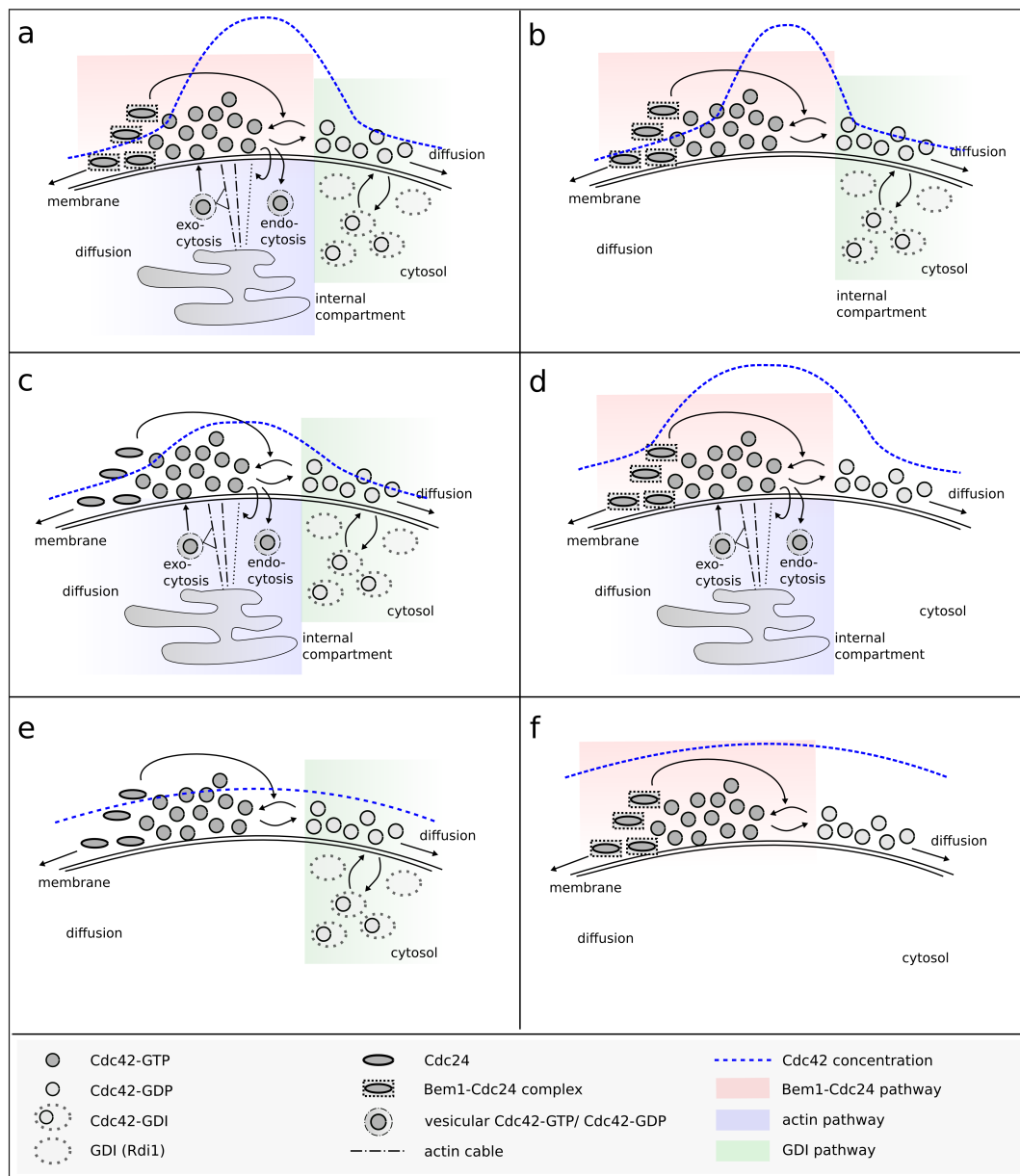


**Figure 2.8.: Schematic representation of the pathological cases observed by biological experiments.** (a) In the presence of the most important pathways, Bem1-mediated activation, Rdi1-mediated cytosolic exchange, and vesicular-mediated molecule delivery, the cell is able to polarize. (b) Even in the absence of the transport machinery, the cell forms a polarized Cdc42 patch. (c) Without Bem1-Cdc24-Cdc42-GTP complex formation, the cell is still able to polarize, albeit with less intensity. (d) The lack of a cytosolic exchange induced by GDI disruption does not impede polarization. The simultaneous disruption of (e) actin and Bem1 or (f) actin and Rdi1 leads to an unpolarized cell.

### 2.4.2. Models for yeast cell polarity

Although this chapter is concerned with biological preliminaries, the findings achieved by interdisciplinary research should not be omitted. For instance, mathematical models provide a useful tool to simulate biological processes. They support biological research and help to gain new scientific insights.

Through the years many mathematical models have been developed to simulate the establishment and maintenance of yeast cell polarity. The aim of these models is to achieve a better understanding of the fundamental processes of cell polarization. This led to a huge number of model systems with focus on different aspects as well as mechanisms of polarity. Dependent on the model objectives, the systems are either based on continuous or stochastic equations. As we will see in Section 3.1, partial differential equations (PDEs) provide a good approach to simulate reactions and dispersions of proteins mathematically. For the mathematical simulation of actin cable nucleation as well as exocytosis and endocytosis, stochastic approaches are suitable.

In this section we will concentrate on models for the establishment and maintenance of yeast cell polarization that gave direction to further studies in this field. We will give an overview of model systems focusing on the aforementioned pathways that may contribute to polarity. Thus, each model is of particular importance since it provides an accurate description of various mutant phenotypes which arise from disturbed polarization. Furthermore, the models contributed to a deeper knowledge of the protein interactions and mechanical processes involved. However, it is difficult to keep track of the key messages that we learn from it. Therefore, we classify the models into three categories and summarize them into a table of each class (see Figures 2.9-2.11). The first one includes transport models that solely focus on the impact of actin-mediated transport. The second class comprises reaction-diffusion models which ignore transport mechanisms and simulate polarization by protein interactions and diffusion. Models which couple systems of the first two categories are summarized in the last one.

#### Transport models

To investigate whether actin-mediated vesicle delivery could contribute to cell polarization in yeast cells, mathematical models simulating transport mechanisms became increasingly important. So far, the simulations of actin cable nucleation and the associated vesicle transport are mostly based on stochastic equations. The first model simulating the Cdc42-GTP cluster formation, based on a Poisson process

for actin nucleation, was introduced in [96]. Although the results have shown that actin-mediated feedback is able to cluster Cdc42, this system only considers one active form of the GTPase and ignores reactions or nucleotide exchange mechanisms. Furthermore, this conceptual model is confined to the transport from an internal infinite pool to the plasma membrane. It does not include Cdc42 diffusion or a description of endocytosis, the internalization of molecules from the membrane back to internal compartments. However, together with biological experiments, this was the first study which indicated that vesicle trafficking could contribute to the establishment and maintenance of cell polarity. Thereby, this model laid the foundation of further research with focus on vesicle delivery.

Using a deterministic PDE-based model to simulate the maintenance of cell polarity, MARCO ET AL. [56] developed a more realistic approach to simulate vesicular trafficking. The model incorporates actin cable nucleation and the definition of an exocytic transport window. Furthermore, it simulates endocytosis of molecules off the plasma membrane and away from actin cables as well as diffusion of molecules on the plasma membrane. In that way, their model could also show that a positive feedback induced by directed transport can dynamically stabilize polarity. But interestingly, their key finding was the role of endocytosis in optimizing the shape of the polar cluster for a given transport rate [56].

However, the model described above also only simulates active Cdc42 and does not consider the GTPase cycle. With the aim of investigating the role of GDI, SLAUGHTER ET AL. [81] extended this model by separating between two domains. The first one defines internalization by endocytosis. The second one specifies the region of removal by GDI-binding. By this implementation of a second delivery window which defines GDI-mediated exchange, their model has shown that endocytosis and GDI-mediated recycling are restricted to the same region of the nascent bud. Moreover, the rates of Cdc42 recycling are adjusted not to reach maximum polarity, but to control the shape of the polar cluster. Especially the rate of internalization within the polarized region influences the morphogenetic outcome [81].

The aforementioned models had one thing in common. They all rely on the assumption that vesicle transport contributes to robust cell polarity. LAYTON ET AL. [52] initially postulated the contrary. Their stochastic approach to simulate maintenance of polarity explicitly incorporates the membrane that mediates the traffic. Considering vesicular intermediates as a result of exocytosis and endocytosis, contrary to previous vesicle transport models, their simulations have shown that vesicle trafficking rather disturbs than reinforces polarization. More precisely, the model demonstrated that, with previously measured diffusion rates for Cdc42, polarity via actin-mediated



vesicle recruitment cannot establish. In this case, secretory vesicles would only reinforce polarization if the cargo diffuses very slowly and is selectively concentrated into endocytic vesicles [52, 95]. Thus, their findings contradict experimental results that have shown the impact of actin-mediated transport to robust polarity [96, 98]. For instance, biological research using mutant cells containing a constitutively active form of Cdc42 has shown that cells can polarize through actin-based transport. These cells polarize only with an intact actin pathway. In contrast, cells treated with latrunculin A (LatA), a drug that disrupts the organization of microfilaments and inhibits the polymerization of actin, were not able to concentrate Cdc42 [97]. Biological experiments with  $\Delta bem1$  or  $\Delta rdi1$  cells additionally support the role of actin-mediated delivery. These mutant cells cannot polarize when treated with latrunculin [28, 84]. Therefore, it remains to define the cases and circumstances under which vesicle trafficking either positively or negatively affects polarization.

The main assumption of the model proposed in [52] is that exocytosis add and endocytosis remove parts of the plasma membrane. Using this approach, their findings revealed that the polarity regulator must diffuse very slowly and must be highly concentrated into exocytic and endocytic vesicles to exploit positive feedback. However, the model does not consider different diffusion rates for lipids. Lipids could diffuse much faster than Cdc42 and hence counteract the dilution effect. Furthermore, the model uses simplifying assumptions on kinetics of lipids and proteins during vesicle fusion. Higher rates of vesicle fusion could also counter against a dilution [28]. Nevertheless, their results have indicated that there must be further mechanisms which prevent vesicle transport from disturbing polarity in budding yeast cells. Motivated by this work, SLAUGHTER ET AL. [83] investigated the influence of non-uniform membrane diffusion of Cdc42. Using the similar approach proposed in [52], the extended model has shown that a spatial separation of exocytosis and endocytosis as well as inhomogeneous membrane diffusion enables the maintenance of a stable polarized patch. Moreover, their research has initially demonstrated a critical role for membrane microdomains [83]. However, to what extent different diffusion rates as well as membrane microdomains influence the impact of vesicular trafficking to cell polarity has to be studied.

## Reaction-diffusion models

Alan Turing was the first to analyze reaction-diffusion systems for the possibility of instabilities that lead to spatial patterns. He suggested that diffusion could disrupt the stable homogeneous state by a process called *diffusion-driven instability*. By linear stability analysis of a simple non-linear two component reaction-diffusion

system he demonstrated how spatial patterns can arise by a small perturbation of the homogeneous state. Under certain conditions for the reaction and diffusion rates, this perturbation can destabilize the system. As a result it tends to an inhomogeneous concentration of the components, leading to spatial patterns [92]. Such a pattern formation process is now commonly termed *Turing-type pattern formation* which forms the foundation for development of structure formation systems. We will go into detail in Section 3.3.

GIERER AND MEINHARD were the first to use this *diffusion-driven* process in the context of cell polarity [59, 60]. To simulate the polarization in yeast cells, a more detailed reaction-diffusion system based on a Turing-type mechanism was finally introduced by GORYACHEV AND POKHILKO [32]. This model system was based on the assumption that the nucleotide cycling of Cdc42, including slow diffusion on the plasma membrane and fast diffusion in the cytosol, is sufficient to induce Cdc42 cluster formation. Since it includes many important biochemical reactions, this model was frequently extended or readjusted by other authors [38, 45, 47, 76]. Importantly, their simulations have shown that molecular interactions between Cdc42, its regulatory molecules, and its effector Bem1 are sufficient to explain spontaneous polarity by a Turing-type instability. However, the investigation of a reduced model based on two reaction-diffusion equations demonstrated the need of a cubic reaction term to achieve a non-homogeneous distribution of molecules. Furthermore, in their simulations multiple clusters arose which finally merged together [32]. Thus, the pattern formation process was the result of a cubic feedback that dominates the system behavior but does not fit biological evidence.

A conceptual stochastic, particle-based model also simulates polarity using a positive feedback activation [1]. It is based on the assumption that the recruitment of molecules from the cytosol and its subsequent membrane association is proportional to the fraction of particles on the plasma membrane. Importantly, their simulations have shown that a positive feedback alone is sufficient to generate a polar cluster at low particle numbers. However, the polarity was metastable and higher particle numbers led to stochastic unstable polarization [1]. These results lack biological evidence or even disagree with findings that high particle numbers in cells overexpressing Cdc42 do not affect polarity efficiency [28, 37].

SMITH ET AL. [84] were then the first who developed a deterministic, conceptual model that does not rely on a (Bem1-mediated) positive feedback activation. Based on the assumption that both Rdi1 and the Rdi1-Cdc42 complex activity depend on active Cdc42, they simulated cell polarization by a positive feedback recruitment. They assumed that a certain activity proportional to squared density of active

membrane-bound Cdc42 can break the Rdi1-Cdc42 complex. Together with biological experiments, their results have demonstrated that neither Bem1 nor the ability of Bem1 to bind Cdc42-GTP is required for cell polarization. In this case Bem1 serves as a catalyst to boost GEF activity [84]. Although the model is very simple and does not simulate the full GTPase cycle, it emphasizes the importance of the GDI pathway.

KLÜNDER ET AL. [48] developed a more detailed deterministic, PDE-based model for the simulation of GDI-mediated cell polarity. Contrary to [84] it simulates the full geometry of the cell as well as a GEF-complex-mediated GDI displacement and the associated recruitment of Cdc42 from the cytosol. Furthermore, their approach includes a Bem1-mediated recruitment of Cdc24 towards Cdc42. Interestingly, the simulations have shown that GDI-mediated polarity provides precise spatial and temporal control of Cdc42 signaling. In this way the GDI pathway ensures the development of a single polarized patch by counteracting the formation of multiple clusters [48]. These results underscore the role of GDI-based cell polarization. However, this approach is also based on an assumption that lacks experimental evidence. There currently exists no research which proves the GEF-mediated Cdc42-GDI recruitment.

To investigate the impact of GEF phosphorylation on the establishment of cell polarization, KUO ET AL. [51] recently published a deterministic model based on the system proposed in [32]. They expanded this model by using the assumption that GEF phosphorylates the Bem1-GEF-Cdc42-GTP complex which then lacks activity. Interestingly, the results have demonstrated that such a negative feedback generates oscillatory dynamics and reduces the level of Cdc42 concentration in the polar cluster. Nevertheless, the role of GEF phosphorylation is still under debate and requires further research.

### **Coupled reaction-diffusion-transport models**

To gain a better understanding of the influence of different parallel acting pathways on the establishment and maintenance of cell polarity, coupled reaction-diffusion-transport models became increasingly important.

The first model proposed in [76] combines previously developed mechanistic reaction-diffusion and vesicle trafficking models to simulate the maintenance of cell polarization [32,52]. As a result, it comprises all three (Bem1-,GDI- and actin-mediated) pathways which are known to contribute to yeast cell polarity. Since the simulations of the coupled system have shown that an actin-mediated recycling would disturb polarity, it calls the Cdc42-actin feedback hypothesis into question as well. As suggested

in [52], it supports the assumption that vesicle delivery would not enforce polarization if the vesicles do not carry significant amounts of Cdc42. Since the model ignores the possibility of yeast cells to polarize in the absence of Bem1 or Rdi1 and hence via actin-mediated transport [28, 84], the results are still under debate. For example, the systems proposed in [28] and [47] have demonstrated how vesicle trafficking could positively affect cell polarity. The stochastic particle-based model by FREISINGER ET AL. [28] includes exocytosis as well as endocytosis. It simulates the nucleotide exchange and reactions under consideration of the active and inactive form of Cdc42. It is the first stochastic model for the establishment of cell polarization simulating combined GDI- and actin-mediated Cdc42 recycling. Interestingly, their results have shown that, whereas actin-mediated recycling induces robust polarity, GDI-mediated recycling restricts polarity to a single site. Both pathways act in parallel to establish a robust unique cluster. However, like in [48], the approach uses a GEF-mediated Cdc42 recruitment from the cytosol which lacks experimental evidence. Furthermore, it considers only two actin cables that nucleate at the plasma membrane.

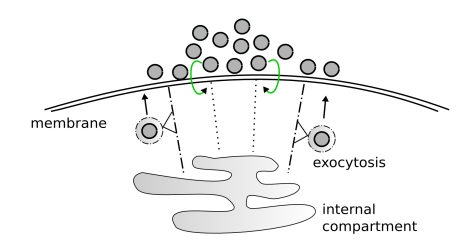
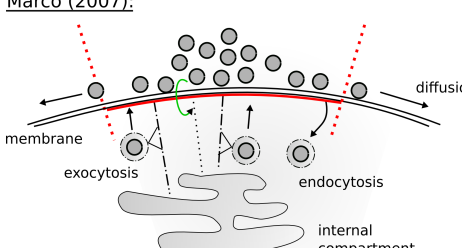
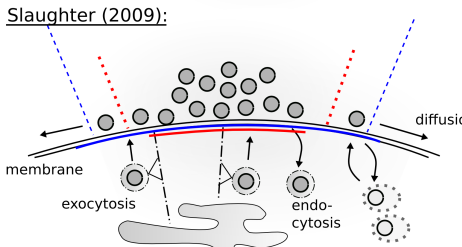
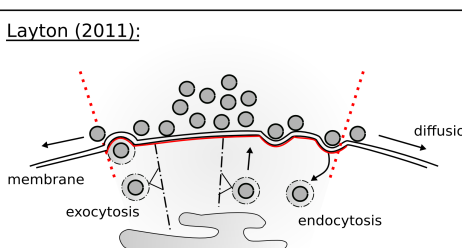
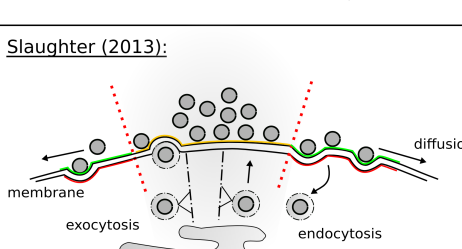
A more detailed model that combines the described system of GORYACHEV AND POKHILKO [32] with a stochastic simulation for vesicular trafficking has finally been introduced in [47]. The simulations have emphasized the importance of a spatial organization of exocytosis and endocytosis. According to biological findings, the mathematical results have demonstrated that exocytosis and endocytosis are spatially coordinated. More specifically, robust polarity requires that endocytic vesicles corral a central exocytic zone. Although the model could account for several biological phenotypes, it could not explain polarity in  $\Delta bem1$  cells. In their simulations a reduced autoamplification led to a vanishing pole [47]. Furthermore, whereas the GTPase cycle was based on a system of PDEs, exocytic and endocytic events were simulated by stochastic equations. This approach complicates the performance of analytical studies of the complete model. Moreover, the last two systems simulate Cdc42 trafficking as a simple protein flux between an internal pool and the plasma membrane and do not explicitly consider vesicular intermediates. To what extent vesicle fusion and pinch-off contributes to cell polarity and whether such effects can possibly even be neglected need further research.

### Concluding remarks

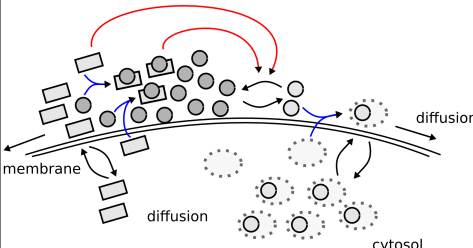
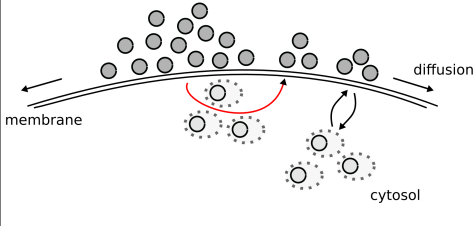
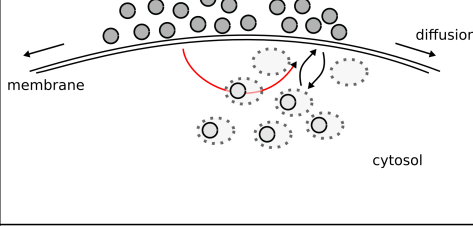
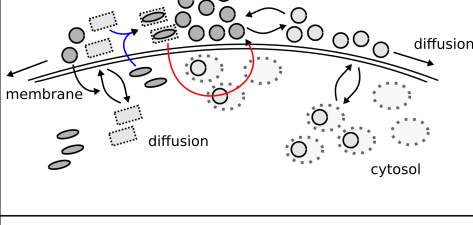
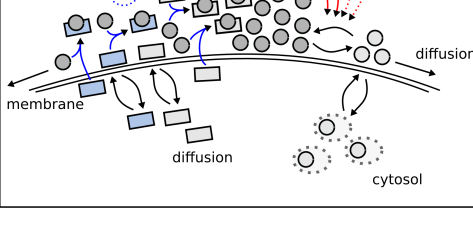
Summarized, each model of yeast cell polarity helped gain insight into the underlying processes generating Cdc42 cluster formation. Although the described models are able to demonstrate polarized Cdc42 distribution using parameter value estimates based on *in vitro* experiments and capture many features of the establishment

---

and maintenance of polarization, they are incomplete and fail in describing many qualities of cell polarity. For instance, some scientists observed the change or even the disappearance of the polarity axis during the process of polarization [38, 66, 98]. Furthermore, as already mentioned, some models are based on assumptions that lack experimental evidence or even disagree with biological results. In these cases, further research is required to find out the reasons for contradictory results.

<b>Transport models</b>	
<p><b>Wedlich-Söldner (2003):</b></p> 	<p><i>Description:</i> Conceptual, stochastic model that simulates establishment of polarity by an actin-mediated feedback mechanism</p> <p><i>Main assumptions:</i></p> <ul style="list-style-type: none"> <li>- actin cables transport vesicles with Cdc42 from an internal pool to the plasma membrane</li> <li>- the rate is proportional to available Cdc42</li> <li>- cable nucleation is a Poisson process that depends on active Cdc42 at the membrane</li> </ul> <p><i>Key message:</i> An increase in the local Cdc42-GTP concentration on the plasma membrane enhances the probability of actin polymerization and increases the probability of further Cdc42 accumulation</p> <p><i>pros:</i></p> <ul style="list-style-type: none"> <li>- cable nucleation</li> <li>- conceptual model</li> </ul> <p><i>cons:</i></p> <ul style="list-style-type: none"> <li>- no diffusion</li> <li>- no reactions</li> <li>- no endocytosis</li> <li>- only active Cdc42</li> </ul>
<p><b>Marco (2007):</b></p> 	<p><i>Description:</i> Deterministic PDE-based model that simulates maintenance of Cdc42 polarity by exo- and endocytosis within one circular transport window</p> <p><i>Main assumptions:</i></p> <ul style="list-style-type: none"> <li>- direct transport from a limited internal pool of proteins</li> <li>- endocytosis of molecules off the membrane at and away from the actin cables</li> <li>- cable nucleation rate is proportional to Cdc42</li> <li>- transport window depends on cables</li> </ul> <p><i>Key message:</i> Endocytosis optimizes the shape of polarity for a given transport rate (maximal sharpness)</p> <p><i>pros:</i></p> <ul style="list-style-type: none"> <li>- membrane diffusion</li> <li>- cable nucleation</li> </ul> <p><i>cons:</i></p> <ul style="list-style-type: none"> <li>- no reactions</li> <li>- only active Cdc42</li> </ul>
<p><b>Slaughter (2009):</b></p> 	<p><i>Description:</i> Deterministic PDE-based model which is based on the model of Marco (2007), but further combines the actin and GDI pathway by separating between two domains of internalization and removal respectively</p> <p><i>Main assumptions:</i></p> <ul style="list-style-type: none"> <li>- actin-mediated transport as in Marco (2007)</li> <li>- a second delivery window defines GDI-mediated exchange</li> </ul> <p><i>Key message:</i> Both pathways, actin-mediated and GDI-mediated, are important to maintain polarity and influence the shape of polarity</p> <p><i>pros:</i></p> <ul style="list-style-type: none"> <li>- membrane diffusion</li> <li>- cable nucleation</li> <li>- incorporates cytosolic exchange</li> </ul> <p><i>cons:</i></p> <ul style="list-style-type: none"> <li>- no reactions</li> <li>- no GTPase cycle</li> </ul>
<p><b>Layton (2011):</b></p> 	<p><i>Description:</i> Stochastic approach that simulates maintenance of polarity by explicitly simulating vesicular intermediates as a result of exo- and endocytosis</p> <p><i>Main assumptions:</i></p> <ul style="list-style-type: none"> <li>- vesicular transport was not modeled as a simple flux but rather as the stochastic transfer of membrane packets carrying Cdc42 between a well-mixed internal compartment</li> <li>- exocytosis adds, endocytosis removes parts of the plasma membrane</li> </ul> <p><i>Key message:</i> Fusion of vesicles causes a dilution of the polar cap so that vesicular trafficking rather disturbs than reinforces polarization</p> <p><i>pros:</i></p> <ul style="list-style-type: none"> <li>- membrane diffusion</li> <li>- explicit description of vesicle tracking steps</li> </ul> <p><i>cons:</i></p> <ul style="list-style-type: none"> <li>- no reactions</li> <li>- no GTPase cycle</li> <li>- same diffusion rates</li> <li>- no exp. evidence</li> </ul>
<p><b>Slaughter (2013):</b></p> 	<p><i>Description:</i> Stochastic approach based on Layton (2011) that simulates maintenance of polarity by considering inhomogeneous diffusion coefficients</p> <p><i>Main assumptions:</i></p> <ul style="list-style-type: none"> <li>- vesicle fusion and pinch-off by exo- and endocytosis as in Layton (2011)</li> <li>- spatially segregated exo- and endocytosis</li> <li>- slow diffusion in domains with exocytosis</li> <li>- fast diffusion in domains with endocytosis</li> </ul> <p><i>Key message:</i> Non-uniform membrane diffusion and spatially separated exo- and endocytosis enable the maintenance of a stable polar cluster</p> <p><i>pros:</i></p> <ul style="list-style-type: none"> <li>- non-uniform diffusion</li> <li>- spatially separated endocytic and exocytic sites</li> <li>- mechanical change of plasma membrane</li> </ul> <p><i>cons:</i></p> <ul style="list-style-type: none"> <li>- no reactions</li> <li>- mainly active Cdc42</li> </ul>

**Figure 2.9.: Overview of mathematical models for transport-mediated yeast cell polarity.** The most important models for actin-mediated vesicular trafficking in budding yeast cells are shown.

<b>Reaction-diffusion models</b>	
<p><b>Goryachev (2008):</b></p> 	<p><i>Description:</i> Deterministic, PDE-based system that simulates establishment of polarity by modeling its experimentally determined molecular mechanism</p> <p><i>Main assumptions:</i></p> <ul style="list-style-type: none"> <li>- Bem1-mediated feedback activation by complex formation with GEF-Cdc24 and Cdc42-GTP</li> <li>- slow diffusion on the plasma membrane</li> <li>- fast diffusion in the cytosol</li> <li>- mass conservation</li> </ul> <p><i>Key message:</i> Molecular interactions between Cdc42, its regulatory molecules and its effector Bem1 are sufficient to explain spontaneous polarity by a Turing-type instability</p> <div style="border: 1px solid gray; padding: 5px; margin-top: 10px;"> <p><i>pros:</i></p> <ul style="list-style-type: none"> <li>- complex reactions</li> <li>- full GTPase cycle</li> </ul> <p><i>cons:</i></p> <ul style="list-style-type: none"> <li>- multiple clusters which merge</li> <li>- no evidence for cubic feedback</li> </ul> </div>
<p><b>Altschuler (2008):</b></p> 	<p><i>Description:</i> Stochastic, particle-based model that simulates establishment of polarity by a positive feedback activation</p> <p><i>Main assumptions:</i></p> <ul style="list-style-type: none"> <li>- spontaneous membrane asso- and dissociation</li> <li>- membrane association through recruitment proportional to the fraction of particles on the plasma membrane</li> <li>- diffusion on the membrane</li> </ul> <p><i>Key message:</i> While linear positive feedback can generate a polar cluster at low particle numbers, higher particle numbers lead to stochastic unstable polarity</p> <div style="border: 1px solid gray; padding: 5px; margin-top: 10px;"> <p><i>pros:</i></p> <ul style="list-style-type: none"> <li>- conceptual model of pattern formation</li> </ul> <p><i>cons:</i></p> <ul style="list-style-type: none"> <li>- mainly active form</li> <li>- metastable</li> <li>- no exp. evidence (high particle numbers do not affect polarity efficiency)</li> </ul> </div>
<p><b>Smith (2013):</b></p> 	<p><i>Description:</i> Deterministic, conceptual PDE-based model that simulates establishment of polarity by a positive feedback recruitment</p> <p><i>Main assumptions:</i></p> <ul style="list-style-type: none"> <li>- a certain activity proportional to the squared density of active membrane Cdc42 can break the Rdi1-Cdc42 complex</li> <li>- both Rdi1 and Rdi1-Cdc42 depend on Cdc42</li> </ul> <p><i>Key message:</i> Neither Bem1 nor the ability of Bem1 to bind Cdc42-GTP is required for cell polarization and its role in polarity establishment is mainly to boost GEF activity</p> <div style="border: 1px solid gray; padding: 5px; margin-top: 10px;"> <p><i>pros:</i></p> <ul style="list-style-type: none"> <li>- conceptual model of pattern formation</li> <li>- no Bem1 feedback</li> </ul> <p><i>cons:</i></p> <ul style="list-style-type: none"> <li>- not the full GTPase cycle</li> <li>- uncertain positive feedback recruitment</li> </ul> </div>
<p><b>Klünder (2013):</b></p> 	<p><i>Description:</i> Deterministic, PDE-based model for the simulation of GDI-mediated polarity</p> <p><i>Main assumptions:</i></p> <ul style="list-style-type: none"> <li>- GEF-complex-mediated recruitment of Cdc42 from the cytosol by GDI displacement</li> <li>- Bem1-mediated recruitment of Cdc24 towards active Cdc42</li> <li>- fast cytosolic vs slow membrane diffusion</li> </ul> <p><i>Key message:</i> GDI-mediated polarity provides precise spatial and temporal control of Cdc42 signaling and ensures the development of a single polar cluster by counteracting the formation of multiple polarity sites</p> <div style="border: 1px solid gray; padding: 5px; margin-top: 10px;"> <p><i>pros:</i></p> <ul style="list-style-type: none"> <li>- simulates full geometry of the cell</li> <li>- one single cluster with narrowing dynamics</li> </ul> <p><i>cons:</i></p> <ul style="list-style-type: none"> <li>- no evidence for GEF-mediated Cdc42-GDI recruitment</li> </ul> </div>
<p><b>Kuo (2014):</b></p> 	<p><i>Description:</i> Deterministic, PDE-based model for the simulation of polarity (based on Goryachev (2008))</p> <p><i>Main assumptions:</i></p> <ul style="list-style-type: none"> <li>- Bem1-mediated feedback activation as in Goryachev (2008) but implicit GDI</li> <li>- phosphorylation of the GEF as a Hill function of the Bem1-GEF-Cdc42 complex concentration</li> <li>- phosphorylated GEF lacks activity</li> <li>- dephosphorylation in the cytoplasm</li> </ul> <p><i>Key message:</i> Negative feedback by GEF phosphorylation generates oscillatory dynamics and reduces the level of Cdc42 concentration in the polar cluster</p> <div style="border: 1px solid gray; padding: 5px; margin-top: 10px;"> <p><i>pros:</i></p> <ul style="list-style-type: none"> <li>- complex reactions</li> <li>- includes negative feedback</li> </ul> <p><i>cons:</i></p> <ul style="list-style-type: none"> <li>- role of GEF phosphorylation is still under debate</li> </ul> </div>

**Figure 2.10.: Overview of reaction-diffusion models for yeast cell polarity without consideration of active transport.** The reaction schemes used to simulate polarization in LatA-treated yeast cells are illustrated.

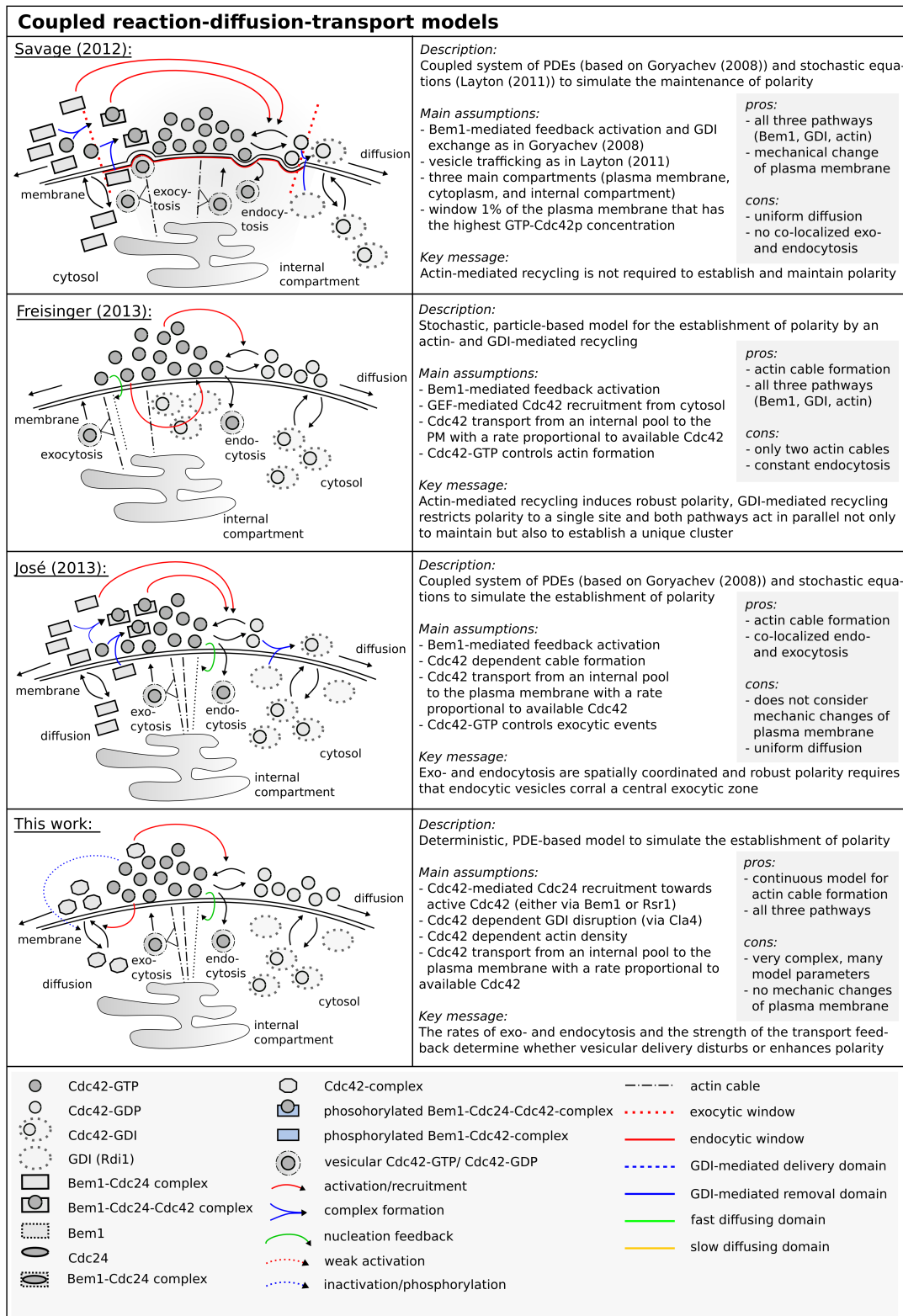


**Figure 2.11.: Overview of coupled reaction-diffusion-transport models for yeast cell polarity.** The most important models for yeast cell polarization which consider reaction kinetics as well as vesicular delivery are shown.



## 3 | Mathematical preliminaries

In this chapter we will provide the mathematical background that we apply in this thesis. Before we introduce the tools for modeling pattern formation in biological systems, we derive reaction-diffusion and reaction-diffusion-advection equations. This is followed by fundamental definitions and properties of the stability theory and its application in partial differential equations. The Turing mechanism provides an example that uses principles of the stability theory in biological systems. Since Turing instabilities gained importance in the modeling of pattern formation, we will derive the conditions for a Turing instability and give a short example. Following this, traveling wave solutions which are another phenomenon of reaction-diffusion equations are addressed. To solve partial differential equations numerically, it is common to apply the Galerkin method which is based on weak formulations using test functions belonging to a so-called Sobolev space. Therefore, we further introduce the basic concepts for solutions of reaction-diffusion-advection equations. We conclude this chapter with an introduction to coupled bulk-surface partial differential equations which are the mathematical basis of the model presented in this thesis.

### 3.1. Mathematics of reaction-diffusion-advection equations

Parabolic PDEs of second order are the basis of the time-dependent reaction-diffusion-advection problems which were initially used to model physical processes. The increasing scope and complexity in new branches of science has made these equations applicable in other fields. This lay the foundation of *mathematical modeling*. Fluid dynamics, reactions, and transport of molecules play an important role in many biological processes. Dependent on these mechanisms, the standard reaction-diffusion-advection model simulates the time evolution of biological or chemical substances. Whereas advection and diffusion are responsible for directed transport or the dispersion of certain enzymes or proteins within the cell, biochemical reactions

achieve the transformation of one molecule to another. To understand how cells achieve and control reactions and transport of substances as well as to predict its behavior, the mathematics of such processes provides an important tool and is essential for biological applications.

In this part, we derive PDEs that simulate the evolution of scalar fluid properties using certain conservation principles. The content of this section is mainly based upon [40, 58].

The reaction-diffusion-advection equation is a combination of the diffusion equation, a parabolic PDE and the advection equation, a hyperbolic PDE. It is a result of the modeling of natural laws and mathematical facts.

Let  $t \geq 0$  be a time point of an interval  $[0, T]$ ,  $\Omega$  an open set, and  $x \in \Omega \subset \mathbb{R}^n$ , where  $n = 1, 2$ , or  $3$  is the space dimension. A reaction-diffusion-advection equation for a state variable  $u = u(x, t)$  has the typical form

$$\partial_t u = \underbrace{f(u)}_{\text{reaction}} + \underbrace{\nabla \cdot (D \nabla u)}_{\text{diffusion}} - \underbrace{\nabla \cdot (\vec{a} u)}_{\text{advection}}, \quad (3.1)$$

where  $\nabla$  is the divergence operator. The function  $u$  describes the density or concentration of a substance, a protein, a population, and suchlike considered at a point  $x$  and time  $t \geq 0$ .  $D$  is the diffusion coefficient and  $\vec{a}$  describes the average velocity. Thus, the second and third term on the right-hand side describe the diffusion and advection respectively. The first term  $f(u)$  is a smooth scalar function  $f : \mathbb{R} \rightarrow \mathbb{R}$ . This function simulates how  $u$  changes due to distinct processes in space unrelated to diffusion or advection. For instance, it could model a chemical reaction between molecules, its source or depletion, or alternatively death and birth of a population. Typical and simple reactions are exponential growth

$$f(u) = au, \quad a = \text{const},$$

or logistic growth

$$f(u) = au \left( 1 - \frac{u}{K} \right),$$

with the carrying capacity  $K$  as a limiting factor of growth.

Commonly, the diffusion coefficient  $D$  is a constant and the velocity field describes an incompressible flow (i.e., it has zero divergence). In this case, (3.1) changes to

$$\partial_t u = f(u) + D \Delta u - \vec{a} \cdot \nabla u,$$

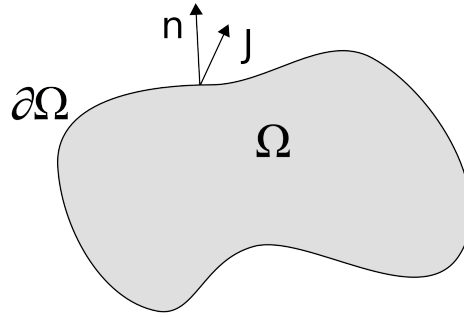


**Figure 3.1.: Scheme of a control volume.** Control volume  $\Omega$  with boundary  $\partial\Omega$  and outer normal  $\vec{n}$ .

where  $\Delta = \nabla \cdot \nabla$  is the Laplace operator.

The reaction-diffusion-advection equation is a direct result of the conservation law and Fick's law.

### 3.1.1. Conservation principles

Consider an arbitrary *control volume*  $\Omega \subset \mathbb{R}^n$ , with  $n = 1, 2, 3$ , and its *control surface*  $\Gamma := \partial\Omega$  (see Figure 3.1). Let  $u(x, t) \in \mathbb{R}$  further denote the concentration of a state variable at point  $x \in \Omega$  and at time  $t \geq 0$ . The total amount of  $u$  at time  $t$  inside  $\Omega$  is then given by

$$M(t) = \int_{\Omega} u(x, t) \, dx.$$

Mass conservation now implies that the change of the total amount  $M$  of substances in a domain must be equal to the total amount of flow into the domain and the increase or decrease of the quantity produced or depleted inside it.

**Remark 3.1** (Conservation law). Let  $\Omega$  be an arbitrary bounded domain with boundary  $\Gamma := \partial\Omega$  and  $u$  be the concentration of some chemical species at  $x \in \Omega$  and at time  $t \geq 0$ . Let  $f$  further describe the local production of  $u$  per unit volume and  $\mathbf{J}$  be the flux of  $u$  in  $\Omega$ . Using the outward unit normal  $\vec{n}$  to  $\Gamma$ , it holds that

$$\frac{d}{dt} \int_{\Omega} u \, dx = \int_{\Omega} f \, dx - \int_{\Gamma} \mathbf{J} \cdot \vec{n} \, d\sigma. \quad (3.2)$$

Whereas the mass produced inside  $\Omega$  per unit time is given by the volume integral on the right-hand side of (3.2), the surface integral corresponds to the mass that drifts out of the domain  $\Omega$  per unit area and time.

If  $\mathbf{J}$  is sufficiently smooth and hence differentiable, we can apply the divergence

theorem so that the surface integral can be expressed by the volume integral

$$\int_{\Gamma} \mathbf{J} \cdot \vec{n} \, d\sigma = \int_{\Omega} \nabla \cdot \mathbf{J} \, dx. \quad (3.3)$$

Substitution of (3.3) into (3.2) yields the equation

$$\frac{d}{dt} \int_{\Omega} u \, dx = \int_{\Omega} f \, dx - \int_{\Omega} \nabla \cdot \mathbf{J} \, dx$$

and hence

$$\int_{\Omega} [\partial_t u - f + \nabla \cdot \mathbf{J}] \, dx = 0.$$

Since the control volume  $\Omega$  is arbitrary, the term in the brackets must vanish. This fact implies that

$$\partial_t u = f - \nabla \cdot \mathbf{J}. \quad (3.4)$$

We finally get a PDE for the evolution of  $u(x, t)$ . Equation (3.4) is also known as *continuity equation* which generalizes the advection equation.

### 3.1.2. Diffusion and advection

To simulate the nature of involved transport mechanisms by the flux function  $\mathbf{J}$ , we further separate the total flux  $\mathbf{J}$  by diffusive and advective fluxes:

$$\mathbf{J} = \mathbf{J}_{\text{diffusive}} + \mathbf{J}_{\text{advective}}.$$

The process of diffusion is illustrated in Figure 3.2 which shows two kind of particles dissolved in a fluid separated by a permeable membrane. Even if the fluid is at

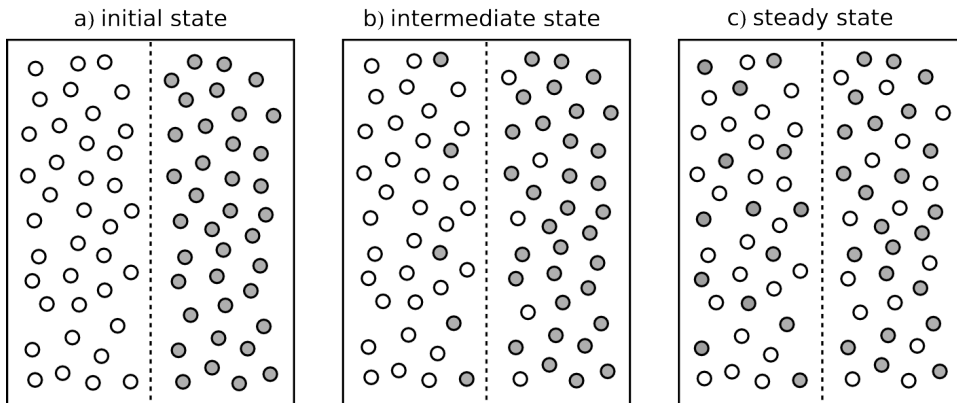


**Figure 3.2.:** Illustration of diffusion through a permeable barrier. Starting with an inhomogeneous arrangement of molecules, diffusive flux leads to its spreading which results in an equilibrium state.

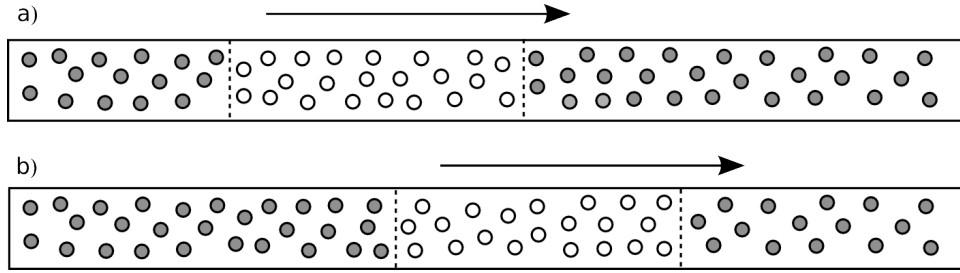


**Figure 3.3.: Advective transport trough a domain.** Particles move in a certain direction which depends on a velocity field.

rest, random motion of initially unequally distributed molecules causes its spatial displacement. This random movement finally leads to a mixed pool of particles. Thus, diffusive flux functions as an equalizing process. Fick's law relates the diffusive flux to the concentration. It hypothesizes that molecules tend to flow from regions of higher concentrations to regions of lower concentrations with magnitude that is proportional to the concentration gradient.

**Remark 3.2** (Fick's law of diffusion). Let  $\mathbf{J}$  be the flux of any chemical species and  $D$  the diffusion coefficient. The simplest description of the flux of a chemical species is then given by

$$\mathbf{J}_{\text{diffusive}} = -D\nabla u. \quad (3.5)$$

In contrast to diffusion, advection describes the transport of all of the quantity  $u$  at point  $x$  due to a flux given by a vector field  $\vec{a}(x)$ . That way, advective flow is able to generate and maintain an inhomogeneous distribution of molecules. Figure 3.3 shows an example for advective transport. The sketch shows how small particles move through a tube driven by the flow of a fluid. For example, this fluid could be water that runs from the left to the right of this pipe. In this case, the advective flux corresponds to the density times the velocity field or expressed in a formula, it is

$$\mathbf{J}_{\text{advective}} = \vec{a}(x, t) \cdot u. \quad (3.6)$$

Finally, using (3.5) and (3.6), for (3.4) we obtain

$$\partial_t u = f(u) + \nabla \cdot (D\nabla u) - \nabla \cdot (\vec{a}u), \quad (3.7)$$

where  $D$  may be a function of  $x$  and  $u$ . This is by definition the typical form of a reaction-diffusion-advection equation.

### 3.1.3. Initial and boundary conditions

In the last section we derived the reaction-diffusion-advection equation (3.7), a second order parabolic partial differential equation. This equation is referred to evolution equations as it describes biological phenomena or other time-dependent processes. The problem is that a multitude of resulting structures can be simulated by the same differential equation. Furthermore, evolution equations are generally non-linear. Although in these equations the diffusive and advective terms are mostly linear as it is assumed that the diffusion coefficient  $D$  and the velocity field  $\vec{a}$  are given and independent of the concentration  $u(x, t)$ ,  $f$  may be a function of  $u, x$ , and  $t$ . These conditions can lead to an ill-posed problem so that this non-linear reaction-diffusion-advection equation is not explicitly solvable and hence permits no exact solution. For that reason, we need additional information to ensure that the problem is well-posed. More to the point, the choice of reasonable initial and well-posed boundary conditions is required for the existence of solutions of non-linear reaction-diffusion-advection equations. Furthermore, the addition of appropriate initial as well as boundary conditions allows us to derive important propositions about the system evolution through time  $t$  regarding the behavior and the appearance of solutions.

Whereas the choice of the domain and of the time interval depends on conditions of the considered model problem, including the specified objectives, the definition of initial and boundary conditions requires further assumptions.

Initial conditions describe the state of the system at a certain time

$$u(x, t_0) = u_0(x), \quad x \in \Omega,$$

and boundary conditions define the behavior of  $u$  at  $x \in \Gamma := \partial\Omega$ . Consider a partitioning of  $\Gamma$  into  $\Gamma_D, \Gamma_N$  and let  $g_D$  and  $g_N$  be given (non-linear) functions. Typical boundary conditions are:

**The Dirichlet boundary condition:**

$$u(x, t) = g_D(x, t) \quad \text{for all } x \in \Gamma_D, t > t_0.$$

In the case of  $g_D(x, t) = 0$ , we call this boundary condition *homogeneous Dirichlet boundary condition*.

**The Neumann boundary condition:**

$$-D\nabla u \cdot \vec{n} = g_N(x, t) \quad \text{for all } x \in \Gamma_N, t > t_0,$$

where  $\vec{n}$  is the outer normal to  $\Omega$  at  $x \in \Gamma_N$ . If  $g_N = 0$ , no molecules or individuals can move in or out of the domain  $\Omega$ . This homogeneous condition or so-called *no flux condition* simulates an isolated domain.

**The Robin boundary condition:**

$$(\vec{a}u - D\nabla u) \cdot \vec{n} = g_M \quad \text{for all } x \in \Gamma_M, t > t_0,$$

where  $\vec{n}$  is the outer normal to  $\Omega$  at  $x \in \Gamma_M$ . This condition is referred to as *mixed condition*.

Note that it is possible to combine different types of boundary conditions. Furthermore, the boundary  $\Gamma$  will be subdivided according to its relation with the velocity field  $\vec{a}$ . The part of boundary where  $\vec{n} \cdot \vec{a} < 0$  is referred to as *inflow boundary*. By contrast, the relation  $\vec{n} \cdot \vec{a} > 0$  characterizes the *outflow boundary*.

As we will see later, the nature of an analytical or numerical solution does not only depend on the posed initial and boundary conditions. The interaction of the different processes simulated in the equation essentially dictates the result. Here, we remark already that, depending on the relative contribution of advection and diffusion, the equation (3.7) can be either diffusion or advection dominated. For example, if the diffusive and reactive terms are zero, i.e  $D = 0$  and  $f \equiv 0$ , the equation directly results in the pure advection equation

$$\partial_t u = -\nabla \cdot (\vec{a} \cdot u), \quad x \in \Omega, t \in [0, T],$$

a hyperbolic PDE of first order. In this case, the solution often exhibits a steep gradient in parts of the domain. This behavior complicates the design of effective numerical solvers. By contrast, if the velocity field and the reaction term vanishes, the equation results in the diffusion equation

$$\partial_t u = \nabla \cdot (D\nabla u), \quad x \in \Omega, t \in [0, T],$$

a second order parabolic PDE which is also known as the heat equation. This type of PDE can be solved relatively easily and robustly. That way, various approaches may not only change the properties of exact solutions but also affect the efficiency of numerical methods.

### 3.1.4. Systems of reaction-diffusion-advection equations

So far, we considered the reaction-diffusion-advection equation for a single species  $u$ . However, this study is concerned with the time-dependent evolution of multiple interacting molecules. For that reason, we further generalize equation (3.7) to get a system of moving and interacting substances. Using a vector  $u(x, t) \in \mathbb{R}^m$  of concentrations of species  $u = (u_1, \dots, u_m)$ , a vector of smooth functions  $f = (f_1, \dots, f_m)$ , and control parameters  $\lambda \in \mathbb{R}^k$ , the general system of reaction-diffusion-advection equations reads

$$\partial_t u = f(u, \lambda) + \nabla(D\nabla u) - \nabla \cdot (\mathbf{a}u). \quad (3.8)$$

Note that  $\mathbf{a} = (\vec{a}_1, \dots, \vec{a}_m)$  is the row vector containing the velocity fields of each species. The diffusion constant is given by a symmetric and positive semi-definite matrix  $D \in \mathbb{R}^{m \times m}$ . If the system does not exhibit any cross diffusion, this is simply a diagonal matrix composed of the positive diffusion coefficients  $D_1, \dots, D_m$  of each species. As before, if the diffusion and advection are independent of  $x, t$ , and  $u$ , the respective terms are linear. By contrast, the reaction term given by function  $f$  might be non-linear.

Unless otherwise stated, throughout this thesis we assume constant diffusion without cross diffusion as well as divergence-free velocity fields. The system (3.8) then reduces to

$$\partial_t u = f(u, \lambda) + D\Delta u - \mathbf{a} \cdot \nabla(u). \quad (3.9)$$

The product  $\mathbf{a} : \Omega \rightarrow \mathbb{R}^{m \times n}$  with the divergence operator in (3.9) is understood componentwise, i.e.

$$\vec{a} \cdot \nabla = \text{diag}(\vec{a}_1 \cdot \nabla u_1, \dots, \vec{a}_m \cdot \nabla u_m).$$

Furthermore, the diffusion and advection parts are given in terms of the diagonal matrices

$$\Delta = \begin{pmatrix} \Delta & & \\ & \ddots & \\ & & \Delta \end{pmatrix}, \quad \nabla = \begin{pmatrix} \nabla & & \\ & \ddots & \\ & & \nabla \end{pmatrix}.$$

As before, this system requires appropriate initial and boundary conditions to ensure the existence of a solution. Furthermore, it is important to accurately simulate the functions  $f$  which describe the non-linear chemistry part between the species  $u = (u_1, \dots, u_m)$ . Section A of the appendix gives a short introduction into the modeling of chemical interactions.



## 3.2. Stability analysis

Since many biological processes involve passive and active transport of molecules, equations and systems given by (3.7) and (3.8) are essential for the mathematical study of biological systems. As mentioned before, the exclusion of terms or addition of model assumptions can lead to various models with different solutions. As a result, they became increasingly important for the study of pattern formation. Since it turned out that reaction-diffusion systems can exhibit a large variety of solutions that are of interest to the study of structure formation, these reduced equations are commonly considered. The solutions show very complex and interesting behavior. Oscillations can occur which then spread in time and space due to diffusion. As a result, instabilities of the system can lead to spatial phenomena like pattern formation.

Cell polarity is a kind of pattern which arises due to instabilities in the system. Hence, it seems obvious to make use of these equations to describe the mechanisms underlying cell polarization.

In order to investigate a system of reaction-diffusion equations related to the possibility of instabilities, it is often useful to analyze the long term behavior of solutions. With this approach, it can be identified if the solution will reach a time-independent equilibrium that is not always stable against small perturbations. Since stable and unstable steady states play distinguished roles in the dynamic of such a system, it is helpful to be able to find and classify the equilibrium points according to their stability properties.

The main issue of the qualitative theory of ordinary differential equations (ODEs) is the stability analysis. It is based on the analysis of initial value problems and deals with the stability behavior of steady states. Using fixed initial time but slightly modified initial values it allows a classification of the solutions.

Because cell polarity is qualitatively the change from a homogeneous to an unstable state, the stability behavior of steady states is of great interest to the modeling of polarization. For that purpose we will define the term *stability*, especially *linear stability*, and show methods to investigate the stability of an equilibrium. Throughout, we will use the notation of [5, 22].

For the sake of convenience we will take an autonomic system of differential equations as the basis. The system

$$x' = f(x) \tag{3.10}$$

satisfies the conditions for global existence and uniqueness. Let  $f : X \rightarrow \mathbb{R}^n$  be a Lipschitz-continuous function in  $x$  and  $X \subseteq \mathbb{R}^n$  an open domain. For each  $x_0 \in X$

let  $x(x_0, t)$  be the unique solution of the initial value problem

$$x' = f(x), \quad x(0) = x_0.$$

**Definition 3.3** (Steady state, stationary state or equilibrium). A stationary state  $x^* \in X$  of the continuous system (3.10) is a constant solution  $f(x^*) = 0$  of the system. These are just the time-independent solutions  $x^*$  of (3.10).

Given a steady state  $x^*$ , the question of its stability naturally arises. But what does stability mean? To explain this, consider a system that starts at an equilibrium and is suddenly perturbed by some cues that induce a variation from the steady state. What will the result of the small perturbation be? Will the system return to its stationary point or remain close to it? Or will it further move away from the equilibrium?

The definition of stability and asymptotic stability is very easy and descriptive for constant solutions and, as we will see, especially for trivial solutions. Because of this, the question for the qualitative behavior of solutions is commonly linked to the behavior of solutions with an initial value near the equilibrium. We define the following notions of stability:

**Definition 3.4.** Let  $x^*$  be a steady state of the system  $x' = f(x)$ .

- (i) (Lyapunov Stability) The stationary state  $x^*$  is a stable equilibrium, if for an arbitrary neighborhood  $B_1$  of  $x^*$  a neighborhood  $B_2$  of  $x^*$  exists, such that for any solution of the initial value problem

$$x' = f(x), \quad x(0) = x_0 \in B_2,$$

holds that

$$x(t) \in B_1 \text{ for all } t > 0.$$

- (ii) If  $x^*$  is not stable, it is unstable.
- (iii) (Asymptotic stability) Let  $x^*$  be a stable steady state of the system  $x' = f(x)$  (e.g.  $x^*$  is Lyapunov stable). The stable stationary state  $x^*$  is locally (globally) asymptotically stable, if additionally a neighborhood  $B_3$  of  $x^*$  can be chosen, such that the solutions of the initial value problem  $x_0 \in B_3$  converge uniformly to  $x^*$ . Then, it holds that

$$\lim_{t \rightarrow \infty} x(t) = x^*$$

for each solution of the initial value problem

$$x' = f(x), \quad x(0) = x_0 \in B_3.$$

- (iii) The stationary state  $x^*$  is locally (globally) exponentially stable, if given any environment  $B_1$  ( $B_1 = \mathbb{R}^n$ ) of  $x^*$  there exist constants  $a, \gamma > 0$ , such that all  $x_0$  of this neighborhood fulfil the inequality

$$\|x(t) - x^*\| \leq ae^{-\gamma t} \|x_0 - x^*\| \quad \text{for all } t \geq 0.$$

In other words, if  $x^*$  is stable, regardless of how small a ball  $B_1$  centred at  $x^*$  is chosen, another (possibly smaller) ball  $B_2$  can always be found such that any solution  $x(t)$  starting at some point of  $B_1$  around  $x^*$  remains within the ball  $B_2$ . Moreover in the case of asymptotic stability the trajectories that get sufficiently close to  $x^*$  converge to  $x^*$  as  $t \rightarrow \infty$  (see Figure 3.4). The definition also implicates that an exponentially stable equilibrium is asymptotically stable and hence Lyapunov stable.

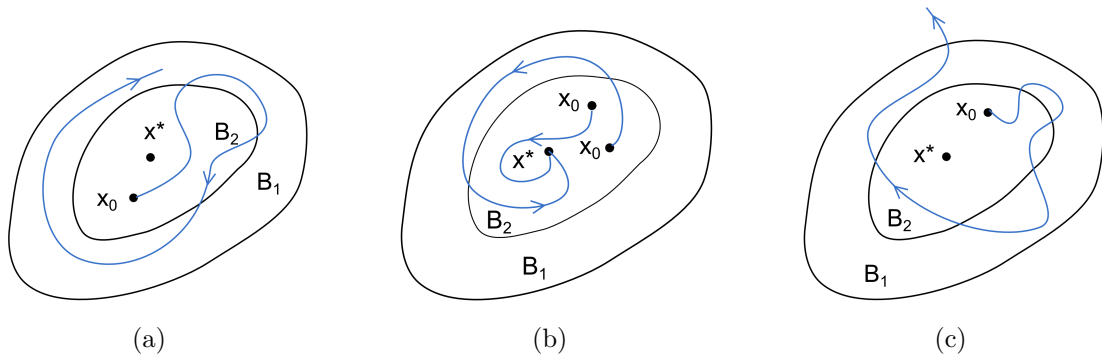


**Figure 3.4.: Visualization of stability of steady states.** For an equilibrium  $x^*$  (a) stability, (b) asymptotic stability, and (c) instability are illustrated.

### 3.2.1. Stability of linear systems

Below we will consider the stability question in more detail. We investigate to what extent the stability behavior depends on the algebraic structure and the associated solution spaces of systems of linear differential equations. We show that the class of linear systems exhibits a uniform stability behavior of all solutions. For that reason, these systems are referred to stability, instability, or asymptotic stability per se.

Consider the linear inhomogeneous system

$$x'(t) = A(t)x(t) + g(t) \tag{3.11}$$

with continuous functions  $A : (T, \infty) \rightarrow \mathbb{C}^{n \times n}, g : (T, \infty) \rightarrow \mathbb{C}^n$  on the interval  $(T, \infty) \in \mathbb{C}$ . Then the reduced case, the linear homogeneous equation

$$x'(t) = A(t)x(t), \quad (3.12)$$

plays an important role for the general theory of linear systems. That this also applies to stability questions shows the following proposition:

**Proposition 3.1.** *The stability behavior of any solution of the inhomogeneous System (3.11) is equivalent to the stability behavior of the trivial solution  $x^*$  of the homogeneous system (3.12).*

This proposition is a direct consequence of the following proposition for the non-autonomous equation:

**Proposition 3.2.** *Let*

$$x' = f(t, x) \quad (3.13)$$

*be a differential equation with a continuous function  $f : X \rightarrow \mathbb{R}^n$  on the infinite domain  $X \subseteq \mathbb{R}^{n+1}$ . Furthermore, let  $f$  be Lipschitz-continuous in relation to the right-hand side and  $\varphi : (t^-, \infty) \rightarrow \mathbb{R}^n$  be a solution of this equation. Consider the differential equation of the disturbed motion*

$$y' = f(t, y + \varphi(t)) - f(t, \varphi(t)),$$

*as result of the transformation*

$$y = x - \varphi(t).$$

*Then, the differential equation (3.13) has the trivial solution on the interval  $(t^-, \infty)$  which is stable and accordingly asymptotically stable if and only if the solution  $\varphi(t)$  of (3.13) is stable and accordingly asymptotically stable.*

By applying this proposition, any solution  $\varphi : (T, \infty) \rightarrow \mathbb{R}^n$  of (3.11) has the same differential equation of the disturbed motion. It is

$$y' = [A(t)(y + \varphi(t)) + g(t)] - [A(t)\varphi(t) + g(t)]$$

and hence

$$y' = A(t)y.$$

The prediction now directly results from Proposition 3.2.

However, the most important class of linear systems are those with constant coefficients of the form

$$x'(t) = Ax(t) \text{ with } A \in \mathbb{C}^{n,n},$$

where  $A$  is independent of  $t$ . Since these systems are explicitly solvable, it is possible to develop good criteria for the stability and asymptotic stability of the equilibria. We will see that the stability behavior then completely depends on the matrix  $A$ . Particularly the eigenvalues of  $A$  play a crucial role.

Obviously, this system has the trivial steady state  $x^* = 0$ . Its stability can be investigated as follows:

**Proposition 3.3** (Eigenvalue conditions for stability). *Let  $A \in \mathbb{C}^{n,n}$  be an arbitrary matrix. For the linear homogeneous system  $x'(t) = Ax(t)$  are equivalent:*

- (i) *The steady state  $x^* = 0$  is stable.*
- (ii) *For any eigenvalue  $\lambda_i$  of  $A$  holds the inequality  $\operatorname{Re} \lambda_i \leq 0$ . Furthermore, the eigenvalues with  $\operatorname{Re} \lambda_i = 0$  are semi-simple.*
- (iii) *For all  $t \geq 0$  exist a constant  $M \geq 1$ , such that  $\|e^{At}\| \leq M$ .*

**Proposition 3.4** (Asymptotic stability). *Let  $A \in \mathbb{C}^{n,n}$  be an arbitrary matrix. For the linear homogeneous system  $x'(t) = Ax(t)$  are equivalent:*

- (i) *The steady state  $x^* = 0$  is asymptotically stable.*
- (ii) *For any eigenvalue  $\lambda_i$  of  $A$  holds the inequality  $\operatorname{Re} \lambda_i < 0$ .*
- (iii) *The equilibrium  $x^* = 0$  is exponentially stable, whereby the constant  $\gamma > 0$  of Definition 3.4 can be any value of the interval  $(0, -\rho_{max})$ .  $\rho_{max}$  is the (negative) maximum of the real part of the eigenvalues.*

For the sake of compactness, we refer to [5] and [34] for the proof of Propositions 3.3 and 3.4.

Interestingly, the stability behavior of the equilibrium  $x^* = 0$  of the system is independent of the basis  $A$ . The following Lemma holds:

**Lemma 3.5.** *Let  $A, T \in \mathbb{C}^{n \times n}$  be matrices. Furthermore, let  $T$  be invertible and  $\tilde{A} = T^{-1}AT$  the transformed matrix. Then, the stability classification of the equilibrium  $x^* = 0$  of*

$$x'(t) = Ax(t)$$

*is equivalent to the classification of the steady state  $y^* = 0$  of*

$$y'(t) = \tilde{A}y(t).$$

For the proof see [34].

### 3.2.2. Principle of linearized stability

So far, we have discussed stability classifications for linear systems. For our investigations we also need good results for the stability behavior of steady states of non-linear differential equations.

Consider the system of differential equations

$$x' = f(x),$$

with  $f : X \rightarrow \mathbb{R}^n$  a Lipschitz-continuous function in  $x$  and  $X \subseteq \mathbb{R}^n$  an infinite domain. Suppose that  $x^* \in X$  is an equilibrium of the system. The principle of linearized stability is based on the idea to linearize the differential equations around  $x^*$ . Defining  $y(t) \approx x(t) - x^*$  and  $A := Df(x^*)$  the derivative, a multivariate Taylor expansion of the right-hand side yields

$$y' = x'(t) - \underbrace{\frac{d}{dt}x^*}_{=0} = x'(t) \approx f(y(t) + x^*) = \underbrace{f(x^*)}_{=0} + \underbrace{Df(x^*)}_{=A} y(t) + \underbrace{\mathcal{O}(|y|^2)}_{R(u)}. \quad (3.14)$$

Because  $R(u) \rightarrow 0$  as  $|u| \rightarrow 0$ , it is reasonable to assume that solutions of (3.14) behave similarly to solutions of the linear approximation

$$y' = Ay. \quad (3.15)$$

Note that (3.15) has the steady state  $y^* = 0$ , so that we can easily classify the equilibria using Propositions 3.3 and 3.4.

**Definition 3.5.** Let  $x^*$  be an equilibrium of a differential equation.  $x^*$  is linearly stable (linearly unstable or linearly asymptotically stable), if 0 is a stable (unstable or asymptotically stable) solution of the linearized equation.

The *principle of linearized stability* now implicates the stability behavior for  $x^*$  of (3.11) by that of the trivial solution  $y^* = 0$  of (3.12).

**Proposition 3.6** (Principle of linearized stability).

(i)  $x^*$  is asymptotically stable, if  $x^*$  is linearly asymptotically stable, e.g.  $\operatorname{Re} \lambda_i < 0$  for all eigenvalues  $\lambda_i$  of  $Df(x^*)$ .

(ii)  $x^*$  is unstable, if  $Df(x^*)$  has at least one eigenvalue  $\lambda_i$  with  $\operatorname{Re} \lambda_i > 0$ .

For the proof we refer to [22].

The Proposition 3.6 together with the Definition 3.5 eventually yields:

**Remark 3.6.** The stability behavior of stationary solutions of a non-linear system can be derived by the investigation of the stability of the zero point of the linearized system. For this, the algebraic sign of the real parts of all eigenvalues of the linearized approximation are relevant.

Note that this statement fails to provide information about the system behavior if at least one eigenvalue exists with  $\operatorname{Re} \lambda = 0$  while the real parts of the other eigenvalues are negative. In this case, it is generally not possible to classify the steady state based on linear stability analysis. Dealing with this case requires the non-linear theory.

### 3.3. Turing instability and pattern formation

We already got some ideas about non-uniform solutions of reaction-diffusion equations. In this section we will especially address reaction-diffusion systems that have the possibility to develop spatial patterns. For this we follow the work presented in [22] and [63].

We start with the idea of Alan Turing [92]. In 1952 he assumed that chemicals can react and diffuse in a certain way such that steady state heterogeneous pattern of morphogene concentrations or chemicals can occur. He investigated this behavior for different reaction-diffusion systems and derived variegated scenarios of pattern formation. This simple assumption is based on the observation that systems which are stable on their own can become unstable if they are merged with another system. For a better understanding consider two linear systems

$$x'(t) = Ax(t), \quad x'(t) = Bx(t), \quad \text{with } x(t) \in \mathbb{R}^2, A, B \in \mathbb{R}^{2 \times 2}.$$

Both systems have the trivial solution  $x \equiv 0$ . As we have already seen, the stability of this steady state depends on the eigenvalues of  $A$  and  $B$ . This means that the solution  $x \equiv 0$  is stable if  $A$  and  $B$  only have eigenvalues with negative real parts. But in contrast to expectations,  $x \equiv 0$  is not immediately a stable solution for the merged system

$$x' = (A + B)x(t).$$

Although if both eigenvalues of  $A$  and  $B$  are negative, it is possible that  $A + B$  has an eigenvalue with positive real part.

Let  $M \in \mathbb{R}^{2 \times 2}$  be an arbitrary matrix with negative eigenvalues  $\lambda_1$  and  $\lambda_2$ . It holds that

$$\lambda_1 + \lambda_2 = \operatorname{tr} M < 0 \quad \text{and} \quad \lambda_1 \lambda_2 = \det M > 0.$$

The matrices

$$A = \begin{pmatrix} -1 & 0 \\ 0 & -d \end{pmatrix}, \quad B = \begin{pmatrix} a & e \\ c & b \end{pmatrix}, \quad a, b, c, e \in \mathbb{R},$$

can easily fulfil the inequalities

$$a + b < 0, \quad ab > ce \quad \text{and} \quad (a - 1)(b - d) < ce.$$

Thus, it is possible that

$$\operatorname{tr} A < 0, \det A > 0,$$

$$\operatorname{tr} B < 0, \det B > 0,$$

but

$$\det(A + B) < 0.$$

In the following we transfer these results to the case of reaction-diffusion equations. Consider the system

$$\partial_t U = F(U, V) + D_U \Delta U,$$

$$\partial_t V = G(U, V) + D_V \Delta V,$$

where  $U$  and  $V$  represent, for instance, two chemical species. The kinetics are described by non-linear functions  $F$  and  $G$ . Alan Turing observed that under certain conditions for  $F$  and  $G$  as well as  $D_U$  and  $D_V$  the system tends to form inhomogeneous spatial patterns. Whereas for  $D_U = D_V = 0$  the species tend to a linear stable state, the presence of diffusion can destabilize the system. This process is termed as *diffusion-driven instability* or *Turing instability* [92].

This situation is comparable with that discussed in the beginning of this section. Using the knowledge of stability analysis, we are now able to derive the necessary and sufficient conditions for a Turing instability.

Consider the non-dimensionalized and scaled system in its general form

$$\partial_t u = \gamma f(u, v) + \Delta u,$$

$$\partial_t v = \gamma g(u, v) + d \Delta v,$$



where  $d$  is the ratio of diffusion coefficients. Taking into account boundary and initial conditions, we can formulate the problem mathematically.

**Proposition 3.7** (Turing instability). *Let*

$$\partial_t u = \gamma f(u, v) + \Delta u, \quad \partial_t v = \gamma g(u, v) + d\Delta v \quad (3.16)$$

be a system of two PDEs on a domain  $\Omega$  with closed boundary  $\Gamma := \partial\Omega$ . Let further  $\vec{n}$  be the unit outward normal to  $\Gamma$ . Given zero flux boundary conditions

$$(\vec{n} \cdot \nabla)u = (\vec{n} \cdot \nabla)v = 0, \quad x \text{ on } \Gamma, \quad (3.17)$$

and initial conditions

$$u(0, x) = u_0, \quad v(0, x) = v_0,$$

the homogeneous steady state  $(u^*, v^*)$  of (3.16) is Turing unstable if the following inequalities are satisfied:

$$f_u + g_v < 0, \quad f_u g_v - f_v g_u > 0, \quad (3.18)$$

$$df_u + g_v > 0, \quad (df_u + g_v)^2 - 4d(f_u g_v - f_v g_u) > 0. \quad (3.19)$$

*Proof.* Since we are interested in a diffusion-driven instability, we have to analyze which conditions are necessary so that the steady state for the system is stable without diffusion but unstable if diffusion is included. In this case, the linear instability of the equilibrium is solely spatial dependent.

First, we derive the conditions for stability of the system with no spatial variations

$$\partial_t u = \gamma f(u, v), \quad \partial_t v = \gamma g(u, v).$$

Linearization around the steady state  $(u^*, v^*)$  yields

$$\partial_t w = \gamma A w, \quad A = \begin{pmatrix} f_u & f_v \\ g_u & g_v \end{pmatrix} \Big|_{(u^*, v^*)},$$

with  $w := \begin{pmatrix} u - u^* \\ v - v^* \end{pmatrix}$  small. According to the preliminaries of Section 3.2, all eigenvalues of the stability matrix  $A$  must have negative real parts so that  $(u^*, v^*)$  is a stable equilibrium of the system. Using above preliminaries, this is satisfied if

$$\text{tr } A = f_u + g_v < 0, \quad \det A = f_u g_v - f_v g_u.$$

We now consider the full reaction-diffusion system (3.16) and again linearize around the stationary state  $(u^*, v^*)$  to get

$$\partial_t w = D\Delta w + \gamma Aw, \quad D = \begin{pmatrix} 1 & 0 \\ 0 & d \end{pmatrix}. \quad (3.20)$$

To solve the system with boundary conditions (3.17), consider the spatial eigenvalue problem defined by

$$\nabla^2 W + k^2 W = 0, \quad (\vec{n} \cdot \nabla)W = 0, \quad \text{for } x \text{ on } \Gamma, \quad (3.21)$$

with the time-independent solution  $W(x)$  and eigenvalue  $k$ . For convenience we first confine to a one-dimensional domain  $0 \leq x \leq a$ . In this case, the solution can be easily derived by separation of variables

$$w(t, x) = cw_1(t)w_2(x), \quad \text{with } c \in \mathbb{R}^2.$$

Thus, we obtain a solution of the linearized equation if and only if

$$cw_1'(t)w_2(x) = cDw_1(t)w_2''(x) + c\gamma A.$$

If  $w_1(t) \neq 0, w_2(x) \neq 0$ , this is equivalent to

$$c \frac{w_1'(t)}{w_2(t)} = cD \frac{w_2''(x)}{w_2(x)} + c\gamma A.$$

Since the left-hand side only depends on  $t$  while the right-hand side depends on  $x$ , there exist constants  $\lambda, \mu \in \mathbb{R}$  such that

$$w_1'(t) = \lambda w_1(t), \quad w_2'' = -\mu w_2(x),$$

where  $w_2'(0) = w_2'(a) = 0$ .

If, with an integer  $n$ ,

$$\mu = \mu_n = \left(\frac{n\pi}{a}\right)^2,$$

this equation exhibits solutions that are multiples of  $\cos(n\pi x/a)$ . The eigenvalue is  $k = n\pi/a$ . It is also called wavenumber because the measure of the wavelike pattern  $1/k = a/n\pi$  is proportional to the wavelength  $\omega = 2\pi/k = 2a/n$ . Since  $n$  is an integer, there are a discrete set of possible wavenumbers if the domain is finite. Referred to  $W_k(x)$  as the eigenfunction corresponding to the wavenumber  $k$ , we

develop the Fourier series of solutions of (3.20) such that

$$w(x, t) = \sum_k c_k e^{\lambda t} W_k(x). \quad (3.22)$$

The constants  $c_k$  are the coefficients of the Fourier expansion and  $\lambda$  is the eigenvalue which determines temporal growth. Substitution of (3.22) into (3.20) and cancellation of  $e^{\lambda t}$  lead to

$$\lambda W_k = \gamma A W_k + D \nabla^2 W_k.$$

Using (3.21), this is equivalent to

$$\lambda W_k = \gamma A W_k - D k^2 W_k = (\gamma A - D k^2) W_k := M W_k,$$

and the stability of the spatial system is determined by the eigenvalues of the matrix  $M$  for  $k \neq 0$ . Thus, the system becomes unstable even if the matrix  $M$  has eigenvalues with real part  $> 0$ . This is particularly the case if both solutions of the characteristic polynomial

$$\begin{aligned} \chi_M(\lambda(k)) &= \lambda^2 + \lambda[k^2(1+d) - \gamma(f_u + g_v)] + h(k^2), \\ h(k^2) &= dk^4 - \gamma(df_u + g_v)k^2 + \gamma^2 \det A \end{aligned} \quad (3.23)$$

have  $\text{Re } \lambda(k) > 0$  for some  $k \neq 0$ . Notice that for the case  $k = 0$  this is precisely the system without any spatial effects for which we have already derived the stability conditions (3.18).  $\text{Re } \lambda(k) > 0$  can only occur either if the coefficient  $\lambda$  in (3.23) is negative or if  $h(k^2) < 0$  for some  $k \neq 0$ . Furthermore, with  $k^2(1+d) > 0$  for all  $k \neq 0$  and (3.18) it follows that

$$[k^2(1+d) - \gamma(f_u + g_v)] > 0.$$

Thus, to get a positive eigenvalue, we need that  $h(k^2) < 0$  for some  $k$ . The roots of (3.23) are

$$\lambda_{1,2}(k) = -\frac{1}{2}[k^2(1+d) - \gamma(f_u + g_v)] \pm \sqrt{[k^2(1+d) - \gamma(f_u + g_v)]^2 - 4h(k^2)}.$$

In addition, the conditions  $f_u + g_v < 0$  as well as  $d > 0$  implicate

$$k^2(1+d) - \gamma(f_u + g_v) \geq 0,$$

for  $k \neq 0$ ,  $h(k^2) < 0$  only if

$$df_u + g_v > 0.$$

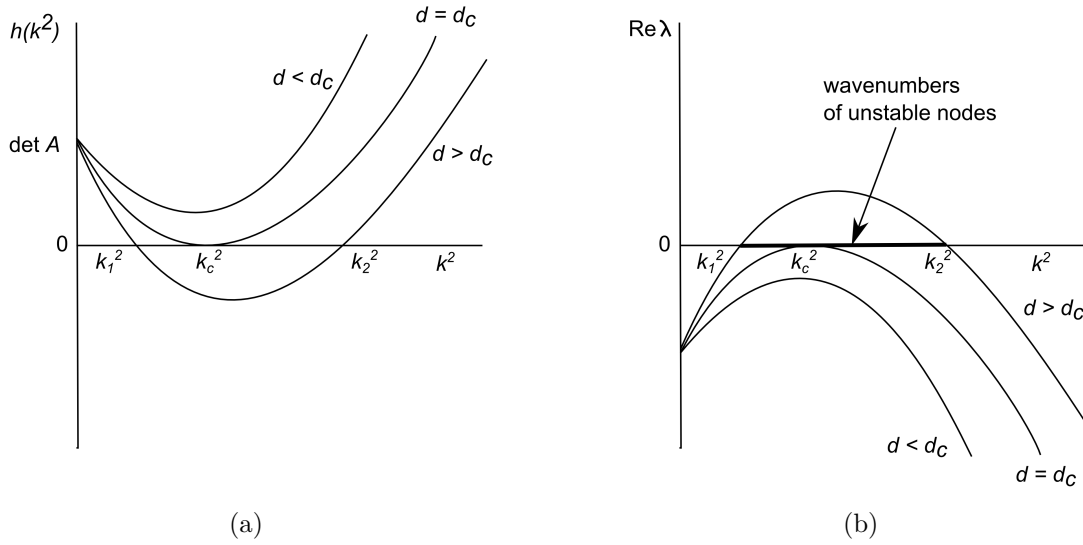


**Figure 3.5.: Plot of functions determining a Turing-type instability.** (a) Plot of  $h(k^2)$  defined by (3.23) for typical kinetics.  $h(k^2)$  becomes negative for a finite range of  $k^2 > 0$  when the ratio of the diffusion coefficient  $d$  increases beyond the critical value  $d_c$ . (b) Plot of the largest of the eigenvalues  $\lambda(k^2)$  from (3.23) against  $k^2$ . The wavenumbers of the range  $k_1^2 < k_2^2$  are linearly unstable when  $d > d_c$  (on [63]).

This yields the necessary condition  $d \neq 1$  and shows that  $f_u$  and  $g_v$  must have opposite signs. To observe solutions with positive real part we need one further sufficient condition. Consider  $f_u > 0$  and  $g_v < 0$ , then for  $h(k^2)$  to be negative for some  $k \neq 0$ , the minimum

$$h_{min} = h(k_m^2) = \gamma^2 \left[ \det A - \frac{(df_u + g_v)^2}{4d} \right], \quad k^2 = k_m^2 = \gamma \frac{df_u + g_v}{2d}, \quad (3.24)$$

must be negative. With (3.24) and  $\det(A) = f_u g_v - f_v g_u$  we can finally derive the last condition (3.19) for a Turing instability

$$(df_u + g_v)^2 - 4d(f_u g_v - f_v g_u) > 0.$$

□

Summarized, whether or not the system is capable of generating diffusion-driven spatial patterns is determined by the functions  $f$  and  $g$  as well as by the values of  $\gamma$  and  $d$  (see Figure 3.5).

A simple example for a system that exhibits Turing-type patterns is the Schnakenberg system suggested in [77]. With positive constants  $a$  and  $b$  the model reads in non-

dimensional form

$$\begin{aligned}\partial_t u &= \gamma(a - u + u^2 v) + \Delta u, \\ \partial_t v &= \gamma(b - u^2 v) + d \Delta v.\end{aligned}$$

Figure 3.6 shows the resulting patterns depending on different diffusion constants. Many more examples from biology and biochemistry are presented and investigated in [63].

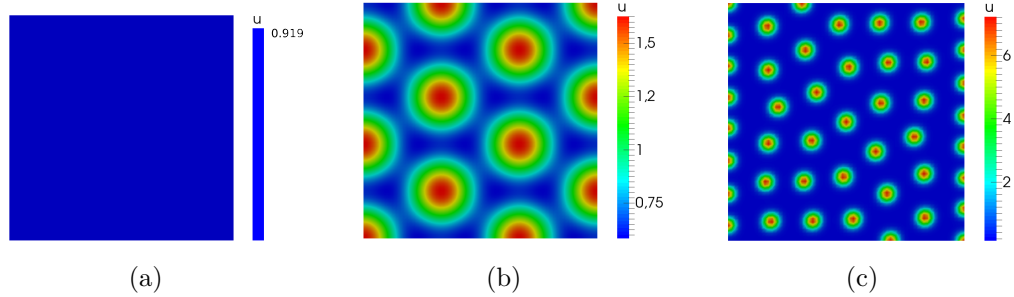


**Figure 3.6.: Illustration of a Turing-type pattern.** Numerical solution  $u$  of the Schnakenberg system on  $[0, 1]^2$  at  $t = 10$  using the estimated parameters  $\gamma = 1000$ ,  $a = 0.126779$ ,  $b = 0.792366$  and  $D_v = 10$  (a)  $D_u = 2$ , (b)  $D_u = 1$ , (c)  $D_u = 0.1$ .

### 3.4. Traveling waves in reaction-diffusion equations

Another interesting aspect of non-linear parabolic systems and hence reaction-diffusion systems are *traveling wave solutions*. Such solutions describe transitions from one steady state to another. Thus, systems generating *traveling waves* are often used to simulate a variety of biological phenomena. In this section we will expand on the role of waves in reaction-diffusion systems and its impact on the emergence of structures. The content of this section is mainly based upon [62].

**Definition 3.7.** A solution of the form

$$u(x, t) = v(x - ct) = v(z), \quad z = x - ct$$

with a constant  $c \in \mathbb{R}$ , is a *traveling wave solution*. The value  $c$  thereby describes the traveling speed of the wave and  $z$  is the wave variable.

Since it is usual that  $f(u)$  admits two stationary states, for instance  $f(0) = f(1) = 0$ , small perturbations to the system can lead to a traveling wave propagating through the domain. In the case  $x - ct$ , the wave moves in positive  $x$ -direction. Contrarily, a

wave which travels in the negative  $x$ -direction has the form  $u(x + ct, t)$ . This implies that for a traveling wave represented by  $u(x, t)$  and a constant value  $c$ , the shape of the solution and the speed of the wave will be the same for all time. Furthermore, it is clear that if  $x - ct$  is a constant,  $u$  is a constant. In this case, the coordinate system simply moves with speed  $c$ . To exemplify this behavior we study Fisher's equation

$$\partial_t u = qu(1 - u) + D\Delta u, \quad D, q, u, x, t \in \mathbb{R}.$$

This equation was first used to model the expansion of mutant genes. Later it was also applied in the study of autocatalytic chemical reactions as well as in the description of population development. In the non-dimensional case, Fisher's equation is given by

$$\partial_t u = u(1 - u) + \Delta u. \quad (3.25)$$

It has the steady states  $u \equiv 0$  and  $u \equiv 1$ . According to Definition 3.7 a traveling wave solution can be written in the form

$$u(x, t) = U(z), \quad z = x - ct, \quad (3.26)$$

where  $c$  is the wave speed and

$$\lim_{z \rightarrow -\infty} U(z) = 0, \quad \lim_{z \rightarrow \infty} U(z) = 1.$$

Replacement of (3.26) into (3.25) yields

$$U' + cU' + U(1 - U) = 0,$$

where primes denote differentiation with respect to  $z$ . Setting  $V = U'$  we can reduce the PDE to a system of ODEs

$$\begin{aligned} U' &= V, \\ V' &= -cV - U(1 - U). \end{aligned}$$

The problem of finding a traveling wave which connects two stationary states is now equivalent to finding a curve in the phase plane  $(U, V)$  that connects the points  $(0, 0)$  and  $(0, 1)$ . By linear stability analysis of the eigenvalues  $\lambda$  that are given by

$$\lambda_{\pm} = \frac{1}{2}(-c \pm \sqrt{c^2 - 4}),$$

it can be shown that for  $c \geq 2$  a traveling wave solution exists (see Figure 3.7 and [62])

for more details).

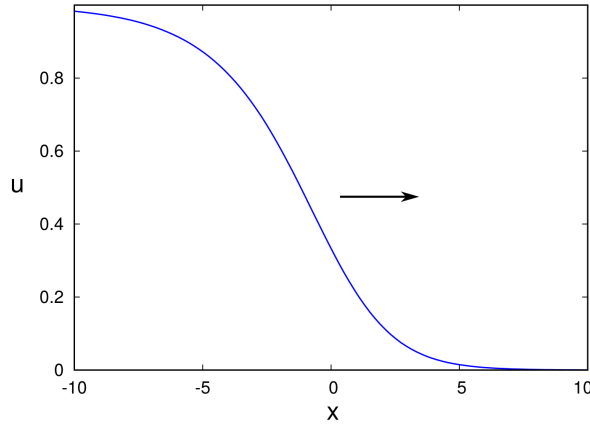


**Figure 3.7.: Plot of a traveling wave solution for the Fisher equation.** For large times, the Fisher equation with compact initial conditions admits traveling wave solutions. An example for a traveling wave solution is given by the function  $f(x) = (1 + \exp(x/\sqrt{6}))^{-2}$ .

### 3.5. Sobolev spaces and the weak formulations

Up to now, we defined reaction-diffusion-advection and reaction-diffusion equations using the strong formulation of a model problem. This approach implies that the classical solution  $u$  must be a function with continuous partial derivative of first and second order. Such functions belong to the so-called *classical function spaces*. However, partial differential equations are often not solvable in the classical sense. The existence of a classical solution requires that all parameters are sufficiently smooth and that the domain satisfies certain regularity conditions. In this case, it is desirable to consider an integral or weak form of the conservation law. This procedure requires the concept of weak formulation and so-named Sobolev spaces which we will introduce in this section. We restrict ourselves to the main definitions and theorems needed to formulate variational equations for the model problem used in this thesis. Note that the study of variational equations requires many tools from functional analysis. For a detailed introduction we refer to [14, 27].

Let  $\Omega \in \mathbb{R}^n$  be an open set and  $C^\infty(\Omega)$  the space of infinitely differentiable functions  $\varphi : \Omega \rightarrow \mathbb{R}$ . Then,  $\varphi$  is often denoted as *test function*.

**Definition 3.8** (Weak partial derivative). Let  $\alpha = (\alpha_1, \dots, \alpha_N)$  be a multiindex of order  $|\alpha| = \sum_{i=1}^N \alpha_i$  and  $u, v \in L^1_{\text{loc}}(\Omega)$ . The function  $v$  with

$$\int_{\Omega} v \varphi \, dx = (-1)^{|\alpha|} \int_{\Omega} u D^\alpha \varphi \, dx$$

for all test functions  $\varphi \in C_0^\infty(\Omega)$  is termed *weak partial derivative* of  $\alpha$ -th order. The weak partial derivative is often written as

$$D^\alpha u = v, \quad D^\alpha = \frac{\partial^{\alpha_1}}{\partial x_1^{\alpha_1}} \cdots \frac{\partial^{\alpha_N}}{\partial x_N^{\alpha_N}}. \quad (3.27)$$

Note that  $u$  does not have to possess a weak partial derivative. However, if such a derivative exists, the following Lemma says that it is unique.

**Lemma 3.8.** *If  $u \in L_{loc}^1(\Omega)$  has a weak partial derivative of order  $|\alpha|$ , then it is uniquely defined up to a set of measure zero.*

*Proof.* Assume that  $v, w \in L_{loc}^1(\Omega)$  fulfil

$$\int_{\Omega} u D^\alpha \varphi \, dx = (-1)^{|\alpha|} \int_{\Omega} v \varphi \, dx = (-1)^{|\alpha|} \int_{\Omega} w \varphi \, dx, \quad \forall \varphi \in C_0^\infty(\Omega).$$

This implies

$$\int_{\Omega} (v - w) \varphi \, dx = 0, \quad \forall \varphi \in C_0^\infty(\Omega)$$

and hence  $v = w$ . □

Since the function space  $L_{loc}^1(\Omega)$  is not quite convenient, we now define the so-called Sobolev space which considers functions with weak derivatives of various orders in Lebesgue spaces of various orders.

**Definition 3.9.** Let  $\Omega$  be an open set and  $k \in \mathbb{N}$ . Further, let  $1 \leq p \leq \infty$ . The *Sobolev space*  $W^{k,p}(\Omega)$  is defined as

$$W^{k,p}(\Omega) := \{u \in L^p(\Omega) \mid D^\alpha u \in L^p(\Omega) \text{ for all } |\alpha| \leq k\}.$$

The Sobolev space is naturally a Banach Space with the *Sobolev norm*.

**Definition 3.10** (Sobolev norm). For  $u \in W^{k,p}(\Omega)$  and  $1 \leq p < \infty$  the Sobolev norm is defined by

$$\|u\|_{W^{k,p}(\Omega)} := \left( \sum_{|\alpha| \leq k} \int_{\Omega} |D^\alpha u|^p \, dx \right)^{1/p}.$$

For  $p = \infty$  it is

$$\|u\|_{W^{k,\infty}(\Omega)} := \sum_{|\alpha| \leq k} \operatorname{ess\,sup}_{\Omega} |D^\alpha u|.$$

**Remark 3.11.** In the case  $p = 2$ ,  $W^{k,p}(\Omega)$  is a Hilbert space and we usually write

$$H^k = W^{k,2}(\Omega), \quad k \in \mathbb{N}.$$



**Definition 3.12.** For given  $1 \leq p < \infty$  the closure of  $C_c^\infty(\Omega)$  in  $W^{k,p}(\Omega)$  is denoted by  $W_0^{k,p}(\Omega)$ . For  $p = 2$  we write

$$H_0^k(\Omega) = W_0^{k,2}(\Omega).$$

Since it is important to have an explicit characterization of the dual space of  $H_0^1(\Omega)$  to  $H_0^1(\Omega)$  we define

**Definition 3.13.**  $H^{-1}(\Omega)$  denotes the dual space to  $H_0^1(\Omega)$ .

The next theorem provides a basic characterization of functions belonging to  $W_0^{1,p}(\Omega)$  and explains its central role. Boundary conditions are coupled with PDEs and prescribe the value of  $u$  on  $\Gamma := \partial\Omega$ .

**Theorem 3.9.** *Let  $u \in W^{1,p}(\Omega)$ . Then  $u \in W_0^{1,p}(\Omega)$  if and only if  $u$  vanishes on  $\Gamma$ .*

For the proof we refer to [14].

The method of weighted residuals now provides a general approach to the derivation of weak forms for partial differential equations. The starting point is the variational formulation of the model problem. This can be obtained by the multiplication of the differential equations with test functions and integration by parts. Consider the general time-independent reaction-diffusion-advection equation

$$-\nabla \cdot (D\nabla u) + \vec{a} \cdot \nabla u = f, \quad x \in \Omega, \quad (3.28)$$

with incompressible flow  $\vec{a}$  implying  $\nabla \vec{a} = 0$ . The variational form of the reaction-diffusion-advection equation with boundary conditions on  $\Gamma = \Gamma_D \cup \Gamma_N$  given by

$$u = g_D \text{ on } \Gamma_D, \quad D\nabla u \cdot n = g_N \text{ on } \Gamma_N, \quad (3.29)$$

can be obtained as follows. We multiply (3.28) with an appropriate test function  $\varphi$ . Then,

$$\begin{aligned} & \int_{\Omega} [-\nabla \cdot (D\nabla u) + \vec{a} \cdot \nabla u] \varphi \, dx \\ &= -D \int_{\Gamma_N} (\nabla u \cdot n) \varphi \, d\sigma + \int_{\Omega} (D\nabla u \cdot \nabla \varphi + (\vec{a} \cdot \nabla u) \varphi) \, dx \\ &= - \int_{\Gamma_N} g_N \varphi \, d\sigma + D \int_{\Omega} \nabla u \cdot \nabla \varphi \, dx + \int_{\Omega} (\vec{a} \cdot \nabla u) \varphi \, dx = \int_{\Omega} f \varphi \, dx, \end{aligned}$$

where  $\vec{n}$  is the outward pointing unit normal vector on  $\Gamma$ . Since the test functions are zero on the Dirichlet boundary, the respective boundary integral on the left-hand

side vanishes. Denoting the inner scalar product of  $L^2(\Omega)$  by  $(\cdot, \cdot)$ , we can rewrite this term in a more compact form.

**Definition 3.14** (Variational or weak formulation of the time-independent problem). Let  $\vec{a} \in L^\infty$  and  $f \in H^{-1}(\Omega)$ . The variational or weak formulation of the stationary reaction-diffusion-advection equation (3.28) with boundary conditions (3.29) reads: Find  $u \in H^1(\Omega)$  such that

$$a(u, \varphi) = l(\varphi) \quad (3.30)$$

for all  $\varphi \in H_0^1(\Omega)$ . The bilinear form  $a$  and the linear functional  $l$  are given by

$$a(u, \varphi) := D \int_{\Omega} \nabla u \cdot \nabla \varphi \, dx + \int_{\Omega} (\vec{a} \cdot \nabla u) \varphi \, dx$$

and

$$l(\varphi) := \int_{\Omega} f \varphi \, dx + \int_{\Gamma_N} g_N \varphi \, d\sigma.$$

The existence and uniqueness of weak solutions is a result of the Lax-Milgram Theorem.

**Theorem 3.10** (Lax-Milgram Theorem). *Assume  $H$  is a Hilbert space with norm  $\|\cdot\|$  and inner product  $(\cdot, \cdot)$ . Let  $l : H \rightarrow \mathbb{R}$  be a bounded linear functional on  $H$ . Further assume that the bilinear mapping  $b : H \times H \rightarrow \mathbb{R}$  is continuous and coercive. In other words, there exist constants  $\alpha, \beta > 0$  such that*

$$|b(u, \varphi)| \leq \alpha \|u\| \|\varphi\|$$

and

$$\beta \|u\|^2 \leq b(u, u),$$

where  $u, v \in H$ . Then there exists a unique  $u \in H$  such that

$$b(u, v) = l(v)$$

for all  $v \in H$ .

For the proof we refer to [27].

From the Theorem of Lax-Milgram the following statement follows:

**Corollary 3.11** (Existence and uniqueness of a solution of the weak problem (3.30)). *Assume  $f \in H_0^1(\Omega)$  and  $\vec{a} \in L^\infty(\Omega)$ . Then (3.30) has a unique solution.*

To prove the existence and uniqueness of a solution of (3.30), it suffices to show that the associated bilinear form is coercive and bounded.

Since this thesis is concerned with time-dependent processes, we further seek for solutions that satisfy an abstract variational time-dependent problem. Therefore, we need spaces that involves space as well as time.

**Definition 3.15.** Let  $X$  denote a real Banach space with  $\|\cdot\|$  and  $[0, T] \subset \mathbb{R}$  be a time interval. For  $1 \leq p < \infty$  the  $L^p$ -space of functions  $u : [0, T] \rightarrow X$  is defined as

$$L^p(0, T; X) := \{u \mid u(\cdot, t) \in X, t \in [0, T], \text{ is measurable and } \|u\|_{L^p([0, T], X)} < \infty\},$$

$$\|u\|_{L^p([0, T], X)} := \left( \int_0^T \|u(\cdot, t)\|_X^p dt \right)^{1/p}.$$

For  $p = \infty$  we define

$$L^\infty(0, T; X) := \{u \mid u(\cdot, t) \in X, t \in [0, T], \text{ is measurable and } \int_0^T \|u(t)\| \text{ is essentially bounded}\},$$

$$\|u\|_{L^\infty(0, T, X)} := \operatorname{ess\,sup}_{0 \leq t \leq T} \|u(\cdot, t)\|_X.$$

For these spaces we recall the definition of a weak derivative.

**Definition 3.16.** Let  $u \in L^2(0, T; X)$ . The function  $v \in L^2(0, T; X')$  with

$$\int_0^T v(t)\varphi(t)dt = - \int_0^T u(t)\varphi'(t)dt$$

for all test functions  $\varphi \in C_0^\infty(0, T)$  is termed the weak derivative of  $u$ . The weak derivative is often written as

$$u' = v.$$

Consider now the time-dependent model problem

$$\partial_t u - \nabla \cdot (D\nabla u) + \vec{a} \cdot \nabla u = f, \quad x \in \Omega, t \in [0, T], \quad (3.31)$$

with boundary conditions given by (3.29) and initial condition  $u_0 = u(0, x)$ . The weak formulation is then of the form

$$\begin{aligned} & \frac{d}{dt} \int_\Omega u\varphi \, dx + \int_\Omega [-\nabla \cdot (D\nabla u) + \vec{a} \cdot \nabla u]\varphi \, dx \\ &= \frac{d}{dt} \int_\Omega u\varphi \, dx - D \int_{\Gamma_N} (\nabla u \cdot n)\varphi \, d\sigma + \int_\Omega (D\nabla u \cdot \nabla \varphi + (\vec{a} \cdot \nabla u)\varphi) \, dx \\ &= \frac{d}{dt} \int_\Omega u\varphi \, dx - \int_{\Gamma_N} g_N \varphi \, d\sigma + D \int_\Omega \nabla u \cdot \nabla \varphi \, dx + \int_\Omega (\vec{a} \cdot \nabla u)\varphi \, dx = \int_\Omega f\varphi \, dx. \end{aligned}$$

We finally can formulate the problem as follows:

**Definition 3.17** (Variational or weak formulation of the time-dependent problem). Let  $t \in [0, T]$ ,  $\vec{a} \in L^\infty$  and  $f \in H^{-1}(\Omega)$ . The variational or weak formulation of the non-stationary reaction-diffusion-advection equation (3.31) with boundary conditions (3.29) reads:

Find  $u \in L^2(0, T; H^1(\Omega))$  such that

$$\frac{d}{dt}m(u, \varphi) + a(u, \varphi) = l(\varphi) \quad (3.32)$$

for all  $\varphi \in H_0^1(\Omega)$ . The bilinear form  $a$ , the linear functional  $l$ , and the inner product  $m$  are given by

$$\begin{aligned} m(u, \varphi) &:= \int_{\Omega} u \varphi \, dx, \\ a(u, \varphi) &:= D \int_{\Omega} \nabla u \cdot \nabla \varphi \, dx + \int_{\Omega} (\vec{a} \cdot \nabla u) \varphi \, dx, \end{aligned}$$

and

$$l(\varphi) := \int_{\Omega} f \varphi \, dx + \int_{\Gamma_N} g_N \varphi \, d\sigma.$$

In other words, we derived an integral statement that is expected to be satisfied for an infinite number of test functions  $\varphi$ . That way, we reduced the problem of finding a classical solution of the PDE to the problem of finding a weak solution of the variational formulation.

### 3.6. Coupled bulk-surface PDEs

In Sections 3.3 and 3.4 we investigated reaction-diffusion systems for the ability of pattern formation. The equations were posed on a single bounded domain using suitable initial, boundary, or interface conditions. However, many biological processes occur on much more complex domains with complicated shapes. For instance, various cell processes like diffusion or protein interactions take place on the plasma membrane of the cell which is a thin layer around the cell cytosol. Simultaneously, membrane processes could influence cytosolic mechanisms.

All these processes involve a coupling of bulk and surface effects. Mathematically this can be reflected by the application of coupled bulk and surface partial differential equations. Such equations contain some unknowns defined on a spatial domain  $\Omega$ , as well as other unknowns defined on a lower-dimensional manifold  $\Gamma \in \bar{\Omega}$ .

In this thesis we are interested in the modeling of the establishment of polarity. This process also involves volume and interface mechanisms suggesting the application of coupled bulk-surface partial differential equations. To illustrate the concept of

such systems, in this section we study a mass conservative system of two interacting substances introduced in [31]. It is in this respect exemplary as it also simulates cell polarization.

Let  $\Omega \subset \mathbb{R}^3$  be a bounded domain and  $\Gamma := \partial\Omega \subset \mathbb{R}^2$  its boundary. Further, let  $u(x, t)$  and  $v(x, t)$  denote two interacting molecules, where time  $t \in [0, T]$ . With initial concentrations at time  $t = 0$  given by

$$u(x, 0) = u_0(x), \quad v(x, 0) = v_0(x),$$

the shuttling of both substances between the surface and bulk domain can be expressed in formulas as follows:

$$\partial_t u = \nabla_\Gamma \cdot (D_u \nabla_\Gamma u) + f(u, v|_\Gamma) \quad \text{on } \Gamma \times [0, T], \quad (3.33)$$

$$\partial_t v = \nabla \cdot (D_v \nabla v) \quad \text{in } \Omega \times [0, T], \quad (3.34)$$

$$-D_v \nabla v \cdot \vec{n} = f(u, v|_\Gamma) \quad \text{on } \Gamma \times [0, T]. \quad (3.35)$$

Here,  $\vec{n}$  denotes the outer normal to  $\Gamma$  and  $\nabla_\Gamma$  is the surface gradient. For a function  $\eta : \Gamma \rightarrow \mathbb{R}$  we define

$$\nabla_\Gamma \eta := \nabla \eta - (\nabla \eta \cdot \vec{n}) \vec{n}.$$

In case of constant diffusion coefficients  $D_u$  and  $D_v$ , system (3.33)-(3.35) reduces to

$$\partial_t u = D_u \Delta_\Gamma u + f(u, v|_\Gamma) \quad \text{on } \Gamma \times [0, T],$$

$$\partial_t v = D_v \Delta v \quad \text{in } \Omega \times [0, T],$$

$$-D_v \nabla v \cdot \vec{n} = f(u, v|_\Gamma) \quad \text{on } \Gamma \times [0, T],$$

where  $\Delta_\Gamma$  denotes the Laplace-Beltrami operator which is given by the surface divergence gradient defined by

$$\Delta_\Gamma := \nabla_\Gamma \cdot \nabla_\Gamma.$$

In order to apply finite element methods to solve (3.33)-(3.35) (see Section 4.2) we can proceed as presented in Section 3.5 and consider the weak formulation. Let  $V^{vol} := H^1(\Omega)$  denote the usual Sobolev space containing weak solutions in the bulk domain and  $V^{sur} := H^1(\Gamma)$  be the surface Sobolev space containing weak solutions on the hypersurface  $\Gamma$ . Taking some test functions  $\varphi_u \in V^{sur}$  and  $\varphi_v \in V^{bulk}$ , multiplication of (3.33) and (3.34) with  $\varphi_u$  and  $\varphi_v$  respectively leads to

$$\frac{d}{dt} \int_\Gamma u \varphi_u \, d\sigma = \int_\Gamma \nabla_\Gamma \cdot (D_u(x) \nabla_\Gamma u) \varphi_u \, d\sigma + \int_\Gamma f(u, v|_\Gamma) \varphi_u \, d\sigma,$$

$$\frac{d}{dt} \int_{\Omega} v \varphi_v \, dx = \int_{\Omega} \nabla \cdot (D_v(x) \nabla v) \varphi_v \, dx.$$

Using the surface divergence theorem and integration by parts (see [21] for more details), we obtain

$$\begin{aligned} \frac{d}{dt} \int_{\Gamma} u \varphi_u \, d\sigma &= - \int_{\Gamma} D_u(x) \cdot \nabla_{\Gamma} u \cdot \nabla_{\Gamma} \varphi_u \, d\sigma + \int_{\Gamma} f(u, v|_{\Gamma}) \varphi_u \, d\sigma, \\ \frac{d}{dt} \int_{\Omega} v \varphi_v \, dx &= - \int_{\Omega} D_v(x) \cdot \nabla v \cdot \nabla \varphi_v \, dx + \int_{\Gamma} (D_v(x) \nabla v \cdot \vec{n}) \varphi_v \, d\sigma. \end{aligned}$$

The boundary condition (3.35) finally yields

$$\frac{d}{dt} \int_{\Gamma} u \varphi_u \, d\sigma = - \int_{\Gamma} D_u(x) \cdot \nabla_{\Gamma} u \cdot \nabla_{\Gamma} \varphi_u \, d\sigma + \int_{\Gamma} f(u, v|_{\Gamma}) \varphi_u \, d\sigma, \quad (3.36)$$

$$\frac{d}{dt} \int_{\Omega} v \varphi_v \, dx = - \int_{\Omega} D_v(x) \cdot \nabla v \cdot \nabla \varphi_v \, dx - \int_{\Gamma} f(u, v|_{\Gamma}) \varphi_v \, d\sigma. \quad (3.37)$$

Assuming that  $f$  is a known function on  $\Gamma$ , we now seek a solution  $(u, v) \in L^2(0, T, V^{sur}) \times L^2(0, T, V^{bulk})$ , where  $u : \Omega \rightarrow \mathbb{R}$  and  $v : \Gamma \rightarrow \mathbb{R}$ , such that (3.36)-(3.37) holds for each  $t \in [0, T]$  and for all  $\varphi_u \in V^{sur}$ ,  $\varphi_v \in V^{bulk}$ .

In [31] the weak formulation (3.36)-(3.37) has been solved for different functions  $f$  simulating two well-known polarization mechanisms. The first exhibits a classical Turing instability introduced in Section 3.3. The second shows the so-called *Wave-Pinning*. This mechanism is characterized by a traveling wave which moves through the domain and finally stops [44, 61].

Figure 3.8 shows a simulation of the Wave-Pinning model with reaction kinetics given by

$$f(u, v) := v \left( k_0 + \frac{\gamma u^2}{K^2 + u^2} \right) - \delta u. \quad (3.38)$$

To obtain a solution, it is common to derive a discrete formulation of the variational form. This can be done using finite elements or finite volume methods. The next chapter describes the discretization schemes used in this work.

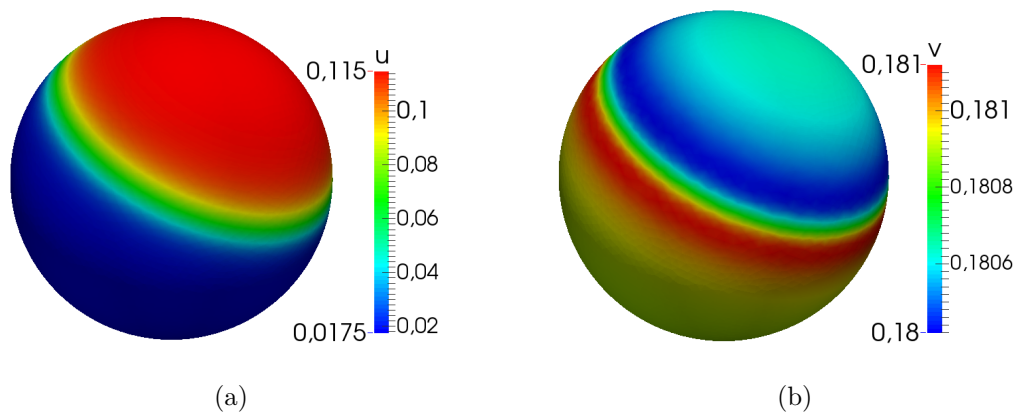


**Figure 3.8.: Illustration of pattern formation by the *Wave-Pinning* mechanism.** Numerical solution of (3.36)-(3.37) using kinetics given by (3.38) and parameters  $k_0 = 0.067, \gamma = 1, \delta = 1, K = 0.1, D_u = 0.015, D_v = 3$ . An initial perturbation of the homogeneous steady state leads to an inhomogeneous spatial pattern. Whereas  $u$  clusters at one site of the cell,  $v$  is nearly homogeneously distributed. (a) Concentration of  $u$  at time  $t = 120s$ . (b) Concentration of  $v$  at time  $t = 120s$





## 4 | Numerical methods

In this chapter we present the numerical approaches which are used for the class of mathematical models presented in this thesis. The Finite Element Method (FEM) and the Finite Volume Method (FVM) are well-known discretization methods which are well suited for the numerical simulation of partial differential equations. We explain the concepts of these two schemes which are closely related to one another. Throughout this work we concentrate on finite elements and the so-called Galerkin method to simulate reaction-diffusion systems. To compute solutions of systems containing advection-dominated equations, we apply the vertex-centered finite volume scheme which is also known as Petrov-Galerkin method. The fundamental idea of both methods is to discretize the mathematical model. In this way, the infinite-dimensional Hilbert Space  $V := H^1(\Omega)$  can be replaced by a finite-dimensional space  $V_h \subset V$ . Such a discrete space allows an approximation of the analytical solution  $u$  by a discrete solution  $u_h$  which is constructed as the sum of piecewise polynomial functions. In this introduction we fundamentally follow the description in [12, 23].

### 4.1. Triangulations and ansatz spaces

Numerical methods like the FEM or FVM are based on a prescribed discretization of the solution domain  $\Omega$  in an infinite number of simple subsets. This is usually done by a triangulation.

**Definition 4.1** (Triangulation). Let  $\Omega$  be an open set with boundary  $\partial\Omega$ . A conforming triangulation  $\mathcal{T}_h = \{T_k \mid k \in \{0, \dots, N\}\}$  with  $T_i \subseteq \Omega$  open, for all  $k \in [0, N]$  and non-overlapping partition  $T_k \cap T_l = \emptyset$  for all  $k, l \in [0, N]$ ,  $k \neq l$ , satisfying  $\bar{\Omega} = \bigcup_{k=1}^N \bar{T}_k$ , is called triangulation of  $\Omega$  with mesh size

$$h = \max \{ \text{diam}(T) \mid T \in \mathcal{T}_h \}.$$

In higher dimensions triangulations or meshes are usually constructed using simplices or cuboids. Note that the mesh then only approximates domains which are not

of polygonal shape. In this work, we exclusively consider simplicial partitions, i.e. partitions of the domain  $\Omega$  in a finite number of simplices. Furthermore, we consider consistent triangulations. This implies that the intersection of two simplices  $T_k \cap T_l$  for all  $k, l \in [0, N]$ ,  $k \neq l$ , is either empty or corresponds to a lower-dimensional boundary simplex of  $T_k$  and  $T_l$ . This approach prevents the occurrence of hanging nodes.

For FEMs, triangulations serve as constructions for finite dimensional ansatz spaces consisting of piecewise polynomial functions with fixed degree. To create an ansatz space we define the following polynomials:

**Definition 4.2.** Let  $\alpha$  be a multiindex. The space of polynomial functions  $\mathcal{P}_k$  of degree  $k$  is given as

$$\mathcal{P}_k = \left\{ p : \mathbb{R}^n \rightarrow \mathbb{R} \mid p(x) = \sum_{|\alpha| \leq k} c_\alpha x^\alpha \right\}.$$

By an appropriate operation of polynomial spaces  $\mathcal{P}_k(T) \in \mathcal{T}$ , different *ansatz spaces* for each triangulation can be defined. We restrict ourselves to piecewise constant or piecewise linear ansatz functions and define the following spaces:

**Definition 4.3** (Ansatz spaces). Let  $\Omega \subset \mathbb{R}^n$  be an open set and  $\mathcal{T}_h$  a triangulation of  $\Omega$ . The following function spaces of polynomial functions

$$\begin{aligned} \mathcal{P}_0(\mathcal{T}_h) &:= \{u_h \in L^2(\Omega) : u_h|_T \in \mathcal{P}_0(T) \text{ for } T \in \mathcal{T}_h\}, \\ \mathcal{P}_1(\mathcal{T}_h) &:= \{u_h \in L^2(\Omega) : u_h|_T \in \mathcal{P}_1(T) \text{ for } T \in \mathcal{T}_h\}, \\ \mathcal{P}_{1,D}(\mathcal{T}_h) &:= \{u_h \in \mathcal{P}_1(\mathcal{T}_h) : u_h = 0 \text{ on } \Gamma\} \end{aligned}$$

are called *ansatz spaces*. The functions  $u_h$  of  $\mathcal{P}_0(\mathcal{T}_h)$ ,  $\mathcal{P}_1(\mathcal{T}_h)$ ,  $\mathcal{P}_{1,D}(\mathcal{T}_h)$  are the related *ansatz functions*.

Figure 4.1 shows an example of a 1D  $\mathcal{P}_1$  space. These ansatz functions, as well as functions of the space  $\mathcal{P}_{1,D}(\mathcal{T}_h)$ , are continuous. This implies that the dimension of these spaces closely relates to the number of vertices of  $\mathcal{T}_h$ . By contrast, the ansatz space  $\mathcal{P}_0(\mathcal{T}_h)$  in general comprises of discontinuous functions and its dimension complies with the number of elements  $T \in \mathcal{T}_h$ .

Ansatz functions are typically defined in terms of a reference element  $E$ , e.g. the unit triangle in 2D, for the grid cell  $T$ . In this case, affine transformations are useful to map between a given simplex and the related reference element.

**Remark 4.4.** Given a finite set of reference elements  $\{E\}$ , we assume that for each

$T_k$  with  $k \in [0, N]$  exists an affine transformation  $F_{T_k}$  with

$$T_k = F_{T_k}(E). \quad (4.1)$$

Lastly, we need the concept of so-called degrees of freedom (DOFs). For a consistent triangulation  $\mathcal{T}_h$ , the DOFs of functions  $u_h \in \mathcal{P}_1(\mathcal{T}_h)$  are the function values at the vertices  $\mathcal{N}_{h,D} := \{x_1^h, \dots, x_{N_h,D}^h\}$  which do not lay on the boundary of  $\Omega$ . For all vertices we write  $\mathcal{N}_h := \{x_1^h, \dots, x_{N_h}^h\}$ .

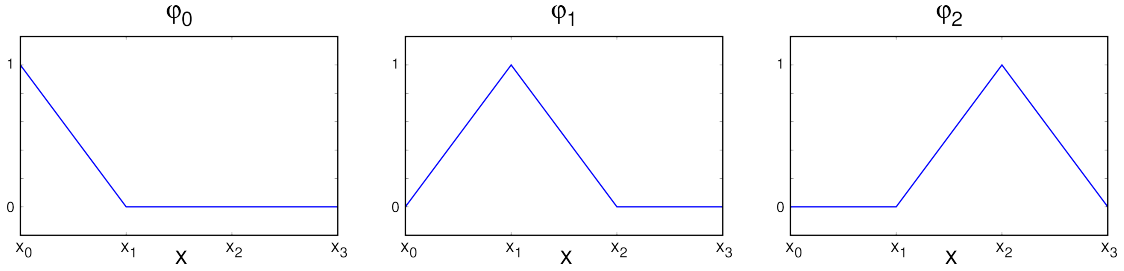


**Figure 4.1.: Basis functions for a finite element space.**  $\mathcal{P}_1$  basis functions for a finite element space in 1D are shown.

## 4.2. Finite Elements and the Galerkin method

To solve a variational formulation derived in the Section 3.5, the Galerkin finite element method is a common approach to determine the space discretization of spatial operators. Let  $\mathcal{T}_h$  be a consistent triangulation of  $\Omega$ . The Galerkin-ansatz for (3.32) with ansatz space  $V_h := \mathcal{P}_{1,D}(\mathcal{T}_h)$  leads to the semi-discrete problem:

$$\text{Find } u_h(t) \in V_h \text{ with } \frac{d}{dt}m(u_h, \varphi_h) + a(u_h, \varphi_h) = l(\varphi_h), \quad \varphi_h \in V_h, t > 0, \quad (4.2)$$

$$u_h(0) = u_0^h. \quad (4.3)$$

The inner product  $m$ , the bilinear form  $a$ , and the linear functional  $l$  are given by

$$\begin{aligned} m(u_h, \varphi_h) &:= \int_{\Omega} u_h \varphi_h \, dx, \\ a(u_h, \varphi_h) &:= D \int_{\Omega} \nabla u_h \cdot \nabla \varphi_h \, dx - \int_{\Omega} (\vec{a} \cdot \nabla u_h) \varphi_h \, dx, \\ l(\varphi_h) &:= \int_{\Omega} f \varphi_h \, dx + D \int_{\Gamma_N} g_N \varphi_h \, d\sigma. \end{aligned}$$

As mentioned before, the dimension of the ansatz space  $V_h$  is the number of vertices of  $\mathcal{T}_h$  that do not lie on  $\Gamma$ . Denoted by  $N_{h,D} \leq N_h$  the vertices are numbered such

that  $x_j^h$  is a boundary point if  $N_{h,D} \leq j \leq N_h$ . Let  $\Phi_h = \{\phi_1^h, \phi_2^h, \dots, \phi_{N_{h,D}}^h\}$  describe a convenient basis of  $V_h$  and let  $\phi_{N_{h,D}+1}^h, \dots, \phi_{N_h}^h$  be additional functions to extend the basis in order to ensure that the Dirichlet condition is satisfied. The finite element approximation is then the sum of a set of shape functions and boundary functions

$$u_h(x, t) = \sum_{j=1}^{N_{h,D}} u_{h,j}(t) \phi_j^h(x) + \sum_{j=N_{h,D}+1}^{N_h} u_{h,j}(t) \phi_j^h(x). \quad (4.4)$$

For simplicity we further consider only Neumann boundary or homogeneous Dirichlet boundary conditions. Formulation (4.2)-(4.3) can then be transformed to the equivalent linear system

$$\frac{d}{dt} \sum_{j=1}^{N_{h,D}} m(\phi_j^h, \phi_i^h) + \sum_{j=1}^{N_{h,D}} a(\phi_j^h, \phi_i^h) = l(\phi_i^h), \quad 1 \leq i \leq N_{h,D}, \quad (4.5)$$

$$u_{h,j}(0) = u_{0,j}^h, \quad 1 \leq j \leq N_{h,D}, \quad (4.6)$$

with unknowns  $u_{h,j}(t)$ . Here,  $u_{0,j}^h$  denote the nodal values of the given initial approximation  $u_0^h$ . In matrix notation (4.5)-(4.6) may be written as

$$M_h u_h'(t) = A_h u_h(t) + F_h(t), \quad \text{for } t > 0, \quad \text{with } u_h(0) = (u_{0,j}^h), \quad (4.7)$$

where  $M_h$  denotes the consistent mass matrix with elements

$$M_{h,i,j} = \int_{\Omega} \phi_j^h \phi_i^h \, dx$$

and

$$F_{h,i} = \int_{\Omega} f(t) \phi_i^h \, dx + D \int_{\Gamma_N} g_N(t) \phi_i^h \, d\sigma.$$

The vector  $u_h$  contains the entries  $u_{h,j}(t)$  and the matrix  $A_h$  is the negative of the discrete transport term and so-called stiffness matrix. It comprises of two parts, the global diffusion matrix with entries

$$A_{h,i,j}^{\text{diff}} := -D \int_{\Omega} \nabla \phi_j^h \cdot \nabla \phi_i^h \, dx,$$

and the global advection matrix with elements

$$A_{h,i,j}^{\text{adv}} := \int_{\Omega} (\vec{a} \cdot \nabla \phi_j^h) \phi_i^h \, dx.$$

Summarized, the problem of solving a time-dependent PDE is reduced to solving one full matrix problem.

## 4.3. Finite volume methods

We already mentioned the difficulties involved in numerical solutions of advection-driven systems. It can be shown that with dominating advection the convergence of the Galerkin discretization could be very bad. This is expressed by strong oscillations of the approximation  $u_h$  near boundary layers. In such cases the discretization must be stabilized. The implementation of an upwind scheme or the streamline diffusion method provide good ways to optimize the results. Throughout this work, to solve advection-dominated equations, we implement a finite volume upwind scheme. The FVM, which is also known as box method, uses the conservation law explained in Section 3.1.1. It subdivides each triangulation element into cells and evaluates the integral form of field equations. Since it associates control volumes and unknowns to vertices, it is denoted as vertex-centered finite volume method.

### 4.3.1. Dual box-grids

Besides the general finite element triangulation, the FVM requires so-called dual box grids. These grids have to satisfy specific balancing and regularity conditions to ensure optimal error estimates in  $L^2$ . In literature, different variants can be found:

- (i) Cell-centered finite volume methods
- (ii) Cell-vertex finite volume methods
- (iii) Vertex-centered finite volume methods

They differ in their construction of partitions. The presented work refers to vertex-centered finite volume methods. Let  $\mathcal{T}_h$  be a triangulation of a domain  $\Omega$  with vertices  $\mathcal{N}_h = \{x_1^h, \dots, x_{N_h}^h\}$ . For each vertex we assign a control volume  $b_j^h$ . To guarantee that the resulting equation systems are well-conditioned, we require that  $b_j^h$  contains  $x_j^h$  and is in turn contained in a neighborhood of  $x_j^h$ . We define a dual box grid or dual mesh as follows:

**Definition 4.5** (Dual box grid). Let  $\Omega$  be a domain and  $\mathcal{T}_h$  a consistent triangulation of  $\Omega$  with vertices  $x_1^h, \dots, x_{N_h}^h$ . Further, let  $\mathcal{B}_h = \{b_1^h, \dots, b_{N_h}^h\}$  be a non-overlapping partition  $b_i^h \subset \bar{\Omega}$  with  $b_i^h \cap b_j^h = \emptyset$  for all  $i, j \in [0, N_h]$ ,  $i \neq j$ . We call  $\mathcal{B}_h$  dual box grid if it satisfies

- (i)  $b_j^h$  is a closed Lipschitz domain,  $1 \leq j \leq N_h$ ,
- (ii)  $x_j^h \in b_j^h$  for  $1 \leq j \leq N_h$ ,

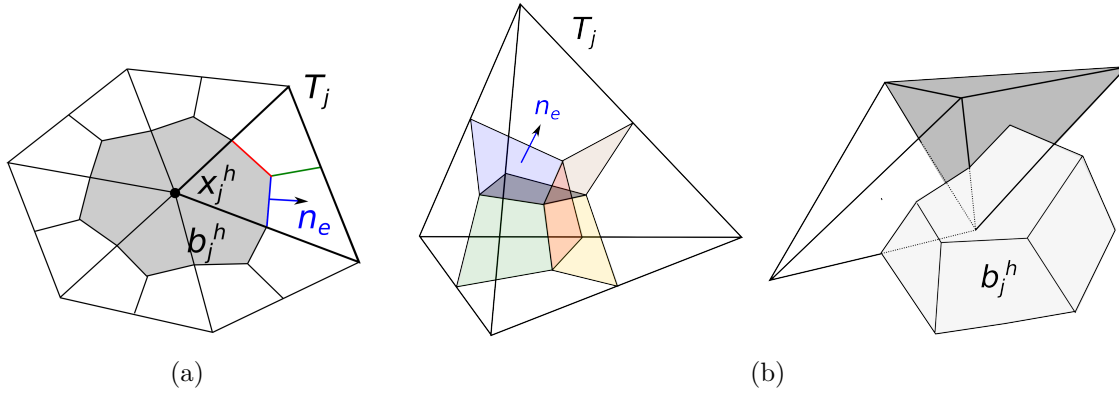


**Figure 4.2.: Visualization of the dual grid for a two- or three-dimensional simplex.** Dual grid creation for a vertex-centered finite volume scheme. (a) In 2D, the dual mesh can be created by connecting the barycenter of each cell with the middle points of its boundary edges. The control volume of a node  $x_j^h$  is then given by  $b_j^h$  (shaded in gray). (b) In 3D dual faces are given by the planes crossing through the barycenter of the tetrahedron, the barycenter of its faces, and the middle points of its edges. The control volume in this case is given by the resulting hexahedron around each node.

$$(iii) \quad b_j^h \in \Omega_j \text{ for } 1 \leq j \leq N_h,$$

$$(iv) \quad \bar{\Omega} = \bigcup_{j=1}^{N_h} b_j^h.$$

The control volumes  $b_j^h \in \mathcal{B}_h$  to the associated DOFs are now given by the volume of associated dual elements.

In 2D, the usual procedure to create a dual grid is to connect the barycenters of each simplex  $T$  of  $\mathcal{T}_h$  with the midpoints of its boundary edges. This results in a subdivision of the elements of the domain triangulation into three parts with equal area. In 3D we consider a separation into four equal parts (see Figure 4.2).

As for the FEM, we define appropriate ansatz functions for the dual grid.

**Definition 4.6.** Let  $\mathcal{T}_h$  be a consistent triangulation of the domain  $\Omega$  with vertices  $x_1^h, \dots, x_{N_h}^h$ . Further, let  $\mathcal{B}_h = \{b_1^h, \dots, b_{N_h}^h\}$  be a dual box grid of  $\mathcal{T}_h$ . The ansatz spaces with piecewise constant functions regarding  $\mathcal{B}_h$  are given as

$$\begin{aligned} \mathcal{P}_0(\mathcal{B}_h) &:= \{\varphi_h \in L^2(\Omega) : \varphi_h|_b \in \mathcal{P}_0(b) \text{ for } b \in \mathcal{B}_h\}, \\ \mathcal{P}_{0,D}(\mathcal{B}_h) &:= \{\varphi_h \in \mathcal{P}_0(\mathcal{B}_h) : \varphi_h|_{b_j^h} = 0, N_{h,D} < i \leq N_h\}. \end{aligned}$$

Figure 4.3 shows the basis functions for a finite volume space in 1D.

Similar to the FEM, it is necessary to define a basis for  $\mathcal{P}_0(\mathcal{B}_h)$  which is used to construct a discrete solution  $u_h$ . These are given by characteristic functions  $\chi_j^h$  of boxes  $b_j^h$ . We call this basis *characteristic basis* and define

**Definition 4.7** (The characteristic basis). Let  $\mathcal{T}_h$  be a consistent triangulation of the domain  $\Omega$  and  $\mathcal{B}_h = \{b_1^h, \dots, b_{N_h}^h\}$  be a dual box grid of  $\mathcal{T}_h$ . The *characteristic basis*  $\chi_h = \{\chi_1^h, \dots, \chi_{N_h}^h\}$  of  $\mathcal{P}_0(\mathcal{B}_h)$  reads

$$\chi_j^h \in \mathcal{P}_0(\mathcal{B}_h), \quad \chi_j^h|_{b_i^h} = \delta_{ij}, \quad 1 \leq i, j, \leq N_h.$$

Analogously,  $\chi_{h,D} := \{\chi_1^h, \dots, \chi_{N_{h,D}}^h\}$  denotes the *characteristic basis* of  $\mathcal{P}_{0,D}(\mathcal{B}_h)$ .

We write  $V_B := \mathcal{P}_{0,D}(\mathcal{B}_h)$ . By means of these ansatz spaces, we are now able to formulate the FVM for the reaction-diffusion-advection equation. Let  $\Omega$  be a domain with consistent triangulation  $\mathcal{T}_h$  and  $\mathcal{B}_h$  a corresponding dual box grid. Let further  $H_0^1(\Omega)$  be the solution space and  $H_0^1(\mathcal{B}_h)$  be the test space of the weak form. Applying Green's formula to each dual cell  $b \in \mathcal{B}_h$ , the abstract formulation of the semi-discrete problem related to  $B_h$  reads:

$$\text{Find } u_h(t) \in V_h \quad \text{with} \quad \frac{d}{dt} m(u_h, \varphi_h) + a(u_h, \varphi_h) = l(\varphi_h), \quad \varphi_h \in V_B, t > 0, \quad (4.8)$$

$$u_h(0) = u_{h,0}, \quad (4.9)$$

where

$$\begin{aligned} m(u_h, \varphi_h) &:= \int_{\Omega} u_h \varphi_h \, dx, \\ a(u_h, \varphi_h) &:= \sum_{b \in \mathcal{B}_h} \left( - \int_{\partial b} D \nabla u_h \varphi_h \cdot d\sigma + \int_{\partial b} \vec{a} u_h \varphi_h \cdot d\sigma \right), \\ l(\varphi_h) &:= \int_{\Omega} \varphi_h \, dx + D \int_{\Gamma_N} g_N \varphi_h \, d\sigma. \end{aligned}$$

The FEM and FVM are closely related. It can be shown that the stiffness matrices are equal for both schemes. By this close relationship, all negative properties transfer from the FEM to the FVM. This implies that for advection-dominated problems, the standard finite volume scheme induces oscillations as well. These oscillations can be explained by the fact that the stiffness matrix is not a M-matrix. In this case, the linear system can even be singular. However, the approach by finite volumes allows the application of a simple upwind scheme which is not possible with the finite element approach.

### 4.3.2. Upwind stabilization

In order to derive the upwind scheme, we further consider the dual edges  $\mathcal{E}(\mathcal{B}_h)$  of the corresponding dual box grid.

**Definition 4.8** (Upwind solution). Let  $[\varphi] = \varphi_{b_i^h} - \varphi_{b_j^h}$  for all  $\varphi \in V_{\mathcal{B}}$  denote the jump of  $\varphi$  across  $e$  separating the control volumes  $b_i^h$  and  $b_j^h$ . The upwind solution  $\bar{u}_h$  follows the streamlines and is given as

$$\bar{u}_h(t) := \begin{cases} u_h^-(t), & \vec{a} \cdot \vec{n}_e \geq 0, \\ u_h^+(t), & \vec{a} \cdot \vec{n}_e < 0, \end{cases}$$

where  $n_e$  denotes the unit outer normal of  $e$ .

As the unit normal  $\vec{n}_e$  is independent of the element containing  $e$ , we shall fix the direction  $\vec{n}_e$  of  $e$ . Then, for all  $\varphi_h \in V_{\mathcal{B}}$  and  $u_h \in V_h$ , the flux equations of the semi-discrete problem (4.8) can be written in terms of integrals over dual elements and dual faces

$$a(u_h, \varphi_h) = - \sum_{e \in \mathcal{E}(\mathcal{B}_h)} \int_e (D\nabla u_h) \cdot \vec{n}_e \cdot [\varphi_h] \, d\sigma + \sum_{e \in \mathcal{E}(\mathcal{B}_h)} \int_e (\vec{a} \cdot \vec{n}_e) \bar{u}_h \cdot [\varphi_h] \, d\sigma.$$

To get a linear system of equations, (4.8)-(4.9) can be written in terms of

$$\frac{d}{dt} \sum_{j=1}^{N_{h,D}} m(\phi_j^h, \chi_i^h) + \sum_{j=1}^{N_{h,D}} a(\phi_j^h, \chi_i^h) = l(\chi_i^h), \quad 1 \leq i \leq N_{h,D}, \quad (4.10)$$

$$u_{h,j}(0) = u_{0,j}^h, \quad 1 \leq j \leq N_{h,D}, \quad (4.11)$$

where  $\phi_j^h$  are appropriate basis functions. In matrix form this formulation reads

$$M_h u_h'(t) = A_h u_h(t) + F_h(t), \quad \text{for } t > 0, \quad \text{with } u_h(0) = (u_{0,j}^h). \quad (4.12)$$

Again, the vector  $u_h$  contains the entries  $u_{h,j}(t)$  and  $M_h$  denotes the consistent mass matrix with elements

$$M_{h,i,j} = \int_{\Omega} \phi_j^h \chi_i^h \, dx.$$

The components of  $F_h$  are given by

$$F_{h,i} = \int_{\Omega} f(t) \chi_i^h \, dx + D \int_{\Gamma_N} g_N(t) \chi_i^h \, d\sigma.$$

Note that whereas for the standard FEM the trial space corresponds to the test space, in this method the trial and test space are different. Such approach is known as Petrov-Galerkin method. For further details we refer to [12].

The entries of the comprehensive stiffness matrix  $A_h := A^{\text{diff}} + A_{\text{up}}^{\text{adv}}$  regarding the



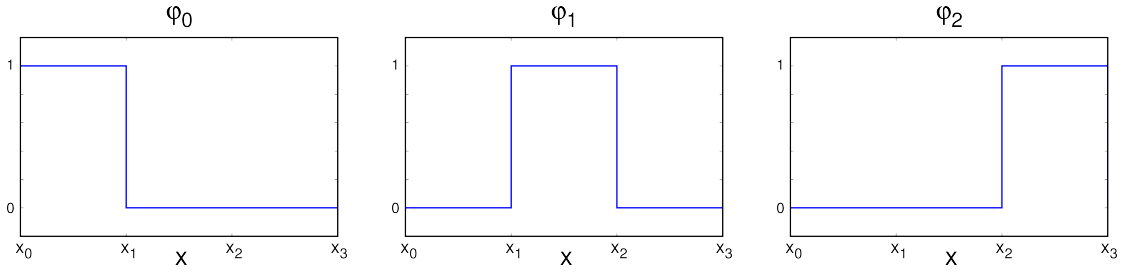


**Figure 4.3.:** Basis functions for a finite volume space. The basis functions in 1D are illustrated.

advection part now reads

$$A_{\text{up},i,j}^{\text{adv}} = \begin{cases} \sum_{k \neq i} J_{i,k}(T), & i = j, \\ \bar{J}_{i,k}(T) \geq 0 \\ J_{i,k}(T), & i \neq j, \quad J_{i,k}(T) < 0, \\ 0, & i \neq j, \quad J_{i,k}(T) \geq 0, \end{cases}$$

where  $J_{i,k}(T) := \text{vol}(e_{i,j}) \cdot \vec{a} \cdot \vec{n}_{e_{i,k}}$ . Here  $e_{i,k}$ ,  $k \neq l$ , denotes the volume of the hyper-face between the dual elements  $b_i$  and  $b_k$ . The vector  $\vec{n}_{e_{i,k}}$  describes the corresponding unit outer normal.

Contrary to the finite element scheme presented above, the finite volume upwind scheme implies a weak diagonal dominant stiffness matrix. Such matrices are advantageous with respect to solving advection-driven problems since they lead to a stable discretization (see [12] for further details).

## 4.4. Time discretization

Up to now, we have only discussed the spatial discretization of reaction-diffusion-advection equations. However, the variational formulations (4.2)-(4.3) and (4.8)-(4.9) are time-dependent. Whereas stationary problems only need to be discretized in space, such non-stationary problems are semi-discrete and must be integrated in time. For this reason, the time interval  $[0, T]$  has to be discretized as well in a similar way. Furthermore, in order to solve a semi-discrete system it is useful to decouple the space and time coordinates. This can be done by the method of lines (MOL) approach that separately considers space and time discretizations. This method is attractive and practical since a huge number of schemes exist developed for numerical integration of ordinary differential equations. In this work, we use an implicit one-step- $\theta$ -scheme to compute the time-dependent solution.

**Definition 4.9** ( $\theta$ -method). Consider a general formulation of an initial value problem for a system of ODEs

$$\frac{d}{dt}x(t) = F(t, x(t)), \quad t > 0,$$

with initial value  $x(0) = x_0$  and given  $F : \mathbb{R} \times \mathbb{R}^m \rightarrow \mathbb{R}^m$ . The requested solution  $x$  on the time interval  $[0, T]$  can be obtained by a so-called  $\theta$ -scheme. If the time interval is subdivided into  $0 = t_0 < t_1 < \dots < t_M = T$  with  $\Delta t_n = t_{n+1} - t_n$ , the approximation of  $x_{n+1}$  by the one-step- $\theta$ -scheme is given as

$$x_{n+1} - \Delta t_n(1 - \theta)F(t_{n+1}, x_{n+1}) = x_n + \Delta t_n\theta F(t_n, x_n).$$

The value  $\theta \in [0, 1]$  parameterizes this scheme and determines whether the resulting time discretization is implicit or explicit. For  $\theta > 0$  this method is implicit. For example,  $\theta = 1$  leads to the implicit Euler method and  $\theta = 1/2$  implies an implicit Crank-Nicolson scheme. For  $\theta = 0$  this is just the explicit Euler scheme.

Applying such approach, the question of convergence and stability naturally arises. The *Courant number* given by  $C = \frac{u\Delta t}{h}$  relates the time step to the mesh size. Whereas the explicit Euler scheme is only stable if  $C < 1$ , the implicit Euler and the Crank-Nicolson schemes are unconditionally stable. For more details we refer to [40].

# 5 | Computational implementation

The implementation of models presented in this thesis is based on the *Distributed and Unified Numerics Environment* (DUNE) framework. For that reason, in this chapter we give a short introduction into the concepts of DUNE. For further details we refer to [8–10] or to the website<sup>1</sup> which provides all the documentation, implementation, and development details.

Our approach to solve coupled bulk-surface problems is based on the DUNE modules multidomain and multidomaingrid [64]. We provide an explanation of the module principles and explain how these allow for a solution of surface partial differential equations.

## 5.1. The DUNE framework

DUNE is a set of C++ libraries which uses grid-based methods to numerically solve PDEs. It is an open source software framework composed of *core modules* which are the basis for supplementary modules and applications. The following three main design principles characterize the DUNE framework

**Flexibility:** Through abstract interfaces, it differentiates between data structures and algorithms. This allows the user to build programs that can change the underlying implementation without changing the user code. Another aspect is the usage of generic components which allow the reuse of different applications.

**Efficiency:** Since simulations of real-world problems can become performance heavy, software performance is of particular importance. By the usage of generic programming techniques DUNE manages to avoid performance losses and hence ensures high performance.

---

<sup>1</sup><https://www.dune-project.org>

**Extensibility:** Appropriate interface design makes it possible to incorporate existing code as well as libraries. Through this, it allows the reuse of existing finite element software. Furthermore, the module concept provides a clear separation between different parts of the framework, e.g. grid interface or linear algebra. Thus, it is easy to try different simulations by swapping out specific modules.

DUNE provides many important features to ensure a robust and performance optimized numerical treatment of PDEs. In order to achieve these targets, it applies the C++ template feature. Furthermore, it supports the application of different kinds of grids, supplies a flexible solver package, permits parallel implementations, and the incorporation of free software.

### 5.1.1. DUNE core modules

A team of *core developer* implemented the DUNE *core modules* which are the basis for grid-based simulations. Whereas so-called add-on modules refer to those which provide additional functionality, the core modules are required to create a program based on the DUNE framework. The core modules are

**dune-common:** This module provides the basic infrastructure used by all DUNE modules. This includes classes for exception handling and debugging as well as dense vectors and matrices.

**dune-geometry:** All things related to reference elements are compiled in the dune-geometry module. For instance, it supplies geometry transformations and quadrature rules as well as the reference elements themselves.

**dune-grid:** This module is the most mature one. It contains adapters for different pre-existing grid managers and components that implement the infrastructure providing grid in- and output. This module further defines nonconforming, hierarchically nested, multi-element-type, and parallel grids in arbitrary space dimensions.

**dune-istl:** ISTL is the abbreviation for *iterative solver template library* which comprises classes of vectors, matrices, algorithms, and solvers provided for sparse linear algebra.

**dune-localfunctions:** This module prescribes the interface of shape functions defined on the DUNE reference elements which are required for FEMs. It further

contains the implementation of this interface which includes interpolation operators as well as common elements like the Lagrange elements.

While the core modules contain all classes and methods required to realize a finite element approach for a model problem, the user still has to write a lot of infrastructure to run a simulation. Currently, there are three different additional modules which provide this functionality, the `dune-fem`, `dune-fufem`, and `dune-pdelab` module. The implementations of models presented in this thesis are based on the latter.

The DUNE PDELAB framework considerably simplifies the implementation of discretization schemes. It uses the weighted residual formulation to solve PDEs. Considering  $r(u_h, \varphi_h) = a(u_h, \varphi_h) - l(\varphi_h)$ , this method is based on a minimization of the residual  $r$ . For the time-dependent weak form, the modified residual form of (4.2)-(4.3) reads:

$$\text{Find } u_h(t) \in V_h \text{ with } \frac{d}{dt}m(u_h, \varphi_h) + r(u_h, \varphi_h) = 0, \quad \varphi_h \in V_h, t > 0, \quad (5.1)$$

$$u_h(0) = u_0^h. \quad (5.2)$$

To compute the residual, PDELAB uses a discrete function space which is bound to a grid view and based on local finite elements. That way, the matrix entries are calculated elementwise. Among others, the objectives of this module include time reduction of the implementation of such schemes to solve systems of PDEs and the suitability for teaching. This is achieved through a schematized procedure by using a general approach to constraints handling and a generic generation of product spaces. In this manner, it allows a fast and relatively easy implementation of a simple discretization scheme for a simple equation or a system of equations [11].

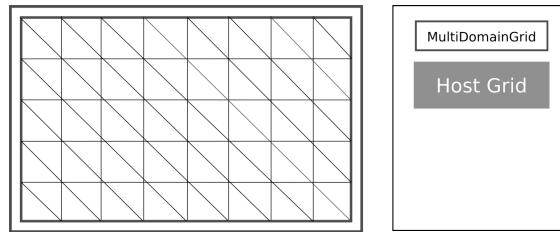
### 5.1.2. Dune-multidomain and dune-multidomaingrid

As already mentioned, the `dune-pdelab` module provides the infrastructure to solve PDEs and systems of PDEs in a simple manner. But the infrastructure is restricted to a single domain. Since most real-world problems involve more than a single domain, it was obvious to enhance this module by classes and functions providing the simulation of coupled multi-domain problems. To simulate multi-domain PDEs, DUNE has been extended by `dune-multidomaingrid` and `dune-multidomain`. These modules are add-on modules based on the concepts of existing models in the subdomains. Together they allow the use of different sets of equations in multiple subdomains and employ coupling conditions at a distinct interface. We will shortly explain the main concept of these modules and refer the reader to [64] for a detailed description.

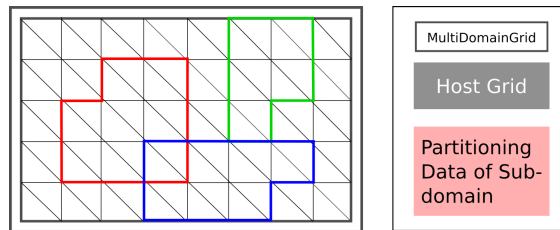
The `dune-multidomaingrid` module provides a mechanism to subdivide any existing DUNE mesh into multiple subdomains. The module is implemented in terms of two cooperating grids, `MULTIDOMAINGRID` and `SUBDOMAINGRID`. The `MULTIDOMAINGRID` wraps an existing *host grid*. In this way, it is extended by an interface provided to create and access subdomains. `MULTIDOMAINGRID` also handles spatial information about subdomains and stores all data required to manage separate meshes for those spatial subdomains. Each subdomain is then available to the user as a distinct `SUBDOMAINGRID`.

The procedure is as follows:

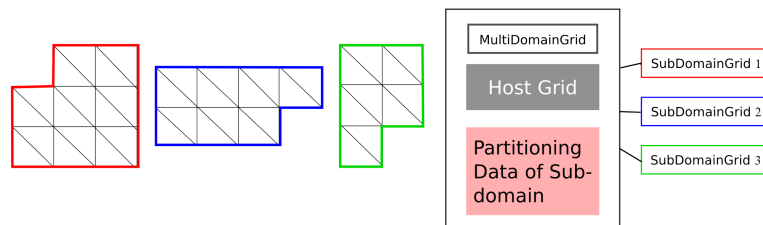
1. Take an existing grid and wrap it in a multi-domain grid which supports multiple subdomains



2. Mark the respective overlapping or non-overlapping subdomains by simply assigning grid cells to them



3. Expose subdomains as separate meta grids



Based on `dune-multidomaingrid` for subdomain information, the `dune-multidomain` software library implements the mathematical framework for the definition of multi-domain problems. It includes a set of extensions of `dune-pdelab` and makes the

components of the mathematical framework available within the solvers of PDELAB. It uses many of the abstractions introduced in `dune-pdelab` as well as the associated terminology. For instance, it allows the implementation of function spaces on parts of the whole domain. It further includes classes and functions required to connect different operators and function spaces as well as to couple between subdomains. For this purpose, based on the `MULTIDOMAINGRID`, it implements a `MULTIDOMAIN-GRIDFUNCTIONSPACE` which contains child grid function spaces related either to the `MULTIDOMAINGRID` or a `SUBDOMAINGRID`. Associated with a child function space it defines subproblem subspaces required for problem assembly as well as the respective subproblem. Usually each subproblem can be solved by an operator defined on the subspace. The coupling conditions are implemented in a coupling operator completing the numerical framework.

## 5.2. Numerical treatment of coupled bulk-surface problems

So far, `dune-multidomain` and `multidomaingrid` separate subdomains with the same dimension and so were not designed to solve coupled bulk-surface problems. However, by implementation of a coupled operator considering the lower dimensional surface between subdomains, these modules provide the possibility to restrict equations to a surface. Furthermore, it allows assembly of constraints on subspaces in a more capable way than the default PDELAB constraints assembler. To compute solutions

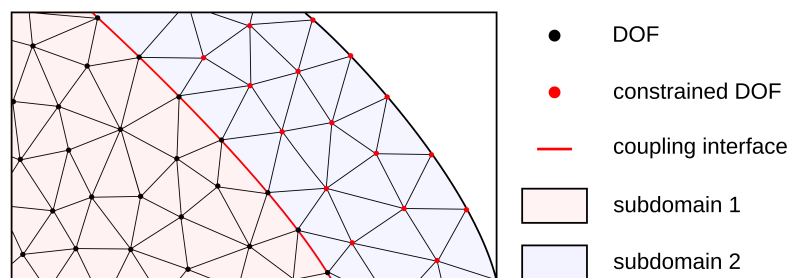


**Figure 5.1.:** Illustration of the numerical approach to solve a coupled bulk-surface problem with `dune-multidomaingrid` and `dune-multidomain`. The DOFs of the second subdomain are constrained. The surface PDEs are implemented in the coupling operator defined on the coupling interface.

of a coupled bulk-surface problem, we proceed as follows. We construct a model geometry composed of two bulk domains. In terms of `dune-multidomain`, each of these domains relates to a subdomain. The two subdomains are chosen such that

the interface between them is the surface of interest. Then, the surface PDEs can be computed using the coupling operator applying surface gradients. The bulk equations can be solved by the respective operator for each subdomain. Since there are no equations posed on the second subdomain, for this subproblem there is no implementation needed and we can constrain the DOFs which are not related to the coupling surface (see Figure 5.1). In general, in DUNE the constraints are created like this:

```

1 // define constraints, in the case of bulk-surface coupling
2 typedef Dune::PDELab::NoConstraints NOCON;
3 NOCON nocon;
4
5 // for the multi-domain gridview (mdgv) define not coupling node
6 // constraints on the outer bulk
7 typedef Dune::PDELab::NotCouplingNodeConstraints<MDGV> NOTCOUPCON;
8 NOTCOUPCON notcoupcon(mdgv);
9 ncon.updateNotCouplingNodes(mdgv,0,1);

```

Using these constraints we define a GRIDFUNCTIONSPACE for both domains:

```

1 // create grid function spaces for the outer bulk domain (not
2 // coupling nodes are constrained to only consider the coupling
3 // surface)
4 typedef Dune::PDELab::GridFunctionSpace<
5     SDGV,
6     FEMSurface,
7     NOTCOUPCON,
8     VBE
9 > GFSSurface;
10 GFSSurface gfssurface(sdgv0,femsurface,notcoupcon);
11
12 // create grid function space for the bulk
13 typedef Dune::PDELab::GridFunctionSpace<
14     SDGV,
15     FEMBulk,
16     NOCON,
17     VBE
18 > GFSBulk;
19 GFSBulk gfsbulk(sdgv1,fembulk,nocon);

```

Both GRIDFUNCTIONSPACES are now combined to generate a MULTIDOMAINGRIDFUNCTIONSPACE:

```

1 // create composite grid function space
2 typedef Dune::PDELab::MultiDomain::MultiDomainGridFunctionSpace<

```



```

3      Grid,
4      VBE,
5      Dune::PDELab::LexicographicOrderingTag,
6      GFSSurface,
7      GFSBulk
8 > MultiGFS;
9 MultiGFS multigfs(grid, gfssurface, gfsbulk);

```

This MULTIDOMAINGRIDFUNCTIONSPACE finally builds the basis to solve coupled multi-domain problems (see [64] for further details). Together with our constraints handling, it provides a simple method to compute coupled bulk-surface PDEs.

### 5.3. Dual grid assembly

To apply the presented finite volume upwind scheme, in addition to the domain triangulation, we require a dual grid. Since the dune-pdelab module is designed for calculations on reference elements of a domain triangulation, we implement a class that creates a dual grid to the simplex reference element. Applying an appropriate transformation, this allows us to calculate all matrix entries in terms of reference elements.

The construction of the box grid used in this work is based on the barycenter method. Figure 5.2 shows the resulting dual grid for the reference element in 2D. The class contains all information about coordinates of dual nodes and dual faces. It further stores the unit outer normals to each dual face with respect to a vertex of the domain triangulation.

The proceeding for a local operator which accumulates residual contributions of each grid cell is as follows:

```

1 // loop over vertices of this element
2 for ( int i = 0; i<lfsu.size(); i++){
3     // counterclockwise in dimension 2
4     for(int k=0; k<dim-1; k++){
5         int iInside=i; int iOutside;
6         if (iInside == 3)
7             continue;
8         if ( k==1 )

```

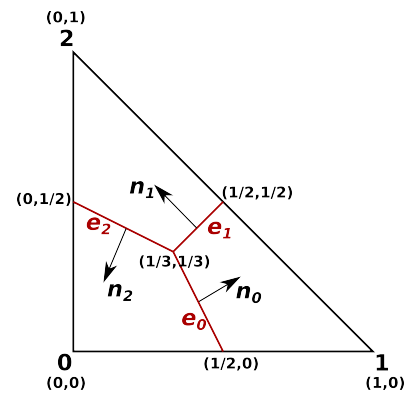


**Figure 5.2.:** Dual nodes and edges in a 2D reference element. The unit outer normals to dual edges are fix for each vertex. The normals are  $\vec{n}_0 = [0.8944, 0.4472]$ ,  $\vec{n}_1 = [-0.7071, -0.7071]$ ,  $\vec{n}_2 = [-0.4472, -0.8944]$ .

```

9             iOutside = 3;
10            else{
11                if (i == 2 )
12                    iOutside = 0;
13                else
14                    iOutside = i+1;}
15
16            // get local positions of actual vertex
17            LC insideVertex = dualGrid.thisVertex(iInside);
18
19            // get function values at the vertex relating to dual edge i
20            RF uInside = x(lfsu,iInside);
21            RF uOutside = x(lfsu,iOutside);
22            RF flux, term, diffusion;
23
24            // get local unit outer normal to this vertex
25            LC localnormal = dualGrid.localUnitOuterNormal(iInside,k);
26
27            // transform local normal of dual face to global normal
28            GC normal;
29            jac.mv(localnormal,normal);
30            normal /= normal.two_norm();
31
32            // compute flux over dual entity i
33            flux = c*normal;
34
35            // evaluate flux and choose upwind value for u
36            RF u=0.0;
37            if (flux >= 0.0)
38                u = uInside;
39            else
40                u = uOutside;
41
42            // calculate global volume of dual edge relating to actual vertex
43            RF volume = dualGrid.globalVolume(eg,iInside,k);
44            term = (u*flux-d*(ub.gradient(x,insideVertex,jac)
45                *normal))*volume; // calculate contribution
46
47            // accumulate to residual, contribution to both vertices
48            // of the edge where the dual face crosses the middle point
49            r.accumulate(lfsu,iInside,term*1.0);
50            r.accumulate(lfsu,iOutside,term*-1.0);
51        }
52    }

```

For each element of the triangulation, the contribution of fluxes to each vertex are calculated. By a loop over vertices, the fluxes related to the right-hand outer unit normal are accumulated.

## 5.4. The implementation of test problems

We proceed with the implementation of a test problem. To investigate stability and convergence of our numerical approach, we consider two different test problems with known analytical solution. The first example is a system of stationary coupled bulk-surface PDEs. This example allows us to verify the implementation of our approach to solve coupled bulk-surface problems applying dune-multidomain and dune-multidomaingrid. Furthermore, errors for the implemented finite element and finite volume schemes to test the efficiency are calculated.

The second model problem, an advection-dominated PDE, serves to test the implemented dual grid construction and the upwind approach.

### 5.4.1. A coupled-bulk-surface test problem

Consider a domain  $\Omega \subset \mathbb{R}^2$  and its boundary  $\Gamma := \partial\Omega \subset \mathbb{R}$ . The model problem reads

$$-\Delta_\Gamma u = f(u, v|_\Gamma) + g(u) \quad \text{on } \Gamma := \partial\Omega, \quad (5.3)$$

$$-\nabla v \cdot \vec{n} = f(u, v|_\Gamma) \quad \text{on } \Gamma, \quad (5.4)$$

$$-\Delta v = h(v) \quad \text{in } \Omega := \{x \in \mathbb{R}^2 \mid \|x\| < 1\}, \quad (5.5)$$

with given data functions  $f(u, v|_\Gamma) : \Gamma \rightarrow \mathbb{R}$ ,  $g(u) : \Gamma \rightarrow \mathbb{R}$ , and  $h(v) : \Omega \rightarrow \mathbb{R}$ .

For  $f(u, v|_\Gamma) := v|_\Gamma - u$ ,  $g(u)(x) := -u(x) + 17x_1x_2$  and  $h(v) := 0$ , the system has the classical unique solution  $(u, v)$  with  $u(x) = 3x_1x_2$  and  $v(x) = x_1x_2$  (see Figure 5.3).

The multiplication of both equations with suitable test functions leads to the weak form. In its discrete form, the model problem is given as:

Find  $u_h, v_h \in V_h$  with

$$\begin{aligned} \int_\Gamma \nabla_\Gamma u_h \nabla_\Gamma \varphi_{u_h} \, d\sigma &= \int_\Gamma f(u_h, v_h|_\Gamma) \varphi_{u_h} + g(u_h) \varphi_{u_h} \, d\sigma, \quad \forall \varphi_{u_h} \in V_h, \\ \int_\Omega \nabla v_h \nabla \varphi_{v_h} \, dx &= \int_\Omega h(v_h) \varphi_{v_h} \, dx + \int_\Gamma f(u_h, v_h|_\Gamma) \varphi_{v_h} \, d\sigma, \quad \forall \varphi_{v_h} \in V_h. \end{aligned}$$

Let  $(u_h, v_h)$  denote the numerical solution of (5.3)-(5.5) depending on the mesh size

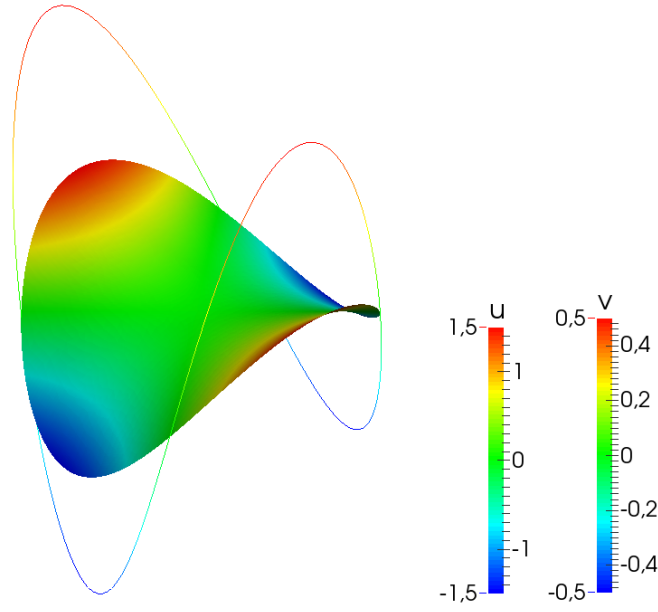


**Figure 5.3:** Analytical solution of the coupled bulk-surface test problem. Analytical surface ( $u$ ) and bulk solution ( $v$ ) of equations (5.3)-(5.5) are illustrated.

$h$ . In order to analyze the convergence of the numerical schemes, we compute relative errors for the bulk and surface domain respectively

$$\begin{aligned} \|u - u_h\|_{L^2(\Gamma)} / \|u\|_{L^2(\Gamma)}, & \quad \|u - u_h\|_{H^1(\Gamma)} / \|u\|_{H^1(\Gamma)}, \\ \|v - v_h\|_{L^2(\Omega)} / \|v\|_{L^2(\Omega)}, & \quad \|v - v_h\|_{H^1(\Omega)} / \|v\|_{H^1(\Omega)}, \end{aligned}$$

where

$$\begin{aligned} s \in H^1(\Gamma) : \quad \|s\|_{H^1(\Gamma)} &:= \left( \|s\|_{L^2(\Gamma)}^2 + \|\nabla_{\Gamma} s\|_{L^2(\Gamma)}^2 \right)^{1/2}, \\ b \in H^1(\Omega) : \quad \|b\|_{H^1(\Omega)} &:= \left( \|b\|_{L^2(\Omega)}^2 + \|\nabla b\|_{L^2(\Omega)}^2 \right)^{1/2}. \end{aligned}$$

The convergence order is given as follows:

**Definition 5.1** (Experimental Order of Convergence (EOC)). Let  $u$  be a given function and  $u_{h_1}, u_{h_2}$  approximations depending on the mesh size  $h_1$  and  $h_2$ . The Experimental Order of Convergence (EOC) is defined as

$$EOC_h = \frac{\log(\|u - u_{h_1}\| / \|u - u_{h_2}\|)}{\log(h_1/h_2)}, \quad (5.6)$$

where  $\|\cdot\|$  is a given norm.

$h$	FEM		FVM	
	$\text{Err}_{L^2(\Omega)}$	$\text{EOC}_{L^2(\Omega)}$	$\text{Err}_{L^2(\Omega)}$	$\text{EOC}_{L^2(\Omega)}$
$5.7735 \times 10^{-1}$	$3.44123 \times 10^{-2}$	—	$3.70483 \times 10^{-2}$	—
$3.40275 \times 10^{-1}$	$1.00415 \times 10^{-2}$	2.32969	$9.1557 \times 10^{-3}$	2.64396
$1.89769 \times 10^{-1}$	$2.8705 \times 10^{-3}$	2.14444	$2.87338 \times 10^{-3}$	1.98458
$1.05668 \times 10^{-1}$	$8.12065 \times 10^{-4}$	2.15654	$7.77696 \times 10^{-4}$	2.23211
$5.29919 \times 10^{-2}$	$2.0021 \times 10^{-4}$	2.02881	$1.98422 \times 10^{-4}$	1.97915
$2.66646 \times 10^{-2}$	$4.99792 \times 10^{-5}$	2.0206	$4.96615 \times 10^{-5}$	2.01683
$1.38788 \times 10^{-2}$	$1.25472 \times 10^{-5}$	2.11665	$1.23513 \times 10^{-5}$	2.13098
$7.07785 \times 10^{-3}$	$3.14446 \times 10^{-6}$	2.05505	$3.08389 \times 10^{-6}$	2.06057

**Table 5.1.:** Overview over bulk  $L^2$ -errors and EOCs calculated for the test problem. Errors and EOCs dependent on the gridwidth  $h$  as well as the distinct schemes, the FEM and FVM, are compared.

$h$	FEM		FVM	
	$\text{Err}_{H^1(\Omega)}$	$\text{EOC}_{H^1(\Omega)}$	$\text{Err}_{H^1(\Omega)}$	$\text{EOC}_{H^1(\Omega)}$
$5.7735 \times 10^{-1}$	$3.67039 \times 10^{-1}$	—	$4.06846 \times 10^{-1}$	—
$3.40275 \times 10^{-1}$	$1.9629 \times 10^{-1}$	1.18381	$2.01193 \times 10^{-1}$	1.3319
$1.89769 \times 10^{-1}$	$1.06239 \times 10^{-1}$	1.0513	$1.07037 \times 10^{-1}$	1.08074
$1.05668 \times 10^{-1}$	$5.42648 \times 10^{-2}$	1.14741	$5.43782 \times 10^{-2}$	1.15663
$5.29919 \times 10^{-2}$	$2.6893 \times 10^{-2}$	1.01716	$2.69072 \times 10^{-2}$	1.01942
$2.66646 \times 10^{-2}$	$1.34249 \times 10^{-2}$	1.01157	$1.34267 \times 10^{-2}$	1.01215
$1.38788 \times 10^{-2}$	$6.69768 \times 10^{-3}$	1.06491	$6.6979 \times 10^{-3}$	1.06506
$7.07785 \times 10^{-3}$	$3.36034 \times 10^{-3}$	1.02424	$3.36037 \times 10^{-3}$	1.02428

**Table 5.2.:** Overview over bulk  $H^1$ -errors and EOCs calculated for the test problem. Errors and EOCs dependent on the gridwidth  $h$  as well as the distinct schemes, the FEM and FVM, are compared.

$h$	FEM		FVM	
	$\text{Err}_{L^2(\Gamma)}$	$\text{EOC}_{L^2(\Gamma)}$	$\text{Err}_{L^2(\Gamma)}$	$\text{EOC}_{L^2(\Gamma)}$
$5.17638 \times 10^{-1}$	$9.29044 \times 10^{-2}$	–	$1.28441 \times 10^{-1}$	–
$2.61052 \times 10^{-1}$	$2.54193 \times 10^{-2}$	1.89329	$3.3467 \times 10^{-2}$	1.96464
$1.42678 \times 10^{-1}$	$7.68856 \times 10^{-3}$	1.97934	$1.00943 \times 10^{-2}$	1.984
$7.47824 \times 10^{-2}$	$2.11119 \times 10^{-3}$	2.00071	$2.79028 \times 10^{-3}$	1.99041
$3.73977 \times 10^{-2}$	$5.27774 \times 10^{-4}$	2.00057	$6.99164 \times 10^{-4}$	1.99721
$1.86997 \times 10^{-2}$	$1.31957 \times 10^{-4}$	1.99998	$1.74875 \times 10^{-4}$	1.99943
$9.34994 \times 10^{-3}$	$3.29793 \times 10^{-5}$	2.00047	$4.37349 \times 10^{-5}$	1.9995
$4.67498 \times 10^{-3}$	$8.25016 \times 10^{-6}$	1.99908	$4.37349 \times 10^{-5}$	2.00066

**Table 5.3.: Overview over surface  $L^2$ -errors and EOCs calculated for the test problem.** Errors and EOCs dependent on the gridwidth  $h$  as well as the distinct schemes, the FEM and FVM, are compared.

$h$	FEM		FVM	
	$\text{Err}_{H^1(\Gamma)}$	$\text{EOC}_{H^1(\Gamma)}$	$\text{Err}_{H^1(\Gamma)}$	$\text{EOC}_{H^1(\Gamma)}$
$5.17638 \times 10^{-1}$	$8.19414 \times 10^{-1}$	–	$8.453 \times 10^{-1}$	–
$2.61052 \times 10^{-1}$	$4.0425 \times 10^{-1}$	1.03214	$4.07238 \times 10^{-1}$	1.06681
$1.42678 \times 10^{-1}$	$2.19595 \times 10^{-1}$	1.01013	$2.20085 \times 10^{-1}$	1.01863
$7.47824 \times 10^{-2}$	$1.14874 \times 10^{-1}$	1.003	$1.14947 \times 10^{-1}$	1.00547
$3.73977 \times 10^{-2}$	$5.74156 \times 10^{-2}$	1.00079	$5.74248 \times 10^{-2}$	1.00147
$1.86997 \times 10^{-2}$	$2.87051 \times 10^{-2}$	1.0002	$2.87063 \times 10^{-2}$	1.00037
$9.34994 \times 10^{-3}$	$1.43522 \times 10^{-2}$	1.00005	$1.43524 \times 10^{-2}$	1.00009
$4.67498 \times 10^{-3}$	$7.17608 \times 10^{-3}$	1.00001	$7.17609 \times 10^{-3}$	1.00002

**Table 5.4.: Overview over surface  $H^1$ -errors and EOCs calculated for the test problem.** Errors and EOCs dependent on the gridwidth  $h$  as well as the distinct schemes, the FEM and FVM, are compared.

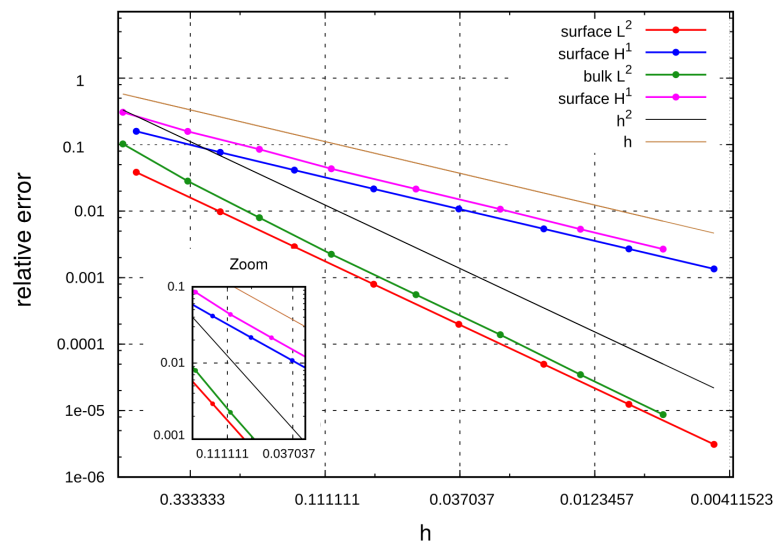


**Figure 5.4.:** Plot of relative errors computed with the test problem. Relative Errors in  $L^2$  and  $H^1$  in terms of changes of the maximal grid width  $h$ .

All computations presented in this thesis are based on non uniform grids. For the test problem, calculations were done for a sequence of simplex grids with decreased cell size. The grids which are constructed in Gmsh, a three-dimensional finite element mesh generator [29], are successively loaded. Calculating the discrete solution using  $\mathcal{P}_1$  basis functions, we obtain relative errors in  $L^2$  and  $H^1$  (see Figure 5.4). Tables 5.1 and 5.2 show the EOC in  $L^2$  and  $H^1$  of the discrete bulk component  $u_h$  and Tables 5.3 and 5.4 of the discrete surface solution  $v_h$  respectively. The convergence order is nearly optimal for both schemes, the FEM and FVM. It holds that  $\|u - u_h\|_{L^2(\Gamma)} \propto h^2$  and  $\|v - v_h\|_{L^2(\Omega)} \propto h^2$  as well as  $\|u - u_h\|_{H^1(\Gamma)} \propto h$  and  $\|v - v_h\|_{H^1(\Omega)} \propto h$ .

### 5.4.2. An advection-dominated test problem

Since the prior presented coupled bulk-surface model does not include advection, the standard Galerkin approach shows good results for this test problem. But these results can not be transferred to advective-driven situations. Consider the stationary reaction-diffusion-advection equation

$$-D\Delta u + \vec{a} \cdot \nabla u = f \quad (5.7)$$

with Dirichlet boundary conditions

$$u(x_1, 1) = 0, \quad u(x_1, -1) = x_1,$$

$$u(-1, x_2) \approx -1, \quad u(1, x_2) \approx 1,$$

$\vec{a} = (0, 1)$  and  $f \equiv 0$ . From the analytical solution given by the function

$$u(x_1, x_2) = x_1 \left( \frac{1 - e^{\frac{x_2-1}{D}}}{1 - e^{\frac{-2}{D}}} \right),$$

it is directly clear that the boundary values vary considerably close to  $x_2 = 1$ .

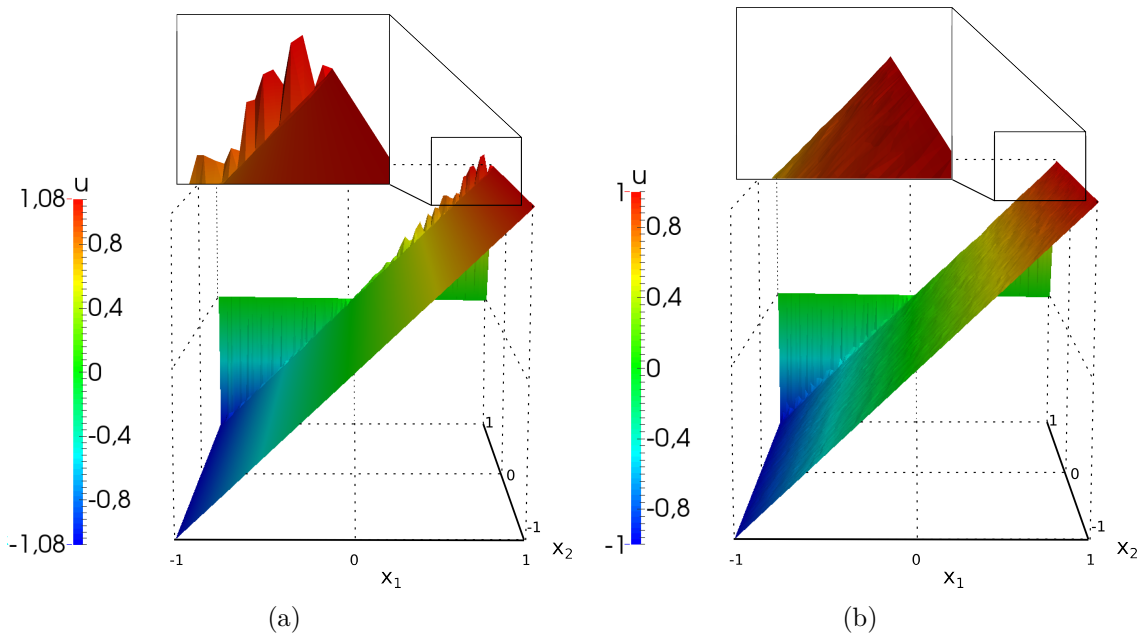


**Figure 5.5.: Comparison of the Galerkin method and the vertex-centered finite volume upwind scheme.** Comparison of numerical solutions of the reaction-diffusion-advection equation (3.7) with  $f \equiv 0$  and parameters  $d = 0.01$ ,  $\vec{a} = [1, 0]$ . (a) Discrete solution  $u$  using the standard Galerkin method. (b) Discrete solution  $u$  using the vertex-centered finite volume upwind scheme.

For very small diffusion constants  $D$ , the solution approximates  $x_1$  except at  $x_2 = 1$ . Near this outflow boundary  $u$  vanishes. This extreme change of the solution near  $x_2 = 1$  induces a boundary layer so that the standard Galerkin method may involve errors in this region. Figure 5.5 shows the numerical solution of (5.7) with  $D = 0.01$ . If the mesh is not fine enough to resolve steeply varying layers in the solution, the Galerkin method is inaccurate and give erroneous results. Such inaccuracies may also affect the numerical solution in regions of the domain where the exact solution is well-behaved resulting in so-called *wiggles*. For these cases, the vertex-centred finite volume upwind scheme provides an elegant approach to ameliorate the problem by increasing stability (see Figure 5.5 (b)).



## 5.5. Discussion

For a coupled bulk-surface problem the stability and convergence behavior of the FEM and FVM using dune-multidomain and dune-multidomaingrid is investigated. The results show that the *coupled multi-domain approach* to solve diffusion-driven coupled bulk-surface PDEs on a fix domain is suitable for grids with convenient grid size. With increasing fineness of the mesh, the FEM as well as FVM show optimal convergence order in  $L^2$  and  $H^1$ .

In contrast, the numerical implementation of an advection-driven problem applying a method without stabilizing mechanisms leads to oscillations that distort the results. For this case, a finite volume upwind scheme operating on a dual grid is used to stabilize the discretization. The dual grid is constructed for the reference element. In the setting of dune-multidomain, dune-multidomaingrid, and dune-pdelab, this proceeding makes it very easy to implement a finite volume upwind approach in terms of finite elements. A comparison with the standard FEM shows that this method is able to give results on relatively coarse grids without the occurrence of oscillations.



## 6 | A continuous reaction-diffusion-advection model for yeast cell polarization

Up to now, we have provided a lot of information about the modeling, the numerical simulation, and the analysis of partial differential equations. By means of these preliminaries, as well as the biological background provided in Chapter 2, we are now able to derive a mathematical model for yeast cell polarity. The preceding analysis of experimental data and mathematical models made clear that many different processes act in parallel to achieve symmetry breaking. Starting with a complex model simulating the mentioned pathways, we are aiming to develop a minimal continuous mathematical model bringing together all the findings that are known to be required for cell polarization. Under consideration of different pathways the model should account for the pathological cases shown in Figure 2.8.

### 6.1. The reaction-diffusion system

To simulate yeast cell polarization, we start with a simple reaction-diffusion system modeling the actin-independent pathways presented in Chapter 2. We avoid simply extending the model introduced in [32] and provide a new approach which does not rely only on the Bem1-mediated complex formation. We combine the results of [28, 32, 48, 84] and introduce a new model that considers a different approach to the reactions between Cdc42, Cla4, Bem1, and its GEF Cdc24 as well its GDI Rdi1. This allows us to focus on the identification of the mechanism required for GDI-mediated polarity.

As already mentioned, it is well known that Bem1 forms a complex with Cdc24, the exchange factor of Cdc42, which is able to change between the cytosol and the plasma membrane [13, 16]. Cdc24 also attaches to the plasma membrane by binding to the GTPase Rsr1. Since Rsr1 is required for polarity even in the absence

of actin [68], the disruption of both shows that the established polar cap exhibits drastically reduced spatial and temporal stability. In addition,  $\Delta rsr1 \Delta bem1$  double mutants fail to polarize. This leads to the assumption that Bem1 and Rsr1 share a role in Cdc24 localization [84]. We are aiming to include this alternative explanation into our approach and assume that Cdc24 generally shuttles between the cytosol and the plasma membrane by binding to Bem1 or Rsr1 at the plasma membrane. Thus, we simulate a stable Cdc24 GEF complex that cycles between the plasma membrane and the cytosol. Additionally, we include a GDI-mediated feedback mechanism proposed by [48, 84]. Since it has been shown that the PAK family kinase Cla4 as an effector of Cdc42-GTP can disrupt the binding of Cdc42 with its GDI Rdi1 and hence lead to the membrane attachment [91], we assume that the unbinding rate of GDI is proportional to Cdc42 in its active form.

To incorporate the suggested Cdc24 phosphorylation via Cla4 which leads to a decreased GEF activity, we take the simplified assumption that Cdc24 in its membrane-bound state decreases proportional to Cdc42-GTP. Similar to several previous studies we formulate simplified model assumptions. These are the basis used to derive a system of PDEs which simulates the proposed protein interactions and diffusion of molecules.

### Model assumptions

1. The species only change between distinct forms. Neither depletion nor synthesis during cell polarization occurs. This means that the total mass of the substances remains constant over the time scale on which the cell polarizes.
2. The GTPase Cdc42 has a basal rate of activation (GTP-association), and a basal turnover or inactivation rate (GTP-hydrolysis). Activation and inactivation of Cdc42 are indirect processes via the GEFs and GAPs respectively. These basal reactions are represented by a first-order rate constant. Furthermore, the membrane-bound Cdc24 GEF complex catalyzes the Cdc42-GDP/GTP exchange.
3. The GTPase Cdc42 switches between a plasma membrane-bound and, by binding to GDI, a cytosolic state. Cdc42 cannot exchange GDP for GTP while bound to GDI, but Cdc42-GTP indirectly disrupts the Cdc42-GDI complex via its effector Cla4.
4. The GEF Cdc24 transfers between the plasma membrane and the cytosol by binding to either Bem1 or Rsr1. Since Cdc42 is also able to bind to both Bem1

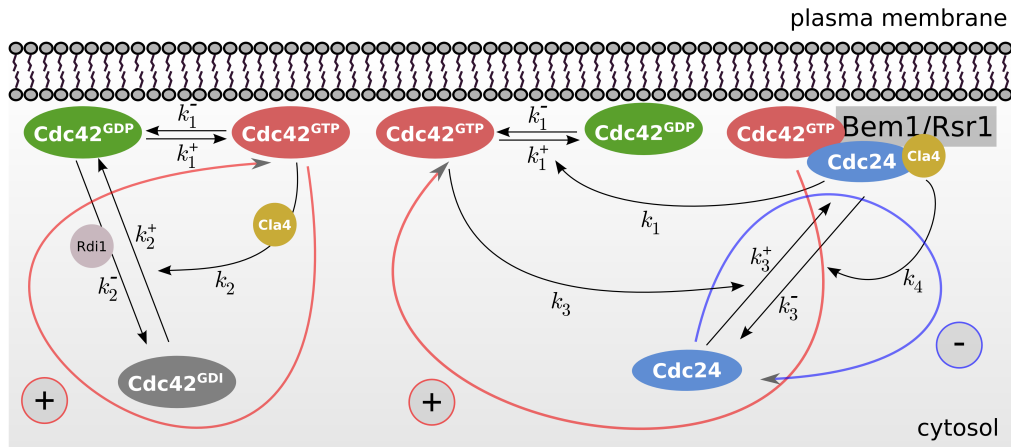


**Figure 6.1.: Reaction scheme of the model system.** A schematic representation of the modeled reactions. Cdc42 in its active form is able to induce two independent pathways leading to a further recruitment of Cdc42 to the plasma membrane. A negative feedback represents phosphorylation of Cdc42. The respective reaction rates are given in Table 6.1.

and Rsr1, the localized membrane attachment of Cdc24 leads to the activation of Cdc42. This induces a further recruitment of Bem1 that in turn stabilizes Cdc24 at this site. Summarized, it is assumed that the membrane-bound Cdc24 increases proportional to the local amount of Cdc42-GTP.

5. Cla4 as an effector of active Cdc42 disrupts the Cdc42-GDI complex. As a consequence, the GDI release rate indirectly depends on the rate of active Cdc42.
6. The PAK kinase Cla4 phosphorylates the GEF Cdc24 resulting in a detachment from the plasma membrane. This rate is also proportional to the amount of Cdc42-GTP.
7. The membrane-bound species have equal diffusion rates.
8. The diffusion in the cytosol is much faster than on the plasma membrane. This implies a well mixed and approximately spatially homogeneous cytosolic pool.
9. The amount of GDI in the cell is sufficiently large and no limiting factor. The exchange of Cdc42 in its GDI-bound state between the plasma membrane and the cytosol is very fast and quickly reaches a steady state. Hence, it suffices to consider one cytosolic GDI-bound state of Cdc42.

The modeled interactions are summarized in the reaction scheme illustrated in Figure 6.1.

To account for the geometry of the cell, we distinguish between the interior domain ( $\Omega_C$ ) and its surface ( $\Gamma_C$ ). Whereas  $\Omega_C$  represents the cytosol,  $\Gamma_C$  defines the plasma membrane. In the two-dimensional case the cell is represented by a disc-shaped geometry. In 3D the cell is reflected by a sphere (see Figure 6.2).

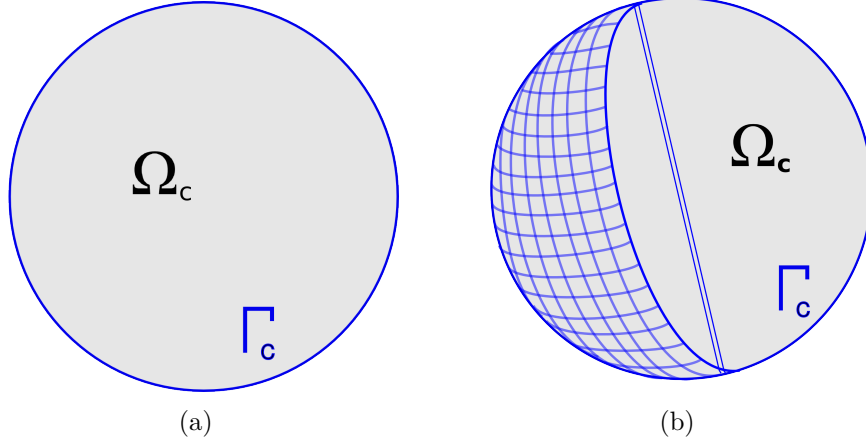


**Figure 6.2.: Model geometry for the reaction-diffusion system.** Scheme of the computational domain for the reaction-diffusion system.  $\Omega_C$  represents the cytosolic volume with boundary  $\Gamma_C$ , which is the one- or two-dimensional surface of the domain  $\Omega_C$ . (a) In 2D the cell is represented by a disc-shaped cell. (b) In 3D the cell is represented by a three-dimensional sphere.

The model variables are defined as follows:

- $C_T$  plasma membrane-bound (GTP-bound) active Cdc42
- $C_D$  plasma membrane-bound (GDP-bound) inactive Cdc42
- $C_I$  cytosolic (GDI-bound) inactive Cdc42
- $G_B$  plasma membrane-bound (active) GEF Cdc24
- $G_F$  cytosolic (inactive) GEF Cdc24

Based on Figure 6.1 and on the instructions provided in Appendix A, the respective reaction-diffusion equations can be derived. For  $t \in [0, T]$ , on  $\Omega_C$ , the system reads

$$\partial_t C_I = \nabla \cdot (D_c \nabla C_I), \quad (6.1)$$

$$\partial_t G_F = \nabla \cdot (D_c \nabla G_F). \quad (6.2)$$

The set of PDEs describing the time evolution of protein concentrations on the surface  $\Gamma_C$  is given by

$$\partial_t C_T = (k_1^+ + k_1 G_B) C_D - k_1^- C_T + \nabla_{\Gamma_C} \cdot (D_m \nabla_{\Gamma_C} C_T), \quad (6.3)$$

$$\begin{aligned} \partial_t C_D = & k_1^- C_T - (k_1^+ + k_1 G_B + k_2^-) C_D + (k_2^+ + k_2 C_T) C_I \\ & + \nabla_{\Gamma_C} \cdot (D_m \nabla_{\Gamma_C} C_D), \end{aligned} \quad (6.4)$$

$$\partial_t G_B = (k_3^+ + k_3 C_T) G_F - (k_3^- + k_4 C_T) G_B + \nabla_{\Gamma_C} \cdot (D_m \nabla_{\Gamma_C} G_B). \quad (6.5)$$

and the equations

$$-D_c \nabla C_I \cdot \vec{n} = (k_2^+ + k_2 C_T) C_I - k_2^- C_D, \quad (6.6)$$

$$-D_c \nabla G_B \cdot \vec{n} = (k_3^+ + k_3 C_T) G_F - (k_3^- + k_4 C_T) G_B, \quad (6.7)$$

describe the cytosolic flux of proteins to the membrane.

## 6.2. The reaction-diffusion-advection system

We further extend model (6.1)-(6.7) by incorporating a transport mechanism for Cdc42. To differentiate our model system from prior ones, we prefer to use continuous equations instead of a stochastic approach and make use of advection-diffusion equations.

The derivation of equations that simulate the suggested actin-mediated feedback require further model assumptions on actin cable nucleation, exocytosis, and endocytosis.

For actin cable nucleation we suppose the following:

1. The movement of actin cables depends indirectly on Cdc42-GTP.
2. The number of actin cable ends at the plasma membrane can be described as a (actin cable) *density*.
3. Due to polymerization and depolymerization, cables attach to or disappear from the plasma membrane. This process depends on active Cdc42 so that cable nucleation can be described by inhomogeneous diffusion relative to Cdc42-GTP concentration.

Mathematically, the last point can be written in terms of

$$\partial_t A = \nabla_{\Gamma_C} \cdot \left( D_A \nabla_{\Gamma_C} \left( \frac{A}{c(C_T)} \right) \right).$$

Here,  $A$  denotes the actin cable density and  $c(C_T)$  describes a capacity function depending on the concentration of active Cdc42-GTP that is given by  $C_T$ . Throughout

this thesis, we consider a simple linear function of the form  $c(C_T) = v \cdot C_T$ .

For endocytosis and exocytosis we take the following model assumptions:

1. Exocytosis and endocytosis enforce the shuttling between the interior of the cell and the plasma membrane.
2. Endocytosis extracts vesicles containing Cdc42 from the plasma membrane to internal compartments. Cables transport vesicles with Cdc42 from internal compartments to the plasma membrane.
3. Since the transport direction of exocytosis depends on actin cables, the velocity field driving vesicle movement depends on the actin cable *density*.
4. The rate of exocytosis is proportional to the number of delivered vesicles near the plasma membrane.
5. The respective rate of endocytosis is proportional to the amount of Cdc42 in its active or inactive form on the plasma membrane.
6. Vesicle trafficking involves Cdc42-GTP as well as Cdc42-GDP.

The cell contains different large components like the nucleus, the endoplasmic reticulum, or the Golgi apparatus. Furthermore, actin cables are aligned along the plasma membrane. For this reason, we restrict the molecule transport to a specific domain defined by a ring along the plasma membrane. This implies changes in the model geometry. We differentiate between a cytosolic domain ( $\Omega_C := \Omega_{C_1} \cup \Omega_{C_2}$ ) and a transport domain ( $\Omega_{C_1}$ ) (see Figure 6.3).

Up to now, vesicle transport has not been investigated in detail. It is supposed that endocytic vesicles move to internal compartments where they are converted and finally delivered back to the plasma membrane [79]. Here, we derive two approaches for vesicle transport through the cell.

### 6.2.1. Transport from and to internal membranes

As a first issue we consider an exchange of vesicles between internal membranes and the plasma membrane. We assume that vesicles which are internalized at the plasma membrane move to internal membranes or other compartments. There, the vesicles may diffuse or be converted before they are released to be transported back to the plasma membrane.

Transferring these assumptions to our model problem implies changes in the model



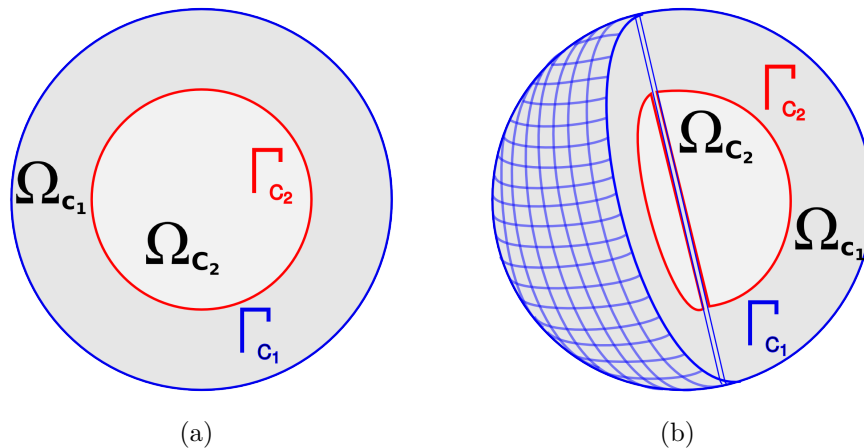


**Figure 6.3.: Model geometry for the reaction-diffusion-advection system.** Scheme of the computational domain for the reaction-diffusion-advection system.  $\Omega_{C_1}$  represents the outer transport domain of the cell with inner surface boundary  $\Gamma_{C_2}$ .  $\Omega_{C_2} \cup \Omega_{C_1}$  describes the cytosolic volume. The surface  $\Gamma_{C_1}$  finally defines the plasma membrane. (a) In 2D the cell is represented by a disc-shaped cell. (b) In 3D the cell is represented by a three-dimensional sphere.

geometry. It is required to consider an additional surface in the interior of the cell reflecting internal membranes. Furthermore, it is necessary to explicitly model the movement of vesicles in both directions. Let  $C_{TV_a}$  and  $C_{DV_a}$  as well as  $C_{TV_r}$  and  $C_{DV_r}$  denote the vesicles containing Cdc42-GTP and Cdc42-GDP moving in anterograde (outward) and retrograde (inward) direction. With  $C_{TV_i}$  and  $C_{DV_i}$  we denote the amount of active and inactive Cdc42 on internal membranes respectively. Further, let  $\vec{v}_a$  and  $\vec{v}_r$  be the velocity fields for each transport direction. Based on the simple idea that a potential flow describes the velocity field as the gradient of a scalar function, we introduce potential functions to calculate the velocity fields.

Consider the reaction-diffusion-advection equation for an arbitrary  $u(x, t)$  with  $x \in \mathbb{R}^n$  and  $t \in \mathbb{R}_+$

$$\partial_t u = \Delta u - \nabla \cdot (\vec{a}u) + f. \quad (6.8)$$

We can now define a potential function  $\Phi(x, t)$  as a continuous function

$$\vec{a} = \nabla \Phi. \quad (6.9)$$

In the case  $\vec{a}$  irrotational it holds

$$\nabla \times \vec{a} = 0. \quad (6.10)$$

Finally, with  $\vec{a}$  divergence free and substitution of (6.9) into (6.10), it follows

$$\nabla \vec{a} = \nabla^2 \Phi = 0.$$

Summarized, considering equation (6.9), for (6.8) the reduced problem is given by

$$\begin{aligned} \partial_t u &= \Delta u - \nabla \cdot (u \nabla \Phi) + f, \\ \Delta \Phi &= 0. \end{aligned}$$

Thus, the velocity field is simply given by a calculation of the Laplace equation. When applying these results, the PDEs on  $\Omega_{C_1}$  for  $C_{TV_a}$ ,  $C_{DV_a}$ ,  $C_{TV_r}$  and  $C_{DV_r}$  as well as  $\Phi_a$  and  $\Phi_r$  read

$$\begin{aligned} \partial_t C_{TV_a} &= \nabla \cdot (D_v \nabla C_{TV_a}) - \nabla \cdot (C_{TV_a} \nabla \Phi_a), \\ \partial_t C_{DV_a} &= \nabla \cdot (D_v \nabla C_{DV_a}) - \nabla \cdot (C_{DV_a} \nabla \Phi_a), \\ \partial_t C_{TV_r} &= \nabla \cdot (D_v \nabla C_{TV_r}) - \nabla \cdot (C_{TV_r} \nabla \Phi_r), \\ \partial_t C_{DV_r} &= \nabla \cdot (D_v \nabla C_{DV_r}) - \nabla \cdot (C_{DV_r} \nabla \Phi_r), \\ 0 &= \Delta \Phi_a, \\ 0 &= \Delta \Phi_r, \end{aligned}$$

where  $t \in [0, T]$ . To get a unique solution for the potential flow, appropriate initial and boundary conditions are required. Since the direction of transport towards the plasma membrane depends on actin cables, on  $\Gamma_{C_1}$  we set

$$\nabla \Phi_a \cdot \vec{n} = c_1 \cdot A.$$

We further assume that the inward transport extends in radial direction and define

$$-\nabla \Phi_r \cdot \vec{n} = c_2.$$

On the interior surface  $\Gamma_{C_2}$  we assume homogeneous Dirichlet boundary conditions. Furthermore, we suppose that the rate of exocytosis depends on the amount of vesicles containing Cdc42. This means that on  $\Gamma_{C_1}$  the coupling equations read

$$\begin{aligned} -(D_v \nabla C_{TV_a} - C_{TV_a} \nabla \Phi_a) \cdot \vec{n} &= e_1 \cdot C_{TV_a}, \\ -(D_v \nabla C_{DV_a} - C_{DV_a} \nabla \Phi_a) \cdot \vec{n} &= e_1 \cdot C_{DV_a}, \\ -(D_v \nabla C_{TV_r} - C_{TV_r} \nabla \Phi_r) \cdot \vec{n} &= -e_2 \cdot \left(1 - \frac{A}{A_{max}}\right) \cdot C_T, \end{aligned}$$

$$-(D_v \nabla C_{DV_r} - C_{DV_r} \nabla \Phi_r) \cdot \vec{n} = -e_2 \cdot \left(1 - \frac{A}{A_{max}}\right) \cdot C_D.$$

The surface equations (6.3)-(6.4) change to

$$\begin{aligned} \partial_t C_T &= (k_1^+ + k_1 G_B) C_D - k_1^- C_T + e_1 \cdot C_{TV_a} - e_2 \cdot \left(1 - \frac{A}{A_{max}}\right) \cdot C_T \\ &\quad + \nabla_{\Gamma_{C_1}} \cdot (D_m \nabla_{\Gamma_{C_1}} C_T), \\ \partial_t C_D &= k_1^- C_T - (k_1^+ + k_1 G_B + k_2^-) C_D + (k_2^+ + k_2 C_T) C_I + e_1 \cdot C_{DV_a} \\ &\quad - e_2 \cdot \left(1 - \frac{A}{A_{max}}\right) \cdot C_D + \nabla_{\Gamma_{C_1}} \cdot (D_m \nabla_{\Gamma_{C_1}} C_D). \end{aligned}$$

The parameters  $e_1$  and  $e_2$  describe the rate of exocytosis and endocytosis respectively.  $A_{max}$  is a limiting factor regulating the rate of endocytosis dependent on the total number of actin cables. By this limiting factor we keep rates of endocytosis in regions with a high number of actin cables low. Note that for the case  $A_{max} > A$  we set  $e_2 = 0$ .

On the internal surface  $\Gamma_{C_2}$  the equations are given by

$$\begin{aligned} \partial_t C_{TV_i} &= e_3 \cdot C_{TV_r} - e_4 \cdot C_{TV_i} + \nabla_{\Gamma_{C_2}} \cdot (D_m \nabla_{\Gamma_{C_2}} C_{TV_i}), \\ \partial_t C_{DV_i} &= e_3 \cdot C_{DV_r} - e_4 \cdot C_{DV_i} + \nabla_{\Gamma_{C_2}} \cdot (D_m \nabla_{\Gamma_{C_2}} C_{DV_i}), \end{aligned}$$

where  $e_3$  and  $e_4$  denote the exchange rates between the internal membranes and the transport domain. The equations describing the flux between both domains are represented by

$$\begin{aligned} -(D_v \nabla C_{TV_r} - C_{TV_r} \nabla \Phi_r) \cdot \vec{n} &= e_3 \cdot C_{TV_r}, \\ -(D_v \nabla C_{DV_r} - C_{DV_r} \nabla \Phi_r) \cdot \vec{n} &= e_3 \cdot C_{DV_r}, \\ -(D_v \nabla C_{TV_a} - C_{TV_a} \nabla \Phi_a) \cdot \vec{n} &= -e_4 \cdot C_{TV_i}, \\ -(D_v \nabla C_{DV_a} - C_{DV_a} \nabla \Phi_a) \cdot \vec{n} &= -e_4 \cdot C_{DV_i}. \end{aligned}$$

Summarized, we derive a coupled bulk-surface reaction-diffusion-advection system.

On  $\Gamma_{C_1}$  it holds

$$\partial_t C_T = (k_1^+ + k_1 G_B) C_D - k_1^- C_T + e_1 \cdot C_{TV_a} - e_2 \cdot \left(1 - \frac{A}{A_{max}}\right) \cdot C_T \quad (6.11a)$$

$$+ \nabla_{\Gamma_{C_1}} \cdot (D_m \nabla_{\Gamma_{C_1}} C_T),$$

$$\partial_t C_D = k_1^- C_T - (k_1^+ + k_1 G_B + k_2^-) C_D + (k_2^+ + k_2 C_T) C_I + e_1 \cdot C_{DV_a} \quad (6.11b)$$

$$- e_2 \cdot \left(1 - \frac{A}{A_{max}}\right) \cdot C_D + \nabla_{\Gamma_{C_1}} \cdot (D_m \nabla_{\Gamma_{C_1}} C_D),$$

$$\partial_t G_B = (k_3^+ + k_3 C_T) G_F - (k_3^- + k_4 C_T) G_B + \nabla_{\Gamma_{C_1}} \cdot (D_m \nabla_{\Gamma_{C_1}} G_B), \quad (6.11c)$$

$$\partial_t A = \nabla_{\Gamma_C} \cdot \left( D_A \nabla_{\Gamma_C} \left( \frac{A}{c(C_T)} \right) \right). \quad (6.11d)$$

Whereas the flow of molecules from the cytosol ( $\Omega_C$ ) to the plasma membrane ( $\Gamma_{C_1}$ ) is given by

$$-D_c \nabla C_I \cdot \vec{n} = (k_2^+ + k_2 C_T) C_I - k_2^+ C_D, \quad (6.11e)$$

$$-D_c \nabla G_F \cdot \vec{n} = (k_3^+ + k_3 C_T) G_F - (k_3^- + k_4 C_T) G_B, \quad (6.11f)$$

the flow of molecules from internal compartments ( $\Omega_{C_1}$ ) to the plasma membrane ( $\Gamma_{C_1}$ ) is described by

$$-(D_v \nabla C_{TV_a} - C_{TV_a} \nabla \Phi_a) \cdot \vec{n} = e_1 \cdot C_{TV_a}, \quad (6.11g)$$

$$-(D_v \nabla C_{DV_a} - C_{DV_a} \nabla \Phi_a) \cdot \vec{n} = e_1 \cdot C_{DV_a}, \quad (6.11h)$$

$$-(D_v \nabla C_{TV_r} - C_{TV_r} \nabla \Phi_r) \cdot \vec{n} = -e_2 \cdot \left( 1 - \frac{A}{A_{max}} \right) \cdot C_T, \quad (6.11i)$$

$$-(D_v \nabla C_{DV_r} - C_{DV_r} \nabla \Phi_r) \cdot \vec{n} = -e_2 \cdot \left( 1 - \frac{A}{A_{max}} \right) \cdot C_D. \quad (6.11j)$$

On  $\Omega_{C_1}$  it holds that

$$\partial_t C_{TV_a} = \nabla \cdot (D_v \nabla C_{TV_a}) - \nabla \cdot (C_{TV_a} \nabla \Phi_a), \quad (6.11k)$$

$$\partial_t C_{DV_a} = \nabla \cdot (D_v \nabla C_{DV_a}) - \nabla \cdot (C_{DV_a} \nabla \Phi_a), \quad (6.11l)$$

$$\partial_t C_{TV_r} = \nabla \cdot (D_v \nabla C_{TV_r}) - \nabla \cdot (C_{TV_r} \nabla \Phi_r), \quad (6.11m)$$

$$\partial_t C_{DV_r} = \nabla \cdot (D_v \nabla C_{DV_r}) - \nabla \cdot (C_{DV_r} \nabla \Phi_r), \quad (6.11n)$$

$$0 = \Delta \Phi_a, \quad (6.11o)$$

$$0 = \Delta \Phi_r, \quad (6.11p)$$

and on  $\Omega_{C_2}$  the equations read

$$\partial_t C_I = \nabla \cdot (D_c \nabla C_I), \quad (6.11q)$$

$$\partial_t G_F = \nabla \cdot (D_c \nabla G_F). \quad (6.11r)$$

Finally, on  $\Gamma_{C_2}$  it holds that

$$\partial_t C_{TV_i} = e_3 \cdot C_{TV_r} - e_4 \cdot C_{TV_i} + \nabla_{\Gamma_{C_2}} \cdot (D_m \nabla_{\Gamma_{C_2}} C_{TV_i}),$$

$$\partial_t C_{DV_i} = e_3 \cdot C_{DV_r} - e_4 \cdot C_{DV_i} + \nabla_{\Gamma_{C_2}} \cdot (D_m \nabla_{\Gamma_{C_2}} C_{DV_i}),$$

with the flux conditions

$$-(D_v \nabla C_{TV_r} - C_{TV_r} \nabla \Phi_r) \cdot \vec{n} = e_3 \cdot C_{TV_r}, \quad (6.11s)$$

$$-(D_v \nabla C_{DV_r} - C_{DV_r} \nabla \Phi_r) \cdot \vec{n} = e_3 \cdot C_{DV_r}, \quad (6.11t)$$

$$-(D_v \nabla C_{TV_a} - C_{TV_a} \nabla \Phi_a) \cdot \vec{n} = -e_4 \cdot C_{TV_i}, \quad (6.11u)$$

$$-(D_v \nabla C_{DV_a} - C_{DV_a} \nabla \Phi_a) \cdot \vec{n} = -e_4 \cdot C_{DV_i}. \quad (6.11v)$$

This model is very complex and contains many unknown parameters. As we will see later, the results are very similar to those of a simpler system.

### 6.2.2. Transport through a domain

In this section we present a system which is based on the assumption that vesicles which are exchanged by transport generally move through a defined domain. Although these molecules attach and detach to and from internal membranes as well as cross internal compartments, they finally move from one side to another. From this point of view, it is sufficient to consider only one gradient driving vesicles through the domain. Let  $C_{TV}$  and  $C_{DV}$  denote vesicles containing Cdc42-GTP and Cdc42-GDP respectively. Let  $\Phi$  be a continuous function for a velocity field that simulates the movement along cables. Then, we can reduce (6.11a)-(6.11v) by simulating only the concentrations  $C_{TV}$  and  $C_{DV}$  in the transport domain. In  $\Gamma_{C_1}$  it holds that

$$\partial_t C_T = (k_1^+ + k_1 G_B) C_D - k_1^- C_T + e_1 \cdot C_{TV} - e_2 \cdot \left(1 - \frac{A}{A_{max}}\right) \cdot C_T \quad (6.12a)$$

$$+ \nabla_{\Gamma_{C_1}} \cdot (D_m \nabla_{\Gamma_{C_1}} C_T),$$

$$\partial_t C_D = k_1^- C_T - (k_1^+ + k_1 G_B + k_2^-) C_D + (k_2^+ + k_2 C_T) C_I + e_1 \cdot C_{DV} \quad (6.12b)$$

$$- e_2 \cdot \left(1 - \frac{A}{A_{max}}\right) \cdot C_D + \nabla_{\Gamma_{C_1}} \cdot (D_m \nabla_{\Gamma_{C_1}} C_D),$$

$$\partial_t G_B = (k_3^+ + k_3 C_T) G_F - (k_3^- + k_4 C_T) G_B + \nabla_{\Gamma_{C_1}} \cdot (D_m \nabla_{\Gamma_{C_1}} G_B), \quad (6.12c)$$

$$\partial_t A = \nabla_{\Gamma_C} \cdot \left( D_A \nabla_{\Gamma_C} \left( \frac{A}{c(C_T)} \right) \right). \quad (6.12d)$$

Whereas the flow of molecules from the cytosol ( $\Omega_C$ ) to the plasma membrane ( $\Gamma_{C_1}$ ) is given by

$$-D_c \nabla C_I \cdot \vec{n} = (k_2^+ + k_2 C_T) C_I - k_2^+ C_D, \quad (6.12e)$$

$$-D_c \nabla G_F \cdot \vec{n} = (k_3^+ + k_3 C_T) G_F - (k_3^- + k_4 C_T) G_B, \quad (6.12f)$$

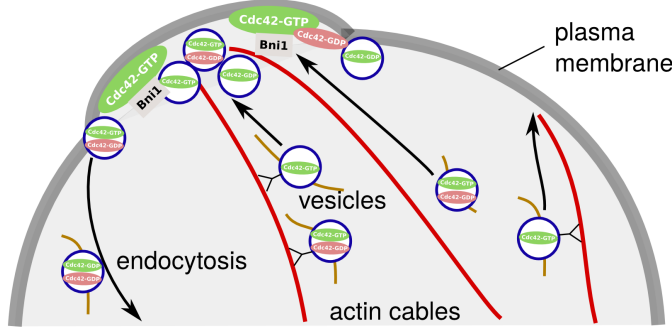


**Figure 6.4.: Transport scheme of the vesicle trafficking machinery.** Schematic representation of vesicle trafficking in budding yeast. Actin cables deliver vesicles containing Cdc42-GTP and Cdc42-GDP from internal membranes via actin cables towards the polar cap. In turn, endocytosis recycles plasma membrane-bound Cdc42.

the flow of molecules from internal compartments ( $\Omega_{C_1}$ ) to the plasma membrane ( $\Gamma_{C_1}$ ) is described by

$$-(D_v \nabla C_{TV} - C_{TV} \nabla \Phi) \cdot \vec{n} = e_1 \cdot C_{TV} - e_2 \cdot \left(1 - \frac{A}{A_{max}}\right) \cdot C_T, \quad (6.12g)$$

$$-(D_v \nabla C_{DV} - C_{DV} \nabla \Phi) \cdot \vec{n} = e_1 \cdot C_{DV} - e_2 \cdot \left(1 - \frac{A}{A_{max}}\right) \cdot C_D. \quad (6.12h)$$

On  $\Omega_{C_1}$  it holds that

$$\partial_t C_{TV} = \nabla \cdot (D_v \nabla C_{TV}) - \nabla \cdot (C_{TV} \nabla \Phi), \quad (6.12i)$$

$$\partial_t C_{DV} = \nabla \cdot (D_v \nabla C_{DV}) - \nabla \cdot (C_{DV} \nabla \Phi), \quad (6.12j)$$

$$0 = \Delta \Phi - \alpha \Phi, \quad (6.12k)$$

and on  $\Omega_C$  we set

$$\partial_t C_I = \nabla \cdot (D_c \nabla C_I), \quad (6.12l)$$

$$\partial_t G_F = \nabla \cdot (D_c \nabla G_F). \quad (6.12m)$$

The boundary condition for the potential function  $\Phi$  on  $\Omega_{C_1}$  reads

$$\nabla \Phi \cdot \vec{n} = c_0 \cdot A. \quad (6.12n)$$

Note that (6.12k) now includes the linear term  $\alpha \Phi$  to ensure uniqueness and existence of a solution. This is in contrast to the equations (6.11o) and (6.11p) and is a result of not posing homogeneous boundary conditions on the interior surface.

Figure 6.4 schematically shows the actin-mediated transport of active Cdc42 and inactive Cdc42 that is bound to vesicles.

The equations for the transport mechanism in the latter system are very similar to a coupled bulk-surface reaction-diffusion-advection model proposed in [2]. This study investigates a system of two interacting molecules, an internal component  $V$  and a membrane-bound component  $u$ . It is given by equations

$$\begin{aligned}\partial_t V &= D\Delta V - \nabla \cdot (V\nabla c), \\ 0 &= \Delta c - \alpha c\end{aligned}$$

in  $\Omega \times (0, T)$  and

$$\partial_t u = d\Delta_\Gamma u + q(V, u)$$

on  $\Gamma \times (0, T)$ . With the flux conditions

$$\begin{aligned}-(D\nabla V - V\nabla c) \cdot \vec{n} &= q(V, u), \\ \nabla c \cdot \vec{n} &= \beta u\end{aligned}$$

on  $\Gamma \times (0, T)$  it simulates actin-mediated spontaneous cell polarization. The model resembles the Patlak-Keller-Segel (PKS) chemotaxis system. It is shown that for a certain smallness condition on the initial data the system is well-posed and features a classical solution [2]. However, this system does not include the reaction machinery and hence does not account for the whole process of cell polarization.

### 6.3. Numerical simulations

Let us now investigate the models presented using numerical simulations. In order to apply finite element methods for discretization in space, we derive a weak formulation of model equations (6.12a)-(6.12n). Therefore, we define the Sobolev spaces  $\mathcal{V}^{sur} := H^1(\Gamma_{C_1})$ ,  $\mathcal{V}^{bulk} := H^1(\Omega_{C_1} \cup \Omega_{C_2}) = H^1(\Omega_C)$ , and  $\mathcal{V}^{ring} := H^1(\Omega_{C_2})$  containing weak solutions of equations.

#### Weak formulation

$$\begin{aligned}\frac{d}{dt} \int_{\Gamma_{C_1}} C_T \varphi_1 \, dS &= \int_{\Gamma_{C_1}} \left[ (k_1^+ + k_1 G_B|_{\Gamma_{C_1}}) C_D - k_1^- C_T + e_1 \cdot C_{TV}|_{\Gamma_{C_1}} \right] \varphi_1 \, dS \\ &\quad + \int_{\Gamma_{C_1}} \left[ -e_2 \cdot \left( 1 - \frac{A}{A_{max}} \right) \cdot C_T \right] \varphi_1 \, dS\end{aligned}$$

$$\begin{aligned}
& + \int_{\Gamma_{C_1}} \nabla_{\Gamma_{C_1}} \cdot (D_m \nabla_{\Gamma_{C_1}} C_T) \varphi_1 \, dS, \\
\frac{d}{dt} \int_{\Gamma_{C_1}} C_D \varphi_2 \, dS &= \int_{\Gamma_{C_1}} \left[ k_1^- C_T - (k_1^+ + k_1 G_B|_{\Gamma_{C_1}} + k_2^+) C_D \right] \varphi_2 \, dS \\
& + \int_{\Gamma_{C_1}} \left[ (k_2^- + k_2 C_T) C_I|_{\Gamma_{C_1}} \right] \varphi_2 \, dS \\
& + \int_{\Gamma_{C_1}} \left[ e_1 \cdot C_{DV}|_{\Gamma_{C_1}} - e_2 \cdot \left( 1 - \frac{A}{A_{max}} \right) \cdot C_D \right] \varphi_2 \, dS \\
& + \int_{\Gamma_{C_1}} \nabla_{\Gamma_{C_1}} \cdot (D_m \nabla_{\Gamma_{C_1}} C_D) \varphi_2 \, dS, \\
\frac{d}{dt} \int_{\Gamma_{C_1}} G_B \varphi_3 \, dS &= \int_{\Gamma_{C_1}} \left[ (k_3^+ + k_3 C_T) G_F|_{\Gamma_{C_1}} - (k_3^- + k_4 C_T) G_B|_{\Gamma_{C_1}} \right] \varphi_3 \, dS \\
& + \int_{\Gamma_{C_1}} \nabla_{\Gamma_{C_1}} \cdot (D_m \nabla_{\Gamma_{C_1}} G_B) \varphi_3 \, dS, \\
\frac{d}{dt} \int_{\Gamma_{C_1}} A \varphi_4 \, dS &= \int_{\Gamma_{C_1}} \nabla_{\Gamma_{C_1}} \cdot \left[ D_A \nabla_{\Gamma_{C_1}} \left( \frac{A}{v \cdot C_T} \right) \right] \varphi_4 \, dS, \\
\frac{d}{dt} \int_{\Omega_C} C_I \varphi_5 \, dB &= \int_{\Omega_C} \nabla \cdot (D_c \nabla C_I) \varphi_5 \, dB, \\
\frac{d}{dt} \int_{\Omega_C} G_F \varphi_6 \, dB &= \int_{\Omega_C} \nabla \cdot (D_c \nabla G_F) \varphi_6 \, dB, \\
\frac{d}{dt} \int_{\Omega_{C_1}} C_{TV} \varphi_7 \, dR &= \int_{\Omega_{C_1}} [\nabla \cdot (D_v \nabla C_{TV}) - \nabla(C_{TV} \cdot \nabla \Phi)] \varphi_7 \, dR, \\
\frac{d}{dt} \int_{\Omega_{C_1}} C_{DV} \varphi_8 \, dR &= \int_{\Omega_{C_1}} [\nabla \cdot (D_v \nabla C_{DV}) - \nabla(C_{DV} \cdot \nabla \Phi)] \varphi_8 \, dR, \\
0 &= \int_{\Omega_{C_1}} [\nabla \cdot (\nabla \Phi) - \alpha \Phi] \varphi_9 \, dR.
\end{aligned}$$

Using the integration by parts formula for Sobolev spaces and the respective boundary conditions, we have

$$\begin{aligned}
\frac{d}{dt} \int_{\Gamma_{C_1}} C_T \varphi_1 \, dS &= \int_{\Gamma_{C_1}} \left[ (k_1^+ + k_1 G_B) C_D - k_1^- C_T + e_1 \cdot C_{TV}|_{\Gamma_{C_1}} \right] \varphi_1 \, dS \\
& + \int_{\Gamma_{C_1}} \left[ -e_2 \cdot \left( 1 - \frac{A}{A_{max}} \right) \cdot C_T \right] \varphi_1 \, dS \\
& - \int_{\Gamma_{C_1}} D_m \nabla_{\Gamma_{C_1}} C_T \cdot \nabla_{\Gamma_{C_1}} \varphi_1 \, dS, \\
\frac{d}{dt} \int_{\Gamma_{C_1}} C_D \varphi_2 \, dS &= \int_{\Gamma_{C_1}} \left[ k_1^- C_T - (k_1^+ + k_1 G_B + k_2^+) C_D \right] \varphi_2 \, dS \\
& + \int_{\Gamma_{C_1}} \left[ (k_2^- + k_2 C_T) C_I|_{\Gamma_{C_1}} \right] \varphi_2 \, dS \\
& + \int_{\Gamma_{C_1}} \left[ e_1 \cdot C_{DV}|_{\Gamma_{C_1}} - e_2 \cdot \left( 1 - \frac{A}{A_{max}} \right) \cdot C_D \right] \varphi_2 \, dS
\end{aligned}$$



$$\begin{aligned}
& - \int_{\Gamma_{C_1}} D_m \nabla_{\Gamma_{C_1}} C_D \cdot \nabla_{\Gamma_{C_1}} \varphi_2 \, dS, \\
\frac{d}{dt} \int_{\Gamma_{C_1}} G_B \varphi_3 \, dS &= \int_{\Gamma_{C_1}} \left[ (k_3^+ + k_3 C_T) G_F \Big|_{\Gamma_{C_1}} - (k_3^- + k_4 C_T) G_B \right] \varphi_3 \, dS \\
& - \int_{\Gamma_{C_1}} D_m \nabla_{\Gamma_{C_1}} G_B \cdot \nabla_{\Gamma_{C_1}} \varphi_3 \, dS, \\
\frac{d}{dt} \int_{\Gamma_{C_1}} A \varphi_4 \, dS &= - \int_{\Gamma_{C_1}} D_A \nabla_{\Gamma_{C_1}} \left( \frac{A}{v \cdot C_T} \right) \cdot \nabla_{\Gamma_{C_1}} \varphi_4 \, dS, \\
\frac{d}{dt} \int_{\Omega_C} C_I \varphi_5 \, dB &= - \int_{\Omega_C} D_c \nabla C_I \cdot \nabla \varphi_5 \, dB - \int_{\Gamma_{C_1}} \left[ (k_2^- + k_2 C_T) C_I \Big|_{\Gamma_{C_1}} \right] \varphi_5 \Big|_{\Gamma_{C_1}} \, dS, \\
\frac{d}{dt} \int_{\Omega_C} G_F \varphi_6 \, dB &= - \int_{\Omega_C} D_c \nabla G_F \cdot \nabla \varphi_6 \, dB - \int_{\Gamma_{C_1}} \left[ (k_3^+ + k_3 C_T) G_F \Big|_{\Gamma_{C_1}} \right] \varphi_6 \Big|_{\Gamma_{C_1}} \, dS \\
\frac{d}{dt} \int_{\Omega_{C_1}} C_{TV} \varphi_7 \, dR &= - \int_{\Omega_{C_1}} [D_v \nabla C_{TV} - C_{TV} \cdot \nabla \Phi] \cdot \nabla \varphi_7 \, dR \\
& - \int_{\Gamma_{C_1}} \left[ e_1 \cdot C_{TV} \Big|_{\Gamma_{C_1}} - e_2 \cdot \left( 1 - \frac{A}{A_{max}} \right) \cdot C_T \right] \varphi_7 \Big|_{\Gamma_{C_1}} \, dS, \\
\frac{d}{dt} \int_{\Omega_{C_1}} C_{DV} \varphi_8 \, dR &= - \int_{\Omega_{C_1}} [D_v \nabla C_{DV} - C_{DV} \cdot \nabla \Phi] \cdot \nabla \varphi_8 \, dR \\
& - \int_{\Gamma_{C_1}} \left[ e_1 \cdot C_{DV} \Big|_{\Gamma_{C_1}} - e_2 \cdot \left( 1 - \frac{A}{A_{max}} \right) \cdot C_D \right] \varphi_9 \Big|_{\Gamma_{C_1}} \, dS, \\
0 &= - \int_{\Omega_{C_1}} \nabla \Phi \cdot \nabla \varphi_9 \, dR - \int_{\Omega_{C_1}} \alpha \Phi \varphi_9 \, dR + \int_{\Gamma_{C_1}} c_0 \cdot A \varphi_9 \Big|_{\Gamma_{C_1}} \, dS.
\end{aligned}$$

To find a weak solution of the model equations derived above, we now have to look for a solution  $(C_T, C_D, G_B, A, C_I, G_F, C_{TV}, C_{DV}, \Phi) \in L^2([0, T], \mathcal{V}^{sur}) \times L^2([0, T], \mathcal{V}^{bulk}) \times L^2([0, T], \mathcal{V}^{ring})$ , so that

$$\begin{aligned}
\frac{d}{dt} \int_{\Gamma_{C_1}} C_T \varphi_1 \, dS &= \int_{\Gamma_{C_1}} \left[ (k_1^+ + k_1 G_B) C_D - k_1^- C_T + e_1 \cdot C_{TV} \Big|_{\Gamma_{C_1}} \right] \varphi_1 \, dS \\
& + \int_{\Gamma_{C_1}} \left[ -e_2 \cdot \left( 1 - \frac{A}{A_{max}} \right) \cdot C_T \right] \varphi_1 \, dS \\
& - \int_{\Gamma_{C_1}} D_m \nabla_{\Gamma_{C_1}} C_T \cdot \nabla_{\Gamma_{C_1}} \varphi_1 \, dS, \\
\frac{d}{dt} \int_{\Gamma_{C_1}} C_D \varphi_2 \, dS &= \int_{\Gamma_{C_1}} \left[ k_1^- C_T - (k_1^+ + k_1 G_B + k_2^+) C_D \right] \varphi_2 \, dS \\
& + \int_{\Gamma_{C_1}} \left[ (k_2^- + k_2 C_T) C_I \Big|_{\Gamma_{C_1}} \right] \varphi_2 \, dS \\
& + \int_{\Gamma_{C_1}} \left[ e_1 \cdot C_{DV} \Big|_{\Gamma_{C_1}} - e_2 \cdot \left( 1 - \frac{A}{A_{max}} \right) \cdot C_D \right] \varphi_2 \, dS \\
& - \int_{\Gamma_{C_1}} D_m \nabla_{\Gamma_{C_1}} C_D \cdot \nabla_{\Gamma_{C_1}} \varphi_2 \, dS,
\end{aligned}$$

$$\begin{aligned}
\frac{d}{dt} \int_{\Gamma_{C_1}} G_B \varphi_3 \, dS &= \int_{\Gamma_{C_1}} \left[ (k_3^+ + k_3 C_T) G_F \Big|_{\Gamma_{C_1}} - (k_3^- + k_4 C_T) G_B \right] \varphi_3 \, dS \\
&\quad - \int_{\Gamma_{C_1}} D_m \nabla_{\Gamma_{C_1}} G_B \cdot \nabla_{\Gamma_{C_1}} \varphi_3 \, dS, \\
\frac{d}{dt} \int_{\Gamma_{C_1}} A \varphi_4 \, dS &= - \int_{\Gamma_{C_1}} D_A \nabla_{\Gamma_C} \left( \frac{A}{v \cdot C_T} \right) \cdot \nabla_{\Gamma_{C_1}} \varphi_4 \, dS \\
&= \frac{D_A}{(v \cdot C_T^2)} \int_{\Gamma_{C_1}} \left[ A \cdot \nabla_{\Gamma_{C_1}} C_T - C_T \cdot \nabla_{\Gamma_{C_1}} A \right] \nabla_{\Gamma_{C_1}} \varphi_4 \, dS, \\
\frac{d}{dt} \int_{\Omega_C} C_I \varphi_5 \, dB &= - \int_{\Omega_C} D_c \nabla C_I \cdot \nabla \varphi_5 \, dB - \int_{\Gamma_{C_1}} \left[ (k_2^- + k_2 C_T) C_I \Big|_{\Gamma_{C_1}} \right] \varphi_5 \, dS, \\
\frac{d}{dt} \int_{\Omega_C} G_F \varphi_6 \, dB &= - \int_{\Omega_C} D_c \nabla G_F \cdot \nabla \varphi_6 \, dB - \int_{\Gamma_{C_1}} \left[ (k_3^+ + k_3 C_T) G_F \Big|_{\Gamma_{C_1}} \right] \varphi_6 \, dS, \\
\frac{d}{dt} \int_{\Omega_{C_1}} C_{TV} \varphi_7 \, dR &= - \int_{\Omega_{C_1}} [D_v \nabla C_{TV} - C_{TV} \cdot \nabla \Phi] \cdot \nabla \varphi_7 \, dR \\
&\quad - \int_{\Gamma_{C_1}} \left[ e_1 \cdot C_{TV} \Big|_{\Gamma_{C_1}} - e_2 \cdot \left( 1 - \frac{A}{A_{max}} \right) \cdot C_T \right] \varphi_7 \, dS, \\
\frac{d}{dt} \int_{\Omega_{C_1}} C_{DV} \varphi_8 \, dR &= - \int_{\Omega_{C_1}} [D_v \nabla C_{DV} - C_{DV} \cdot \nabla \Phi] \cdot \nabla \varphi_8 \, dR \\
&\quad - \int_{\Gamma_{C_1}} \left[ e_1 \cdot C_{DV} \Big|_{\Gamma_{C_1}} - e_2 \cdot \left( 1 - \frac{A}{A_{max}} \right) \cdot C_D \right] \varphi_8 \, dS, \\
0 &= - \int_{\Omega_{C_1}} \nabla \Phi \cdot \nabla \varphi_9 \, dR - \int_{\Omega_{C_1}} \alpha \Phi \varphi_9 \, dR + \int_{\Gamma_{C_1}} c_0 \cdot A \varphi_9 \, dS.
\end{aligned}$$

for all  $\varphi_1, \varphi_2, \varphi_3, \varphi_4 \in \mathcal{V}^{sur}$ ,  $\varphi_5, \varphi_6 \in \mathcal{V}^{bulk}$ ,  $\varphi_7, \varphi_8, \varphi_9 \in \mathcal{V}^{ring}$  and each  $t \in [0, T]$ .

To compare the impact of distinct spatial effects, the models are excited and probed with different kinds of signals. To generate random initial perturbations we take random numbers  $\theta$  from the interval  $[0, 1]$  and use these numbers to generate a noise function with amplitude  $a$ . We only disturb the initial concentration of active Cdc42. Specifically, for each simulation with initial concentration  $C_{T_0}$ , we assign each node of the subgrid for the surface domain with the value  $C_{T_0} + \theta \cdot a$ .

To simulate one or two local stimuli on a surface area with width  $w$ , we use functions

$$s_1(\vec{x}, t) = \begin{cases} S_0, & \text{if } t < t_1 \text{ and } \text{dist}(\vec{x}_{S_1}, \vec{x}) < w, \\ 0, & \text{otherwise} \end{cases} \quad (6.16)$$

and

$$s_2(\vec{x}, t) = \begin{cases} S_1, & \text{if } t < t_1 \text{ and } \text{dist}(\vec{x}_{S_1}, \vec{x}) < w, \\ S_2, & \text{if } t < t_2 \text{ and } \text{dist}(\vec{x}_{S_2}, \vec{x}) < w, \\ 0, & \text{otherwise.} \end{cases} \quad (6.17)$$

and calculate

$$F^{ST}(C_T, C_I, C_{TV}, G_B, A) = F(C_T, C_I, C_{TV}, G_B, A) + s_i(\vec{x}, t)C_I, \quad i = 1, 2,$$

where  $F$  represents the reaction kinetics in (6.12a).

Here,  $\text{dist}(\vec{x}_1, \vec{x}_2)$  denotes the Euclidean distance between two points  $\vec{x}_1$  and  $\vec{x}_2$ . The stimuli are applied for a time period of  $\Delta t = 5$  minutes.

We are aiming to base all the used model variables on experimental evidence and take parameter values and data concerning the amount and the distribution of Cdc42 and Cdc24 from the literature. Some reaction rates and diffusion constants have already been measured and used for prior simulations (see Table 6.1). The remaining rates are chosen to quantitatively display characteristics of control cells as well as to reflect LatA-treated or  $\Delta bem1$  and  $\Delta rdi1$  cells.

Description	Rate	Units	Value
basal activation of Cdc42	$k_1^+$	$s^{-1}$	0.002
basal inactivation of Cdc42	$k_1^-$	$s^{-1}$	1
activation via Cdc24	$k_1$	$\mu m^2 s^{-1}$	0.2
GDI binding rate	$k_2^+$	$\mu m s^{-1}$	0.5
GDI unbinding rate	$k_2^-$	$s^{-1}$	0.0035
GDI unbinding rate via Cla4	$k_2$	$\mu m^3 s^{-1}$	0.1
Cdc24 membrane attachment	$k_3^+$	$\mu m s^{-1}$	1
Cdc24 membrane detachment	$k_3^-$	$s^{-1}$	0.35
Bem1-mediated recruitment	$k_3$	$\mu m^3 s^{-1}$	0.085
Cla4-mediated phosphorylation	$k_4$	$\mu m^2 s^{-1}$	0.015
diffusion on the membrane	$D_m$	$\mu m^2 s^{-1}$	0.036
diffusion in the cytosol	$D_c$	$\mu m^2 s^{-1}$	11
cell radius	$R$	$\mu m$	3.95
total Cdc42			$\approx 3000$
total Cdc24			$\approx 1000$

**Table 6.1.: Reaction rate constants and parameter estimates used to solve the reaction-diffusion system.** The rates used to solve system (6.1)-(6.7) are shown. To simulate a cell lacking Rdi1 we set  $k_2^+ = 0$ . In order to investigate the  $\Delta bem1$  case, we use strongly reduced rates  $k_3 = 0.035$  and  $k_4 = 0.0055$ .

### 6.3.1. Polarization in the absence of actin-mediated transport

We firstly consider the reaction-diffusion system (6.1)-(6.7). Since this system neglects transport mechanisms, it simulates a cell treated with LatA. It has been shown

that such cells are able to polarize as long as the GDI pathway as well as the local Cdc42 activating pathway are intact. Whereas in  $\Delta rsr1$  cells symmetry breaking occurs due to stochastic fluctuations, polarization in control cells is regulated by local activation. We start with numerical experiments in 3D. For the simulations we use the parameters summarized in Table 6.1.

Figure 6.11 (a) demonstrates actin-independent polarization. Due to random noise or an initial stimulus of the activating factor Cdc24, the system tends to form a polar cluster of Cdc42-GTP. The results are very similar to those achieved using previous models for cell polarity. Starting from a small perturbation of the initial homogeneous distribution of molecules, the system generates a spatial inhomogeneous pattern at the surface. On the other hand, due to fast diffusion in the cytosol, the concentrations in the bulk domain are nearly homogeneously distributed. In this case, the fast diffusion of cytosolic molecules close to the cluster balances the flux resulting from the continuous exchange between the cytosol and the plasma membrane.

As in [32, 48], the inhomogeneous state of approach (6.1)-(6.7) is the result of a mass-conserved Turing-type pattern formation process which is based on distinct diffusion velocities and an autocatalytic activation of Cdc42-GTP. Thus, the system features can be studied in terms of a linear stability analysis.

In order to investigate the model in more detail, we further consider the two-dimensional reduction. In this case, we have to scale the system. Therefore, we multiply the respective parameters and state variables with a scalar given by the ratio between the surface and the bulk volume. As we will see, this approach does not significantly change the qualitative behavior of solutions.

At first, we test the influence of different perturbations on the initial state. Figure 6.5 illustrates how a localized stimulus determines the site and the temporal course of cap formation. For random noise we observe that the cluster slowly forms at a random position of the surface. Contrarily, a single local stimulus leads to the local amplification of Cdc42-GTP at this site. This also implies an acceleration of the polarization process such that the system quickly reaches the maximum value of Cdc42-GTP. For two equal stimuli located at opposite sides we observe two transient clusters that immediately merge together after the fall of excitation. Interestingly, in all cases the initial perturbation only influences the time course of polarization but not the Cdc42-GTP cluster height.

Figure 6.6 shows how parameter changes affect the polar cap of Cdc42-GTP as well as the ratio between cytosolic and membrane-bound Cdc42. For instance, a small hydrolysis rate  $k_1^-$  leads to a high amount of Cdc42 at the plasma membrane and hence to an increased Cdc42-GTP concentration. In contrast to this, a hydrolysis

rate  $k_1^- > 1.5$  impedes the establishment of polarity. In this case, the local amount of Cdc42-GTP at the plasma membrane falls short of a certain threshold which is needed to amplify symmetry breaking by a positive feedback activation and cytosolic recruitment.

Figure 6.6 (c)-(f) illustrate the necessity of a GDI-mediated exchange and a local GEF activation in LatA-treated cells. We see that an increased rate of  $k_2^-$  leads to a high cytosolic pool of Cdc42, preventing the cell from polarizing. A decrease of  $k_2^-$  close to zero also impedes polarization. Similarly, we see that the GEF membrane recruitment rate must exceed a certain threshold to ensure that the system generates an inhomogeneous pattern.

Figure 6.6 (g) demonstrates how the phosphorylation rate influences the maximum value of Cdc42-GTP within the polar cluster. It becomes clear that whereas an increased rate destabilizes the system, a reduced rate facilitates the auto-amplification leading to very high rates of Cdc42-GTP. For instance, for  $k_4 = 0.0$  the maximal amount of the GTPase is nearly three times higher than for the parameter used to simulate control cells. However, it can be shown that the rates  $k_3$  and  $k_4$  are closely related. This means that high amounts of membrane-bound Cdc42-GTP can be buffered by a lower rate of GEF recruitment.

### 6.3.2. Enhanced polarization by actin-mediated transport

Next, we ask whether actin-mediated transport can enhance the polar cluster during cap formation or rather disturb the pattern formation process. Due to computation time and a lot of unknown parameters in (6.11a)-(6.11v), we initially focus on results of (6.12a)-(6.12n).

The simulation illustrated in Figure 6.11 (b) shows how vesicle trafficking can reinforce polarity. It demonstrates that a small perturbation of the initial uniform distribution again generates a polar cluster of active Cdc42. As a consequence thereof, the actin cable density also polarizes. This density in turn controls the gradient driving further molecules from internal compartments to the polarized site. We obtain about 35% of all Cdc42 on the plasma membrane, 42% in the cytosol and 13% on internal membranes. Figure 6.7 shows the final polar cluster of Cdc42-GTP for a two-dimensional disc and the corresponding velocity field.

Concerning the time course of polarity establishment our results nicely fit to biological experiments. A treatment of cells with LatA has demonstrated the effect of actin-mediated transport. Whereas cells with intact actin structures had formed a polar cap of Cdc42 within 30-40 minutes, LatA treated cells polarized within around 70 minutes with significant reduced rate [98]. From Figure 6.11 (b) we observe that

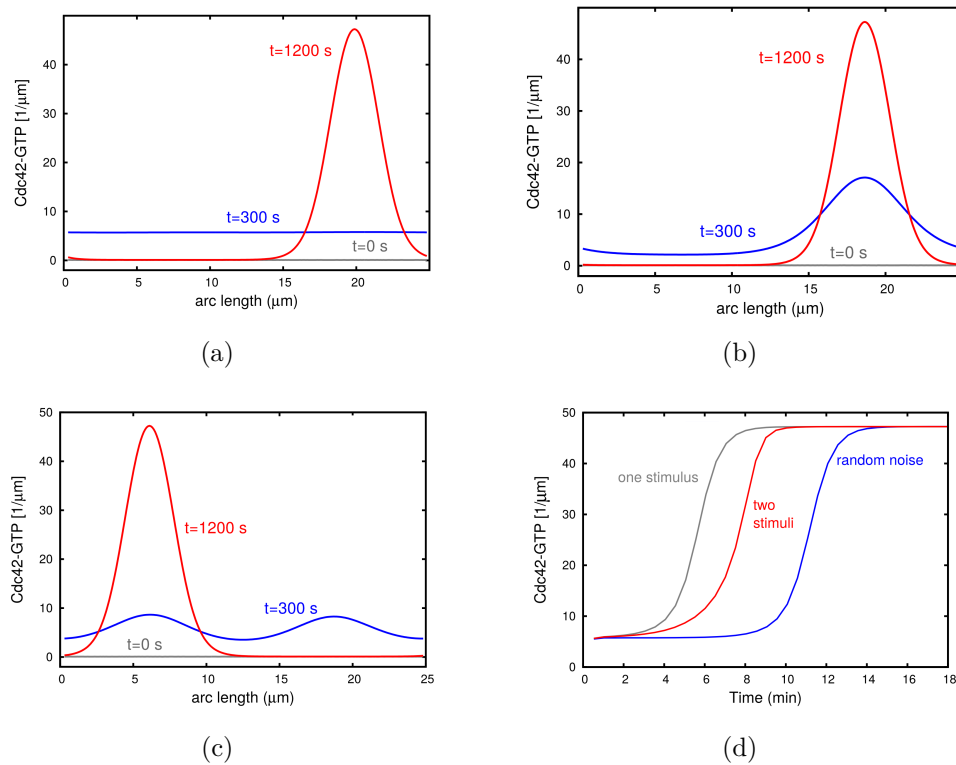


**Figure 6.5.: Comparison of stimuli induced polarity for cells treated with latrunculin A.** (a) A random perturbation on the initial state is sufficient to induce cell polarization. (b) A located transient stimulus induces cell polarity with the same intensity. (c) Two equally strong transient stimuli lead to one single polar cluster. (d) Whereas a single transient stimulus reduces the term of polarization, two transient stimuli increase the duration of the polarization process.

the cluster forms within 25-30 minutes. Compared to Figure 6.11 (a), where cell polarization occurs within 40-45 minutes, we see that transport can accelerate the polarization process. Furthermore, the incorporated advection process leads to an increased amount of polar Cdc42-GTP. These results correspond to those previously reported [28]. It is also important to note that our simulations show an inherent mechanism leading to symmetry breaking. The cell is able to polarize even without any initial spatial perturbation. Thus, the formation of actin leading to the process of exocytosis and endocytosis could be very important not only to maintain polarization but also to initiate it. This confirms the results of studies using an artificial system to investigate polarity that occurs through purely intrinsic mechanisms. In cells expressing a constitutively active form of Cdc42 it has been shown that symmetry breaking completely depends on actin polymerization and actin-based transport [96]. These findings together with our numerical results suggest that polarization does not require any pre-existing asymmetry.

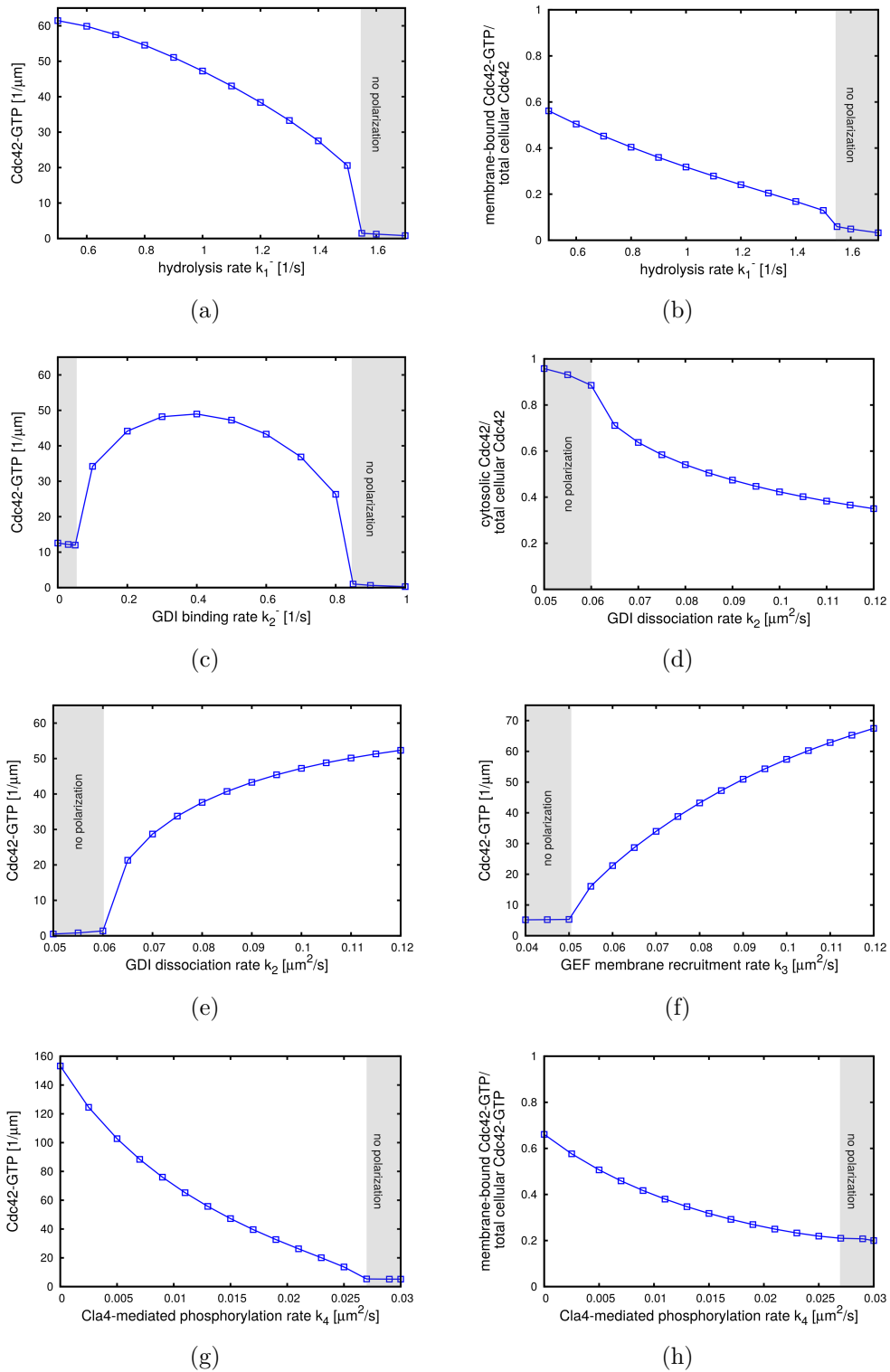


**Figure 6.6.: Effect of parameter changes on polarization.** (a) Maximal Cdc42-GTP concentration and (b) percentage amount of membrane-bound Cdc42 for different hydrolysis rates. (c) Change of the maximum of membrane-bound Cdc42-GTP with respect to changes in the GDI binding rate. (d) Varying values of cytosolic Cdc42 and (e) of active membrane-bound Cdc42 dependent on the GDI dissociation rate. (f) Effect of changes in the GEF membrane recruitment rate on Cdc42-GTP intensity. (g) Maximum of membrane-bound Cdc42 and (h) the percentage of membrane-bound Cdc42 with respect to changes in the phosphorylation rate.

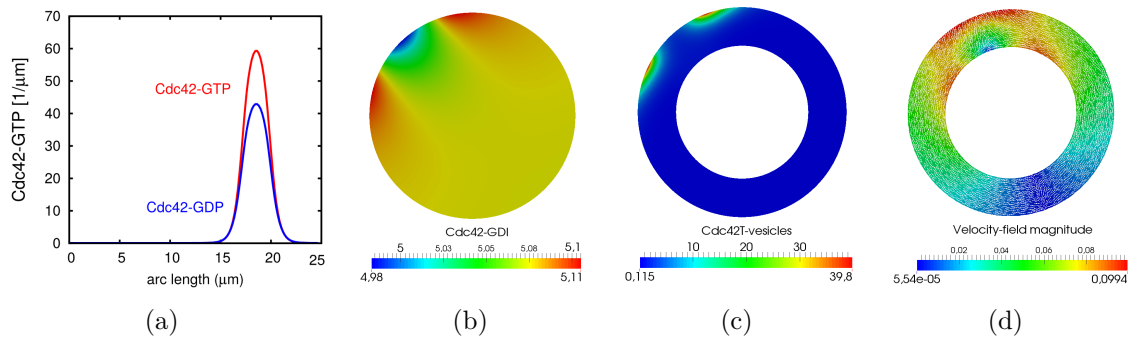


**Figure 6.7.: Computational results of the model considering transport through a defined domain.** Cdc42-GTP cluster formation in the two-dimensional case is shown. (a) Cdc42-GTP and Cdc42-GDP concentration at the plasma membrane after  $t = 1200s$ . (b) The distribution of cytosolic Cdc42 is shown. (c) Visualization of the distribution of internal vesicles containing Cdc42-GTP. (d) Illustration of the velocity field determined by the potential function  $\Phi(x, t)$ .

Another particular feature of our three-dimensional reaction-diffusion-advection system is that it simulates a wandering pole. This wandering polarization site has been reported in  $\Delta rsr1$  cells. It has been supposed that it may be influenced by the balance between endocytosis and cable-directed delivery [53]. Indeed, our findings demonstrate that this movement is controlled by the interplay of exocytosis and endocytosis.

In order to analyze the enhanced model in more detail, we now consider two-dimensional numerical simulations based on different parameter values. From Table 6.2 we obtain how vesicle transport stabilizes the system. Whereas an increase of parameters  $k_3^+$  and  $k_4$  by the factor 2 impedes polarity in approach (6.1)-(6.7), model (6.12a)-(6.12n) is still able to form an inhomogeneous pattern, albeit with less intensity. With the factor 2 reduced values of  $k_3^-$  and  $k_3$  we observe similar results. As we will see later, this stabilizing effect is important for cells lacking Bem1 or Rdi1.

As demonstrated above,  $k_4$ , which simulates phosphorylation via Cla4, buffers the absolute value of Cdc42-GTP within the polar cap. In simulations reflecting control cells we obtain similar results. For  $k_4 = 0.0$  the maximal amount of the GTPase is nearly three times higher. This three fold increase is accompanied by a high amount of Cdc42-GTP at the surface.

The combination of biological experiments with mathematical modeling previously revealed that a balance of exocytosis and endocytosis is important to efficiently maintain polarity. Moreover, it has been shown that polarity depends on the localization of endocytosis relative to the exocytic pole where early endocytic proteins are delivered. Co-localization of endocytosis and exocytosis within the Cdc42 cluster



resulted in severe polarity defects [47].

Figure 6.8 illustrates how changes of parameters that control the transport mechanism affect polarization. We see how values of Cdc42-GTP vary depending on choices of rates for exocytosis and endocytosis. To obtain optimal polarity, both rates have to balance out. Our results also suggest that the spatial organization of exocytosis indeed influences the cluster formation at the bud-site. Interestingly, we see that a change of  $A_{max}$ , the factor controlling local endocytosis, mainly affects the cluster shape. Although a reduced rate leads to a decreased maximum value of Cdc42-GTP within the cap, the total amount of Cdc42-GTP on the plasma membrane increases for reduced values of  $A_{max}$ . This can be explained by the fact that the cap width becomes broader as  $A_{max}$  decreases (see Figure 6.9 (a) and (b)).

We next investigate our model for the possibility to polarize in the presence of endocytosis but in the absence of exocytosis. It is still unknown, whether the actin cytoskeleton and the endocytic machinery operate independently. Experiments, using drugs that disrupt or inhibit the actin cytoskeleton, as well as genetic studies suggest a functional connection between actin and endocytosis [6]. The identification of several proteins that may function between the endocytic machinery and actin supports this assumption [86]. From Figure 6.8 we obtain that our system is not able to achieve robust polarity in the absence of exocytosis when endocytosis occurs. These findings indicate that exocytic secretion is important to balance vesicle internalization. Thus, LatA could negatively influence not only the exocytic but also the endocytic machinery, meaning that actin polymerization could indeed be fundamental for endocytosis.

Conversely, Figure 6.8 (c) and (d) make clear that the endocytic rate may not exceed a certain threshold. In this case, too many molecules are internalized such that vesicle trafficking rather disturbs polarity.

### 6.3.3. Actin-mediated transport in the absence of Bem1

We already mentioned that mutant cells lacking Bem1 are able to polarize as long as the vesicle trafficking pathway is intact [84, 98]. In this case the sole GDI Rdi1 together with the transport machinery is supposed to generate polarization [28, 84]. Biological experiments have demonstrated that Bem1 is able to bind both Cdc42 and Cdc24 [13, 16]. Since SMITH ET AL. [84] found out that the ability of Bem1 to bind Cdc42-GTP is not required for cell polarity, we first solve the system (6.12a)-(6.12n) without consideration of a Bem1-mediated recruitment of Cdc24 via complex formation with active Cdc42 to the plasma membrane. We reflect this in our simulations by a significant reduced rate  $k_3$ . Since phosphorylation of the

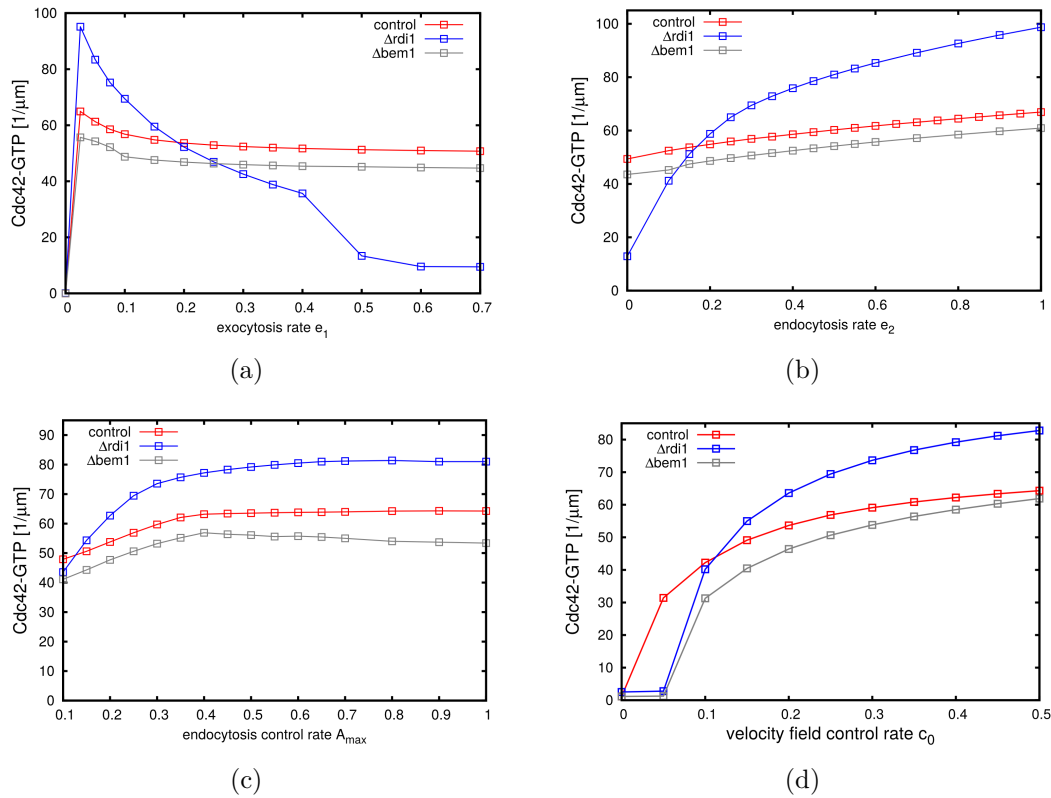


**Figure 6.8.: Effect of transport related parameter changes on actin-mediated polarization in distinct phenotypes.** (a) Maximal Cdc42-GTP concentration for different rates of exocytosis. Reduced rates lead to decreased Cdc42-GTP intensities. (b) The amount of membrane-bound Cdc42-GTP within the polar cluster depends on endocytic rates. (c) Changes of the endocytic control rate  $A_{\text{max}}$  have much less influence on the cap intensity than on its shape. (d) The velocity field control rate  $c_0$  determines the strength of the transport-mediated feedback.

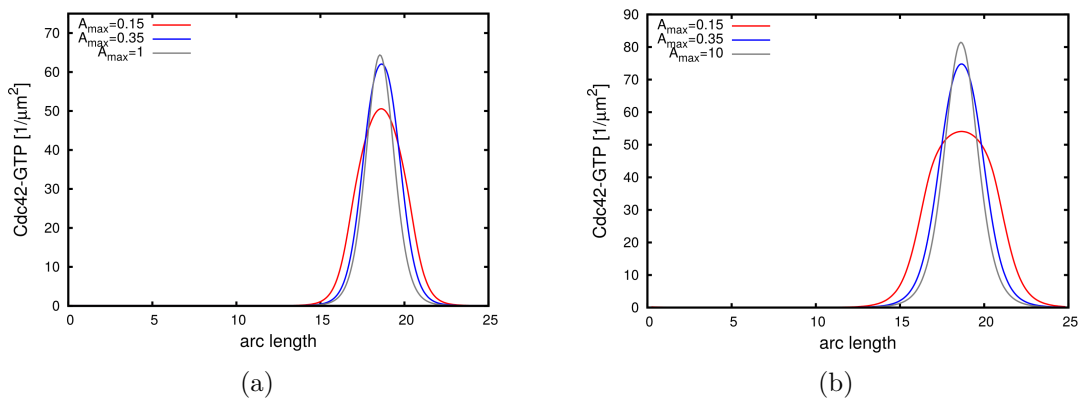


**Figure 6.9.: Effect of the endocytic control rate on the shape of the polar cluster.** The localization of exocytosis and endocytosis in (a) control cells and (b)  $\Delta\text{rdi1}$  cells determines the shape of the polar Cdc42-GTP cap. For increased rates of  $A_{\text{max}}$  exocytosis and endocytosis are co-localized leading to a slightly narrower cap.

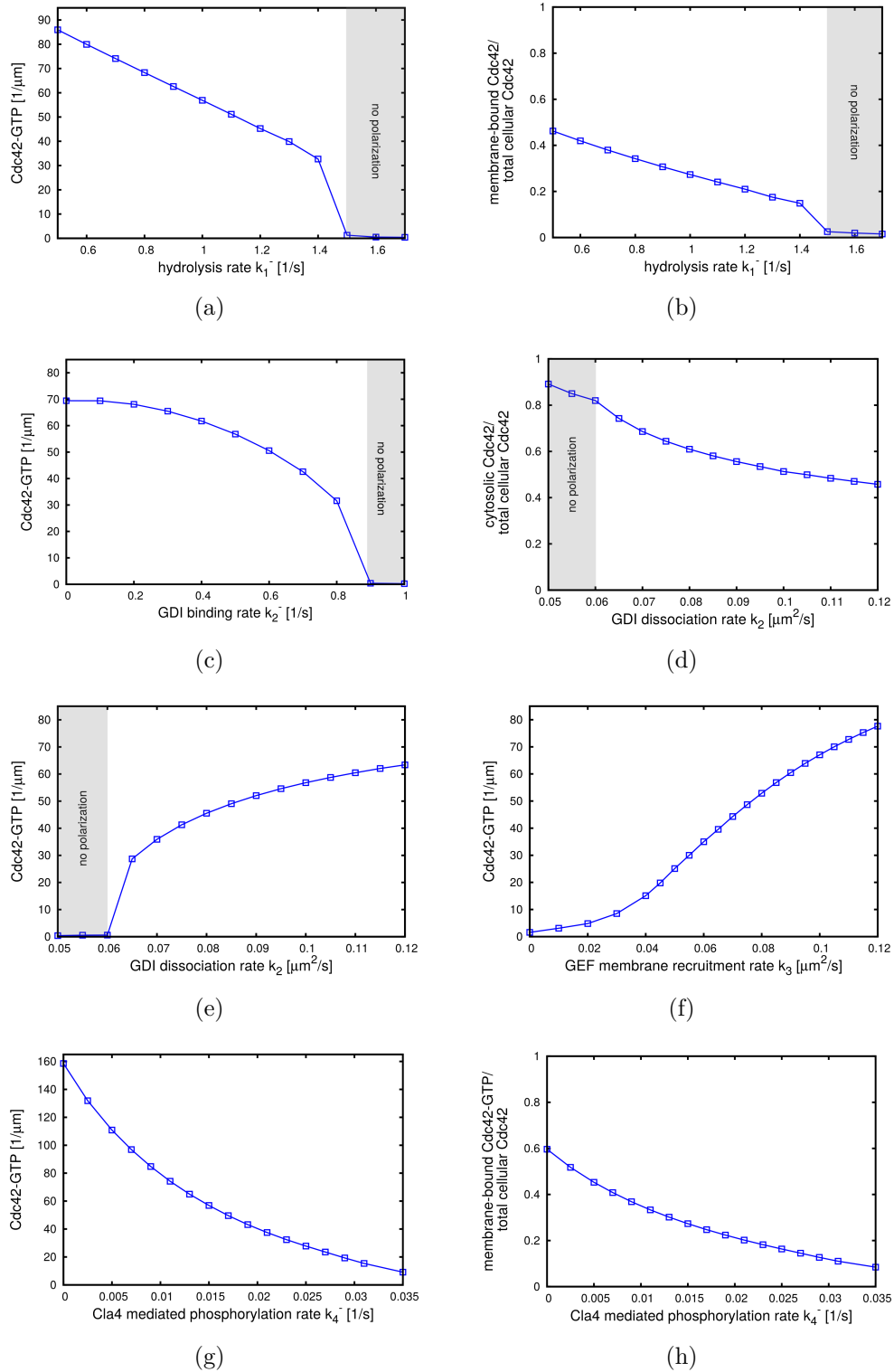


**Figure 6.10.: Effect of parameter changes on transport-mediated polarization.** (a) Maximal Cdc42-GTP concentration for different hydrolysis rates. A large hydrolysis rate prevents polarization. (b) The amount of membrane-bound Cdc42 decreases for increased Cdc42 hydrolysis rates. (c) Change of the maximum of membrane-bound Cdc42-GTP with respect to changes in the GDI binding rate. Even for  $k_2^- = 0$  the system generates a polar cluster. (d) Varying values of cytosolic Cdc42 and (e) of active membrane-bound Cdc42 dependent on the GDI dissociation rate. (f) Effect of changes in the GEF membrane recruitment rate on Cdc42-GTP intensity. (g) Maximum of membrane-bound Cdc42 and (h) the percentage of membrane-bound Cdc42 with respect to changes in the phosphorylation rate.

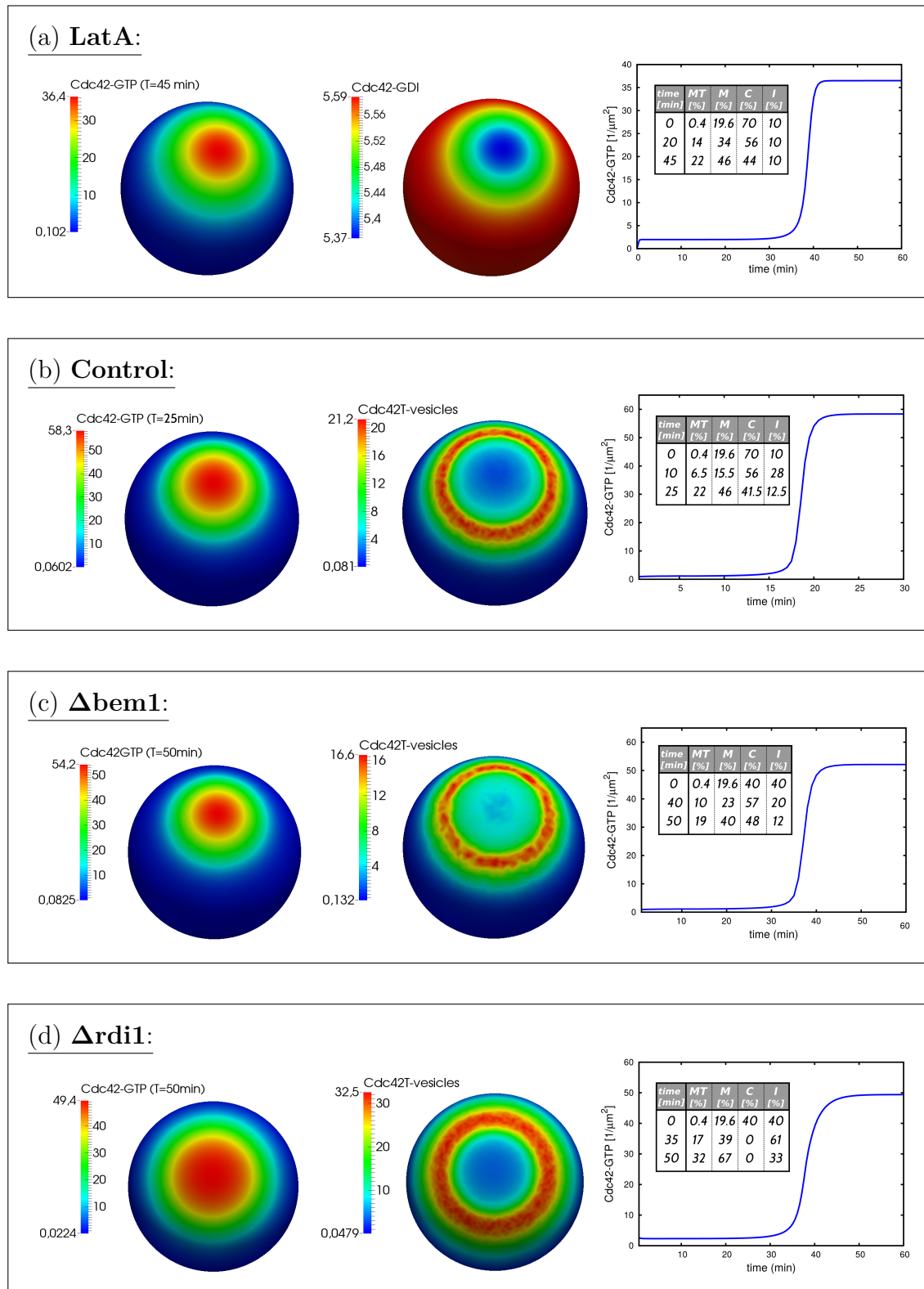


**Figure 6.11.: Numerical simulations of the pathological cases.** Three-dimensional computational results of (6.12a)-(6.12n) are shown. For each case, the right diagram respectively shows the development of Cdc42-GTP over time. The percentage values of cytosolic ( $C$ ), membrane-bound ( $M$ ), and internal ( $I$ ) Cdc42 are summarized in the tables included.  $MT$  denotes the proportion of active membrane-bound Cdc42. (a) Polarization in a cell treated with LatA. (b) Visualization of cell polarity in control cells. (c) Polarization in  $\Delta bem1$  mutants. (d) Symmetry breaking in Rdi1 knock-out cells.

Reaction rate	without transport		with transport	
	$\times 0.5$	$\times 2$	$\times 0.5$	$\times 2$
$k_1^+$	0	0	0	0
$k_1^-$	+30.1	n.p.	+50.9	n.p.
$k_1$	n.p.	+37.1	n.p.	+54.3
$k_2^+$	+1.0	-2.0	+2.0	-4.4
$k_2^-$	-1.2	n.p.	+17.6	n.p.
$k_2$	n.p.	+24.7	n.p.	+30.9
$k_3^+$	+56.7	n.p.	+43.5	-51.4
$k_3^-$	n.p.	+50.4	-51.5	+34.2
$k_3$	n.p.	+74.6	-70.3	+65.7
$k_4$	+80.2	n.p.	+64.7	-70.8

**Table 6.2.: Parameter sensitivity of the system with and without transport.** The relative change in the cluster maximal  $C_T$  concentration in 2D are computed for the model parameter values given in the Table 6.1 multiplied by the factors shown in the head row of the table. Variation of the model parameters either changes the Cdc42 concentration within the cluster or prevents polarity (n.p.). With actin-mediated transport, the system is less sensitive against parameter variations.

	Description	Rate	Units	Value
Model 1	exocytosis	$e_1$	$s^{-1}$	0.1
	endocytosis	$e_2$	$s^{-1}$	0.14
	capacity feedback control rate	$c_0$	$(\mu m^2)^{-1}$	0.1
	velocity control rate	$c_1$	$\mu m^2 s^{-1}$	1
	velocity control rate	$c_2$	$\mu m^2 s^{-1}$	0.1
	internal membrane attachment	$e_3$	$\mu m s^{-1}$	10
	Cdc24 membrane detachment	$e_4$	$s^{-1}$	5
	diffusion of internal Cdc42	$D_v$	$\mu m^2 s^{-1}$	0.01
	endocytosis control rate	$A_{max}$	$(\mu m^2)^{-1}$	0.2
	potential function control rate	$\alpha$	$(\mu m^2)^{-1}$	0.001
	total actin cable density	$A$		6.0
Model 2	exocytosis	$e_1$	$s^{-1}$	0.1
	endocytosis	$e_2$	$s^{-1}$	0.3
	capacity feedback control rate	$c_0$	$(\mu m^2)^{-1}$	0.1
	transport gradient control rate	$c$	$\mu m^2 s^{-1}$	0.5
	diffusion of internal Cdc42	$D_v$	$\mu m^2 s^{-1}$	0.01
	endocytosis control rate	$A_{max}$	$(\mu m^2)^{-1}$	0.25
	potential function control rate	$\alpha$	$(\mu m^2)^{-1}$	0.001
		total actin cable density	$A$	

**Table 6.3.: Reaction rate constants and parameter estimates used to simulate active transport.** Model 1 denotes the system (6.11a)-(6.11v). Model 2 determines the system (6.12a)-(6.12n). For three-dimensional computations we use  $c_0 = 0.3$ .

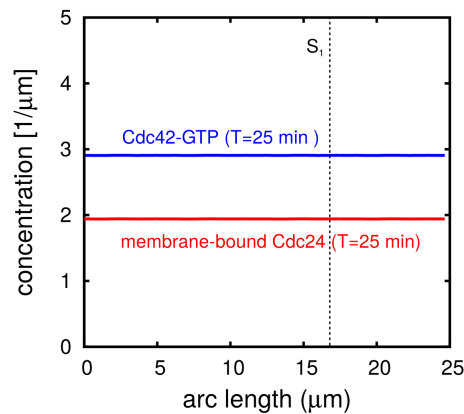


**Figure 6.12.: Predicted dynamics in Bem1 mutant cells exhibiting a homogeneous but high GEF activation.** Simulations are shown for parameters  $k_3 = 0.035$ ,  $k_4 = 0.0$ , and  $k_3^- = 0$ . Furthermore, all Cdc24 is attached to the membrane.

GEF via Cla4 also depends on Bem1, we further assume a decreased rate  $k_4$ . The results which are illustrated in Figure 6.11 (c) agree with biological experiments. We see that polarization is unaffected in mutant cells, where the binding of Bem1 to Cdc42-GTP is disrupted. In this case, Cdc42 polarity is achieved by a GDI- and transport-mediated recycling.

Thus, our simulations support the assumption that in the presence of LatA, through its interaction with Cdc24 and Cdc42, Bem1 is mainly required to stimulate the GEF activity. Actually, a complete disruption or already a decrease in the concentration of membrane-bound Cdc24 leads to a failure of Cdc42 polarity *in silico* (see Figure 6.13 (a)). These results are in complete agreement with biological findings. Whereas a reduced amount of available GEF led to a loss of polarity,  $\Delta bem1$  cells were able to polarize and bud. In this case, Cdc24 localization was strongly reduced or even unobservable to the incipient bud-site [84, 98]. Even in wild type cells Cdc24 was not found to be more focused compared to Cdc42-GTP [98].

However, SMITH ET AL. [84] published a paper where they suggested that Rsr1-Cdc24 and Bem1-Cdc24 interactions are important primarily to activate Cdc24. This implies that localization of Cdc24 would not be necessary for cell polarization as long as there is sufficient GEF activity at the plasma membrane. In this case, local Cdc42 activation is a result of a positive feedback by local delivery. Since this hypothesis has been disproved by a recent study [103], we further test our model for this theory.

Our results confirm those published in [103]. Figure 6.12 shows computational results considering a homogeneous but high GEF activation. We see that a disturbance of the initial homogeneous state by a local stimulus  $S_1$  is not sufficient to induce

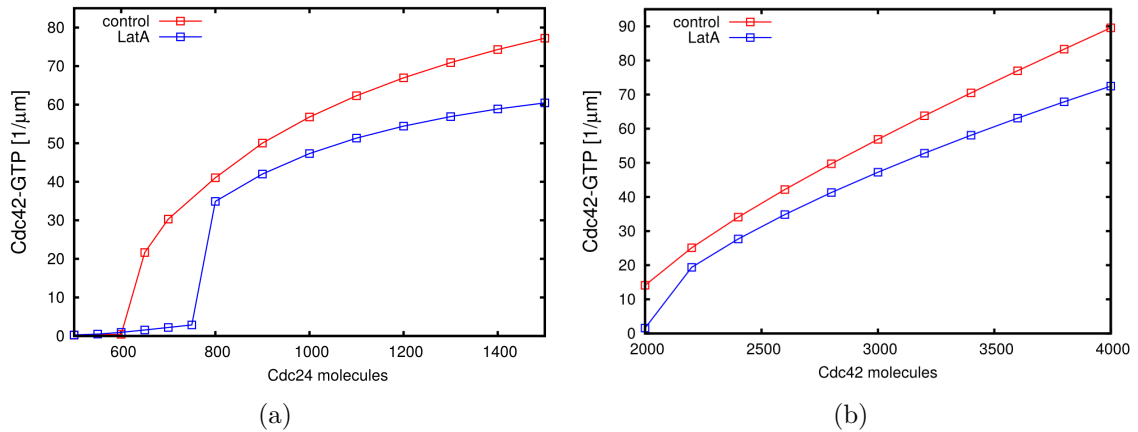


**Figure 6.13.: Cdc42-GTP cluster height for changing molecule numbers.** Maximum height of the polar cluster for changing numbers of (a) Cdc24 and (b) Cdc42 molecules

polarization in  $\Delta bem1$  cells lacking a local GEF concentration. These findings suggest that cells may not polarize and bud without local concentration of the GEF even if the overall cortical GEF level exceeds a certain threshold. We suggest that local Cdc24 activity is sufficient to induce pattern formation but it is not necessary to maintain the polarized cluster. However, biological experiments have demonstrated that Cdc24 is able to localize even in the absence of Bem1 [98]. Thus, there must be another mechanism that leads to the GEF localization. We assume that Rsr1, through interaction with landmark proteins, does not only control Cdc42 polarity in the early stage of polarity establishment by biasing the location of the polarity cluster. Rsr1 could also reinforce cluster formation by interacting with Cdc42-GTP. Indeed, it has already been shown that Rsr1 could contribute to polarization by providing a parallel positive feedback pathway [84]. In other words, Bem1 and Rsr1 could share a role in Cdc24 membrane targeting.

Strikingly, investigations of the Cdc24 activity in  $\Delta bem1$  cells have revealed that Cdc24 caps were unstable and disappeared upon bud emergence [98]. These results together with our simulations indicate that polarity establishment in cells could be achieved by three distinct phases. Initially Rsr1 and Bem1 together control Cdc24 localization in the polar cap. Subsequently, the local GEF activity induces Cdc42 activation at this site. In the last phase, on the one hand local activation of Cdc42 leads to further recruitment of Cdc42 from the cytosol and on the other hand to actin cable formation towards the polar cluster followed by actin-mediated vesicle trafficking to maintain polarity.

### 6.3.4. Actin-mediated transport in the absence of GDI

Finally, we will investigate the reaction-diffusion-advection system (6.12a)-(6.12n) for the possibility of symmetry breaking in cells lacking the sole GDI Rdi1. Therefore, we disable the exchange of Cdc42 between the plasma membrane and the cytosol and set  $k_2^- \equiv 0$ . This implies that the total mass of Cdc42 is bound to the plasma membrane as well as located on internal compartments. Indeed,  $\Delta rdi1$  cells accumulate Cdc42 on membranes due to the defect in extraction of membrane-bound Cdc42 [28].

As demonstrated by biological experiments, we see that the model simulating  $\Delta rdi1$  cells is able to polarize (see Figure 6.11 (d)). Furthermore, our results reflect experiments of such cells that were additionally treated with LatA. The simulations confirm biological findings that without exocytosis and endocytosis as well as an exchange between the cytosol and the plasma membrane, yeast cells fail to generate a robust polar cluster. We ascertain that a disruption of the cytosolic exchange of Cdc42-GTP in approach (6.1)-(6.7) impedes polarity. From Figure 6.6 (c) and 6.10 (c) it becomes clear that this loss of pattern formation is a result of the concurrent lack of transport. In this case, the total amount of Cdc42 is homogeneously distributed on the plasma membrane. To form a spatial pattern, the model requires some recycling mechanism between the interior of the cell and its surface. This confirms the results that targeting of Cdc42 from either the cytosolic Rdi1-bound or the internal membrane-bound pool is crucial for Cdc42 cluster formation.

Concerning the time course, our results also agree with biological findings. We observe a slightly decelerating symmetry breaking process. In  $\Delta rdi1$  cell polarity is mainly based on the actin-mediated delivery of secretory vesicles. This process recycles Cdc42 a lot more slowly than GDI. Whereas Figure 6.11 (b) demonstrates that polarization in control cells takes 20-30 minutes, Figure 6.11 (d) shows that  $\Delta rdi1$  cells need 40-50 minutes to polarize *in silico*.

A further feature of cells lacking Rdi1 is the significant membrane-bound and internal pool of Cdc42 [28]. In our numerical simulations we obtain about 67% of all Cdc42 on the plasma membrane and about 33% on internal membranes.

To further test the impact of actin-mediated recycling on polarization in  $\Delta rdi1$  cells, we investigate the sensitivity of changes in rates of exocytosis and endocytosis. From Figure 6.8 we see that a decreased rate of endocytosis reduces the amount of Cdc42 in the final cluster. Similarly, a lower rate of exocytosis negatively influences polarity establishment. Indeed, it has been shown that a reduction of endocytosis results in less efficient polarization in  $\Delta rdi1$  cells. Furthermore, the blocking of exocytosis leads to a failure of polarization in cells lacking Rdi1 [28]. Interestingly, compared to control cells, cluster formation is much more sensitive to changes in parameters



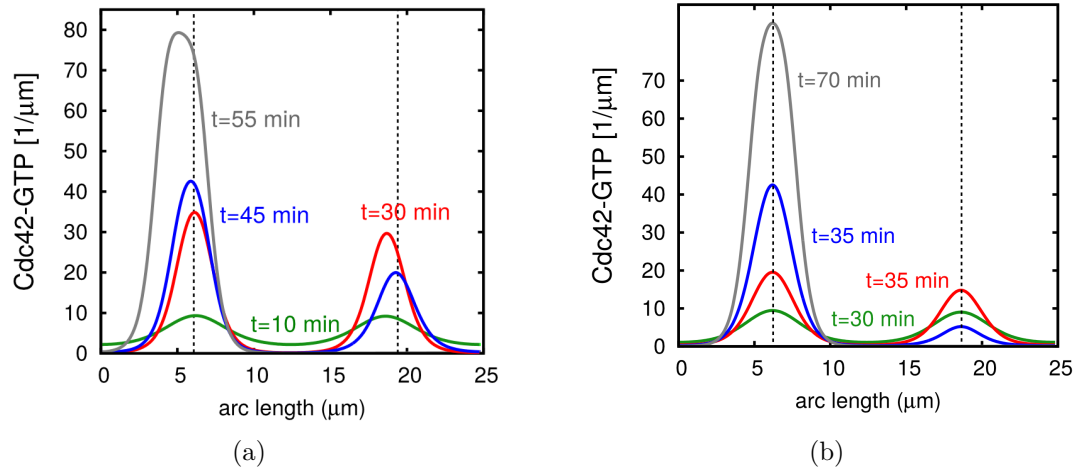


**Figure 6.14.: Computational results showing two transient peaks.** (a) Without a cytosolic exchange and with an increased transport feedback ( $d_c = 0.01$ ,  $c_0 = 0.5$ ) two transient peaks are obtained. (b) A reduced hydrolysis rate ( $k_1^-$ ) can result in transient multiple peaks that finally merge together ( $d_c = 0.01$ ).

that control the transport process.

A particular feature of yeast cells is their capability to simultaneously polarize at multiple sites of the membrane. As a consequence, the cell can form several buds. Since  $\Delta rdi1$  cells are prone to form more than one cluster, it has been suggested that GDI-mediated exchange is required to prevent overexpression of Cdc42. This allows the yeast cell to generate a unique Cdc42-GTP cluster that initiates downstream processes like reorganization of actin at a desired position. Hence, the single cluster formation due to GDI-mediated exchange prevents the development of multiple buds at several places on the membrane [28, 48].

Under other circumstances, yeast cells are also able to form multiple caps. For example overexpression of Bem1 or a reduced hydrolysis rate of Cdc42 induced by the depletion of the GAP Bem2 can initiate several Cdc42-GTP clusters. In biological experiments nearly one-tenth of  $\Delta bem2$  cells formed two buds due to an increased Cdc42 activity. Furthermore, in  $\Delta bem2$  strains, the overexpression of Cdc24 leading to an increased Cdc42 activity induced a significant rise in the number of cells generating multiple polarization sites [28, 38]. Since such overexpression did not generate double buds in control cells, it is assumed that the actin-mediated pathway is susceptible to changes in the Cdc42 activity. In this case there is the possibility that actin bundles nucleate at two (or more) distant sites on the plasma membrane which then promotes the emergence of multiple caps [28, 96].

In order to test if the system (6.12a)-(6.12n) generates multiple clusters under certain conditions, we perform simulations where we simultaneously excite two sites

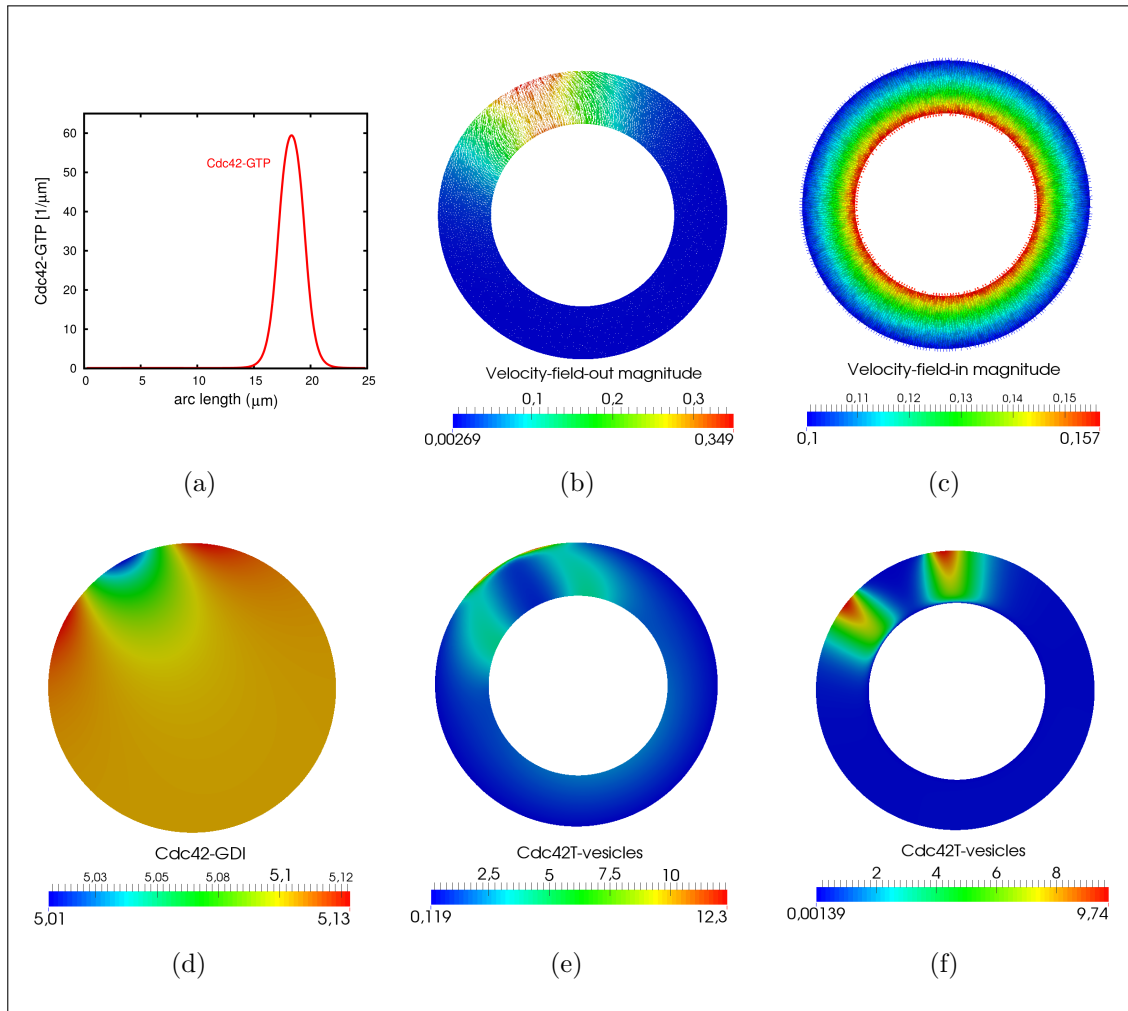


**Figure 6.15.: Computational results of the model considering transport from and to internal membranes.** Cdc42-GTP cluster formation in the two-dimensional case is shown. (a) Cdc42-GTP concentration at the plasma membrane after  $t = 1200s$ . (b) The distribution of cytosolic Cdc42. (c) Illustration of the outward directed velocity field determined by the potential function  $\Phi_a(x, t)$ . (d) Illustration of the inward directed velocity field determined by the potential function  $\Phi_r(x, t)$ . Visualization of the distribution of (e) inward and (f) outward flowing vesicles containing Cdc42-GTP.

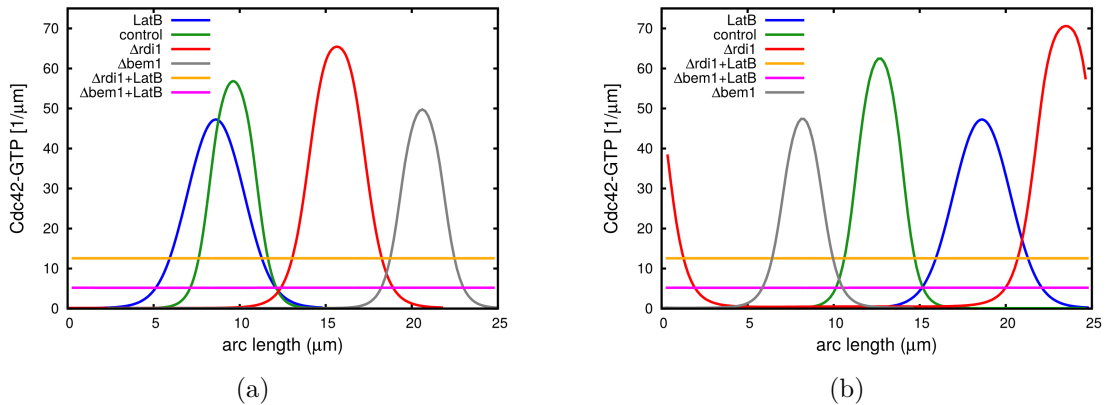


**Figure 6.16.: Comparison of polarization in different mutant cells.** Two-dimensional simulations of the pathological cases. (a) The complex model given by equations (6.11a)-(6.11v) is able to reproduce the experimentally observed pathological cases. (b) The reduced system of equations (6.12a)-(6.12n) shows similar results.

of the cell with a transient stimulus. Figure 6.14 shows the results for different *in silico* experiments. We never obtain two stable clusters. Neither a lack of cytosolic exchange nor a reduced hydrolysis rate leads to a pattern with two stable peaks. Overexpression of Bem1 reflected by an intense increase of the GEF recruitment rate  $k_3$  is also not sufficient to achieve a pattern with two caps. However, we see that compared to the system simulating control cells, the transient stimuli in these cases induce two clusters which persist much longer.

## 6.4. Model comparison

Up to now, we restrict ourselves to system (6.12a)-(6.12n) that simulates vesicle movement through the cell without consideration of detachment from, and attachment to internal components or membranes. That this does not alter the results is shown in Figures 6.16 and 6.15. Using the same parameters for molecule reactions, we take transport parameters given in Table 6.3. The two-dimensional results of (6.11a)-(6.11v) are very similar to those presented before. Considering actin-mediated transport, the system is capable to reproduce pathological cases within similar value ranges. However, our simulations show that this is only the case if changes from and to internal compartments are relatively fast. For parameters  $e_3$  and  $e_4 \ll 1$ , the exchange of internal molecules is so low that the system fails to polarize.

## 6.5. Discussion

In this chapter we derived a set of partial differential equations which was sufficient to describe the polarization mechanism induced by parallel pathways including Bem1, Rdi1, Cla4, and actin. Our simulations have demonstrated that the presented approach robustly induces only one stable cluster. For the simulation of vesicle trafficking we used a completely different and new approach. We modeled the actin cable movement by a capacity (Cdc42-GTP) dependent diffusion process. This approach has the advantage of simulating the actin cable movement on the plasma membrane as a density. Dependent on this density, the system generates a velocity field that controls internal delivery of further Cdc42 to the plasma membrane.

By this consideration of actin-mediated transport, our model was able to reproduce polarity observed in different mutant cells. We showed that this transport is required to ensure symmetry breaking if key proteins like Bem1 or Rdi1 are knocked out. In this case, the feedback mechanism due to vesicle trafficking to the polar cap could compensate a reduced concentration of Cdc42-GTP. These results support the assumption that under certain conditions vesicle trafficking indeed could reinforce the Cdc42 cluster formation to guarantee polarity.

But also, based on the choice of parameters, our results have shown that transport could disturb cell polarization, even if the actin feedback is not strong enough. However, inhomogeneous diffusion of membrane-bound Cdc42-GTP could counter against this perturbation (data not shown). These findings correspond to experiments which have demonstrated that non-uniform membrane diffusion can maintain actin-mediated cell polarization [83].

Summarized, our results suggest that whether actin transport enhances polarization depends on the velocity of moving vesicles as well as the feedback for actin cable nucleation. Furthermore, the ratio between exocytic and endocytic fluxes determines how internal transport affects the polar cluster formation and its stability. We found that the amount of internal Cdc42 plays a subordinated role. These outcomes suggest that actin transport could have different roles in distinct cell types and cell cycles. For example, our model predicts that the inhibition of endocytosis or the overexpression of exocytosis in  $\Delta rdi1$  cells would impede polarization.

Besides a continuous approach for the trafficking machinery, a new aspect of our model is that it does not only rely on a Bem1-mediated feedback mechanism. We based our system on several different pathways shown to contribute to robust polarity. Therefore, we did not explicitly simulate Bem1. We only distinguished between an active membrane-bound and a cytosolic form of Cdc24. In our reaction-diffusion-

advection system, the membrane association of the GEF was based on the assumption that it either binds to Rsr1 or to Bem1. Since both proteins interact with Cdc42, we supposed that the GEF membrane association indirectly depends on Cdc42. This is in contrast to the system presented in [48] which incorporates Bem1. Another new aspect of our approach is that we hypothesized that the GDI-mediated exchange can be achieved by Cla4 and hence indirectly via Cdc42-GTP. For instance, in [48] the GDI pathway is only based on a GEF-mediated Cdc42-GDI disruption. Hence, the omission of Bem1 would destroy the local GEF activation as well as the GDI pathway. This implies that even under consideration of vesicle trafficking, the system presented there would fail to simulate polarity. Contrarily to this, our model is able to reflect polarization in  $\Delta bem1$  mutant cells.

However, which proteins or effectors are involved in the GDI pathway is still unknown and has to be determined. Our results have demonstrated that Cla4 could control this process. However, parameter studies have also shown that a complete disruption ( $k_2 = 0$ ) would prevent polarization. Since  $\Delta cla4$  cells are still able to form a polar Cdc42-GTP cluster, our model suggests that GDI-disruption could be achieved by two parallel mechanisms, a GEF-mediated displacement proposed by [28, 48] and a Cla4-mediated disruption.

Interestingly, biological studies have shown that Cdc24-Cla4 fusion could rescue polarity in cells lacking Bem1. Hence, we assume that in this case localized Cdc24 activates Cdc42 that in turn interacts with Cla4. The PAK kinase then disrupts the binding between Cdc42 and its GDI Rdi1 at the incipient bud, leading to a recruitment of further Cdc42 from the cytosol to the localized cluster. This Cla4-mediated mechanism proposed by our model would be accompanied by several so far unknown phenotypes which could be verified experimentally. For example, one prediction of our model is that  $\Delta bem1 \Delta cla4$  double mutants would fail to polarize. Furthermore, Cla4 would be localized at the incipient bud-site even in the absence of Bem1. Another outcome of our simulations is that a treatment of  $\Delta cla4$  cells with LatA would impede symmetry breaking.

That Cla4 could play a more essential role in polarity establishment is also suggested by experiments investigating the impact of Cla4-mediated phosphorylation. Our parameter studies have shown that this mechanism indeed buffers the total Cdc42-GTP concentration at the polar site. In agreement with biological experiments, we observe highly increased amounts of Cdc42-GTP at the plasma membrane. However, only a few studies have focused on the contribution of Cla4 in the step of polarity establishment. Whether Cla4 could indeed play a more crucial role in the achievement of polarity as previously supposed has to be determined.



# 7 | Derivation of a generic bulk-surface reaction-diffusion-advection system

In the last chapter we have numerically studied a coupled system of bulk-surface reaction-diffusion-advection equations. Based on this complex model, in this chapter we are aiming to derive a generic model that can be studied analytically and applied to other cell geometries. Therefore, we first reduce the full model to get a system which is easier to handle. Following this, we perform a non-dimensionalization and deduce a generic approach. This generic system can be used to simulate transport-mediated cell polarization for different cell geometries and varying functions representing protein kinetics, e.g. for those found in the literature. Here, we study the Wave-Pinning system proposed by MORI ET AL. [61] (WP) as well as the system proposed by GORYACHEV AND POKHILKO [32] (GOR) and compare the results with those from this thesis.

## 7.1. Model reduction

The reduction of complex and large models to their minimal functional form helps to unravel the covered fundamental features of complex reaction mechanisms. Since we are aiming to study our full system for the main processes that lead to polarization, we further reduce the complex approach derived in the last chapter.

For sake of simplicity, we start by a restriction of our model to one bulk ( $\Omega$ ) and one surface domain ( $\Gamma := \partial\Omega$ ) and neglect that actin cables do not cross the nucleus or other perinuclear components. Furthermore, we suppose that the activation of inactive Cdc42, which reaches the plasma membrane by exocytosis, occurs very fast. This allows us to restrict transport to one component representing vesicles containing active Cdc42. Finally, we assume that the complex formation of Cdc42 with its GEF Cdc24 and the protein Bem1 quickly reaches a steady state. This means that

the Cdc24 attachment and detachment events are in equilibrium. Mathematically, considering (6.12c), this is equivalent to

$$\partial_t G_B = (k_3^+ + k_3 C_T) G_F - (k_3^- + k_4 C_T) G_B = 0$$

and hence

$$G_F = \frac{(k_3^- + k_4 C_T) G_B}{(k_3^+ + k_3 C_T)}.$$

Using the conservation law

$$G_0 = G_B + c G_F,$$

where  $c := \frac{|\Omega|}{|\Gamma|}$  and  $[c] = \mu m$ , it follows

$$\begin{aligned} G_0 &= G_B + c \left( \frac{k_3^- + k_4 C_T}{k_3^+ + k_3 C_T} \right) G_B = \left( 1 + \frac{c(k_3^- + k_4 C_T)}{k_3^+ + k_3 C_T} \right) G_B \\ &= \left( \frac{k_3^+ + c k_3^- + (k_3 + c k_4) C_T}{k_3^+ + k_3 C_T} \right) G_B, \end{aligned}$$

so that

$$G_B = \left( \frac{k_3^+ + k_3 C_T}{k_3^+ + c k_3^- + (k_3 + c k_4) C_T} \right) G_0.$$

We define

$$k_1 G_B := \left( \frac{K_3^+ + K_3 C_T}{K_3^- + K_4 C_T} \right), \quad (7.1)$$

where

$$\begin{aligned} K_3^+ &:= k_1 k_3^+ G_0; & K_3 &:= k_1 k_3 G_0; & K_3^- &:= k_3^+ + c k_3^-; & K_4 &:= k_3 + c k_4; \\ [K_3^+] &= [K_3^-] = \frac{\mu m}{s}; & [K_3] &= [K_4] = \frac{\mu m^3}{s}. \end{aligned}$$

With (7.1) and the additional assumptions mentioned above, on  $\Gamma$  the equations (6.12a)-(6.12n) reduce to

$$\begin{aligned} \partial_t C_T &= \left( k_1^+ + \left( \frac{K_3^+ + K_3 C_T}{K_3^- + K_4 C_T} \right) \right) C_D - k_1^- C_T + e_1 \cdot C_{TV} \\ &\quad - e_2 \cdot \left( 1 - \frac{A}{A_{max}} \right) \cdot C_T + \nabla_{\Gamma_{C_1}} \cdot (D_m \nabla_{\Gamma_{C_1}} C_T), \end{aligned} \quad (7.2)$$



$$\partial_t C_D = k_1^- C_T - \left( k_1^+ + \left( \frac{K_3^+ + K_3 C_T}{K_3^- + K_4 C_T} \right) + k_2^- \right) C_D \quad (7.3)$$

$$+ (k_2^+ + k_2 C_T) C_I + \nabla_{\Gamma_{C_1}} \cdot (D_m \nabla_{\Gamma_{C_1}} C_D),$$

$$\partial_t A = \nabla_{\Gamma_C} \cdot \left( D_A \nabla_{\Gamma_C} \frac{A}{c(C_T)} \right). \quad (7.4)$$

On  $\Gamma$  the flux conditions are then given by

$$-D_c \nabla C_I \cdot \vec{n} = (k_2^+ + k_2 C_T) C_I - k_2^- C_D, \quad (7.5)$$

$$-(D_v \nabla C_{TV} - C_{TV} \nabla \Phi) \cdot \vec{n} = e_1 \cdot C_{TV} - e_2 \cdot \left( 1 - \frac{A}{A_{max}} \right) \cdot C_T, \quad (7.6)$$

$$\nabla \Phi \cdot \vec{n} = j(A). \quad (7.7)$$

On  $\Omega$  it holds that

$$\partial_t C_{TV} = \nabla \cdot (D_v \nabla C_{TV}) - \nabla \cdot (C_{TV} \nabla \Phi), \quad (7.8)$$

$$\partial_t C_I = \nabla \cdot (D_c \nabla C_I), \quad (7.9)$$

$$0 = \Delta \Phi - \alpha \Phi. \quad (7.10)$$

As a result, we obtain a simpler system of bulk-surface reaction-diffusion-advection equations for the GTPase cycle. It takes the form of a reaction-diffusion process on the membrane coupled to a diffusion and an advection process in the interior of the cell.

## 7.2. Non-dimensionalization

After the model reduction we proceed with a non-dimensionalization. This technique targets the elimination of units implied by the reaction kinetics and diffusion coefficients. For the PDE system given by (7.2)-(7.10), where  $j(A) = c \cdot A$  and  $c(C_T) = v \cdot C_T$ , we obtain

$$[k_1^+] = [k_1^-] = [k_2^-] = [k_3^-] = [e_2] = \frac{1}{s}; \quad [k_2^+] = [k_3^+] = [e_2] = [K_3^-] = [K_3^+] = \frac{\mu m}{s};$$

$$[k_1] = [k_4] = \frac{\mu m^2}{s}; \quad [k_1] = [k_2] = [k_3] = [K_3] = [K_4] = [c] = \frac{\mu m^3}{s}; \quad [\alpha] = \frac{1}{\mu m^2}$$

$$[v] = \mu m^2; \quad [D_m] = [D_c] = [D_v] = [\Phi] = \frac{\mu m^2}{s}.$$

In order to derive a non-dimensional model that contains equations for unknowns

- $u$  concentration of active membrane-bound GTPase,
- $v$  concentration of inactive membrane-bound GTPase,
- $w$  concentration of membrane-attached actin cables,
- $U$  concentration of internal membrane-bound GTPase,
- $V$  concentration of cytosolic GDI-bound GTPase,

it is reasonable to introduce a typical length  $R > 0$ , where  $[R] = \mu\text{m}$ . We define the following dimensionless spatial and time coordinates

$$\tilde{x} := \frac{1}{R}x; \quad \tau := \frac{D_m}{R^2}t.$$

Let  $R = \sqrt{\gamma}\mathbb{I}$  denote the unit length, where  $\gamma > 0$  and  $\mathbb{I} = 1\mu\text{m}$ . The transformed domains are then given by  $\tilde{\Omega} := \{\tilde{x} \in \mathbb{R}^3 : R\tilde{x} \in \Omega\}$  and  $\tilde{\Gamma} := \partial\tilde{\Omega}$ . Furthermore, we derive the time interval  $\tilde{I} := \{\tau \in \mathbb{R} : \frac{R^2\tau}{D_m} \in I\}$  and introduce the non-dimensional variables

$$u := \frac{C_T}{C_{tot}}, \quad v := \frac{C_D}{C_{tot}}, \quad w := \frac{A}{C_{tot}}, \quad U := \frac{R \cdot C_{TV}}{C_{tot}}, \quad V := \frac{R \cdot C_I}{C_{tot}}, \quad \phi := \frac{\Phi}{D_m}$$

as well as dimensionless parameters

$$\begin{aligned} \tilde{k}_1 &:= \frac{k_1^+ \mathbb{I}^2}{D_m}, & \tilde{k}_2 &:= \frac{k_1^- \mathbb{I}^2}{D_m}, & \tilde{k}_3 &:= \frac{k_2^+ \mathbb{I}^2}{D_m R}, & \tilde{k}_4 &:= \frac{k_2^- \mathbb{I}^2}{D_m}, & \tilde{k}_5 &:= \frac{k_2 C_{tot} \mathbb{I}^2}{D_m R}, \\ a_1 &:= \frac{K_3^+ \mathbb{I}^2}{K_3^- D_m}, & a_2 &:= \frac{K_3 C_{tot} \mathbb{I}^2}{K_3^- D_m}, & a_3 &:= \frac{K_4 C_{tot}}{K_3^-}, & \tilde{e}_1 &:= \frac{e_1 \mathbb{I}^2}{D_m R}, & \tilde{e}_2 &:= \frac{e_2 \mathbb{I}^2}{D_m}, \\ D_u &:= \frac{D_v}{D_m}, & D_v &:= \frac{D_c}{D_m}, & d_w &:= \frac{D_A}{D_m}, & \tilde{v} &:= v \cdot C_{tot}, & \tilde{\alpha} &:= R^2 \cdot \alpha, & \tilde{c} &:= \frac{c R C_{tot}}{D_m}. \end{aligned}$$

Here,  $C_{tot}$  describes the total mass of the GTPase which is given by initial conditions. Due to mass conservation, this is a constant value. Note that  $[C_{tot}] = \frac{1}{\mu\text{m}^2}$  and  $C_{tot} = C_T + C_D + c \cdot C_I + c \cdot C_{TV}$ , where  $c := \frac{|\Omega|}{|\Gamma|}$ . Applying these definitions, the system (7.2)-(7.10) in its non-dimensional form on  $\tilde{\Gamma} \times \tilde{I}$  reads

$$\begin{aligned} \partial_\tau u &= \Delta_\Gamma u + \gamma \left( \left( \tilde{k}_1 + \left( \frac{a_1 + a_2 u}{1 + a_3 u} \right) \right) v - \tilde{k}_2 u + \tilde{e}_1 U - \tilde{e}_2 \left( 1 - \frac{w}{w_{max}} \right) u \right), \\ \partial_\tau v &= d_v \Delta_\Gamma v + \gamma \left( - \left( \left( \tilde{k}_1 + \left( \frac{a_1 + a_2 u}{1 + a_3 u} \right) \right) v - \tilde{k}_2 u + (\tilde{k}_3 + \tilde{k}_5 u) V - \tilde{k}_4 v \right) \right), \\ \partial_\tau w &= d_w \Delta_\Gamma (w \cdot c(u)^{-1}). \end{aligned}$$

In  $\tilde{\Omega} \times \tilde{I}$  we have

$$\begin{aligned}\partial_\tau U &= D_u \Delta U - \nabla \cdot (U \nabla \phi), \\ \partial_\tau V &= D_v \Delta V, \\ 0 &= \Delta \phi - \tilde{\alpha} \phi,\end{aligned}$$

and the flux conditions on  $\tilde{\Omega} \times \tilde{I}$  change to

$$\begin{aligned}-(D_u \nabla U - U \nabla \phi) \cdot \vec{n} &= \gamma \left( \tilde{e}_1 U - \tilde{e}_2 \left( 1 - \frac{w}{w_{max}} \right) u \right), \\ -D_v \nabla V \cdot \vec{n} &= \gamma \left( (\tilde{k}_3 + \tilde{k}_5 u) V - \tilde{k}_4 v \right), \\ \nabla \phi \cdot \vec{n} &= \tilde{c} \cdot w.\end{aligned}$$

For the sake of clarity, we drop all tildes and replace  $\tau$  by  $t$ .

On  $\Gamma \times I$  we obtain

$$\begin{aligned}\partial_t u &= \Delta_\Gamma u + \gamma \left( \left( k_1 + \frac{a_1 + a_2 u}{1 + a_3 u} \right) v - k_2 u + e_1 U - e_2 \left( 1 - \frac{w}{w_{max}} \right) u \right), \\ \partial_t v &= d_v \Delta_\Gamma v + \gamma \left( - \left( \left( k_1 + \frac{a_1 + a_2 u}{1 + a_3 u} \right) v - k_2 u + (k_3 + k_5 u) V - k_4 v \right) \right), \\ \partial_t w &= d_w \Delta_\Gamma (w \cdot c(u)^{-1}).\end{aligned}$$

In  $\Omega \times I$  it holds that

$$\begin{aligned}\partial_t U &= D_u \Delta U - \nabla \cdot (U \nabla \phi), \\ \partial_t V &= D_v \Delta V, \\ 0 &= \Delta \phi - \alpha \phi,\end{aligned}$$

and the coupling boundary conditions on  $\Gamma \times I$  read

$$\begin{aligned}-(D_u \nabla U - U \nabla \phi) \cdot \vec{n} &= \gamma \left( e_1 U - e_2 \left( 1 - \frac{w}{w_{max}} \right) u \right), \\ -D_v \nabla V \cdot \vec{n} &= \gamma \left( (k_3 + k_5 u) V - k_4 v \right), \\ \nabla \phi \cdot \vec{n} &= c \cdot w.\end{aligned}$$

For initial conditions at time  $t = 0$ , given by

$$\begin{aligned}U(\cdot, 0) &= U_0, \quad V(\cdot, 0) = V_0, \quad u(\cdot, 0) = u_0, \quad v(\cdot, 0) = v_0, \quad w(\cdot, 0) = w_0, \\ \phi(\cdot, 0) &= \phi_0, \quad U_0, V_0, \phi_0 : \Omega \rightarrow \mathbb{R}, \quad u_0, v_0, w_0 : \Gamma \rightarrow \mathbb{R},\end{aligned}$$

this system has a solution  $(u, v, w, U, V)$ .

### 7.3. The generic coupled bulk-surface reaction-diffusion-advection system

With the preliminaries presented in Sections 7.1 and 7.2, we are now able to formulate the generic reaction-diffusion-advection system. We will always consider a stationary bulk domain  $\Omega$  and its compact hypersurface  $\Gamma := \partial\Omega$ . We denote by  $\vec{n}$  the outer normal on the smooth, closed surface  $\Gamma$ . The tangential gradient on the surface  $\Gamma$  is described by  $\nabla_\Gamma$ . This implies that the Laplace-Beltrami operator on  $\Gamma$  is given by the tangential divergence of the tangential gradient, that is  $\Delta_\Gamma$ .

Let  $u, v : \Gamma \times I \rightarrow \mathbb{R}$  be smooth functions denoting the chemical concentrations or species that react and diffuse on  $\Gamma$  in a fixed time interval  $I := [0, T] \subset \mathbb{R}$ . For substances that actively move or diffuse through the domain  $\Omega$ , we respectively introduce smooth functions  $U, V : \Omega \times I \rightarrow \mathbb{R}$ . To proceed, a smooth function  $w : \Gamma \times I \rightarrow \mathbb{R}$  represents the component which regulates the transport gradient. In our case, this function describes the density of actin cable ends on the surface  $\Gamma$ . We formulate the generic non-dimensional coupled-reaction-diffusion-advection system as follows:

$$\partial_t u = \Delta_\Gamma u + \gamma(f(u, v) + h(u, w, U)) \quad \text{on } \Gamma \times I, \quad (7.11)$$

$$\partial_t v = d_v \Delta_\Gamma v + \gamma(-f(u, v) + g(u, v, V)) \quad \text{on } \Gamma \times I, \quad (7.12)$$

$$\partial_t w = d_w \Delta_\Gamma (w \cdot c(u)^{-1}) \quad \text{on } \Gamma \times I, \quad (7.13)$$

$$\partial_t U = D_u \Delta U - \nabla \cdot (\vec{v}U) \quad \text{in } \Omega \times I, \quad (7.14)$$

$$\partial_t V = D_v \Delta V \quad \text{in } \Omega \times I, \quad (7.15)$$

with coupling boundary conditions

$$-(D_u \nabla U - \vec{v}U) \cdot \vec{n} = \gamma h(u, w, U) \quad \text{on } \Gamma \times I, \quad (7.16)$$

$$-D_v \nabla V \cdot \vec{n} = \gamma g(u, v, V) \quad \text{on } \Gamma \times I, \quad (7.17)$$

and initial conditions at time  $t = 0$

$$U(\cdot, 0) = U_0, \quad V(\cdot, 0) = V_0, \quad u(\cdot, 0) = u_0, \quad v(\cdot, 0) = v_0, \quad w(\cdot, 0) = w_0, \\ U_0, V_0 : \Omega \rightarrow \mathbb{R}, \quad u_0, v_0, w_0 : \Gamma \rightarrow \mathbb{R}.$$

Here, the non-linear functions  $f$  and  $g$  respectively represent activation and in-activation of the species. The function  $h$  describes adsorption and desorption of molecules and  $\vec{v}$  is the bulk velocity field. The parameters  $D_u$  and  $D_v$  denote the non-dimensional bulk diffusion coefficients and  $d_v, d_w > 0$  the surface diffusion coefficients, which are assumed to be constant. The non-dimensional parameter  $\gamma > 0$  relates to the spatial scale of the cell.

Note that this formulation implies conservation of mass. This means that with  $d\sigma$  denoting the integration with respect to the surface area measure and  $M$  the total mass, the system satisfies the condition

$$\partial_t M = \frac{d}{dt} \left[ \int_{\Omega} [U(x, t) + V(x, t)] dx + \int_{\Gamma} [u(x, t) + v(x, t) + w(x, t)] d\sigma(x) \right] = 0.$$

To determine the velocity field  $\vec{v}$  we use the Poisson equation for a potential function  $\phi$ , given by

$$0 = \Delta\phi - \alpha\phi \quad \text{in } \Omega \times I,$$

and calculate  $\nabla\phi = \vec{v}$ , with boundary and initial conditions

$$\nabla\phi \cdot \vec{n} = j(w), \quad \phi(\cdot, 0) = \phi_0, \quad \phi_0 : \Omega \rightarrow \mathbb{R}.$$

The function  $j(w)$  thereby describes the outflow depending on the concentration of  $w$ .

### 7.3.1. Numerical results

The generic approach for cell polarization presented above allows us to investigate this process under consideration of distinct functions simulating protein kinetics. Together with the possible application to different geometries, it serves as an exemplary model to study transport-mediated polarity in different cell types. We start to compare the following two systems simulating cell polarization in yeast cells.

#### Our approach:

As a first example we consider the non-dimensionalized and reduced system presented in Section 7.1. This system differentiates between one active membrane-bound, one inactive membrane-bound, and a cytosolic state. The functions are given by

$$f(u, v) := \left( k_1 + \left( \frac{a_1 + a_2 u}{1 + a_3 u} \right) \right) v - k_2 u, \quad (7.18)$$

$$g(u, v, V) := (k_3 + k_5 u)V - k_4 v. \quad (7.19)$$

### The bulk-surface model of Rätz and Röger:

In [72] the authors already have investigated a bulk-surface GTPase model that is based on two membrane-bound states and one cytosolic form. This model simulates the GTPase cycle on the full geometry. It uses the following functions representing the reaction kinetics:

$$f(u, v) := \left( a_1 + (a_3 - a_1) \frac{u}{a_2 + u} \right) v - a_4 \frac{u}{a_5 + u}, \quad (7.20)$$

$$g(u, v, V) := a_6 V(1 - (u + v))_+ - a_{-6} v. \quad (7.21)$$

In order to test whether transport has similar influence on cell polarity in both systems, we again consider the function

$$h(u, w, U) := e_1 U - e_2 \left( 1 - \delta(w) \frac{w}{w_{max}} \right) u, \quad (7.22)$$

where

$$\int_{\Gamma} w \, d\sigma(x) \geq w_{max} > 0 \quad (7.23)$$

and

$$\delta(w) := \begin{cases} 1 & \text{if } w_{max} \geq w, \\ 0 & \text{else.} \end{cases} \quad (7.24)$$

To compute the formation of actin cable ends, we again assume a linear feedback on the active membrane-bound form  $u$  and set  $c(u) = v \cdot u$ . Similarly, the boundary conditions for the potential function linearly depend on  $w$  so that  $j(w) = b \cdot w$ .

To numerically simulate system (7.11)-(7.17) with functions (7.18)-(7.19) we calculate the non-dimensional parameters derived in this section. It is noteworthy that we have to adjust  $k_3$  and  $k_4$  to obtain polarity (see Table 7.1). This fact may arise from the simplifications done for the model reduction. For the non-dimensional kinetics given by equations (7.20)-(7.21) parameters are adapted from [72] (see Table 7.1). Since we assume equal diffusion constants on the surface, in both cases it holds that  $d_v = 1$ .

For the model derived in this work, we consider initial concentrations  $u_0 = 0.004$ ,  $v_0 = 0.196$ ,  $w_0 = 0.002$ ,  $U_0 = 1.504$  and  $V_0 = 0.9024$ . To compute the model proposed in [72], we choose  $u_0 = 0.002$ ,  $v_0 = 0.002$ ,  $w_0 = 0.01$ ,  $U_0 = 5.0994$  and  $V_0 = 0.05$ .

In all simulations we disturb the initial homogeneous state either by random noise or located stimuli. Therefore, we use expressions (6.16) and (6.17) with respective non-dimensional parameters.

### The cell shape influences transport-driven cell polarization

Although this thesis is mainly concerned with polarization in yeast cells, this pattern formation process is of particular importance for distinct cell types with different shapes. Furthermore, in many of these cells, active transport of molecules plays a significant role. For example, in the fission yeast, neurons, and the *Caenorhabditis elegans* zygote microtubules may mediate the transport of important regulators of cell polarization and in this way ensure its correct location [57, 80, 89].

In order to understand the influence of the cell shape on the polarization behavior, we start to simulate both systems for different three-dimensional model geometries. We employ a random signal to excite the cell from its uniform state. The results are shown in Figures 7.2-7.4. In all cases we obtain an enhanced peak of the non-dimensional concentration  $u$ , albeit the effect is much less intensive for the model proposed by RÄTZ AND RÖGER [72]. We further call this model the RR system.

For the model derived in this thesis, we see that transport-mediated polarization is much accelerated in cells that are non-spherical. In this case, the gradient increases or decreases with the length or broadness of the shape respectively. This is in contrast to the model derived in [72]. Starting with an initial random perturbation, in an elliptic or rod-shaped cell this system initially tends to form a central pattern so that the transport-mediated feedback anchors this spatial location. As a result, the process takes much more longer until it achieves the final pattern. From Figure 7.6 we see that, for a sufficiently strong transport feedback, this local anchoring may even be strong enough to maintain two transient peaks. It is shown that two equal stimuli initially generate two peaks at each end of the rod-shaped cell. Whereas without transport these two patches are not stable, in the presence of a sufficiently strong transport feedback, two stable peaks are obtained.

With regard to the polarity direction, for our model we obtain that transport may change the spatial location of the polarized patch. This becomes particularly obvious in Figure 7.5 which shows polarity in a cell that features a small bud. In this case, we excite the cell from its homogeneous state by a signal comprising of two stimuli  $S_1$  and  $S_2$  of the same intensity. The signals are imposed on opposite sides of the cell surface, one located at the protrusion. Depending on whether we incorporate transport or not, this excitation leads to different patterns. Whereas the implementation of active movement promotes the formation of a peak at the bud, without

consideration of an active transport mechanism,  $u$  clusters at the opposite side. The influence of protrusions on diffusion-driven polarization in a cell has already been studied in [31]. Their results have shown that protrusions locally limit molecule aggregations. Diffusive transport into the protrusion is slightly hindered so that the cytosolic concentration decreases faster in this region. As a result, the cluster emerges at another location. Interestingly, our results demonstrate that for sufficiently high rates of active molecule transport, this kind of 'bottle neck' can be negotiated. As a result, the cluster forms at the protrusion. However, how far molecule delivery influences cluster formation depends on the interplay between transport and reaction kinetics. For instance, even in the presence of active molecule transport, the RR system generates a patch at the opposed side of the protrusion.

Another aspect are parameter choices. As already demonstrated in Chapter 6.3, depending on the rates and feedback strength, the transport process presented in this thesis can either enhance or disturb polarity. In some cases, this feedback may perturb the system so strongly that it is no longer capable of polarization. This is shown in Figure 7.1. For a reduced rate of the transport gradient control rate  $b$ , the RR system fail to form a polarized patch.

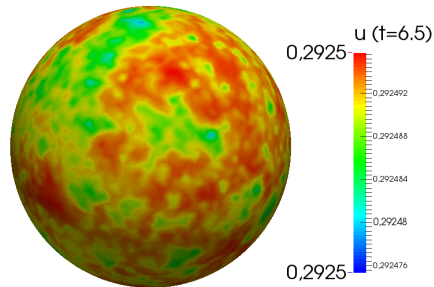


**Figure 7.1.: Illustration of a cell that fails to polarize due to transport.** A simulation of the system derived in [72] including transport with reduced feedback, i.e.  $\mathbf{b} = \mathbf{5}$ , is shown. The endocytic rate is so low that the cell tends to form a homogeneous state.

### The influence of internal components on cell polarization

Cells contain many different cell components of distinct shape and size like for instance the nucleus, the Golgi, or the endoplasmic reticulum. All these structures serve as a kind of diffusion and transport barrier within the cell. In this way, the spatial position of organelles can influence signaling pathways, including the accumulation of polarization molecules.

How internal barriers control diffusion-driven cell polarization has already been investigated in [31]. The results have demonstrated that the cluster formation close to organelles is very unlikely. Diffusion-driven polarization mostly occurred in the neighborhood of large organelles, but not behind them. The local accumulation of substances at the opposite side of protrusions or in regions with low curvature is more likely [31].



Model	Param.	Value	Description
This work	$d_v$	1.0	diffusion coefficient of the inactive membrane-bound species
	$d_w$	27.78	diffusion coefficient of the actin cables
	$D_v$	305.5	diffusion coefficient of the cytosolic component
	$D_u$	0.278	diffusion coefficient of the internal component
	$\gamma$	15.6	spatial scale factor
	$k_1$	0.056	basal activation rate
	$k_2$	27.78	basal inactivation rate
	$k_3$	0.025	basal membrane attachment rate
	$k_4$	13.89	basal membrane detachment rate
	$k_5$	10.77	feedback-mediated membrane attachment rate
	$a_1$	19.41	GEF-mediated activation rate
	$a_2$	59.42	GEF-mediated feedback activation
	$a_3$	2.23	negative feedback/ inactivation rate
	$w_{max}$	0.0163	rate controlling local endocytosis
	$e_1$	0.703	rate of exocytosis
	$e_2$	8.33	rate of endocytosis
	$b$	27.78	transport gradient control rate
	$v$	1.53	capacity function control rate
	$\alpha$	419.94	potential flow control rate
	$u_0$	0.004	initial concentration of the active membrane-bound species
$v_0$	0.196	initial concentration of the inactive membrane-bound species	
$w_0$	0.002	initial concentration of the actin cable density	
$U_0$	1.504	initial concentration of the internal component	
$V_0$	0.902	initial concentration of the cytosolic component	
Rätz & Röger [72]	$d_v$	1.0	diffusion coefficient of the inactive membrane-bound species
	$d_w$	1.0	diffusion coefficient of the actin cables
	$D_v$	100	diffusion coefficient of the cytosolic component
	$D_u$	0.01	diffusion coefficient of the internal component
	$\gamma$	400	spatial scale factor
	$a_1$	0.02	rate regulating activation
	$a_2$	20	rate regulating activation
	$a_3$	160	feedback activation rate
	$a_4$	1	control rate for inactivation
	$a_5$	0.5	control rate for inactivation
	$a_6$	0.36	rate regulating membrane attachment
	$a_{-6}$	5	rate regulating membrane detachment
	$w_{max}$	0.02	rate controlling local endocytosis
	$e_1$	0.1	rate of exocytosis
	$e_2$	0.2	rate of endocytosis
	$b$	25.5	transport gradient control rate
	$v$	5.1	capacity function control rate
	$\alpha$	0.4	potential flow control rate
	$u_0$	0.002	initial concentration of the active membrane-bound species
	$v_0$	0.002	initial concentration of the inactive membrane-bound species
$w_0$	0.01	initial concentration of the actin cable density	
$U_0$	5.099	initial concentration of the internal component	
$V_0$	0.05	initial concentration of the cytosolic component	

**Table 7.1.: Overview over parameters used for computations of the generic system.** Variables and constants used for numerical simulations of the non-dimensionalized system (7.11)-(7.17) considering reaction kinetics derived in this work as well as using the functions proposed by RÄTZ AND RÖGER [72] are shown.

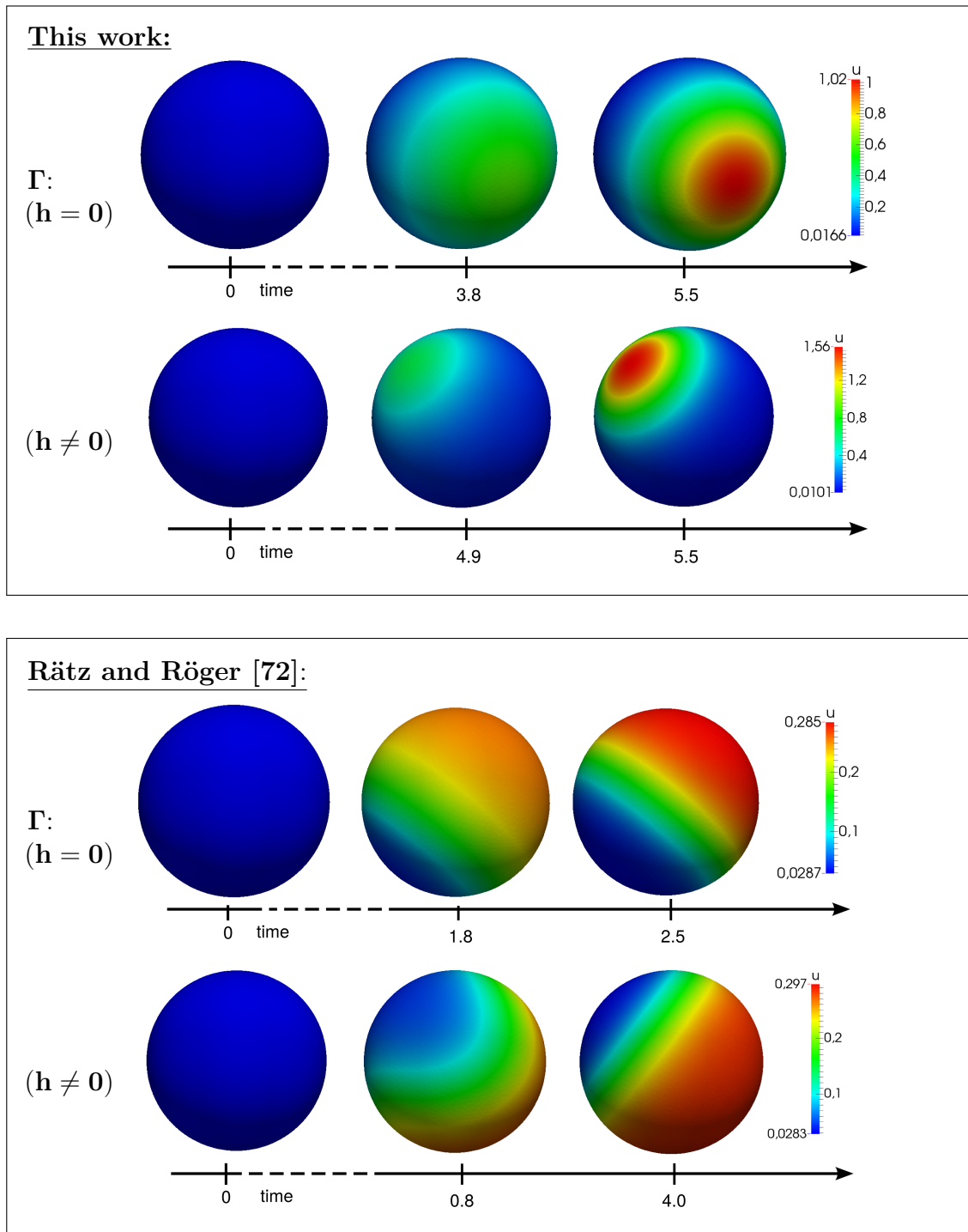


**Figure 7.2.:** Numerical simulations of the generic system using distinct kinetic functions applied to a sphere. Simulations of the model derived in this thesis and of the RR system are shown. Solutions of both models with and without an impact of the proposed active molecule transport are illustrated. A spatial noise signal applied to the initial uniform state  $u_0$  results in both cases in cluster formation. The polarization process in time is shown.

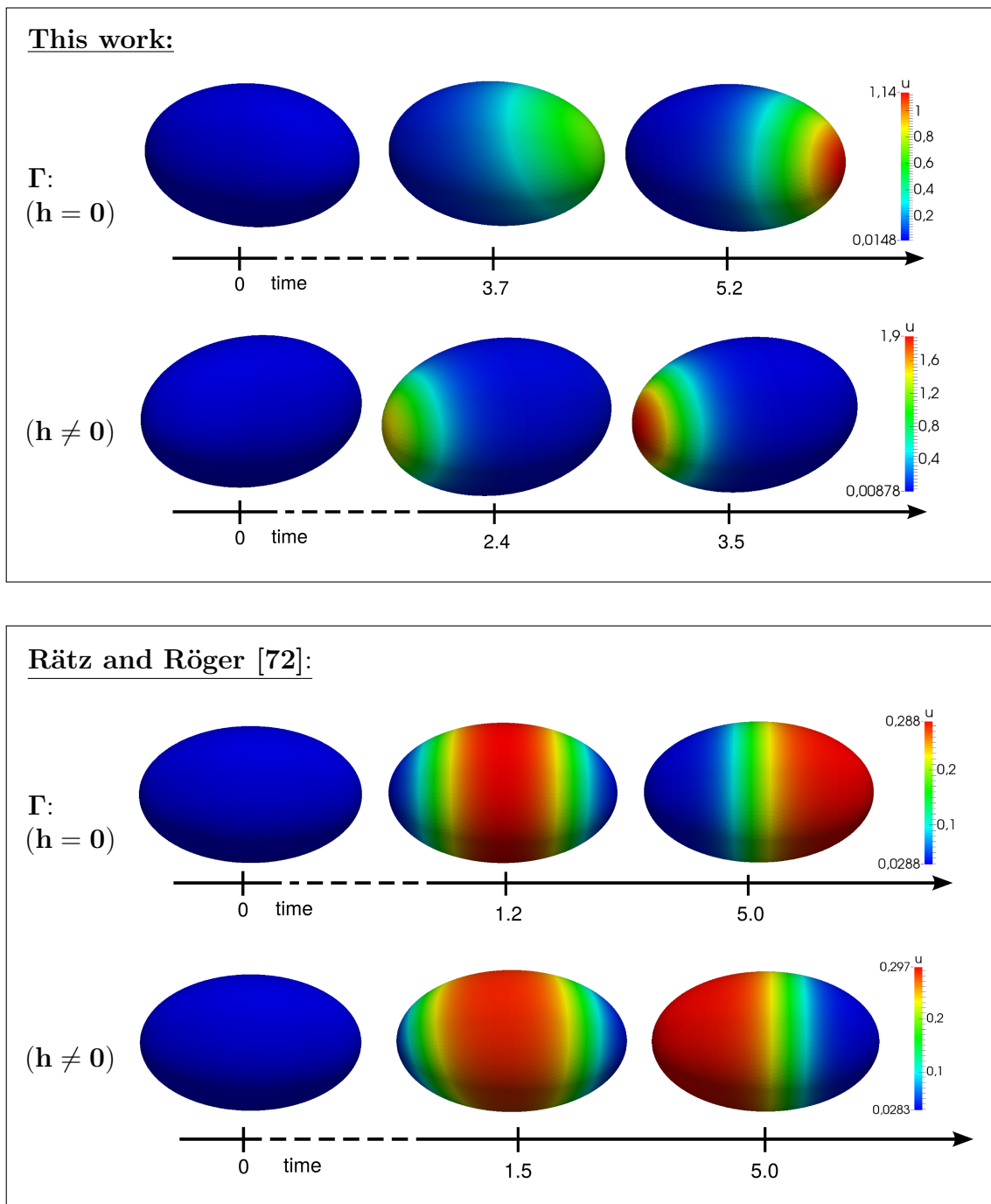


**Figure 7.3.:** Numerical simulations of the generic system using distinct kinetic functions applied to an ellipse. Comparison of pattern formation with and without the proposed transport mechanism. Simulations of the system derived in this work and in [72] are shown. Excitation of the initial homogeneous state  $u_0$  by a spatial noise signal induces pattern formation.

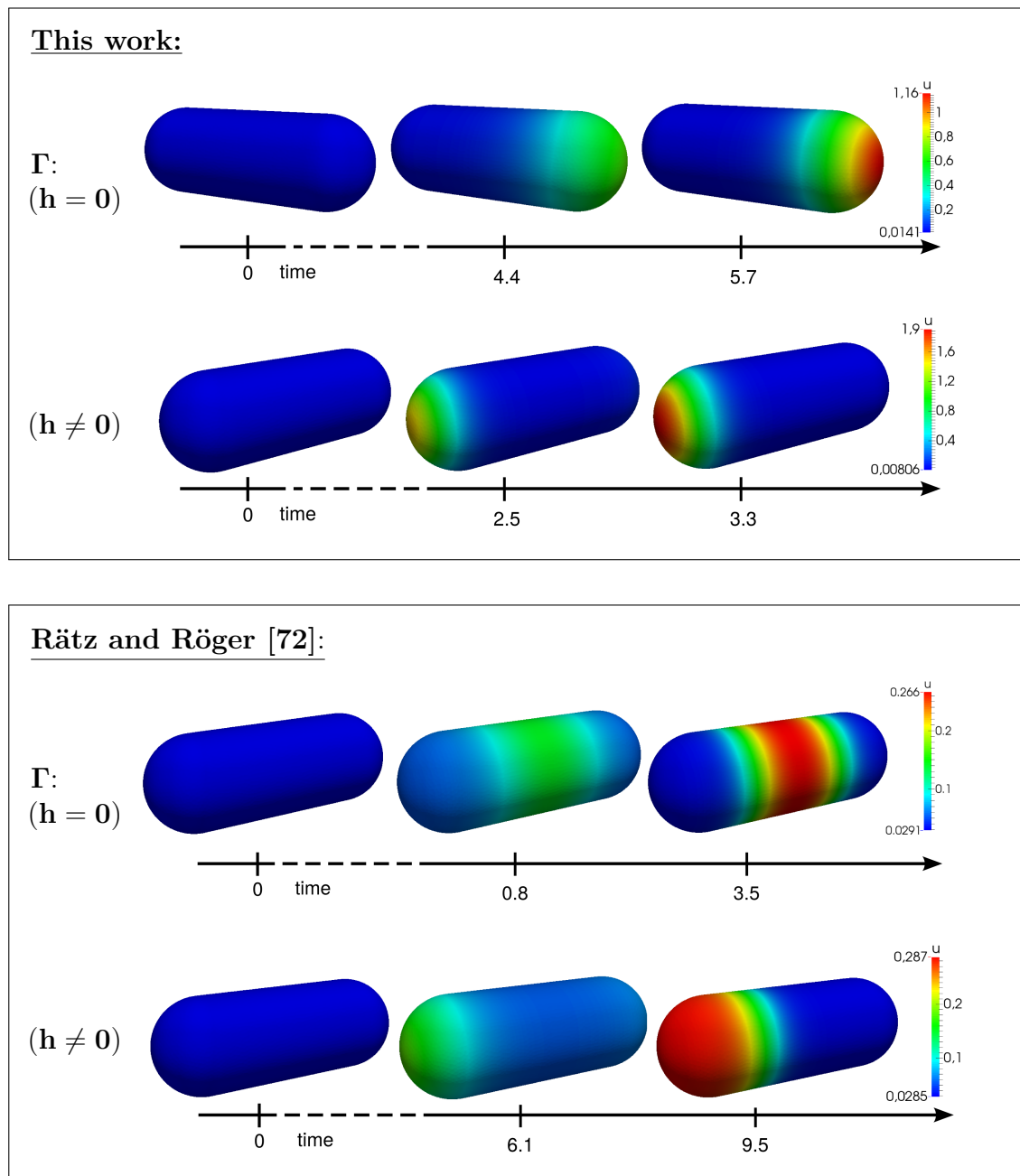


**Figure 7.4.:** Numerical simulations of the generic system using distinct kinetic functions applied to a rod-shaped cell. Cell polarization with and without the proposed transport mechanism are visualized. A spatial noise signal applied to the initial uniform state  $u_0$  leads to polarization. Simulations are shown for the model presented in this work as well as for the RR system.

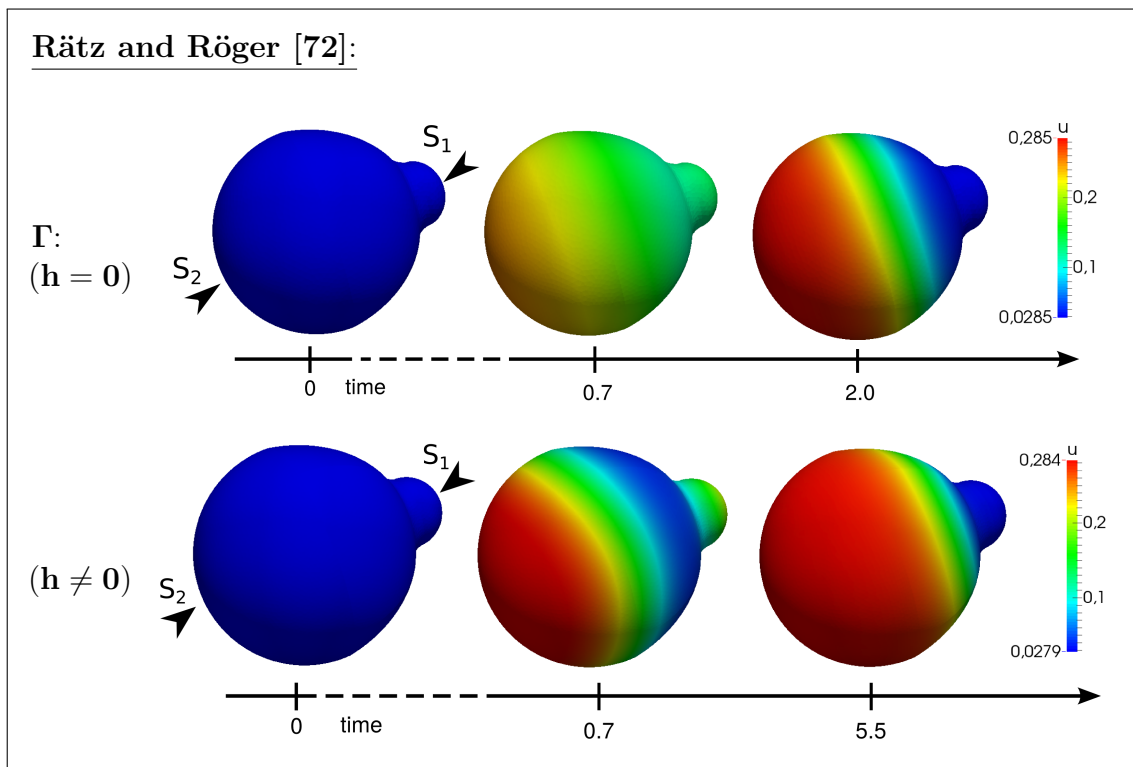
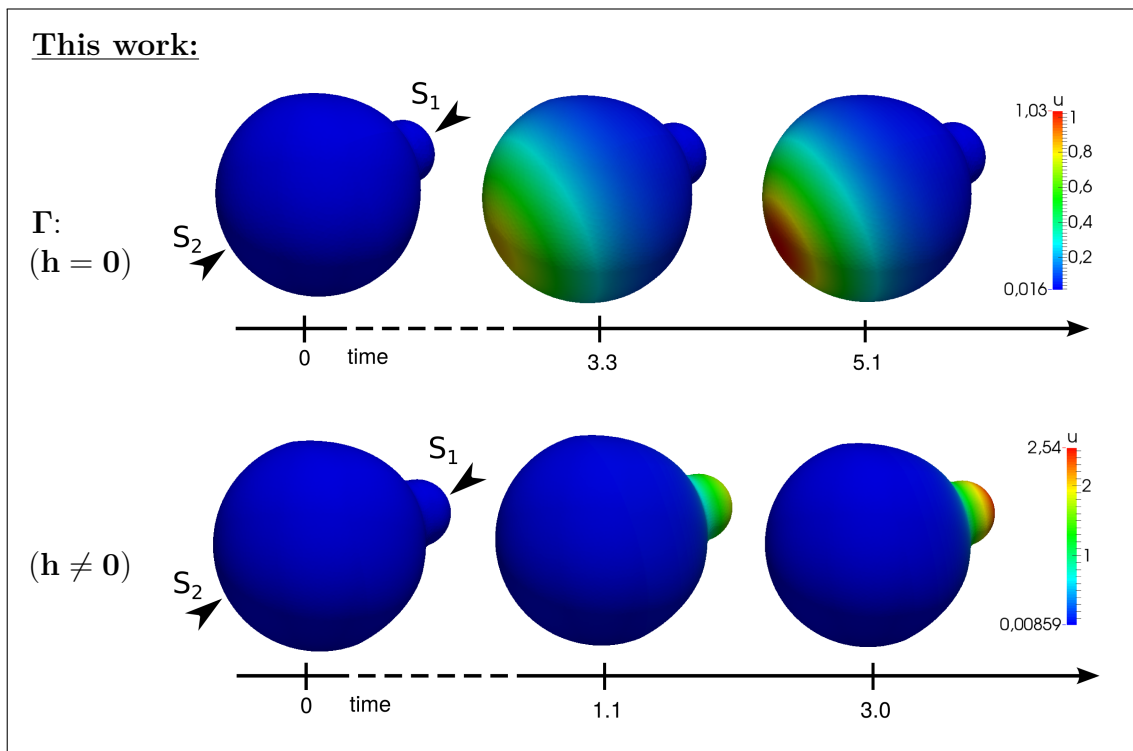


**Figure 7.5.:** Numerical simulations of the generic system using distinct kinetic functions applied to a cell with a protrusion. Comparison of pattern formation with and without the proposed transport mechanism. Simulations are shown for our system and the RR system. Both models are excited for  $\Delta t = 0.69$  with two equal stimuli with  $s_1 = 0.1$  and  $s_2 = 0.001$  respectively.

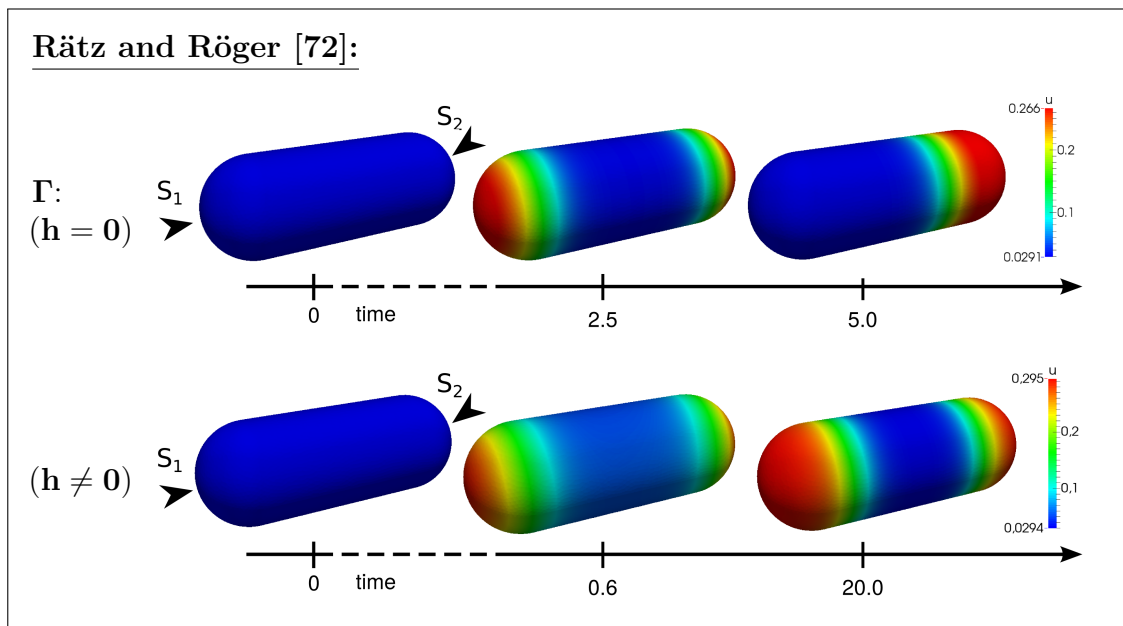


**Figure 7.6.:** Comparison of the impact of transport on cell polarity in a rod-shaped cell. Simulations are shown for the model derived in [72] with and without the proposed transport mechanism. The cell is exposed to two equal stimuli  $S_1$  and  $S_2$  located at both ends for  $\Delta t = 0.69$ . For a sufficiently strong transport feedback ( $e_2 = 2, w_{max} = 0.025$ ), the pattern is characterized by two stable peaks.

In order to investigate whether active transport alters the results, we perform similar computational experiments. We consider the two-dimensional case, where the cell is characterized by a circle. Organelles are modeled by elliptic or circular shapes placed in the cell interior. The results are shown in Figure 7.8. Again, we excite the cell from its homogeneous state by a signal comprising two stimuli  $S_1$  and  $S_2$  of the same intensity. Whereas one signal is located near the organelles, the other is placed at the opposite side.

Without consideration of transport effects, we obtain similar results as presented in [31]. The organelles near the surface negatively affect cluster formation at this site. Contrarily, we see that under consideration of active molecule transport, the polar cluster forms behind the internal component. In this case, organelles support a nearby spatial location of the polarity patch.

As mentioned before, protrusions positively influence transport-mediated polarization too. This raises the question of how polarity behaves in cells exhibiting both a complex shape and internal barriers. Figure 7.9 illustrates this interplay. It becomes clear that since protrusions as well as diffusion barriers can promote polarization, the localization of organelles next to protrusions strongly enhances polarity. Conversely, we see that an opposed position leads to a competing situation. As long as the

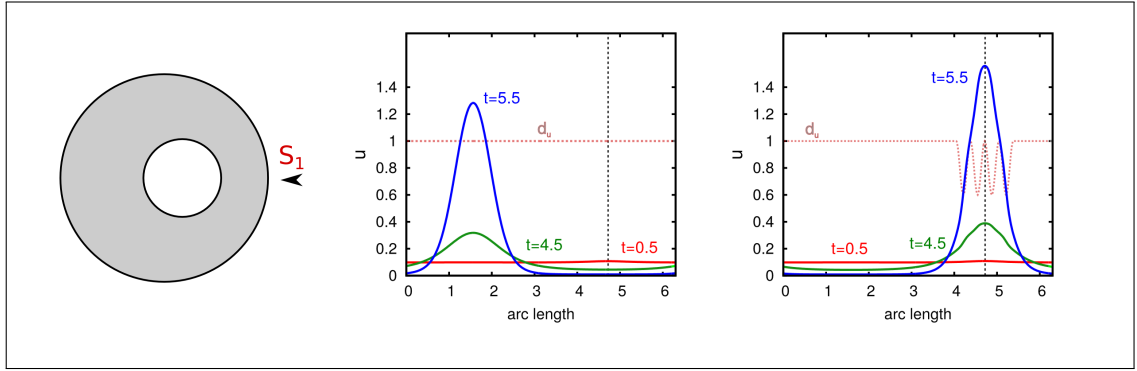


**Figure 7.7.: Computational results showing the influence of non-uniform membrane diffusion on trafficking-mediated cell polarity.** The cell, whose geometry is shown in the left figure, is excited with a local transient stimulus  $S_1$  of strength  $s_1 = 0.2$  for  $\Delta t = 0.69$ . The parameters are chosen as follows:  $a = 4$ ,  $\eta = 0.3$ ,  $w = 0.66$ . The middle image illustrates how a reduced transport feedback ( $b = 0.1$ ) negatively influences polarity. The right diagram demonstrates how non-uniform diffusion ensures sustained polarization.

organelle is sufficiently far away from the surface and centrally located, the cluster still forms at the bud. In contrast, when the organelle is placed near the membrane, but opposed to the protrusion, we obtain polarization behind the organelle. Only a very strong stimulus at the protrusion reverses the outcome. This is demonstrated by the last computational experiment illustrated in Figure 7.9, where the cell is excited at the bud tip with a signal  $S_1$  of strength  $s_1 = 0.33$ .

### The influence of inhomogeneous diffusion

We already mentioned that during cell polarization, the polar cap of budding yeast cells is characterized by microdomains. Here, regions determined by fast diffusing molecules alternate with locations showing slower diffusion. It has been suggested that these membrane microdomains, which also imply co-located exocytosis and endocytosis, play a critical role in vesicular trafficking-mediated cell polarity by temporally sustaining cell polarization [83].

In order to analyze the influence of non-uniform diffusion on transport-mediated polarity, for  $u$  we introduce the spatially inhomogeneous diffusion coefficient

$$d_u(x) = \begin{cases} d_u - \eta(1 - \cos(a \cdot s(\vec{x}) \cdot \pi)), & \text{if } \text{dist}(\vec{x}_{S_1}, \vec{x}) < w, \\ d_u, & \text{otherwise.} \end{cases} \quad (7.25)$$

Here,  $s(\vec{x})$  denotes the arc length measured from  $\vec{x}_{S_1}$  to  $\vec{x}$  multiplied by 1 or  $-1$ , depending on their positional relation. The parameter  $a$  denotes an arbitrary amplitude and  $\eta \leq d_u$  describes a scale factor that determines the maximal reduction

of diffusion. The value of  $w$  serves to define a certain region with inhomogeneous diffusion.

In Figure 7.7 computational results of the generic system with and without inhomogeneous diffusion under consideration of a strongly decreased transport feedback are compared. It can be seen that a 10 times reduced transport feedback leads to a significant decrease in the local concentration of  $u$ . Furthermore, in this case diffusion-driven polarity dominates the system so that a local transient stimulus in the neighborhood of an organelle results in a peak at the opposing side. In addition, we obtain that the local cluster induced by a transient stimulus can not only be sustained but also be enhanced by non-uniform diffusion of the active membrane-bound component. These results make clear that membrane microdomains may not only play an important role in sustaining polarization but also in spatially directing cluster formation.



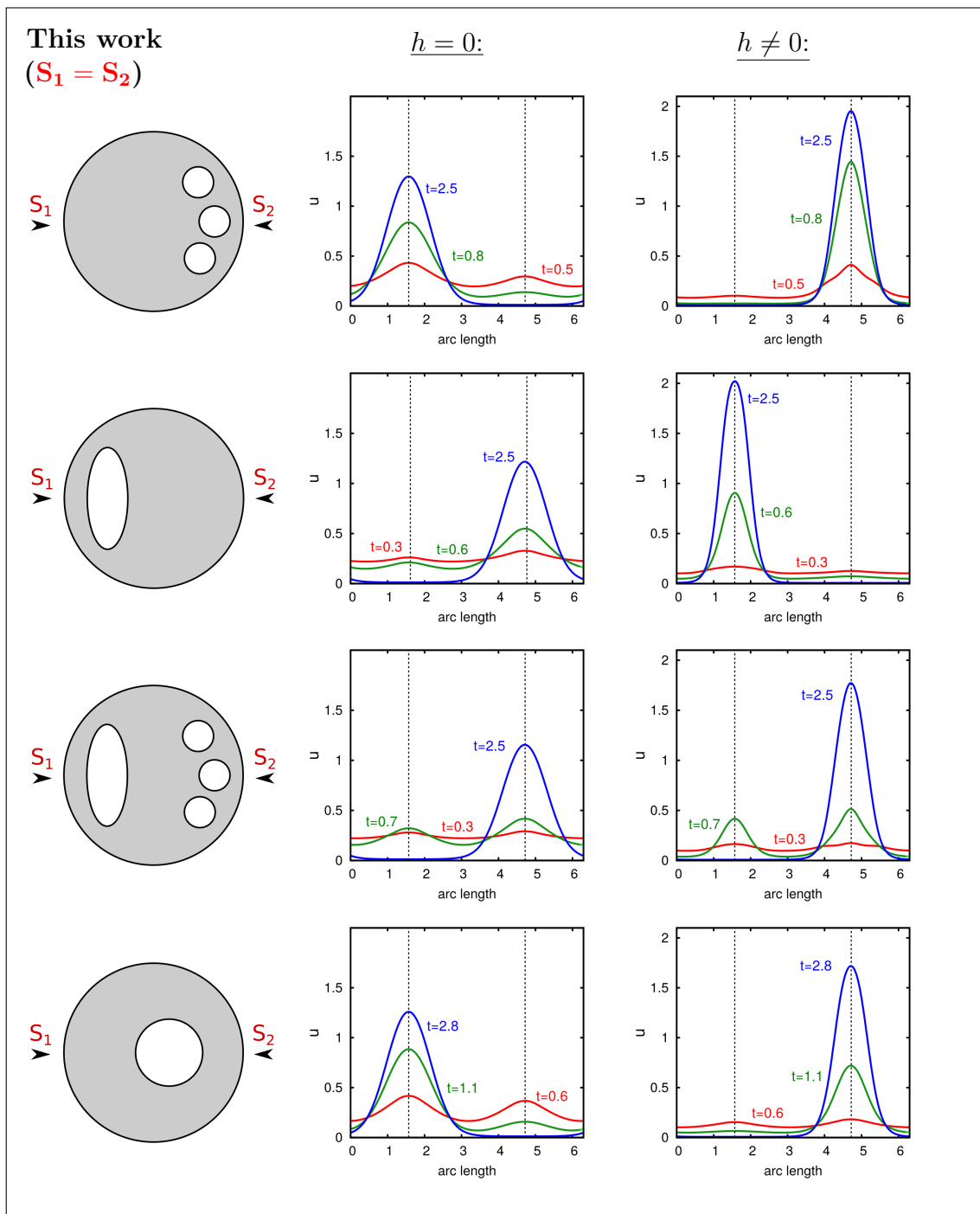


**Figure 7.8.: Illustration of the influence of internal barriers on cell polarization.** Computational results of our non-dimensional model with and without transport are presented. Organelles which are represented by circles or ellipses are placed at distinct positions in the cell. Computations with two equal stimuli exciting the initial uniform state  $u_0$  with  $s_1 = s_2 = 0.2$  for  $\Delta t = 0.69$  are shown.

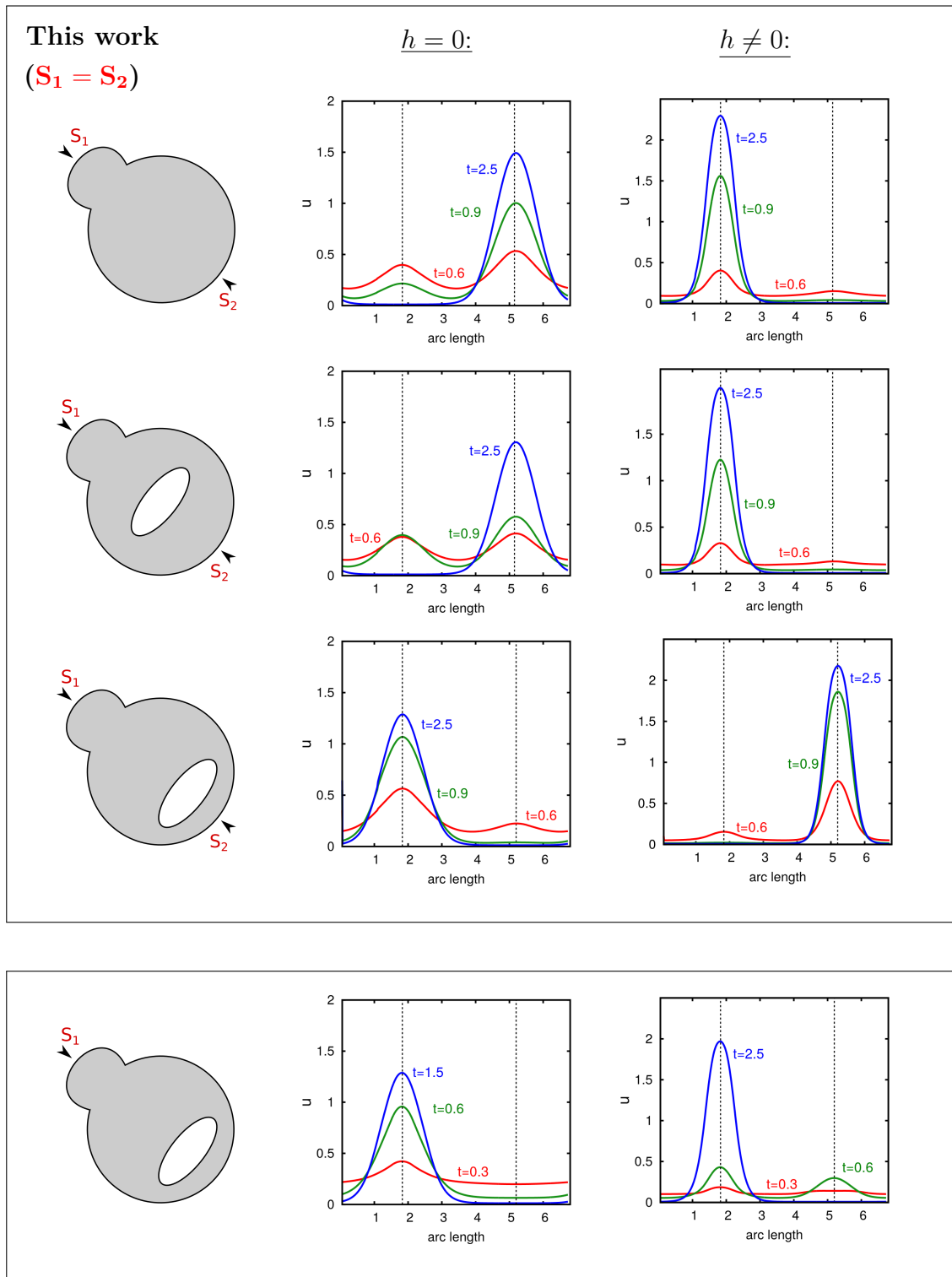


**Figure 7.9.: Comparison of the influence of organelles as well as the cell shape on diffusion- and transport-mediated polarization.** Numerical simulations of our non-dimensional model with and without transport are presented. A large organelle which is represented by an ellipse is placed at distinct positions in a cell exhibiting a small protrusion. Simulations with two equal stimuli exciting the initial uniform state  $u_0$  with  $s_1 = s_2 = 0.2$  for  $\Delta t = 0.69$  are illustrated. Cluster formation either occurs behind the organelle or, if the barrier is sufficiently far away from the surface, at the protrusion. Only a high stimulus  $s_1 = 0.33$  can reverse this feature (bottom computation).

### 7.3.2. Applications of models from the literature

In the following, we simulate the generic system using well known reaction kinetics from literature [32, 61]. Note that these models are usually based on a single active-inactive pair.

#### The Wave-Pinning model:

In Chapter 3.6 we introduced the Wave-Pinning model which is based on only one active membrane-bound form ( $u$ ) and one inactive cytosolic state ( $V$ ) of the GTPase. It uses the bilinear function

$$f_{\text{WP}}(u, V) := V \left( k_0 + \frac{\gamma u^2}{K^2 + u^2} \right) - \delta u$$

to describe the kinetic mechanisms of activation and inactivation as an exchange between the plasma membrane and the cytosol. We considered this model to exemplify a coupled bulk-surface system. In the course of this introduction, we have already shown pattern formation for the reaction-diffusion system.

#### The Goryachev model:

We already mentioned that a system of eight reaction-diffusion equations presented in [32] lay the foundation for many following models for cell polarization. The approach introduced there simulates kinetics between the GTPase Cdc42 and its GEF Cdc24 to analyze polarization in yeast cells. Based on this complex system, the authors finally deduced a two component model. This describes the interplay between an active membrane-bound substance ( $u$ ) and an inactive cytosolic state ( $V$ ) by the kinetic function

$$f_{\text{GOR}}(u, V) := \alpha E_c u^2 V + \beta E_c u V - \gamma u,$$

$$E_c = \frac{E_c^0}{1 + \int_{\Omega} g(u) dA}.$$

Note that the functions  $f_{\text{WP}}$  and  $f_{\text{GOR}}$  are given in its dimensional form. Thus, to investigate both approaches for transport-mediated polarity, consider the minimal system

$$\partial_t u = d_u \Delta_{\Gamma} u + f(u, V) + h(u, w, U) \quad \text{on } \Gamma \times I, \quad (7.26)$$

$$\partial_t w = d_w \Delta_{\Gamma} (w \cdot c(u)^{-1}) \quad \text{on } \Gamma \times I, \quad (7.27)$$

$$\partial_t U = D_u \Delta U - \nabla \cdot (\vec{v} U) \quad \text{in } \Omega \times I, \quad (7.28)$$

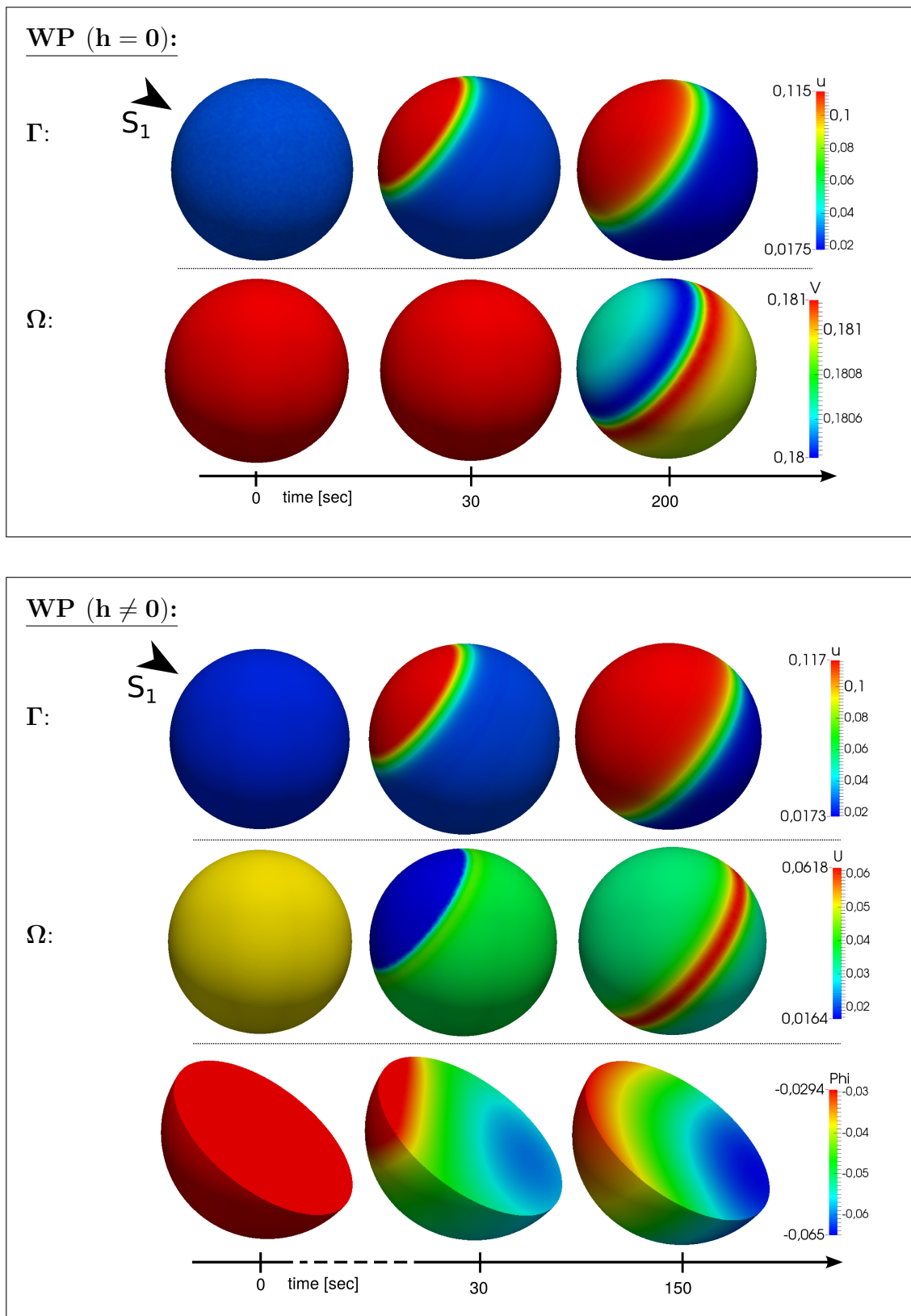


**Figure 7.10.:** Numerical simulations of the WP system. Computational results of the WP system applied to a sphere with radius  $3\mu\text{m}$  are illustrated. Calculations are shown for the model with and without consideration of active molecule transport. A transient spatial perturbation represented by a local stimulus  $s_1 = 0.03\mu\text{m}/\text{s}$  leads to polarization.

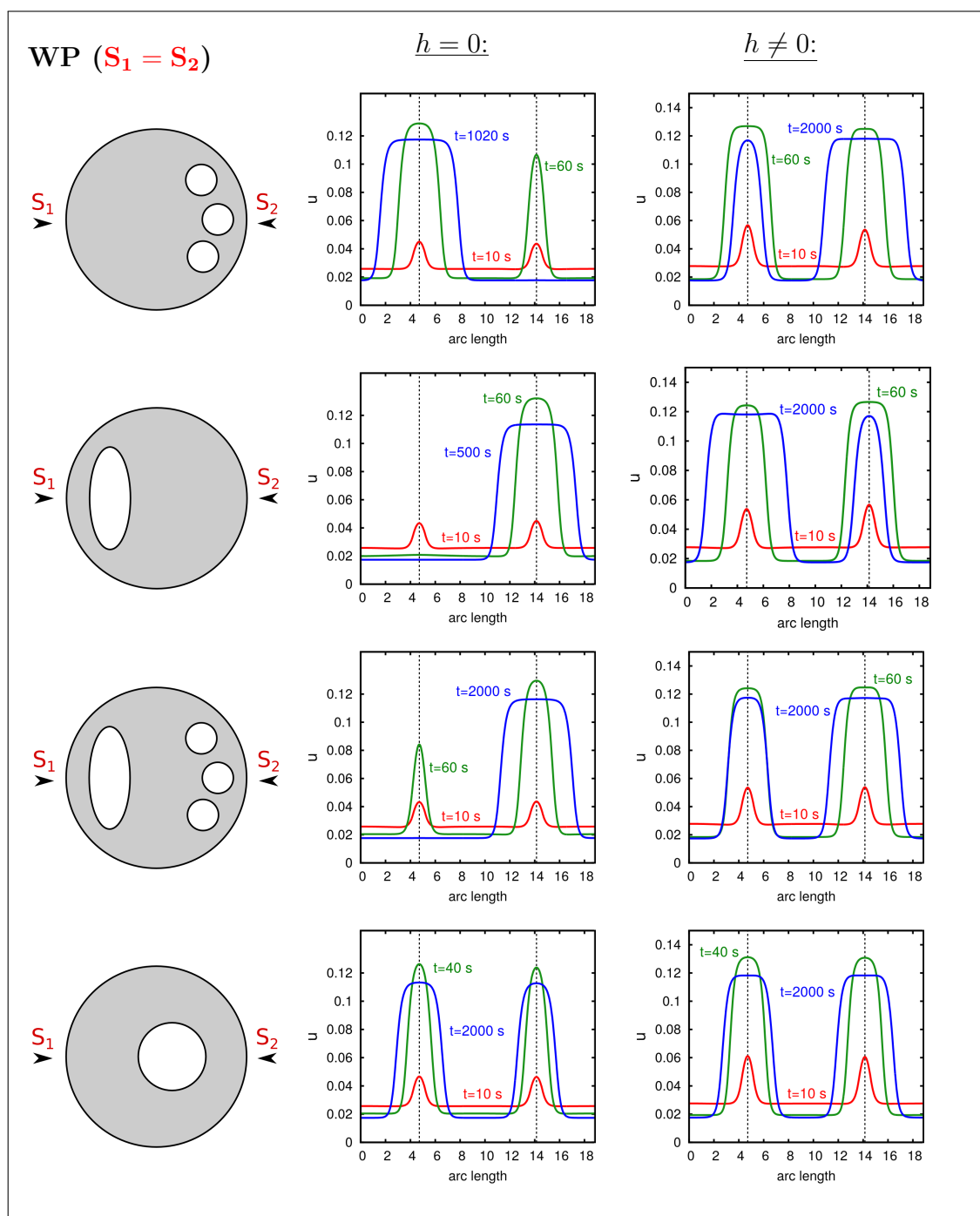


**Figure 7.11.:** Comparison of the influence of internal barriers on diffusion- and transport-mediated polarization calculated with the WP system. Circles and ellipses are placed at different positions in the cell to represent organelles that serve as transport barriers. Depending on the localization of organelles, two equal stimuli  $s_1 = s_2 = 0.01 \mu\text{m}/\text{s}$  for  $\Delta t = 10\text{s}$  lead to different patterns.

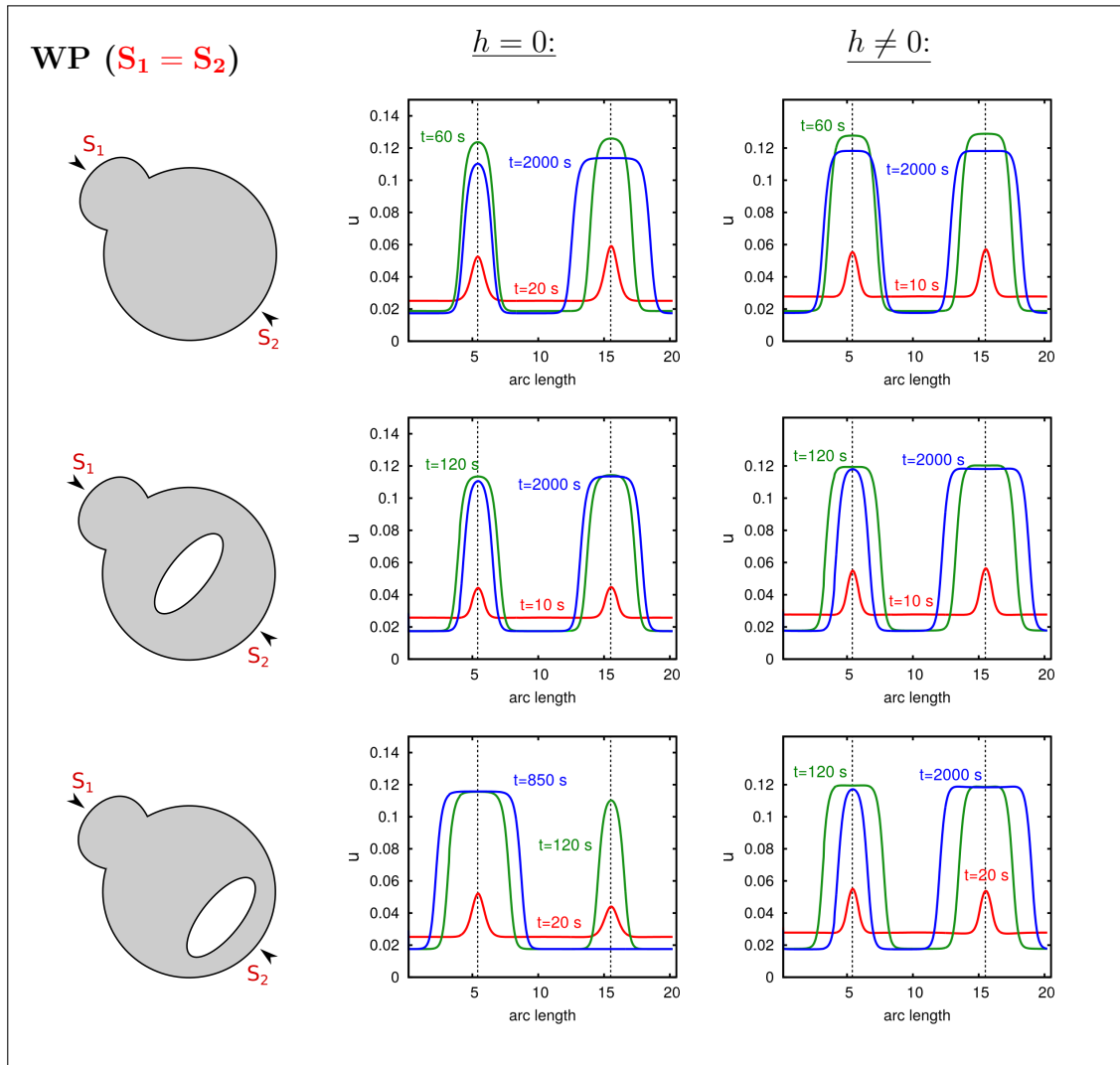


**Figure 7.12.:** Investigation of the influence of internal barriers and the cell shape on diffusion- and transport-mediated polarization calculated with the WP system. Computational results computed for the WP system with and without transport are shown. An ellipse represents an organelle in a cell with a protrusion. Two equal stimuli  $s_1 = s_2 = 0.01 \mu\text{m}/\text{s}$  are applied at the bud and its opposite side for  $\Delta t = 10\text{s}$ . Depending on the position of the internal barrier, peaks with distinct shapes are obtained.

Model	Parameter	Value	Unit	Description
GOR & WP	$f(u, V)$		$\mu m \mu M / s$	flux density between the membrane and cytosol
	$h(u, w, U)$		$\mu m \mu M / s$	flux density defined by transport mechanisms
	$w_0$	0.01	$\mu m \mu M$	initial concentration/ density of actin cables
	$V_0$	0.05	$\mu M$	initial concentration of the inactive cytosolic species
	$d_u$	0.015	$\mu^2 m / s$	diffusion coefficient of the membrane-bound species
	$d_w$	1.0	$\mu m^2 / s$	diffusion coefficient of the actin cables
	$D_u$	3.0	$\mu m^2 / s$	diffusion coefficient of the cytosolic species
	$D_v$	0.01	$\mu m^2 / s$	diffusion coefficient of the internal species
	$e_1$	0.1	$\mu m / s$	exocytic rate
	$e_2$	0.3	$1 / s$	endocytic rate
	$b$	0.3	$\mu^2 m / s$	transport gradient control rate
$v$	1.0	$\mu m \mu M$	control rate for capacity function	
WP	$u_0$	0.026	$\mu m \mu M$	initial concentration of the membrane-bound species
	$U_0$	0.2	$\mu M$	initial concentration of the internal component
	$k_0$	0.067	$\mu m / s$	basal activation rate
	$\delta$	1.0	$1 / s$	basal inactivation rate
	$\gamma$	1.0	$\mu m / s$	maximal rate of auto-activation of $u$
	$K$	0.1	$\mu m \mu M$	concentration of $u$ resulting in half-maximal rate of auto-activation
	$w_{max}$	0.03	$\mu m \mu M$	rate regulating local endocytosis
GOR	$u_0$	0.054	$\mu m \mu M$	initial concentration of the membrane-bound species
	$U_0$	0.2	$\mu M$	initial concentration of the internal component
	$\alpha$	3.3	$\mu m^{-1} \mu M^{-2} s^{-1}$	positive feedback activation
	$\beta$	0.67	$\mu M^{-2} s^{-1}$	noncooperative membrane binding
	$\gamma$	0.017	$1 / s$	basal membrane detachment rate
	$E_c$	0.1	-	membrane-bound GEF complex
	$w_{max}$	0.02	$\mu m \mu M$	rate regulating local endocytosis

**Table 7.2.: Parameters used for numerical simulations of the WP and GOR system.** Parameters related to the transport scheme are estimated to show properties of actin-mediated cell polarization.

$$\partial_t V = D_v \Delta V \quad \text{in } \Omega \times I, \quad (7.29)$$

with coupling boundary conditions

$$-(D_u \nabla U - \vec{v} U) \cdot \vec{n} = h(u, w, U) \quad \text{on } \Gamma \times I, \quad (7.30)$$

$$-D_v \nabla V \cdot \vec{n} = f(u, V) \quad \text{on } \Gamma \times I, \quad (7.31)$$

and initial conditions at time  $t = 0$

$$U(\cdot, 0) = U_0, \quad V(\cdot, 0) = V_0, \quad u(\cdot, 0) = u_0, \quad w(\cdot, 0) = w_0,$$

$$U_0, V_0 : \Omega \rightarrow \mathbb{R}, \quad u_0, w_0 : \Gamma \rightarrow \mathbb{R}.$$

Here,  $f$  is either replaced by  $f_{WP}$  or  $f_{GOR}$ . Note that these functions involve measured units. For  $h$  we choose again (7.22), albeit in its dimensional formula. In all computational simulations we use parameters given by Table 7.2.

The numerical simulations of (7.26)-(7.31) considering the WP and GOR kinetic functions are very similar to those shown by the non-dimensionalized system pre-

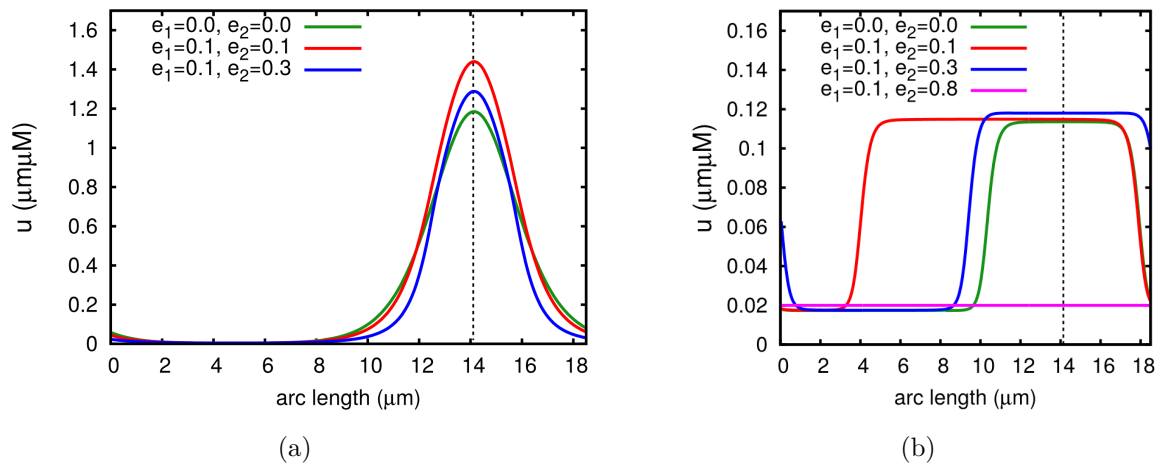


**Figure 7.13.: Computational results of the GOR and WP system using distinct rates of endocytosis.** (a) Related to the WP system the rate of endocytosis determines the width of the polarized patch. (b) The endocytic rate determines the intensity of the polarized patch resulting from the GOR system.

sented in this thesis as well as the enhanced system of RÄTZ AND RÖGER [72]. From Figure 7.10 and 7.14 we obtain that active molecule transport implemented with parameters given by Table 7.2 induces an accelerated and increased polarization process.

Interestingly, whereas for the GOR system we see a raised maximal molecule number within the cap, active molecule transport rather broadens the polar cluster resulting from the WP mechanism (see Figure 7.13).

For numerical experiments with different cell types containing internal barriers, we see again that organelles and the cell shape strongly influences the spatial organisation. But there are small differences between the results calculated by our or the GOR model and those computed with the kinetics of the WP system. For the latter, the double-sides stimulation of a cell containing an organelle that is nearly centrally arranged leads to the development of two stable peaks. Equally, in a cell exhibiting a small protrusion active molecule transport promotes the formation of two longer lasting peaks. Without this mechanism the cluster at the protrusion reduces over time until it finally disappears.



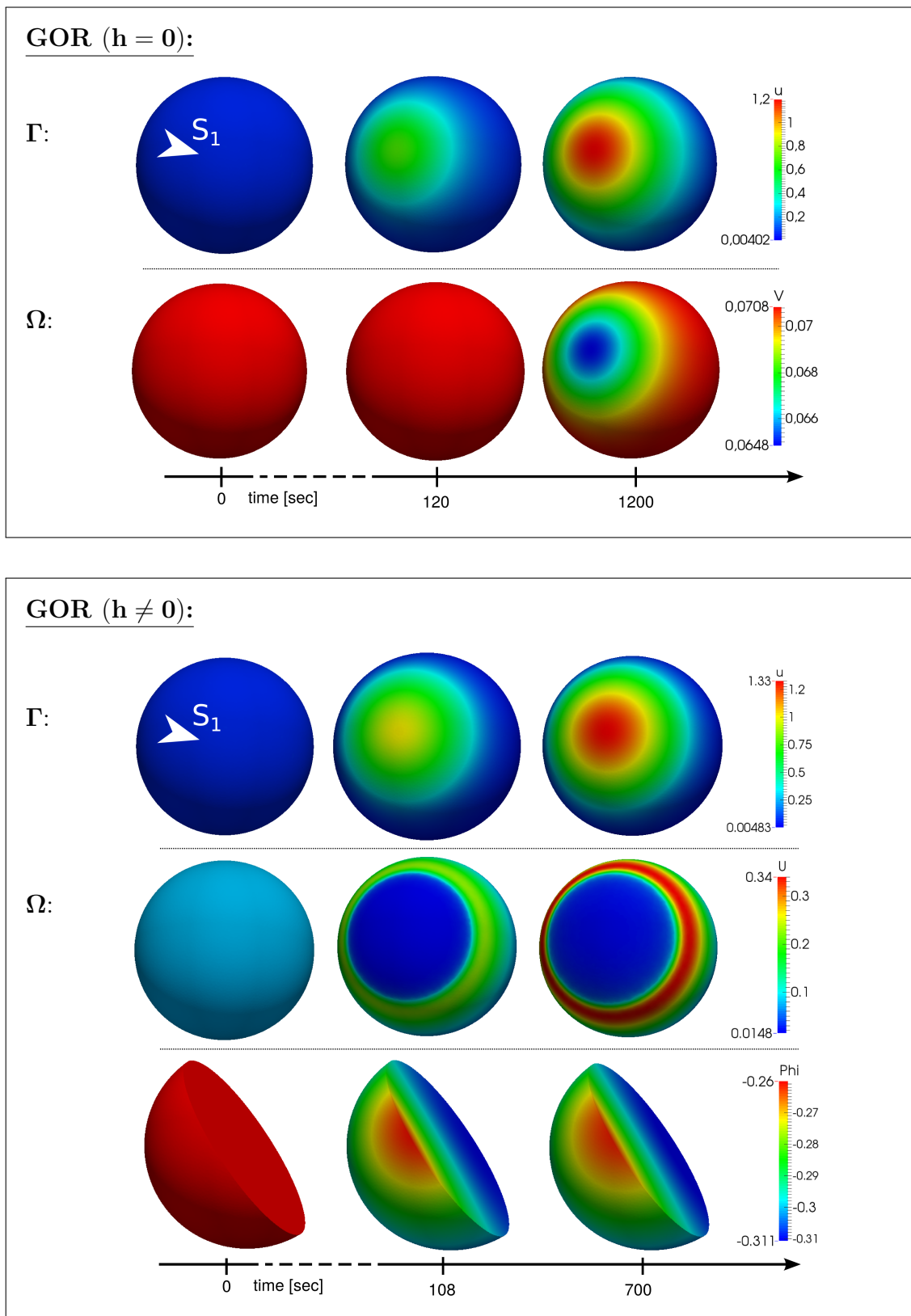


**Figure 7.14.: Computational results of the GOR system applied to a sphere.** Numerical simulations of the GOR system with and without the derived transport feedback are shown. The cell is characterized by a sphere with radius  $3\mu\text{m}$ . A spatial perturbation represented by a local stimulus  $s_1 = 0.03\mu\text{m}/\text{s}$  for  $\Delta t = 100\text{s}$  induces cluster formation of  $u$ .

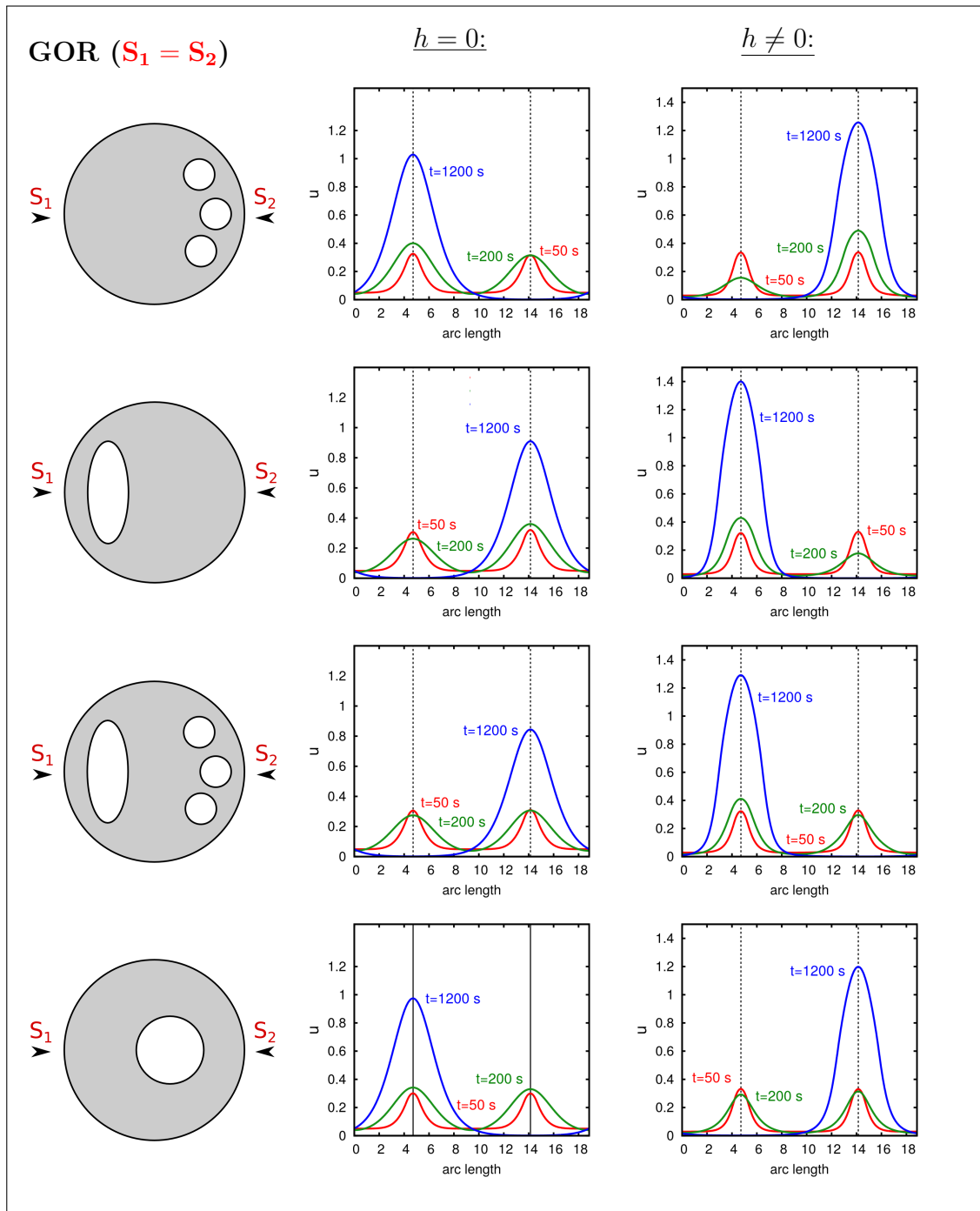


**Figure 7.15.: Computational results of the GOR system considering distinct diffusion barriers.** To investigate the influence of internal barriers on diffusion- and transport-mediated polarization, numerical simulations of the GOR system using distinct geometries are compared. Circles and ellipses are placed at distinct positions in the cell to model organelles that serve as transport barriers. Two equal stimuli  $S_1$  and  $S_2$  with  $s_1 = s_2 = 0.03 \mu\text{m}/\text{s}$  are imposed for  $\Delta t = 100\text{s}$  behind the organelle and at its opposite side.

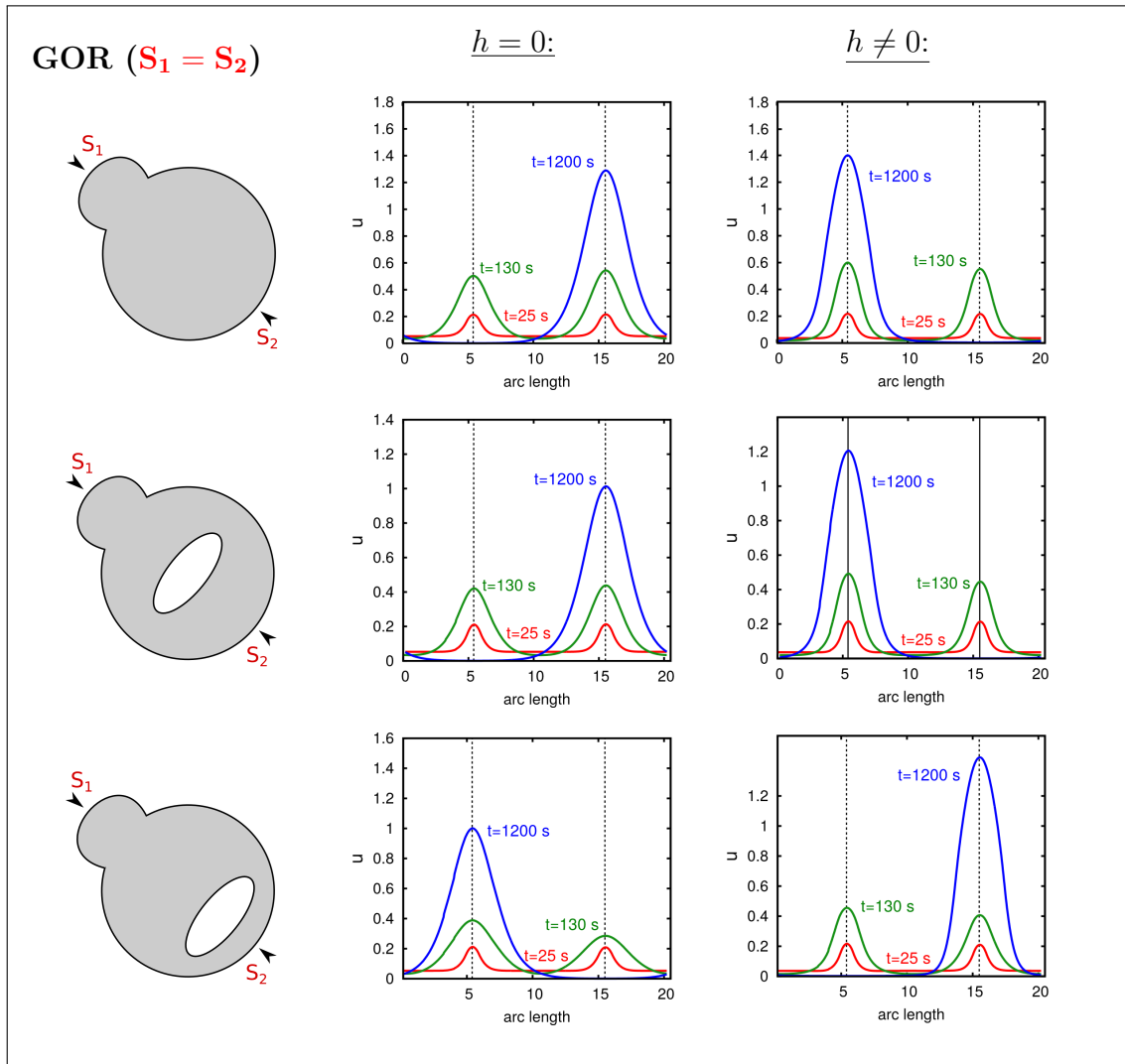


**Figure 7.16.: Investigation of the GOR system for the influence of internal barriers and cell shape on polarization.** Simulations of the GOR system without and with the derived transport mechanism using a cell with protrusion are illustrated. An ellipse is placed at different positions to reflect an internal barrier. Two equal stimuli  $S_1$  and  $S_2$  with  $s_1 = s_2 = 0.03 \mu\text{m}/\text{s}$  are imposed for  $\Delta t = 100\text{s}$  at opposite sides, one located at the bud. Different patterns are obtained.

## 7.4. Linear stability analysis

In the last section we have introduced a generic system for polarization based on reaction-diffusion-advection equations. We performed simulations for different geometries and functions modeling reaction kinetics. The results have demonstrated that coupling of reaction and diffusion together with active transport is able to generate robust polarization.

Here, we present a stability analysis of the generic system to determine conditions required for pattern formation. Therefore, we further restrict ourselves to the case  $\Omega := B_1(0)$  and  $\Gamma := \partial B = S^2$ . Moreover, for sake of convenience, we assume that the internal pool is sufficiently large and that the rate of transport indirectly depends on the amount of  $w$  on  $\Gamma$ .

The system (7.11)-(7.17) then reduces to

$$\partial_t u = \Delta_\Gamma u + \gamma(f(u, v) + h(u, w, U)) \quad \text{on } \Gamma \times I, \quad (7.32)$$

$$\partial_t v = d_v \Delta_\Gamma v + \gamma(-f(u, v) + g(u, v, V)) \quad \text{on } \Gamma \times I, \quad (7.33)$$

$$\partial_t w = d_w \Delta_\Gamma (w \cdot c(u)^{-1}) \quad \text{on } \Gamma \times I, \quad (7.34)$$

$$\partial_t U = D_u \Delta U \quad \text{in } \Omega \times I, \quad (7.35)$$

$$\partial_t V = D_v \Delta V \quad \text{in } \Omega \times I, \quad (7.36)$$

with Robin-type boundary conditions

$$-D_u \nabla U \cdot \vec{n} = \gamma h(u, w, U) \quad \text{on } \Gamma \times I, \quad (7.37)$$

$$-D_v \nabla V \cdot \vec{n} = \gamma g(u, v, V) \quad \text{on } \Gamma \times I, \quad (7.38)$$

and initial conditions at time  $t = 0$

$$U(\cdot, 0) = U_0, \quad V(\cdot, 0) = V_0, \quad u(\cdot, 0) = u_0, \quad v(\cdot, 0) = v_0, \quad w(\cdot, 0) = w_0, \\ U_0, V_0 : \Omega \rightarrow \mathbb{R}, \quad u_0, v_0, w_0 : \Gamma \rightarrow \mathbb{R}.$$

Note that we consider  $D_u \gg 1$  to ensure a well mixed internal pool.

Let  $s := (u, v, w, U, V)^T$  be the vector of concentrations/densities  $u, v, w, U, V$  and  $s_* := (u_*, v_*, w_*, U_*, V_*) \in \mathbb{R}_+^5$  be the spatial homogeneous steady state, that is

$$f(u_*, v_*) = 0, \\ g(u_*, v_*, V_*) = 0, \\ h(u_*, w_*, V_*) = 0.$$

Since we are interested in pattern formation, our aim is now to investigate the stability of the system (7.32)-(7.38) at stationary states. Throughout, we will follow the approach presented in [72]. However, different to their analysis, due to the implemented transport mechanism, we consider a system with five PDEs. This makes the analysis much more costly and sophisticated.

As in [72], we are concerned with the GTPase cycle. This implies that we can interpret  $f$  as an activation rate and  $g$  as the flux describing membrane attachment and detachment of the GTPase. This interpretation of natural conditions can be expressed by the following inequalities

$$\partial_v f \geq 0, \quad \partial_v g \leq 0, \quad \partial_v g \leq \partial_u g.$$

Furthermore, by interpreting the function  $h$  as the flux induced by de- and adsorption of the substances (here exocytosis and endocytosis) at the membrane, we can assume the condition

$$\partial_U h \geq 0.$$

Following the proceeding presented in [72], with notations

$$\begin{aligned} f_u &:= \partial_u f(u_*, v_*), & f_v &:= \partial_v f(u_*, v_*), \\ g_u &:= \partial_u g(u_*, v_*, V_*), & g_v &:= \partial_v g(u_*, v_*, V_*), & g_V &:= \partial_V g(u_*, v_*, V_*), \\ h_u &:= \partial_u h(u_*, w_*, U_*), & h_w &:= \partial_w h(u_*, w_*, U_*), & h_U &:= \partial_U h(u_*, w_*, U_*), \end{aligned}$$

we suppose that in its equilibrium  $(u_*, v_*, w_*, U_*, V_*)$  the functions satisfy the strict inequalities

$$f_v > 0, \quad g_v < 0, \quad g_V > 0, \quad h_U > 0. \quad (7.39)$$

Since we are interested in the stability behavior of steady states, we use preliminaries presented in Section 3.2 and perform a stability analysis of the system (7.32)-(7.38). Therefore, we have to linearize the equations at its steady state. For a better analysis and to eliminate the inconvenient term  $w \cdot c(u)^{-1}$  in (7.34), as a starting point we apply the substitution  $\tilde{w} := \frac{w}{c(u)}$ .

The system (7.32)-(7.38) then reads

$$\partial_t u = \Delta_\Gamma u + \gamma(f(u, v) + h(u, c(u) \cdot \tilde{w}, U)) \quad \text{on } \Gamma \times I, \quad (7.40)$$

$$\partial_t v = d_v \Delta_\Gamma v + \gamma(-f(u, v) + g(u, v, V)) \quad \text{on } \Gamma \times I, \quad (7.41)$$

$$c(u) \cdot \partial_t \tilde{w} = d_w \Delta_\Gamma \tilde{w} \quad \text{on } \Gamma \times I, \quad (7.42)$$

$$\partial_t U = D_u \Delta U \quad \text{in } \Omega \times I, \quad (7.43)$$

$$\partial_t V = D_v \Delta V \quad \text{in } \Omega \times I, \quad (7.44)$$

where the Robin-type boundary conditions are now given by

$$-D_u \nabla U \cdot \vec{n} = \gamma h(u, c(u) \cdot \tilde{w}, U) \quad \text{on } \Gamma \times I, \quad (7.45)$$

$$-D_v \nabla V \cdot \vec{n} = \gamma g(u, v, V) \quad \text{on } \Gamma \times I. \quad (7.46)$$

To obtain the linearization at  $(u_*, v_*, \tilde{w}_*, U_*, V_*)$ , system (7.40)-(7.46) can be written in matrix form  $x' = Fx$ , where  $x := (u, v, \tilde{w}, U, V)$ . The entries of  $F$  are given by the right-hand sides of the original system. With  $\tilde{w}_* = \frac{w_*}{c(u_*)}$ , on  $\Gamma \times I$ , the linearization is then given by  $x' = \mathbf{J}_F x$ , where  $\mathbf{J}_F$  denotes the derivative of  $F$  with respect to  $(u, v, \tilde{w}, U, V)$ .

On  $\Gamma \times I$  we have

$$\partial_t u = \Delta_\Gamma u + \gamma((f_u + h_u + c_u \tilde{w} h_w)u + f_v v + c(u_*) h_w \tilde{w} + h_U U), \quad (7.47)$$

$$\partial_t v = d_v \Delta_\Gamma v + \gamma((-f_u + g_u)u + (-f_v + g_v)v + g_V V), \quad (7.48)$$

$$c(u) \partial_t \tilde{w} = d_w \Delta \tilde{w}. \quad (7.49)$$

In  $\Omega \times I$  it holds that

$$\partial_t U = D_u \Delta U, \quad (7.50)$$

$$\partial_t V = D_v \Delta V, \quad (7.51)$$

and for the flux conditions we finally obtain

$$-D_u \nabla U \cdot \vec{n} = \gamma(h_u u + c_u \tilde{w} h_w u + c(u_*) h_w \tilde{w} + h_U U), \quad (7.52)$$

$$-D_v \nabla V \cdot \vec{n} = \gamma(g_u u + g_v v + g_V V). \quad (7.53)$$

To determine stability conditions for the system (7.32)-(7.38), we utilize the features of spherical harmonics (see Appendix B). Consider the following ansatz for the solution of the linearized system (7.47)-(7.53)

$$u(p, t) = \sum_{l \in \mathbb{N}_0, m \in \mathbb{Z}, |m| \leq l} u_{lm}(t) \varphi_{lm}(p),$$

$$v(p, t) = \sum_{l \in \mathbb{N}_0, m \in \mathbb{Z}, |m| \leq l} v_{lm}(t) \varphi_{lm}(p),$$

$$\tilde{w}(p, t) = \sum_{l \in \mathbb{N}_0, m \in \mathbb{Z}, |m| \leq l} \tilde{w}_{lm}(t) \varphi_{lm}(p),$$

$$\begin{aligned}
 U(p, t) &= \sum_{l \in \mathbb{N}_0, m \in \mathbb{Z}, |m| \leq l} U_{lm}(t) \psi_{lm}(r) \varphi_{lm}(p), \\
 V(p, t) &= \sum_{l \in \mathbb{N}_0, m \in \mathbb{Z}, |m| \leq l} V_{lm}(t) \chi_{lm}(r) \varphi_{lm}(p),
 \end{aligned}$$

with  $u_{lm}, v_{lm}, \tilde{w}_{lm}, U_{lm} : \mathbb{R} \rightarrow \mathbb{R}, V_{lm} : \mathbb{R} \rightarrow \mathbb{R}, \psi_{lm} : [0, 1] \rightarrow \mathbb{R}, \chi_{lm} : [0, 1] \rightarrow \mathbb{R}, p \in \Gamma, 0 \leq r \leq 1$ , and the orthonormal basis  $\{\varphi_{lm}\}_{l \in \mathbb{N}_0, m \in \mathbb{Z}, |m| \leq l}$  of  $L^2(\Gamma)$ . Then, the Laplace operator can be represented as

$$-\Delta_{\Gamma} \varphi_{lm} = l(l+1) \varphi_{lm} \quad \text{on } \Gamma.$$

As a result, the  $L^2(\Gamma)$  scalar product with  $\varphi_{lm}$  leads to the linearized system

$$\begin{aligned}
 u'_{lm} &= -(l+1)u_{lm} + \gamma((f_u + h_u + c_u \tilde{w}_* h_w)u_{lm} + f_v v_{lm}) \\
 &\quad + \gamma(c(u_*)h_w \tilde{w}_{lm} + h_U \psi_{lm}(1)U_{lm}), \tag{7.54}
 \end{aligned}$$

$$\begin{aligned}
 v'_{lm} &= -d_v(l+1)v_{lm} + \gamma(-f_u + g_u)u_{lm} + (-f_v + g_v)v_{lm} \\
 &\quad + \gamma g_V \psi_{lm}(1)V_{lm}, \tag{7.55}
 \end{aligned}$$

$$c(u) \tilde{w}'_{lm} = -d_w l(l+1) \tilde{w}_{lm}, \tag{7.56}$$

$$U'_{lm}(t) \psi(r) = D_u U_{lm}(t) \left( \psi''_{lm}(r) + \frac{2}{r} \psi'_{lm}(r) - \frac{1}{r^2} l(l+1) \psi_{lm}(r) \right), \tag{7.57}$$

$$V'_{lm}(t) \chi(r) = D_v V_{lm}(t) \left( \chi''_{lm}(r) + \frac{2}{r} \chi'_{lm}(r) - \frac{1}{r^2} l(l+1) \chi_{lm}(r) \right), \tag{7.58}$$

$$-D_v U_{lm} \psi_{lm}(1) = \gamma((h_u + c_u \tilde{w}_* h_w)u_{lm} + c(u_*)h_w \tilde{w}_{lm} + h_U \psi_{lm}(1)U_{lm}), \tag{7.59}$$

$$-D_v V_{lm} \chi_{lm}(1) = \gamma(g_u u_{lm} + g_v v_{lm} + g_V \chi_{lm}(1)V_{lm}). \tag{7.60}$$

We further acquire

$$\begin{aligned}
 U_{lm}(t) &= \bar{B}_{lm} e^{\lambda_{lm} t}, \quad \bar{B}_{lm} \in \mathbb{R}, \quad \lambda_{lm} \in \mathbb{R}, \\
 V_{lm}(t) &= \bar{B}_{lm} e^{\mu_{lm} t}, \quad \bar{B}_{lm} \in \mathbb{R}, \quad \mu_{lm} \in \mathbb{R},
 \end{aligned}$$

whereby  $U_{lm}, V_{lm}$  does nowhere vanish or is identically zero.

We first consider the case  $U_{lm}, V_{lm} \neq 0$ . Then, using  $U'_{lm} = \lambda_{lm} U_{lm}$  and  $V'_{lm} = \mu_{lm} V_{lm}$  we obtain from (7.57) and (7.58)

$$0 = r^2 \psi''_{lm}(r) + 2r \psi'_{lm}(r) - \left( l(l+1) + \frac{\lambda_{lm}}{D_u} r^2 \right) \psi_{lm}(r), \tag{7.61}$$

$$0 = r^2 \chi''_{lm}(r) + 2r \chi'_{lm}(r) - \left( l(l+1) + \frac{\mu_{lm}}{D_v} r^2 \right) \chi_{lm}(r). \tag{7.62}$$

In the case  $\lambda_{lm}, \mu_{lm} = 0$  it is easy to recalculate that we have

$$\begin{aligned}\psi_{lm}(r) &= \alpha_{lm}r^l, \\ \chi_{lm}(r) &= \beta_{lm}r^l,\end{aligned}$$

with  $\alpha_{lm}, \beta_{lm} \in \mathbb{R}$ . By contrast, for  $\lambda_{lm}, \mu_{lm} > 0$ , equations (7.61) and (7.62) are modified versions of Bessel differential equations whose solutions are defined by Bessel functions of first kind. Hence, using the respective modified Bessel functions  $J_{l+\frac{1}{2}}$ , we derive

$$\begin{aligned}\psi(r) &= \alpha_{lm}\xi_l \left( \sqrt{\frac{\lambda_{lm}}{D_u}}r \right), \alpha \in \mathbb{R}, \\ \chi(r) &= \beta_{lm}\xi_l \left( \sqrt{\frac{\mu_{lm}}{D_v}}r \right), \beta \in \mathbb{R},\end{aligned}$$

where

$$\xi_l = \sqrt{\frac{\pi}{2r}} J_{l+\frac{1}{2}}(r).$$

We then finally deduce the ODE system

$$u'_{lm} = (-l(l+1) + \gamma f_u)u_{lm} + \gamma f_v v_{lm} - D_u \psi'_{lm}(1)U_{lm}, \quad (7.63)$$

$$v'_{lm} = -\gamma f_u u_{lm} - (d_v l(l+1) + \gamma f_v)v_{lm} - D_v \chi'_{lm}(1)V_{lm}, \quad (7.64)$$

$$c(u)\tilde{w}'_{lm} = -d_w l(l+1)\tilde{w}_{lm}, \quad (7.65)$$

$$U'_{lm} = \lambda_{lm}U_{lm}, \quad (7.66)$$

$$V'_{lm} = \mu_{lm}V_{lm}, \quad (7.67)$$

coupled to two algebraic equations given by

$$0 = \gamma(h_u + c_u \tilde{w}_* h_w)u_{lm} + c(u_*)h_w \tilde{w}_{lm} + (\gamma h_U \psi_{lm}(1) + D_u \psi'_{lm}(1))U_{lm},$$

$$0 = \gamma(g_u u_{lm} + g_v v_{lm}) + (\gamma g_V \chi_{lm}(1) + D_v \chi'_{lm}(1))V_{lm}.$$

We define

$$x'_{lm} := \begin{pmatrix} u'_{lm} \\ v'_{lm} \\ c(u)\tilde{w}'_{lm} \\ U'_{lm} \\ V'_{lm} \end{pmatrix}, \quad x_{lm} := \begin{pmatrix} u_{lm} \\ v_{lm} \\ \tilde{w}_{lm} \\ U_{lm} \\ V_{lm} \end{pmatrix}$$



and

$$\mathbf{J}_F := \begin{pmatrix} -l(l+1) + \gamma f_u & \gamma f_v & 0 & -D_u \psi'_{lm}(1) & 0 \\ -\gamma f_u & -d_v l(l+1) - \gamma f_v & 0 & 0 & -D_v \chi'_{lm}(1) \\ 0 & 0 & -d_w l(l+1) & 0 & 0 \\ \gamma(h_u + c_u \tilde{w}_* h_w) & 0 & \gamma c(u_*) h_w & \xi & 0 \\ \gamma g_u & \gamma g_v & 0 & 0 & \eta \end{pmatrix},$$

where

$$\begin{aligned} \xi &:= \gamma h_U \psi_{lm}(1) + D_u \psi'_{lm}(1) + \lambda_{lm}, \\ \eta &:= \gamma g_V \chi_{lm}(1) + D_v \chi'_{lm}(1) + \mu_{lm}. \end{aligned}$$

Writing

$$x'_{lm} = \mathbf{J}_F x_{lm},$$

the stability analysis reduces to an analysis of the eigenvalues of the matrix  $\mathbf{J}_F$ . To determine stability conditions we have to consider the eigenvalue problem

$$|\mathbf{J}_F - \lambda \mathbf{I}| = 0.$$

Straightforward calculation of the determinant by considering the respective minors leads to

$$|\mathbf{J}_F - \lambda \mathbf{I}| = [-d_w l(l+1) - \lambda] \cdot |\tilde{\mathbf{J}}|,$$

where

$$\tilde{\mathbf{J}} := \begin{pmatrix} -l(l+1) + \gamma f_u - \lambda & \gamma f_v & -D_u \psi'_{lm}(1) & 0 \\ -\gamma f_u & -d_v l(l+1) - \gamma f_v - \lambda & 0 & -D_v \chi'_{lm}(1) \\ \gamma(h_u + c_u \tilde{w}_* h_w) & 0 & \xi - \lambda & 0 \\ \gamma g_u & \gamma g_v & 0 & \eta - \lambda \end{pmatrix}.$$

Thus, we directly see that  $-d_w l(l+1)$  is an eigenvalue of the system. Since  $d_w > 0$ , the first eigenvalue is always less than zero. To find a positive eigenvalue, it remains

to consider the eigenvalues of the remaining matrix, that is

$$\begin{vmatrix} -l(l+1) + \gamma f_u - \lambda & \gamma f_v & -D_u \psi'_{lm}(1) & 0 \\ -\gamma f_u & -d_v l(l+1) - \gamma f_v - \lambda & 0 & -D_v \chi'_{lm}(1) \\ \gamma(h_u + c_u \tilde{w}_* h_w) & 0 & \xi - \lambda & 0 \\ \gamma g_u & \gamma g_v & 0 & \eta - \lambda \end{vmatrix}.$$

It holds that

$$\begin{aligned} |\tilde{\mathbf{J}}| &= (\eta - \lambda) \cdot \begin{vmatrix} -l(l+1) + \gamma f_u - \lambda & \gamma f_v & -D_u \psi'_{lm}(1) \\ -\gamma f_u & -d_v l(l+1) - \gamma f_v - \lambda & 0 \\ \gamma(h_u + c_u \tilde{w}_* h_w) & 0 & \xi - \lambda \end{vmatrix} \\ &\quad - D_v \chi'_{lm}(1) \cdot \begin{vmatrix} -l(l+1) + \gamma f_u - \lambda & \gamma f_v & -D_u \psi'_{lm}(1) \\ \gamma(h_u + c_u \tilde{w}_* h_w) & 0 & \xi - \lambda \\ \gamma g_u & \gamma g_v & 0 \end{vmatrix} \\ &= (\eta - \lambda) \cdot (\xi - \lambda) \begin{vmatrix} -l(l+1) + \gamma f_u - \lambda & \gamma f_v \\ -\gamma f_u & -d_v l(l+1) - \gamma f_v - \lambda \end{vmatrix} \\ &\quad - (\eta - \lambda) \cdot D_u \psi'_{lm}(1) \begin{vmatrix} -\gamma f_u & -d_v l(l+1) - \gamma f_v - \lambda \\ \gamma(h_u + c_u \tilde{w}_* h_w) & 0 \end{vmatrix} \\ &\quad + (\xi - \lambda) \cdot D_v \chi'_{lm}(1) \cdot \begin{vmatrix} -l(l+1) + \gamma f_u - \lambda & \gamma f_v \\ \gamma g_u & \gamma g_v \end{vmatrix} \\ &\quad + D_v \chi'_{lm}(1) \cdot D_u \psi'_{lm}(1) \cdot \begin{vmatrix} \gamma(h_u + c_u \tilde{w}_* h_w) & 0 \\ \gamma g_u & \gamma g_v \end{vmatrix}. \end{aligned}$$

We define the characteristic polynomial

$$\begin{aligned} P_l(\lambda) &:= \\ &(\gamma g_V \chi_{lm}(1) + D_v \chi'_{lm}(1) + \mu_{lm} - \lambda) \cdot (\gamma h_U \psi_{lm}(1) + D_u \psi'_{lm}(1) + \lambda_{lm} - \lambda) \cdot p_{l,1}(\lambda) \\ &+ (\gamma h_U \psi_{lm}(1) + D_u \psi'_{lm}(1) + \mu_{lm} - \lambda) \cdot D_u \psi'_{lm}(1) \cdot p_{l,2}(\lambda) \\ &+ (\gamma g_V \chi_{lm}(1) + D_v \chi'_{lm}(1) + \lambda_{lm} - \lambda) \cdot D_v \chi'_{lm}(1) \cdot p_{l,3}(\lambda) \\ &+ D_u \psi'_{lm}(1) \cdot D_v \chi'_{lm}(1) \cdot p_{l,4}(\lambda), \end{aligned} \tag{7.68}$$

where

$$\begin{aligned}
 p_{l,1}(\lambda) &:= \lambda^2 + [(d_v + 1)(l + 1)l + (-f_u + f_v)\gamma] \lambda + d_v l^2 (l + 1)^2 \\
 &\quad + \gamma(l(l + 1))(-df_u + f_v), \\
 p_{l,2}(\lambda) &:= [-l(l + 1) + \gamma f_u - \lambda] \gamma g_v - \gamma^2 f_v g_u, \\
 p_{l,3}(\lambda) &:= [-d_v l(l + 1) - \gamma f_v - \lambda] \gamma (h_u + c_u \tilde{w}_* h_w), \\
 p_{l,4}(\lambda) &:= \gamma^2 g_v (h_u + c_u \tilde{w}_* h_w).
 \end{aligned}$$

The eigenvalues are now given by the zeros of polynomial (7.68). Hence, from (7.63)-(7.67), as long as  $U_{lm}, V_{lm} \neq 0$ , we acquire that an eigenvalue  $\lambda$  with  $\text{Re}(\lambda) > 0$  exists if and only if first  $\lambda = \lambda_{lm} = \mu_{lm} \in \mathbb{R}_0^+$  and additionally with

$$\kappa_{D_u, l}(\lambda) := \frac{D_u \psi'_{lm}(1)}{\psi_{lm}(1)} = D_u \left( \frac{r \xi'_l(r)}{\xi_l(r)} \right) \Big|_{r=\sqrt{\frac{\lambda}{D_u}}}, \quad (7.69)$$

$$\kappa_{D_v, l}(\lambda) := \frac{D_v \chi'_{lm}(1)}{\chi_{lm}(1)} = D_v \left( \frac{r \xi'_l(r)}{\xi_l(r)} \right) \Big|_{r=\sqrt{\frac{\lambda}{D_v}}} \quad (7.70)$$

$\lambda_{lm}$  fulfils the condition

$$\begin{aligned}
 P_l(\lambda_{lm}) &:= (\gamma g_v + \kappa_{D_v, l}(\lambda_{lm})) \cdot (\gamma h_u + \kappa_{D_u, l}(\lambda_{lm})) \cdot p_{l,1}(\lambda_{lm}) \\
 &\quad + (\gamma h_u + \kappa_{D_u, l}) \cdot \kappa_{D_v, l} \cdot p_{l,2}(\lambda_{lm}) \\
 &\quad + (\gamma g_v + \kappa_{D_v, l}) \cdot \kappa_{D_u, l} \cdot p_{l,3}(\lambda_{lm}) \\
 &\quad + \kappa_{D_u, l} \cdot \kappa_{D_v, l} \cdot p_{l,4}(\lambda_{lm}) \stackrel{!}{=} 0.
 \end{aligned}$$

**Proposition 7.1.** *In  $(u_*, v_*, w_*, U_*, V_*)$  the system (7.32)-(7.38) is stable against spatially homogeneous perturbations in the variables  $u, v$ , and  $w$  if the following condition is satisfied:*

$$\frac{1}{3}(f_u g_v h_u - f_v g_u h_u - g_v h_u f_v) + g_v h_u (f_v - f_u) > 0. \quad (7.71)$$

In this case

$$f_v - f_u > h_u, \quad h_u < 0$$

holds.

If either  $U = 0$  or  $V = 0$  the conditions are as follows:

- Case  $U = 0$ :

$$\frac{1}{3}(f_u g_v - f_v g_u) + g_v(f_v - f_u) > 0. \quad (7.72)$$

In this case

$$f_v > f_u$$

holds.

- Case  $V = 0$ :

$$h_U(f_v - f_u) - \frac{1}{3}f_v h_u > 0. \quad (7.73)$$

In this case

$$h_u < 0$$

holds.

*Proof.* We first consider the case  $l = 0$ . Furthermore, we assume that  $U_{00}, V_{00} \neq 0$ . Note that in this case  $w$  is always constant and  $w = w_0$ . This also implies  $h_w = 0$ . Then the characteristic polynomial (7.68) reduces to

$$\begin{aligned} P_0(\lambda) = & (\gamma g_v + \kappa_{D_v, l}(\lambda)) \cdot (\gamma h_U + \kappa_{D_u, l}(\lambda)) \cdot [\lambda^2 + (-f_u + f_v)\gamma\lambda] \\ & + (\gamma h_U + \kappa_{D_u, l}(\lambda)) \cdot \kappa_{D_v, l}(\lambda) \cdot [\gamma^2 f_u g_v - \lambda\gamma g_v - \gamma^2 f_v g_u] \\ & + (\gamma g_v + \kappa_{D_v, l}(\lambda)) \cdot \kappa_{D_u, l}(\lambda) \cdot [-\gamma^2 f_v h_u - \lambda\gamma h_u] \\ & + \kappa_{D_u, l}(\lambda) \cdot \kappa_{D_v, l}(\lambda) \cdot \gamma^2 g_v h_u. \end{aligned}$$

To obtain that the system is asymptotically stable in  $(u_*, v_*, w_*, U_*, V_*)$ , we require that all eigenvalues are negative. This means that  $P_0(\lambda)$  has no zeros in  $[0, \infty)$ .

We rewrite

$$\begin{aligned} \kappa_{D_u, 0}(\lambda) &= D_u \left( \frac{r\xi'_l(r)}{\xi_l(r)} \right) \Big|_{r=\sqrt{\frac{\lambda}{D_u}}} = \lambda\tilde{\kappa} \left( \sqrt{\frac{\lambda}{D_u}} \right), \\ \kappa_{D_v, 0}(\lambda) &= D_v \left( \frac{r\xi'_l(r)}{\xi_l(r)} \right) \Big|_{r=\sqrt{\frac{\lambda}{D_v}}} = \lambda\tilde{\kappa} \left( \sqrt{\frac{\lambda}{D_v}} \right), \\ \tilde{\kappa}(r) &:= \frac{\xi'_0(r)}{r\xi_0(r)}. \end{aligned}$$

For  $\lambda > 0$  equation  $P_0(\lambda) = 0$  is equivalent to

$$\begin{aligned}
0 &= \left[ \gamma g_V + \lambda \tilde{\kappa} \left( \sqrt{\frac{\lambda}{D_v}} \right) \right] \cdot \left[ \gamma h_U + \lambda \tilde{\kappa} \left( \sqrt{\frac{\lambda}{D_u}} \right) \right] \cdot (\lambda^2 + (-f_u + f_v)\gamma\lambda) \\
&+ \left[ \gamma h_U + \lambda \tilde{\kappa} \left( \sqrt{\frac{\lambda}{D_u}} \right) \right] \cdot \lambda \tilde{\kappa} \left( \sqrt{\frac{\lambda}{D_v}} \right) \cdot (\gamma^2 f_u g_v - \lambda \gamma g_v - \gamma^2 f_v g_u) \\
&+ \left[ \gamma g_V + \lambda \tilde{\kappa} \left( \sqrt{\frac{\lambda}{D_v}} \right) \right] \cdot \lambda \tilde{\kappa} \left( \sqrt{\frac{\lambda}{D_u}} \right) \cdot (-\gamma^2 f_v h_u - \lambda \gamma h_u) \\
&+ \lambda^2 \tilde{\kappa} \left( \sqrt{\frac{\lambda}{D_u}} \right) \cdot \tilde{\kappa} \left( \sqrt{\frac{\lambda}{D_v}} \right) \cdot \gamma^2 g_v (h_u) \\
&\stackrel{(\because \lambda > 0)}{=} \left[ \gamma g_V + \lambda \tilde{\kappa} \left( \sqrt{\frac{\lambda}{D_v}} \right) \right] \cdot \left[ \gamma h_U + \lambda \tilde{\kappa} \left( \sqrt{\frac{\lambda}{D_u}} \right) \right] \cdot (\lambda + (-f_u + f_v)\gamma) \\
&+ \left[ \gamma h_U + \lambda \tilde{\kappa} \left( \sqrt{\frac{\lambda}{D_u}} \right) \right] \cdot \tilde{\kappa} \left( \sqrt{\frac{\lambda}{D_v}} \right) \cdot (\gamma^2 f_u g_v - \gamma^2 f_v g_u - \lambda \gamma g_v) \\
&+ \left[ \gamma g_V + \lambda \tilde{\kappa} \left( \sqrt{\frac{\lambda}{D_v}} \right) \right] \cdot \tilde{\kappa} \left( \sqrt{\frac{\lambda}{D_u}} \right) \cdot (-\gamma^2 f_v h_u - \gamma \lambda h_u) \\
&+ \lambda \tilde{\kappa} \left( \sqrt{\frac{\lambda}{D_u}} \right) \cdot \tilde{\kappa} \left( \sqrt{\frac{\lambda}{D_v}} \right) \cdot \gamma^2 g_v h_u := \tilde{P}_0(\lambda).
\end{aligned}$$

For  $\lambda = 0$  it holds  $P_0(0) = 0$ . Since  $w$  is in this case simply a constant and  $w = w_0$ , the linearized system reduces to

$$0 = (f_u + h_u)u + f_v v + h_U U, \quad (7.74)$$

$$0 = (-f_u + g_u)u + (-f_v + g_v)v + g_V V, \quad (7.75)$$

$$0 = 4\pi(u + v) + \frac{4\pi}{3}(U + V), \quad (7.76)$$

where  $u, v, U, V$  are constant. Addition of (7.74) and (7.75) yields

$$0 = g_u u + g_v v + g_V V + h_u u + h_U U. \quad (7.77)$$

With the stationary equations for  $U$  and  $V$  we obtain

$$0 = g_u u + g_v v + g_V V,$$

$$0 = h_u u + h_U U.$$

Thus, we get

$$h_u = -\frac{h_U U}{u},$$

and hence, since  $u, U$ , and  $h_U > 0$ , it holds that  $h_u < 0$ . Furthermore, together with (7.75) we have

$$0 = f_u u + f_v v \iff u = -\frac{f_v}{f_u} v,$$

so that

$$V = \frac{1}{g_V} \left( \frac{g_u f_v}{f_u} - g_v \right) v, \quad U = \left( \frac{3f_v}{f_u} - 3 - \frac{1}{g_V} \left( \frac{g_u f_v}{f_u} - g_v \right) \right) v.$$

By substitution of these relations into (7.77) and straightforward calculations, as the first condition, we obtain that this system has a non-trivial solution if

$$0 = \frac{1}{3}(f_u g_v h_U - f_v g_u h_U - g_V h_u f_v) + g_V h_U (f_v - f_u). \quad (7.78)$$

With (7.71) and the relation  $g_v \leq g_u$  we further deduce that

$$\begin{aligned} 0 &< \frac{1}{3}(f_u g_v h_U - f_v g_u h_U - g_V h_u f_v) + g_V h_U (f_v - f_u) \\ &\leq \frac{1}{3}(f_u g_v h_U - f_v g_v h_U - g_V h_u f_v) + g_V h_U (f_v - f_u) \\ &= (f_v - f_u)(g_V h_U - \frac{1}{3}g_v h_U) - \frac{1}{3}f_v g_V h_u \\ &= (f_v - f_u - h_u)(g_V h_U - \frac{1}{3}g_v h_U + \frac{1}{3}f_v g_V) + h_u(g_V h_U - \frac{1}{3}g_v h_U) \\ &\leq (f_v - f_u - h_u)(g_V h_U - \frac{1}{3}g_v h_U + \frac{1}{3}f_v g_V). \end{aligned}$$

Together with (7.39) this yields  $f_v - f_u > h_u$ .

Let us now consider the case  $\lambda \in (0, \infty)$ . From [72] we know that

$$\lim_{r \rightarrow 0} \tilde{\kappa}(r) = \frac{1}{3}, \quad \lim_{r \rightarrow \infty} \tilde{\kappa}(r) = 0. \quad (7.79)$$

Since we suppose  $g_V, h_U > 0$ , together with (7.79), we obtain that  $\lim_{\lambda \rightarrow \infty} \tilde{P}_0(\lambda) = +\infty$ . Furthermore, it holds that

$$\lim_{\lambda \rightarrow 0} \tilde{P}_0(\lambda) = g_V h_U (f_v - f_u) + \frac{1}{3}(f_u g_v h_U - f_v g_u h_U - f_v g_V h_u). \quad (7.80)$$

In other words, (7.78), (7.80), and  $\tilde{w}_* = \frac{w_*}{c(u_*)}$  imply that for  $\lambda > 0$ , if the conditions from Proposition 7.1 are satisfied, the characteristic polynomial has no change of sign. This inequality is necessary for the stability of the homogeneous steady state. To investigate if this term is also sufficient to exclude an eigenvalue  $\lambda$  with  $\text{Re } \lambda > 0$ , we recheck

$$\begin{aligned}
 \tilde{P}_0(\lambda) &= \left[ \gamma g_V + \lambda \tilde{\kappa} \left( \sqrt{\frac{\lambda}{D_v}} \right) \right] \cdot \left[ \gamma h_U + \lambda \tilde{\kappa} \left( \sqrt{\frac{\lambda}{D_u}} \right) \right] \cdot [\lambda + \gamma(f_v - f_u)] \\
 &+ \left[ \gamma h_U + \lambda \tilde{\kappa} \left( \sqrt{\frac{\lambda}{D_u}} \right) \right] \cdot \tilde{\kappa} \left( \sqrt{\frac{\lambda}{D_v}} \right) \cdot [\gamma^2 g_v f_u - \gamma^2 f_v h_u - \lambda \gamma g_v] \\
 &+ \left[ \gamma g_V + \lambda \tilde{\kappa} \left( \sqrt{\frac{\lambda}{D_v}} \right) \right] \cdot \tilde{\kappa} \left( \sqrt{\frac{\lambda}{D_u}} \right) \cdot [-\gamma^2 f_v h_u - \gamma h_u] \\
 &+ \lambda \tilde{\kappa} \left( \sqrt{\frac{\lambda}{D_u}} \right) \cdot \tilde{\kappa} \left( \sqrt{\frac{\lambda}{D_v}} \right) \cdot \gamma^2 g_v h_u \\
 &\geq \left[ \gamma g_V + \lambda \tilde{\kappa} \left( \sqrt{\frac{\lambda}{D_v}} \right) \right] \cdot \left[ \gamma h_U + \lambda \tilde{\kappa} \left( \sqrt{\frac{\lambda}{D_u}} \right) \right] \cdot [\gamma(f_v - f_u)] \\
 &+ \left[ \gamma h_U + \lambda \tilde{\kappa} \left( \sqrt{\frac{\lambda}{D_u}} \right) \right] \cdot \tilde{\kappa} \left( \sqrt{\frac{\lambda}{D_v}} \right) \cdot [\gamma^2 g_v f_u - \gamma^2 f_v h_u] \\
 &+ \left[ \gamma g_V + \lambda \tilde{\kappa} \left( \sqrt{\frac{\lambda}{D_v}} \right) \right] \cdot \tilde{\kappa} \left( \sqrt{\frac{\lambda}{D_u}} \right) \cdot [-\gamma^2 f_v h_u]
 \end{aligned}$$

for  $\lambda > 0$ ,  $g_v h_u > 0$ ,  $g_v < 0$ , and  $h_u < 0$ . Thus, we have to distinguish two cases. First, consider

$$f_u g_v - f_v g_u < 0 \quad \text{or} \quad f_v - f_u < 0.$$

Since  $\tilde{\kappa}$  is decreasing and  $\tilde{\kappa} \leq \frac{1}{3}$ , on  $[0, \infty)$  we have the downward estimation

$$\tilde{P}_0(\lambda) > \gamma^2 \left[ \frac{1}{3} (f_u g_v h_U - f_v g_u h_U - f_v g_V h_u) + g_V h_U (f_v - f_u) \right] \geq 0.$$

For the case

$$f_u g_v - f_v g_u > 0, \quad f_v - f_u > 0,$$

we directly conclude that  $\tilde{P}_0(\lambda) > 0$  and prove the assertion for the full system.

In order to investigate the system for stability conditions in the absence of some

species, we proceed with the special cases  $V_{lm}, U_{lm} = 0$ .

**Case  $U_{lm} = 0$ :** The system is overdetermined and it holds that  $\mu_{lm} = 0$ . Furthermore, we obtain

$$\begin{aligned} 0 &= \gamma(h_u u_{lm} + h_w w_{lm}) + (\gamma h_U \psi_{lm}(1) + D_u \psi'_{lm}(1)) U_{lm} \\ &= h_u u_{lm} + h_w w_{lm} \end{aligned}$$

and hence

$$u'_{lm} = (-l(l+1) + \gamma f_u) u_{lm} + \gamma f_v v_{lm}.$$

Moreover, for  $U_{lm} = 0$  the characteristic polynomial reduces to

$$\begin{aligned} G_0(\lambda) &:= \gamma g_V (\lambda^2 + (-f_u + f_v) \gamma \lambda) + \kappa_{D_v,0}(\lambda) (\lambda^2 + (-f_u + f_v) \gamma \lambda) \\ &\quad - \kappa_{D_v,0}(\lambda) (\gamma g_v \lambda - \gamma^2 (f_u g_v - f_v g_u)). \end{aligned}$$

The stability conditions for this case have already been discussed and the proof can be found in [72].

**Case  $V_{lm} = 0$ :** The system is again overdetermined and the matrix has an eigenvalue  $\lambda_{lm} = 0$ . Moreover, it holds that

$$\begin{aligned} 0 &= \gamma(g_u u_{lm} + g_v v_{lm}) + (\gamma g_V \chi_{lm}(1) + D_v \chi'_{lm}(1)) V_{lm} \\ &= \gamma g_u u_{lm} + \gamma g_v v_{lm} \end{aligned}$$

so that for (7.64) we obtain

$$v'_{lm} = \gamma f_u \frac{g_v}{g_u} v_{lm} - (d_v l(l+1) + \gamma f_v) v_{lm}.$$

This implies that any eigenvalue  $\lambda$  corresponding to the linearized system is given by

$$\lambda = \gamma \left( \frac{f_u g_v}{g_u} - f_v \right) - d_v l(l+1).$$

For  $l = 0$  we require that all eigenvalues have negative real parts. We claim that

$$\frac{f_u g_v}{g_u} - f_v < 0.$$

Furthermore, the characteristic polynomial reduces to

$$H_0(\lambda) := -D_u \psi'_{lm}(1) \cdot [\gamma^2 f_v h_u + \lambda \gamma h_u] + (\gamma h_U \psi_{lm}(1) + D_u \psi'_{lm}(1)) \cdot \lambda \gamma (-f_u + f_v).$$



Since  $h_U > 0$ ,  $f_v > 0$ , and  $h_u < 0$  we deduce that  $\lim_{\lambda \rightarrow \infty} H_0(\lambda) = +\infty$ . Using (7.69) and (7.67) we further calculate

$$\tilde{H}_0(\lambda) = -\tilde{\kappa} \left( \sqrt{\frac{\lambda}{D_u}} \right) \cdot [\gamma^2 f_v h_u + \lambda \gamma h_u] + \left[ \gamma h_U + \lambda \tilde{\kappa} \left( \sqrt{\frac{\lambda}{D_u}} \right) \right] \cdot \gamma (f_v - f_u).$$

To prevent that  $\tilde{H}_0$  has only negative eigenvalues, meaning it does not change its sign for  $\lambda \in [0, \infty)$ , consider

$$\lim_{\lambda \rightarrow 0} \tilde{H}_0(\lambda) = \gamma^2 h_U (f_v - f_u) - \frac{1}{3} \gamma^2 f_v h_u.$$

This is fulfilled even if

$$0 < h_U (f_v - f_u) - \frac{1}{3} f_v h_u.$$

Summarized, the derived conditions ensure that  $\tilde{H}_0$  has only negative eigenvalues.  $\square$

We next determine under which conditions small spatial perturbations from the homogeneous steady state  $(u_*, v_*, w_*, U_*, V_*)$  induce instabilities.

**Theorem 7.2.** *Assume that the system (7.32)-(7.38) satisfies the condition (7.71). If in  $(u_*, v_*, w_*, U_*, V_*)$  further holds that*

$$\begin{aligned} & (\gamma g_V + D_v l) \cdot (\gamma h_U + D_u l) \cdot [d_v l^2 (l+1)^2 + \gamma l (l+1) (-d_v f_u + f_v)] \\ & + (\gamma h_U + D_u l) \cdot D_u l [-l(l+1) \gamma g_v + \gamma^2 (f_u g_v - f_v g_u)] \\ & - (\gamma g_V + D_v l) \cdot D_v l \left[ \left( \gamma h_w \left( \frac{w_* c_u}{c(u_*)} \right) + \gamma h_u \right) \cdot (d_v l (l+1) + \gamma f_v) \right] \\ & + D_u D_v l^2 \left[ \left( \gamma h_w \left( \frac{w_* c_u}{c(u_*)} \right) + \gamma h_u \right) \cdot \gamma g_v \right] < 0, \end{aligned} \quad (7.81)$$

then the system is linearly asymptotically unstable in  $(u_*, v_*, w_*, U_*, V_*)$ .

**Remark 7.1.** In the case of  $U_{lm} = 0$  the system is asymptotically unstable in  $(u_*, v_*, w_*, U_*, V_*)$  if it fulfils the condition (7.72) and furthermore

$$\begin{aligned} & (\gamma g_V + D_v l) \cdot [d_v l^2 (l+1)^2 + \gamma l (l+1) (-d_v f_u + f_v)] \\ & - D_v l \cdot [-l(l+1) \gamma g_v + \gamma^2 (f_u g_v - f_v g_u)] < 0. \end{aligned} \quad (7.82)$$

If  $V_{lm} = 0$  and (7.73) is satisfied, then the instability condition is given by

$$(\gamma h_U + D_u l) \cdot [d_v l^2 (l+1)^2 + \gamma l (l+1) (-d_v f_u + f_v)]$$

$$-D_u l \cdot \left[ \left( \gamma h_w \left( \frac{w_* c_u}{c(u_*)} \right) + \gamma h_u \right) \cdot (d_v l(l+1) + \gamma f_v) \right] < 0. \quad (7.83)$$

*Proof.* Again, we first consider the case  $U_{lm}, V_{lm} \neq 0$ . Since we claim that the system becomes unstable in the presence of diffusion, we require that the characteristic polynomial has a positive zero  $\lambda_{lm}$ . As already mentioned, from (7.63)-(7.67), as long as  $U_{lm}, V_{lm} \neq 0$ , we acquire that an eigenvalue  $\lambda$  with  $\text{Re}(\lambda) > 0$  exists if and only if first  $\lambda = \lambda_{lm} = \mu_{lm} \in \mathbb{R}_0^+$  and additionally with (7.69) and (7.70)  $\lambda_{lm}$  fulfils the condition

$$\begin{aligned} P_l(\lambda_{lm}) &= (\gamma g_V + \kappa_{D_v, l}(\lambda_{lm})) \cdot (\gamma h_U + \kappa_{D_u, l}(\lambda_{lm})) \cdot p_{l,1}(\lambda_{lm}) \\ &\quad + (\gamma h_U + \kappa_{D_u, l}(\lambda_{lm})) \cdot \kappa_{D_v, l} \cdot p_{l,2}(\lambda_{lm}) \\ &\quad + (\gamma g_V + \kappa_{D_v, l}(\lambda_{lm})) \cdot \kappa_{D_u, l} \cdot p_{l,3}(\lambda_{lm}) \\ &\quad + \kappa_{D_u, l}(\lambda_{lm}) \cdot \kappa_{D_v, l}(\lambda_{lm}) \cdot p_{l,4}(\lambda_{lm}) = 0. \end{aligned}$$

From [72] we know that

$$\begin{aligned} \lim_{\lambda \rightarrow 0} \kappa_{D_u, l}(\lambda) &= D_u \left( \frac{r \xi_l'(r)}{\xi_l(r)} \right) \Big|_{r=\sqrt{\frac{\lambda}{D_u}}} = D_u l, \\ \lim_{\lambda \rightarrow 0} \kappa_{D_v, l}(\lambda) &= D_v \left( \frac{r \xi_l'(r)}{\xi_l(r)} \right) \Big|_{r=\sqrt{\frac{\lambda}{D_v}}} = D_v l, \\ \lim_{\lambda \rightarrow \infty} \kappa_{D_u, l}(\lambda) &= +\infty, \\ \lim_{\lambda \rightarrow \infty} \kappa_{D_v, l}(\lambda) &= +\infty. \end{aligned}$$

This implies that

$$\lim_{\lambda \rightarrow \infty} P_l(\lambda) = +\infty.$$

For  $P_l(\lambda)$  in order to change its sign, we finally examine  $\lim_{\lambda \rightarrow 0} P_l(\lambda)$  and get the condition (7.81) which is sufficient to ensure a positive zero of  $P_l(\lambda)$ .

Similarly, consider

$$G_l(\mu_{lm}) := (g_V + \kappa_{D_v, l}(\mu_{lm})) \cdot p_{l,1}(\mu_{lm}) - \kappa_{D_v, l}(\mu_{lm}) \cdot p_{l,2}(\mu_{lm}).$$

and

$$H_l(\lambda_{lm}) := (h_U + \kappa_{D_u, l}(\lambda_{lm})) \cdot p_{l,1}(\lambda_{lm}) + \kappa_{D_u, l}(\lambda_{lm}) \cdot p_{l,3}(\lambda_{lm}).$$

Then, (7.82) and (7.83) follow directly with the same argumentation.  $\square$

**Corollary 7.3.** *Assume that the system (7.32)-(7.38) satisfies the condition (7.71) and either  $D_u$  or  $D_v$  are chosen sufficiently large. Then, the instability condition (7.81) is satisfied if the following conditions hold:*

- *Case 1:*

$$\begin{aligned} C_1 &:= f_u g_v - f_v g_u - f_v h_u - \left( \frac{c_u w_*}{c(u_*)} \right) f_v h_w + g_v h_u + \left( \frac{c_u w_*}{c(u_*)} \right) g_v h_w \geq 0, \\ C_2 &:= d_v f_u - f_v + g_v + d_v h_u + d_v \left( \frac{c_u w_*}{c(u_*)} \right) h_w > 0, \\ Q &:= C_1^2 - 4d_v C_2 > 0, \end{aligned}$$

and for

$$r_{\pm} = \frac{1}{2d_v} (C_2 \pm \sqrt{Q})$$

exists an  $l \in \mathbb{N}$  with

$$r_- < \frac{l(l+1)}{\gamma} < r_+.$$

- *Case 2:*

$$C_1 := f_u g_v - f_v g_u - f_v h_u - \left( \frac{c_u w_*}{c(u_*)} \right) f_v h_w + g_v h_u + \left( \frac{c_u w_*}{c(u_*)} \right) g_v h_w < 0$$

and with  $r_+$  as defined above exists an  $l \in \mathbb{N}$  with

$$\frac{l(l+1)}{\gamma} < r_+.$$

**Remark 7.2.** If  $U_{lm} = 0$  and the system fulfils condition (7.72), then the instability condition (7.82) holds for sufficiently large  $D_v$  if the following conditions are satisfied:

- *Case 1:*

$$\begin{aligned} C_1 &:= f_u g_v - f_v g_u \geq 0, \\ C_2 &:= d_v f_u - f_v + g_v > 0, \\ Q &:= C_1^2 - 4d_v C_2 > 0, \end{aligned}$$

and for

$$r_{\pm} = \frac{1}{2d_v}(C_2 \pm \sqrt{Q})$$

exists an  $l \in \mathbb{N}$  with

$$r_- < \frac{l(l+1)}{\gamma} < r_+.$$

- Case 2:

$$C_1 := f_u g_v - f_v g_u < 0$$

and with  $r_+$  as defined above exists an  $l \in \mathbb{N}$  with

$$\frac{l(l+1)}{\gamma} < r_+.$$

**Remark 7.3.** If  $V_{lm} = 0$  and the system fulfils condition (7.73), then the instability condition (7.83) holds for sufficiently large  $D_u$  if the following condition is satisfied

- Case 1:

$$\begin{aligned} C_1 &:= -f_v \left[ h_u + \left( \frac{w_* c_u}{c(u_*)} \right) h_w \right] \geq 0, \\ C_2 &:= d_v f_u - f_v + d_v h_u + d_v \left( \frac{w_* c_u}{c(u_*)} \right) h_w > 0, \\ Q &:= C_1^2 - 4d_v C_2 > 0, \end{aligned}$$

and for

$$r_{\pm} = \frac{1}{2d_v}(C_2 \pm \sqrt{Q})$$

exists an  $l \in \mathbb{N}$  with

$$r_- < \frac{l(l+1)}{\gamma} < r_+.$$

- Case 2:

$$C_1 := -f_v \left[ h_u + \left( \frac{w_* c_u}{c(u_*)} \right) h_w \right] < 0$$

and with  $r_+$  as defined above exists an  $l \in \mathbb{N}$  with

$$\frac{l(l+1)}{\gamma} < r_+.$$

*Proof.* We first restrict ourselves to  $U_{lm}, V_{lm} \neq 0$  and the case  $D_u \gg 1$  as well as  $D_v \gg 1$ . In order to achieve an instability, we consider (7.81) and narrow down to the coefficient of  $D_u \cdot D_v$  which is given by

$$\begin{aligned} \epsilon &= d_v l^2 (l+1)^2 + \gamma l (l+1) (-d_v f_u + f_v) + (-l(l+1)\gamma g_v) + \gamma^2 (f_u g_v - f_v g_u) \\ &\quad - \left[ \left( \gamma h_w \left( \frac{w_* c_u}{c(u_*)} \right) + \gamma h_u \right) \cdot (d_v l (l+1) + \gamma f_v) \right] + \left[ \left( \gamma h_w \left( \frac{w_* c_u}{c(u_*)} \right) + \gamma h_u \right) \cdot \gamma g_v \right] \\ &= d_v l^2 (l+1)^2 + \gamma l (l+1) \left( -d_v f_u + f_v - g_v - d_v h_u - d_v \left( \frac{c_u w_*}{c(u_*)} \right) h_w \right) \\ &\quad + \gamma^2 \left( f_u g_v - f_v g_u - f_v h_u - \left( \frac{c_u w_*}{c(u_*)} \right) f_v h_w + g_v h_u + \left( \frac{c_u w_*}{c(u_*)} \right) g_v h_w \right). \end{aligned}$$

We define

$$\tilde{\epsilon} := d_v^2 l^2 (l+1) - d_v \gamma l (l+1) C_1 + \gamma^2 d_v C_2$$

whose roots are given by

$$r_{\pm} = \frac{C_2}{2d_v} \pm \sqrt{\left( \frac{C_2}{2d_v} \right)^2 - C_1}.$$

In order to satisfy condition (7.81) and to obtain an instability, we now require  $e < 0$ . First, assume  $C_1 \geq 0$  and  $C_2 > 0$ . Then,  $e$  represents a right displaced upward open parabola which intersects the positive axis at points  $r_{\pm}$ . Thus, with  $l \in \mathbb{N}$  to ensure  $e < 0$  we have to satisfy the conditions of Case 1. By contrast, if  $C_1$  is negative, the parabola is shifted to the left and we directly prove Case 2 to obtain  $e < 0$ .

We further consider  $D_u \gg 1$  as well as the case  $D_u \approx 1$ . Since we suppose that  $D_v \gg 1$ , as before, we observe that either  $D_u l e$  or  $D_v l e$  becomes dominant in (7.81). This implies that an instability exists for sufficiently large  $D_u$  or  $D_v$ .

Finally, with the same argumentation as before, the analysis of the coefficient  $D_u$  in (7.82) as well as  $D_v$  in (7.83) deduce Remark 7.2 and 7.3 (for the case  $U = 0$  see also [72]). □

### 7.4.1. Numerical results

In the following, we confirm the results of the linear stability analysis performed in the last section. We numerically solve system (7.32)-(7.38) for the different cases to investigate its behavior. In all computations we use functions  $f, g$  as given in (7.18) and (7.19) respectively. To simulate transport via exocytosis and endocytosis, with (7.23) and (7.24) we define

$$h(u, w, U) := e_1 w U - e_2 \left( 1 - \delta(w) \frac{w}{w_{max}} \right) u.$$

We consider the same initial concentrations as before and use parameters given in Table 7.1.

Note that due to the modification of  $h$  and the nearly homogeneous distribution of  $U$ , we have to rescale  $e_1$  and  $e_2$  to obtain similar results as for the system where molecules are transported via advection. For simulations of the RR system we use  $e_1 = 15.0$  and  $e_2 = 0.2$ . To prevent that transport dominates the system behavior, for our system we have to reduce the rate of endocytosis by the factor 2. The rate of exocytosis is chosen such that we obtain similar ratios between internal and membrane components as before. We set  $e_1 = 84.3$  and  $e_2 = 4.167$ .

The most interesting outcome of the stability analysis is the fact that the conditions determining instability are completely independent of the diffusion parameter  $d_w$ . This implies that the only requirement on  $d_w$  is that it must be non-zero. In this case, the capacity function  $c(u)$  determines whether the system is stable against small perturbations or not. We further call this capacity-driven instability.

Figure 7.17 shows the development of  $u$  in time for distinct values of  $d_w$ . We see that even for large changes of  $d_w$ , provided that  $d_w \neq 0$ , the system is always unstable and tends to form a polarized patch. It becomes clear that the capacity function  $c(u)$  as well as  $w^*$  determine the stability behavior. The constant  $d_w$  only changes the temporal dynamic of polarization (see Figure 7.17). For reduced rates, the maximum value of  $u$  is reached much later. It can be shown that even for  $d_w \ll 1$

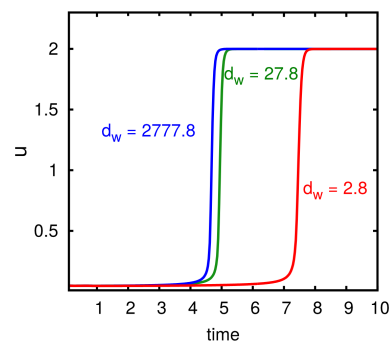


**Figure 7.17.: Computational results demonstrating the influence of the diffusion constant for actin cable movement on the polarization process.** The development of the maximum of  $u$  in time is shown. Computations with different rates for  $d_w$  are compared.

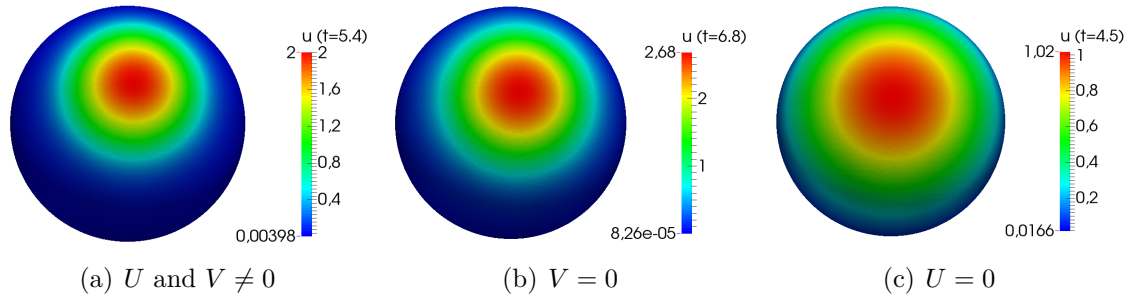


**Figure 7.18.: Numerical simulations of the generic system showing distinct cases of instability.** Computational results of system (7.32)-(7.38) showing distinct cases of instability ( $e_1 = 84.3$ ,  $e_2 = 4.167$ ). (a) The internal as well as cytosolic component is non-zero. A small initial perturbation leads to an instability inducing a polarized patch. (b) Without the cytosolic component a capacity-driven instability causes peak formation. (c) Even if the internal component is zero, the cell is still able to become unstable.

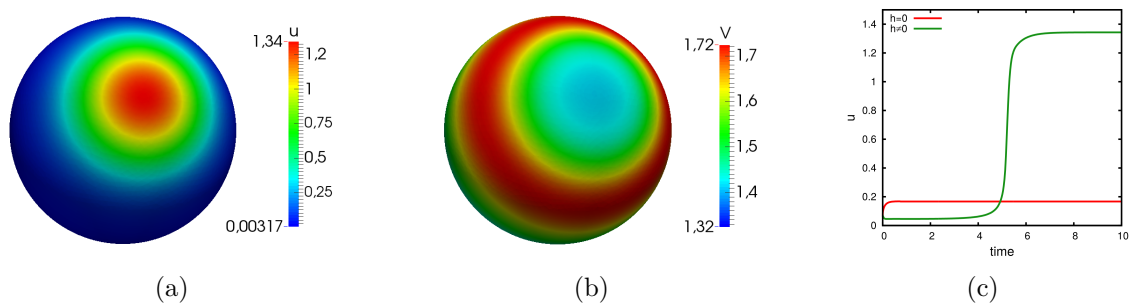


**Figure 7.19.: Numerical simulations of the generic system showing capacity-driven instability.** Computational results of the system (7.32)-(7.38) with drastically reduced diffusion constant  $D_V = 1$ . Even with similar rates of cytosolic and membrane diffusion the cell is able to polarize by transport. (a) Concentration  $u$  after time  $t = 10$  ( $h \neq 0$ ). (b) Concentration  $V$  after time  $t = 10$  ( $h \neq 0$ ). (c) Temporal development of  $u$ .

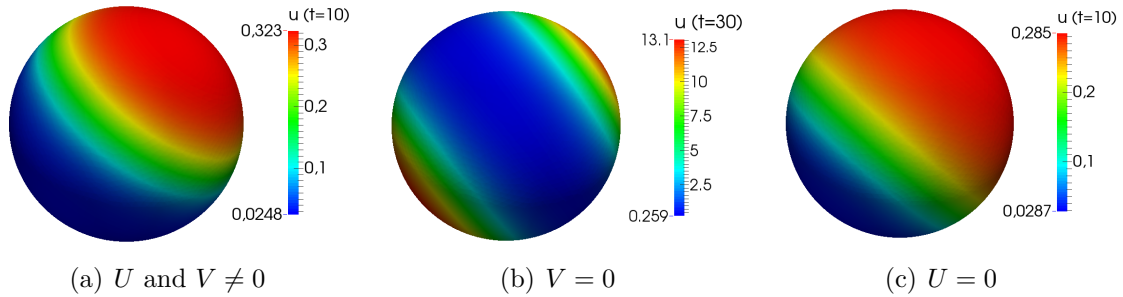


**Figure 7.20.: Numerical simulations of the RR model showing distinct cases of instability.** Computational results of system (7.32)-(7.38) using kinetic function of the RRsystem showing distinct cases of instability ( $e_1 = 15$ ,  $e_2 = 0.2$ ). (a) The internal as well as cytosolic component is non-zero. A small initial perturbation leads to an instability inducing a polarized patch. (b) Without the cytosolic component a capacity-driven instability causes peak formation. (c) Even if the internal component is zero, the cell is still able to become unstable.

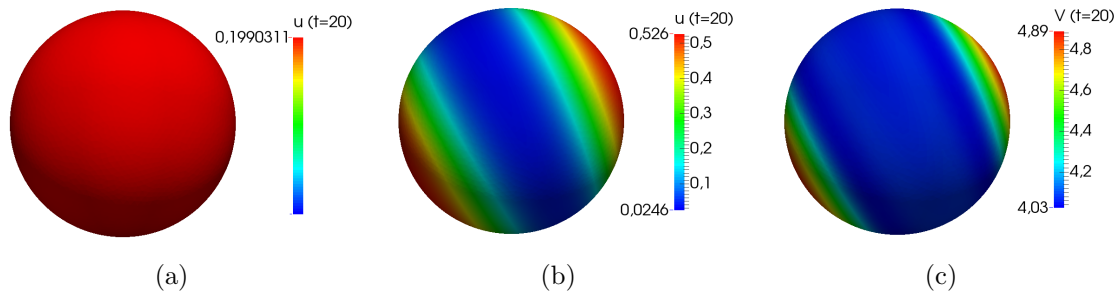


**Figure 7.21.: Numerical simulations of the RR model showing capacity-driven instability for equal membrane and cytosolic diffusion constants.** Computational results with drastically reduced diffusion constant  $D_V = 1$  are shown for the system with and without consideration of transport. (a) Concentration  $u$  after time  $t = 20$  and in the absence of a transport feedback ( $h = 0$ ). (b) Concentration  $u$  after time  $t = 20$  ( $h \neq 0$ ). (c) Concentration  $V$  after time  $t = 20$  ( $h \neq 0$ ).



the system is still able to form a polarized patch, albeit after a very long time ( $t > 30$ ).

Another result of the stability analysis is the fact that we may observe polarization, even if  $V = 0$  or  $U = 0$ . From Figures 7.18 and 7.20 we see that both systems, our non-dimensionalized and the RR model, are able to represent these cases. Even in the absence of a cytosolic exchange or a transport mechanism, the system becomes unstable and forms a polarized cluster.

At this point, it should be emphasized that regarding the intensity and shape of the polarized cluster, the subsequent process of cluster emergence calculated with the presented non-dimensionalized approach shows clear differences to the results computed with the complex model presented in Chapter 6.1. On the one hand this might be the result of the model reduction. This procedure induced the elimination of a local activating component. On the other hand, the simplification by assuming a well mixed internal pool to eliminate the advection term could influence the results. But the conditions for instability provide further predictions. The requirement  $D_u \gg 1$  yields that  $D_v$  must not be very large to ensure an instability. We have seen that even in the case  $D_v \approx 1$  the instability conditions may be satisfied. Our numerical simulations confirm these results. Figure 7.19 illustrates capacity-driven polarization for the system (7.32)-(7.38) where  $D_v = 1$ .

Similar results are obtained by numerical simulations of the RR system (see Figure 7.21). Whereas equal surface and bulk diffusion coefficients have impeded pattern formation in the original system without transport (see [72]), the enhanced system is still able to polarize. Interestingly, in this case the system tends to form two polarized clusters.

## 7.5. Discussion

In this chapter we have introduced a generic system for the simulation of transport-mediated cell polarization. We performed numerical simulations with distinct cell geometries.

The results have shown that vesicular transport may not only influence the robustness, the shape, and the intensity of the polar cluster but also its spatial location. Particularly in cells with complex shapes we observed different patterns between simulations with and without active molecule transport. Here, protrusions and narrower domains differently affected symmetry breaking. Whereas complex shapes rather inhibit diffusion-driven symmetry-breaking, transport-mediated polarization can be enhanced under these circumstances.

However, cells are able to robustly polarize at sites of complex protrusions. For example, the tip of the future axon is strongly polarized during neuronal development. These findings suggest that, especially in non-spherical cells, active transport may be required to ensure the correct location of the polarized patch. For instance, for the system presented in [72] applied to a rod-shaped cell, symmetry breaking was characterized by a central circle of active molecules round the cell. Under consideration of an active transport mechanism however, depending on the strength of the transport feedback, the peak either formed at one end or at both ends of the cell. Indeed, biological experiments have demonstrated that the unicellular rod-shaped fission yeast shows bipolar growth due to polarized transport of growth components along actin cables to sites of cortical polarity. With a disturbed transport machinery, cortical polarity is established at incorrect sites, resulting in bent or 'T'-shaped cells [80].

Contrarily, simulations of the generic model presented here as well as the GOR system always resulted in a pattern characterized by one stable polarized patch. We assume that these systems exhibit a stronger feedback of auto-amplification enhancing the competition between two clusters. At this point it is noteworthy that it was much more difficult to find parameter regimes simulating transport feedback for the system derived in [72]. We assume that this was due to the fact that this system in general seems to be more sensitive to parameter changes.

Another difference in the RR model and our or the GOR system was the spatial location of the polarized patch in a cell exhibiting a small protrusion. Whereas our model resulted in a polarized peak at the bud-site, the system proposed by RÄTZ AND RÖGER led to a cluster at the opposite side. This may result from the reaction kinetics. The function  $g$  representing cytosolic exchange in the RR model includes a negative feedback. Increased rates of the membrane-bound species lead to its membrane detachment. Contrarily, the other models investigated in this work are based on positive feedback activation. The inactivation is always linear. We assume that the negative mechanism in the RR model may counteract the positive transport feedback. Or conversely, the transport may increase the negative feedback. As a result, the polarized patch is obtained in regions where diffusion is less hindered. This could also explain why the initial cluster at sites with low curvature lasts much longer with than without delivery.

Interestingly, for the WP model we obtained that transport rather broadens than raises the polarized patch. The phenomenon of WP is explained by a traveling wave that moves through the domain and suddenly stops. The duration and distance of wave propagation thereby depends on the bi-linearity and mass conservation of the

system. It is a direct result of the integral over kinetic functions (see [61] for more details). Depending on the choice of parameters, the included transport scheme now changes not only the steady states but also the wave speed and the integral that determines the time point when the wave stops. For larger rates of endocytosis, the active membrane-bound component decreases so that the integral quickly becomes zero. In this way, the transport mechanism is also able to induce two transient polarized clusters.

Another outcome of the computational results presented in this chapter is the distinct role of organelles. Whereas internal barriers inhibit diffusion-driven polarization behind them, active transport is able to overcome this negative feedback to facilitate polarity next to organelles. The influence of internal components on the direction of cluster formation has already been shown by biological experiments. To give an example, studies with the fission yeast have demonstrated that the position of the interphase nucleus dictates the future site of cell division [20]. These findings together with our results emphasize that it is of particular importance to consider spatial aspects in the mathematical study of cell polarization. As a consequence, to investigate such biological processes in greater detail, the application of more complex mathematical models, including coupling bulk-surface PDEs, must take on greater significance.

Unfortunately, with growing complexity the analysis of mathematical models becomes increasingly challenging. To enable a linear stability analysis, we continued with a reduction of the generic approach given by reaction-diffusion-advection equations to a minimal coupled bulk-surface reaction-diffusion-transport system. The stability analysis has shown that the reduced generic system is able to generate spatial patterns under certain conditions. These conditions confirm that the transport process derived in this work can increase the robustness of the system. The reason is that two distinct mechanisms act in parallel to generate symmetry breaking. These can explain polarization in  $\Delta rdi1$  and LatA-treated cells. The first one relates to a classical Turing instability which requires a large difference in the cytosolic and membrane diffusion coefficient. Even if there is no transport of molecules from and to an internal compartment, this mechanism is able to achieve polarization. Since this case has already been analyzed in detail, at this point, we refer the reader to [72]. The second mechanism is based on a capacity function that regulates the concentration of the component driving transport. Under certain conditions, this mechanism can induce symmetry breaking, even if the cytosolic exchange is blocked. Hence, this case explains symmetry breaking in cells lacking the cytosolic component. In this case, provided that  $d_w \neq 0$ , the capacity function  $c(u)$  together with the homogeneous

state of  $w$  entirely determines the stability behavior.

By the performance of numerical simulations we finally confirmed the results of the stability analysis and demonstrated that our model as well as the enhanced model of RÄTZ AND RÖGER are able to show the different cases derived. Furthermore, we have shown that this capacity-driven instability also generates pattern when the cytosolic and membrane diffusion rates are equal. For that reason, and since the diffusion constant  $d_w$  has no essential impact on the stability of the system, we assert that this instability mechanism distinguishes from the Turing-type instability.

## 8 | A stochastic approach to vesicular trafficking-mediated cell polarity

Up to now, we have always considered a continuous approach regarding the transport control factor, in our case actin cables. We used a continuous function to describe its density on the membrane, albeit actin cables are discrete and countable. In this chapter we will construct a stochastic model for the movement of actin cable ends on the plasma membrane. In terms of this derivation, we make use of Brownian motion which is of fundamental importance for a random walk on the surface and solve a stochastic differential equation (SDE). For further details we refer the reader to [55].

### 8.1. Brownian motion on a surface

The modeling of particle movement on the circle or the sphere is a challenging question. Here, we use a popular method to calculate the movement of particles or molecules on the sphere  $S^n$ ,  $n = \{1, 2\}$  and follow the formal results described in [39]. The method presented there is based on the generation of random walk on a surface or a line approximated by a tangent plane or tangent line respectively. The results determined on this tangent are then projected back to the original geometry. Consider the SDE

$$d\mathbf{X} = a(\mathbf{X})dt + \sqrt{2D(\mathbf{X})}\mathbf{B}, \quad \mathbf{X}(0) = \mathbf{X}_0.$$

with diffusion matrix  $D(\mathbf{X})$  and drift field  $a(\mathbf{X})$ . The motion on a curve or a sphere can now be approximated by the motion on the tangential line or plane projected back to the sphere or curve respectively. Consider Brownian motion  $\mathbf{X}(t)$  on a

surface  $\Sigma$  and its planar projection  $\tilde{\mathbf{X}}(t)$ . It is

$$\mathbf{X}(t + \Delta t) = \tilde{\mathbf{X}}(t + \Delta t) + \lambda(\Delta t)n(\mathbf{X}(t)), \quad (8.1)$$

where  $n(\mathbf{X}(t))$  denotes the normal to the tangent and  $\lambda(\Delta t) \in \mathbb{R}$ . With the radius of the cell  $\lambda(\Delta t)$  can be calculated by

$$\|\mathbf{X}(t + \Delta t)\| = \|\tilde{\mathbf{X}}(t + \Delta t) + \lambda(\Delta t)n(\mathbf{X}(t))\| = r. \quad (8.2)$$

Thus, the transport mechanism can be implemented as follows.

Starting with a set of evenly distributed points  $\mathbf{X}(0)$  on the circle or sphere with radius  $r$ , for each time step  $t$

1. Compute standard Brownian motion  $\mathbf{B}$  in  $\mathbb{R}$  or  $\mathbb{R}^2$  respectively,
2. Determine the orthogonal projection  $\tilde{\mathbf{X}}(t + \Delta t)$ ,
3. Calculate  $n(\mathbf{X}(t))$  as well as  $\lambda(\Delta t)$  using (8.2), and
4. Use (8.1) to compute  $\mathbf{X}(t + \Delta t)$ .

We will shortly explain the proceeding for standard Brownian motion without drift on a circle and a sphere.

### 8.1.1. The two-dimensional case

To simulate standard Brownian motion  $\mathbf{X} = (x(t), y(t))$  at time  $t$  on a circle  $\Sigma := S^1$  with radius  $r$ , it is useful to define the tangent line  $l$  at the point  $(x, y)$ . For  $x, y \in \mathbb{R}$  it holds that  $l = \{(x_l, y_l) : y_l = y + \tan \alpha(x_l - x), -r \leq x_l \leq r\}$  with  $y = f(x)$  and  $\tan \alpha = f'(x)$ . For standard Brownian motion  $b(t)$  in  $\mathbb{R}$  the movement on the tangent line is given as

$$\tilde{x}(t + \Delta t) = x + \cos \alpha \sqrt{2D(\mathbf{X})\Delta t}, \quad \tilde{y}(t + \Delta t) = y + \sin \alpha \sqrt{2D(\mathbf{X})\Delta t}.$$

Here,  $\alpha$  can be calculated using the equation of a circle  $f(x) = \pm \sqrt{(r^2 - x^2)} = y$  which implies  $f'(x) = \pm \frac{1}{2\sqrt{r^2 - x^2}}$ . Then, dependent on the gradient of the tangent line it is  $\alpha = \pm \arctan(f'(x))$ .

### 8.1.2. The three-dimensional case

Let  $\Sigma$  be the surface of the sphere  $S^2 := \{x \in \mathbb{R}^3 : \|x\| = r\}$ . To construct a projection of a diffusion process from this surface onto a plane we need an explicit

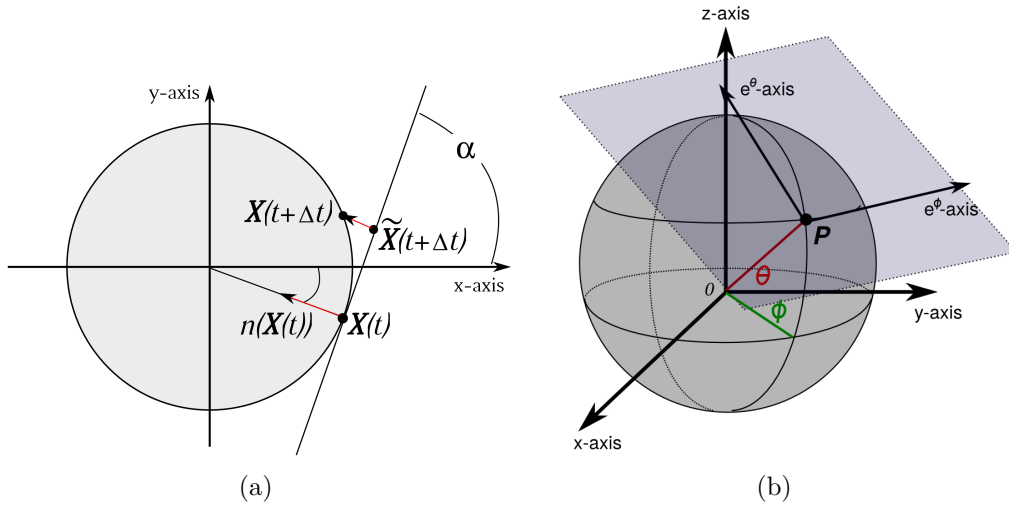


**Figure 8.1.: Schematic representation of the calculation procedure for standard Brownian motion on a surface using the tangent plane.** (a) The orthogonal projection of  $\tilde{\mathbf{X}}(t+\Delta t)$  onto the circle  $C$  in the direction  $n(\mathbf{X}(t))$  defines standard Brownian motion on  $C$ . (b) In 3D the standard Brownian motion on a sphere is calculated using an orthogonal projection from the tangent plane at a point  $P$  of  $\mathbf{X}(t)$  stretched by the vectors  $e^\phi$  and  $e^\theta$ .

representation with a sufficiently smooth function defined in a planar domain  $\mathcal{D}$  in the  $(x, y)$  plane. By considering the spherical coordinate system and a fixed orthonormal frame  $(\mathbf{i}, \mathbf{j}, \mathbf{k})$ , where  $\mathbf{k}$  is the unit vector in  $z$  direction, we have

$$\mathbf{X}(t) = x(t)\mathbf{i} + y(t)\mathbf{j} + z(t)\mathbf{k}, \quad z(t) = f(x(t), y(t)).$$

In spherical coordinates the points of a sphere with radius  $r$  are determined by

$$\begin{aligned} x &= r \sin(\theta) \cos(\phi), \\ y &= r \sin(\theta) \sin(\phi), \\ z &= r \cos(\theta), \end{aligned}$$

where  $r \in [0, \infty)$ ,  $\theta \in [0, \pi]$ ,  $\phi \in [0, 2\pi)$ . The tangent plane  $\Pi$  at  $\mathbf{X}(t) \in \Sigma$  is then defined by the orthonormal frame (see Figure 8.1)

$$\epsilon^\phi = \begin{pmatrix} -\sin(\phi) \\ \cos(\phi) \\ 0 \end{pmatrix} \quad \epsilon^\theta = \begin{pmatrix} \cos(\theta) \cos(\phi) \\ \cos(\theta) \sin(\phi) \\ -\sin(\theta) \end{pmatrix} \quad \epsilon^r = \begin{pmatrix} \sin(\theta) \cos(\phi) \\ \sin(\theta) \sin(\phi) \\ \cos(\theta) \end{pmatrix}. \quad (8.3)$$

For the Brownian motion  $\mathbf{X}(t + \Delta t) \in \Sigma$  the orthogonal projection

$$\tilde{\mathbf{X}}(t + \Delta t) = \tilde{x}(t + \Delta t)\mathbf{i} + \tilde{y}(t + \Delta t)\mathbf{j} + \tilde{z}(t + \Delta t)\mathbf{k}$$

onto  $\Pi$  with the tangential vectors  $e^\phi, e^\theta$  of (8.3) is then given by

$$\tilde{\mathbf{X}}(t + \Delta t) = \mathbf{X}(t) + \Delta s_1\mathbf{i} + \Delta s_2\mathbf{j} + \Delta s_3\mathbf{k},$$

where

$$\begin{aligned}\Delta s_1 &:= \cos(\theta) \cos(\phi) \sqrt{2D(\mathbf{X})} \Delta b_1 - \sin(\phi) \sqrt{2D(\mathbf{X})} \Delta b_2, \\ \Delta s_2 &:= \cos(\theta) \sin(\phi) \sqrt{2D(\mathbf{X})} \Delta b_1 + \cos(\theta) \sqrt{2D(\mathbf{X})} \Delta b_2, \\ \Delta s_3 &:= -\sin(\theta) \sqrt{2D(\mathbf{X})} \Delta b_1,\end{aligned}$$

and the functions  $b_1(t), b_2(t)$  are independent Brownian motions in  $\mathbb{R}$ .

## 8.2. Derivation of the stochastic model

Let  $\mathbf{X}(t)$  be a set of points  $X_1(t), \dots, X_N(t)$  characterizing the positions of actin cables on the surface  $\Gamma$  at time  $t$ . Further, let  $U[u + v + V]$  be a non-local functional determining the internal pool  $U$  by

$$U[u + v + V] = M - c \int_{\Gamma} (u + v) d\sigma - \int_{\Omega} V dx. \quad (8.4)$$

Then, we can incorporate the above results by writing the following reaction-diffusion system

$$\partial_t u = \Delta_{\Gamma} u + \gamma(f(u, v) + h(u, U)) \quad \text{on } \Gamma \times I, \quad (8.5)$$

$$\partial_t v = d_v \Delta_{\Gamma} v + \gamma(-f(u, v) + g(u, v, V)) \quad \text{on } \Gamma \times I, \quad (8.6)$$

$$\partial_t V = D_v \Delta V \quad \text{in } \Omega \times I, \quad (8.7)$$

with coupling boundary condition

$$-D_v \nabla V \cdot \vec{n} = \gamma g(u, v, V) \quad \text{on } \Gamma \times I. \quad (8.8)$$

Denoting with  $d$  the thickness of an actin cable or alternatively an arbitrary value determining the radius of a defined area around an actin cable, the transport can



now be calculated by the function

$$h(u, U) = e_1 G(x)U - \delta_{\text{end}} e_2 u$$

where

$$\delta_{\text{end}} = \begin{cases} 0 & \text{for } \text{dist}(x, X_i(t)) < d, \\ 1 & \text{else,} \end{cases}$$

is a standard Dirac delta function and  $G(x)$  is the Gaussian function of the form

$$G(x) = \frac{1}{\sqrt{2\pi}} e^{-Cx^2}.$$

This system is coupled to the non-local functional  $U$  defined by (8.4). In other words, molecules are deposited in a bell-shaped distribution around the site of nucleation. Simultaneously, particles are removed from the surface proportional to the amount of the active form anywhere else.

Note that throughout we have considered a PDE of the form

$$\partial_t = d_w \Delta_\Gamma \left( \frac{u}{c(u)} \right).$$

where the diffusion process is inhomogeneous. Consider

$$d_w \Delta_\Gamma \left( \frac{u}{c(u)} \right) = d_w \nabla_\Gamma \left( \nabla_\Gamma \left( \frac{1}{c(u)} \right) \cdot w + \frac{1}{c(u)} \cdot \nabla_\Gamma w \right).$$

Then, we use the SDE

$$d\mathbf{X} = a(\mathbf{X})dt + \sqrt{2D(\mathbf{X})}d\mathbf{B} \quad (8.9)$$

to simulate the movement of actin cables on the surface. Here,  $D(\mathbf{X})$  contains the values  $\frac{d_w}{c(u)}$  and  $a(\mathbf{X})$  consists of  $-\frac{c_u}{c(u)^2}$  calculated at the respective points of  $\mathbf{X}$ . The SDE is solved in parallel to the PDEs (8.5)-(8.8) using the proceeding described above. To calculate the drift vector on the tangent, we use a vector projection on the unit vectors of the tangent space.

Note that, depending on the local curvature of the surface, the projection usually implies a change in the diffusion and drift tensor that can be calculated considering the functions describing the surface. We refer the reader to [37] for further details. Here, we assume that the jump distance of cables is very short. Furthermore, smaller

inner time steps are used to solve the SDE. This allows us to simply assume that the local curvature does not significantly influence the results so that we can neglect such terms.

### 8.3. Numerical results

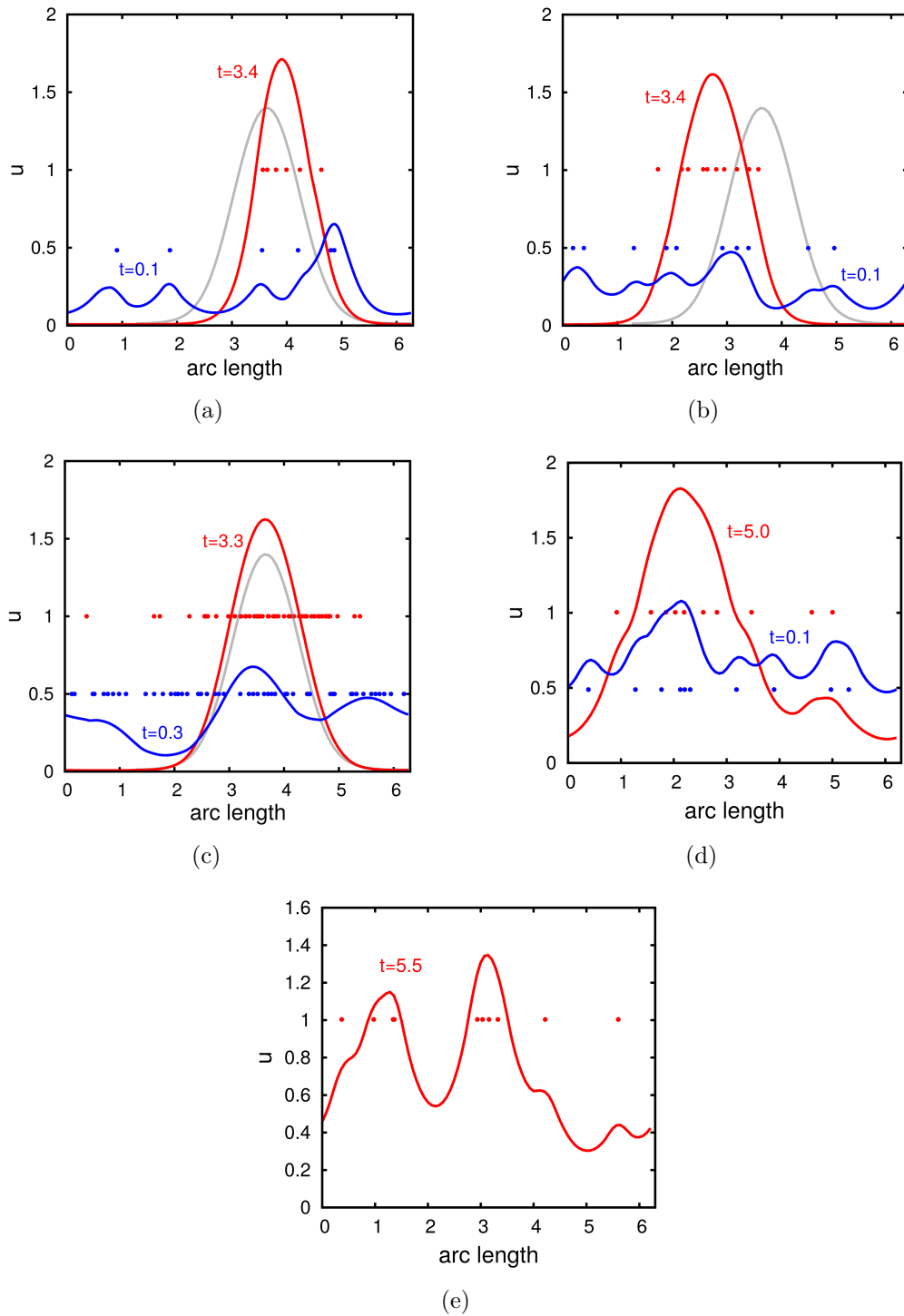
To investigate whether the simplification to simulate actin cables as a density qualitatively distort the results, we proceed with numerical simulations of the system (8.4)-(8.8) coupled to the SDE (8.9).

Figures 8.2 (a)-(c) show numerical simulations for a circle using distinct numbers of cables. We see that that the results are very similar to those observed with the continuous system presented in the previous chapter. Under consideration of a transport mechanism we see that the maximum value of  $u$  is increased compared to simulations without molecule delivery. Starting with a small perturbation on the initial homogeneous state, the system tends to form an inhomogeneous pattern. Due to this, the randomly located cables move towards regions with higher concentration of the active substance. Its local accumulation in turn leads to a further increase of  $u$  such that the motion of cables slows down. In Figures 8.2 (a)-(c) we see that finally almost all cables are localized at the polarized patch.

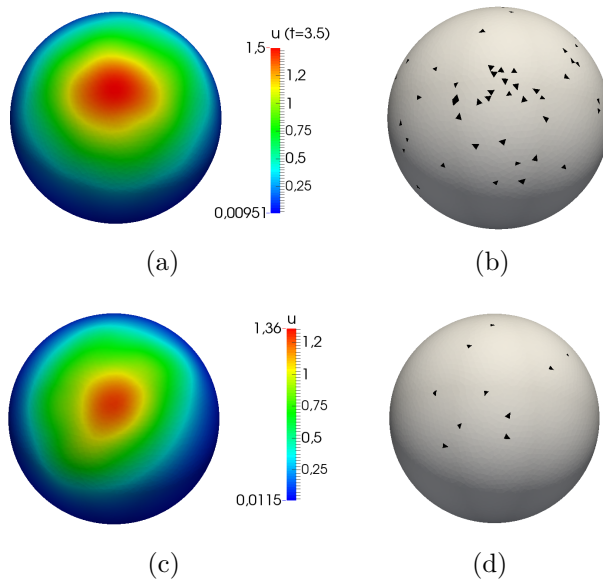
Interestingly, the number of cables does not significantly influence the outcome. Even for few cables, we obtain sustained polarity albeit with less intensity. With increasing number, the rise of  $u$  is more uniform and the final pattern is reached a little faster.

Figure 8.2 (d) demonstrates polarization in a cell where molecules cannot exchange between the plasma membrane and the cytosol. We see that initially the total amount of  $u$  is strongly increased throughout the surface. This leads to a reduced cable movement and an decelerated polarization process. In some cases, when multiple cables randomly accumulate at distinct sites of the cell surface, we also may obtain the emergence of multiple caps (see Figure 8.2 (e)).

Figure 8.3 shows three-dimensional computational results. Again, we see that transport via capacity-driven actin cables can support sustained polarization. With appropriate rates simulating exocytosis and endocytosis, transport via cables reinforces cluster formation, independent of how many cables are considered. However, compared to the results computed for the continuous approach derived in the last chapter, we obtain a broader polarized patch. Furthermore, due to cable motion, the final cluster is much more dynamic and slightly changes its shape.



**Figure 8.2.: Computational results of the stochastic approach in 2D.** Numerical results are shown for the stochastic approach using (a) 6, (b) 10 and (c) 50 discrete points. Cable positions are illustrated by points. The gray curve shows the final peak without consideration of transport. (d) and (e) Transport-mediated polarization in cells lacking the cytosolic exchange. Computational results using 10 cables are illustrated.



**Figure 8.3.: Computational results of the stochastic approach in 3D.** Numerical results are shown for the stochastic approach using 50 and 10 discrete points respectively. (a) and (c) The concentration of  $u$  after  $t = 3.5$  is shown. (b) and (d) Cable positions are illustrated by black simplices.

param.	value
$k_1$	0.056
$k_2$	27.78
$k_3$	0.025
$k_4$	13.89
$k_5$	10.77
$a_1$	19.41
$a_2$	59.42
$a_3$	2.23
$\gamma$	15.6
$dt$	$1.0 \times 10^{-8}$
$d_v$	1.0
$d_w$	1.0
$D_v$	305.5
$v$	1.56
$e_1$	0.1
$e_2$	0.3
$d$	0.2
$C$	25.0

**Table 8.1.:** Parameters used to simulate the stochastic approach.

## 8.4. Discussion

In this chapter we have presented a stochastic approach for the actin cable movement along the surface. We used a SDE to simulate Brownian motion of discrete points that represent actin cable ends. In order to apply this approach to a circle or a sphere, we used an orthogonal projection to the tangent at each point. Linked to the reaction-diffusion processes, this approach led to a system of PDEs coupled to a SDE. We performed numerical simulations in 2D and 3D and compared the results to those calculated with the complete continuous model.

The computational experiments have demonstrated that the simulation for cable nucleation as a capacity-driven diffusion process using Brownian motion with drift effectively reflects biological findings.

We have shown that just like the continuous approach, this system is able to achieve sustained transport-driven polarization, even in the case when cytosolic exchange is blocked. In this regard, the number of actin cables is almost irrelevant. The determining factors for enhanced polarization are again the rates of exocytosis and endocytosis as well as the feedback for cable accumulation.

But there are also slight differences between the results achieved by the continuous

approach and those simulated with the stochastic model. For instance, the intermediate states between the initial perturbation of the homogeneous state and the final inhomogeneous pattern distinguish. Due to the approximation of cables with a density, the continuous system grows very uniformly. In this way, the density of cables has a similar shape function to those of the active substance. The correlation between local cable nucleation and its subsequent delivery, which in turn anchors the cables, are less visible in this case. The results presented above have demonstrated that this coherence can be simulated much better with the stochastic than with the continuous model. In 2D as well as 3D, the results of the stochastic approach show a much more unequally distributed component  $u$  during the process of polarization. Since actin cables are modeled discretely, the molecules reaching the surface accumulate in spots. These patches start to grow until they merge together.

Relating to the simulation of  $\Delta rdi1$  cells, this means that this model is more suitable to simulate polarization characterized by two clusters. The increased total rate of active membrane-bound molecules in this case causes a decelerated motion of cables per se, increasing the probability of multiple peaks.

Interestingly, as opposed to the results of the model proposed by LAYTON ET AL. [52], this also implies that increased rates of exocytosis rather disturb symmetry breaking. In this case, the local concentration near actin cables grows too strongly inducing a competition between multiple small peaks. This behavior then disturbs the reaction-diffusion system so strongly that the cell may form multiple peaks or even fail to polarize. Biological experiments with cells exhibiting strongly enhanced rates of exocytosis could provide a deeper understanding.

Although we obtained minor differences between the results of the stochastic and the continuous approach, all things considered, the results have shown that the process of pattern formation occurs simultaneously in both systems. The continuous model and the stochastic approach yield very similar results. Thus, the numerical simulations have demonstrated that it is sufficient to represent this stochastic process by a continuous approach as presented in this work. The advantage of this continuous model however is that it is much easier to analyze. Furthermore, it is much more flexible. For instance, as presented in the last section, the continuous model allows to investigate spatial effects like internal barriers or the cell shape.

For the stochastic approach we used a well mixed internal compartment. The simulation of active molecule movement through the cell would require the modeling of each cable within the cell interior. This would imply further equations for cable assembly. As a result, the computational experiments as well as the analysis would become much more challenging.



## 9 | Summary and outlook

The ability of cells to polarize is a fundamental feature of almost all cells and crucial for different cell processes.

This study started out focusing on polarization of budding yeast cells and the establishment of the initial polarized state when the key regulator Cdc42 accumulates at one site of the cell. In the course of this, an introduction into the biological processes involved in yeast cell polarization, followed by a short review of the most important related mathematical models published, is given. Together with biological experiments, these models brought insights into molecular mechanisms underlying cell polarization. Based on distinct mathematical methods, the approaches discussed could either confirm or contradict biological observations. In most cases, the systems, which are more or less detailed and analyzable, confine oneself to single aspects of cell polarity. This work exposed advantages and disadvantages and gave an overview of its most important findings.

The model review has demonstrated the contribution of different pathways to symmetry breaking. The goal of this work was to develop a model that incorporates all these various feedbacks known to be important for cell polarization. Moreover, a continuous rather than a stochastic approach was supposed to simulate the vesicle trafficking process. Since the influence of transport effects on the process of polarization is controversially discussed, this work mainly focused on the possibility of a stable polar cluster formation as a result of coupling reaction-diffusion and transport mechanisms. To consider spatial aspects, the model simulated the full geometry of the cell. On this basis, a continuous reaction-diffusion-advection system that incorporates different pathways known to contribute to cell polarity was derived.

The numerical results have shown that this approach features previously experimentally observed phenotypes all of which have been modeled by different systems. It simulates the full process of polarity emergence, including actin cable formation. As a result, it has been shown that vesicular trafficking can have distinct influence on cell polarization. For a sufficiently strong feedback vesicular delivery is able to reinforce and to maintain cluster formation. Contrarily, an insufficiently strong

feedback can result in an unpolarized cell. Biological experiments investigating cells lacking endocytosis or mutants exhibiting highly increased exocytosis could help gain a deeper understanding about the impact of vesicular trafficking.

Another interesting finding of this work is the role of Cla4 in the polarization process. The results have indicated that this protein could play a more critical role in the establishment of polarity than presumed. This implies several, so far unknown, phenotypes that can biologically be examined.

In order to analyze the underlying processes in detail, this work proceeded with a subsequent model reduction and a non-dimensionalization of the complex model for yeast cell polarization. This brought out a general system of coupled bulk-surface reaction-diffusion-advection equations that serves as an exemplary model to study transport-mediated polarization in distinct cell types.

By means of computational simulations using distinct functions from the literature the generic model has shown how active transport cannot only enhance and sustain polarization but also change the polarization behavior. The results have demonstrated that the cell shape as well as internal barriers influence the spatial location of the polarity cluster. These findings have emphasized the importance of considering spatial aspects in cell polarization. Since simple one-dimensional models are incapable of simulating such factors, it became clear that the application and study of coupled bulk-surface systems for cell polarity is particularly decisive. The model presented in this work considers these spatial effects.

Another aspect is the interplay between reaction kinetics and local delivery. The findings of our work suggested that negative feedbacks can be enhanced by a transport process. Thus, to understand the role of vesicular trafficking on symmetry breaking, it is necessary to consider distinct signaling pathways. Depending on the currently dominating feedback different patterns may emerge. The influence of inhomogeneous diffusion should also not be neglected. We have shown that this mechanism can change the polarity direction as well.

But the model presented here allows much more enhanced investigations. For example, it would be interesting to study the behavior of transport-driven polarization in cells exhibiting microdomains characterized by distinct rates of exocytosis and endocytosis. Another aspect that could be of great interest would be time-dependent parameters. In this way, how the system behaves when signaling pathways change its strength or even stop affecting reactions could be investigated.

To get a deeper knowledge into the mechanisms driving pattern formation in the system presented here, the work proceeded with a linear stability analysis of the generic approach. This led to the derivation of stability and instability conditions.



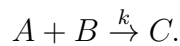
By this analytic study, we determined a Turing-instability and a capacity-driven instability. Whereas the first one explains polarity in LatA-treated cells, the second mechanism is able to explain symmetry breaking in  $\Delta rdi1$  cells. By computational simulations the analytical results were finally confirmed numerically.

To conclude this work, the last chapter dealt with a stochastic approach to the actin cable motion which drives the transport feedback in the continuous model. The stochastic model intended to show that the simulation of actin cables as a density is quite possible. Although this simplification implies the loss of most certainly phenotypes, such as cells with multiple clusters, it is much more flexible and easier to handle. Because of its manageability, our generic model could, for example, serve as a basis for the computational study of transport-driven polarization in cells with moving domains which is still open and subject to further work.



# A | Chemical reactions

In this thesis we are mainly concerned with the modeling of (bio)chemical reactions of proteins and molecules. To understand how to translate such reactions into partial differential equations, some very basic ideas are collected. For more details we refer to [40] and [62]. Consider a very simple irreversible reaction with a reaction rate  $k$



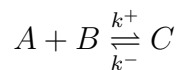
Let  $a = [A]$ ,  $b = [B]$ , and  $c = [C]$  be the concentrations of the species  $A, B, C$ . Let  $r_1$  further be the probability of collisions between the molecules and  $r_2ab\Delta t$  an approximation for the number of collisions in  $\Delta t$ . Assuming that the concentration of the molecules  $A$  and  $B$  changes in time due to their collisions and its probability, the change of  $c$  can be described by

$$\Delta c = kab\Delta t,$$

where  $k = r_1r_2$ . For  $\Delta t \rightarrow 0$  this yields the so-called Law of mass action

$$\frac{dc}{dt} = kab.$$

For a reversible reaction of the form

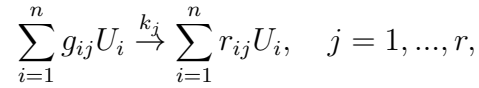


with the reaction rates  $k^+$  and  $k^-$ , this results in the corresponding ODE system

$$\begin{aligned}\frac{da}{dt} &= -k^+ab + k^-c, \\ \frac{db}{dt} &= -k^+ab + k^-c, \\ \frac{dc}{dt} &= k^+ab - k^-c.\end{aligned}$$

Note that we assumed that the split-up of  $C$  is proportional to  $c$ .

Considering  $n$  simultaneously interacting concentrations  $u_i$  of species  $U_i$  and its  $r$  chemical reactions, we can set up a general reaction system. For



the ODEs for the  $u_i$  are given by

$$\frac{du_i}{dt} = \sum_{j=1}^r (r_{ij} - g_{ij}) f_j(t, u(t)), \quad i = 1, \dots, n. \quad (\text{A.1})$$

$g_{ij}$  and  $r_{ij}$  describe the gain and loss of the molecule numbers  $u_i$  in reaction  $j$ . They are the so-called stoichiometric coefficients.  $f_j$ , given by

$$f_j(t, u) = k_j \prod_{l=1}^s (u_l)^{g_{lj}},$$

is the rate function which corresponds to the speed of reaction  $j$  with respective reaction rate  $k_j$ .

With  $u = (u_1, \dots, u_n)^T$ , the stoichiometric matrix  $S = (r_{ij} - g_{ij}) \in \mathbb{R}^{n \times r}$ , and  $f(t, u) = (f_j(t, u)) \in \mathbb{R}^r$  the equations A.1 can also be written in matrix form

$$\frac{du}{dt} = S f(t, u(t)).$$

## B | Spherical harmonics

Since numerical problems and approximations for problems over spheres have increased continuously over the last years, the study of spherical harmonics became increasingly important for solving problems in the sciences. These are specific functions defined on the sphere. Classical spherical harmonics on the three-dimensional unit sphere can be seen as extensions of trigonometric functions on the unit circle. Thereby, Laplace's spherical harmonics are a special set of spherical harmonics. These functions form an orthogonal system. In the following by finding functions that are harmonic in spherical coordinates, we derive the eigenvalue equation for the Laplace equation which is used in Section 7.4. For further details we refer the reader to [4].

With  $r \in \mathbb{R}_+$ ,  $0 \leq \varphi \leq \pi$ ,  $0 \leq \theta \leq 2\pi$ , in spherical coordinates the Laplace equation can be written as

$$\Delta = \nabla^2 = \frac{1}{r^2} \frac{\partial}{\partial r} \left( r^2 \frac{\partial u}{\partial r} \right) + \frac{1}{r^2 \sin^2 \varphi} \frac{\partial^2 u}{\partial \theta^2} + \frac{1}{r^2 \sin \varphi} \frac{\partial}{\partial \varphi} \left( \sin \varphi \frac{\partial u}{\partial \varphi} \right) = 0.$$

Using a separation of the solution by its radial and angular components of the form  $u(r, \varphi, \theta) = R_l(r)Y_{lm}(\varphi, \theta)$ , it holds that

$$\begin{aligned} \nabla^2 &= \frac{1}{r^2} \frac{\partial}{\partial r} \left( r^2 \frac{\partial (R_l Y_{lm})}{\partial r} \right) + \frac{1}{r^2 \sin^2 \varphi} \frac{\partial^2 (R_l Y_{lm})}{\partial \theta^2} + \frac{1}{r^2 \sin \varphi} \frac{\partial}{\partial \varphi} \left( \sin \varphi \frac{\partial (R_l Y_{lm})}{\partial \varphi} \right) \\ &= \frac{Y_{lm}}{r^2} \frac{\partial}{\partial r} \left( r^2 \frac{\partial R_l}{\partial r} \right) + \frac{R_l}{r^2 \sin^2 \varphi} \frac{\partial^2 Y_{lm}}{\partial \theta^2} + \frac{R_l}{r^2 \sin \varphi} \frac{\partial}{\partial \varphi} \left( \sin \varphi \frac{\partial Y_{lm}}{\partial \varphi} \right) \\ &= \frac{1}{R_l} \frac{\partial}{\partial r} \left( r^2 \frac{\partial R_l}{\partial r} \right) + \frac{1}{Y_{lm} \sin^2 \varphi} \frac{\partial^2 Y_{lm}}{\partial \theta^2} + \frac{1}{Y_{lm} \sin \varphi} \frac{\partial}{\partial \varphi} \left( \sin \varphi \frac{\partial Y_{lm}}{\partial \varphi} \right) \\ &= Y_{lm}(\varphi, \theta) \Delta_r R_l(r) + \frac{R_l(r)}{r^2} \Delta_{\varphi, \theta} Y_{lm}(\varphi, \theta) \\ &= \Delta R_l(r) Y_{lm}(\varphi, \theta) = 0. \end{aligned}$$

Now, each of this components must be equal to a constant. Thus, we can define

$$l(l+1) := \frac{1}{R} \frac{d}{dr} \left( r^2 \frac{dR}{dr} \right), \quad (\text{B.1})$$

$$-l(l+1) := \frac{1}{Y \sin^2 \varphi} \frac{\partial^2 Y}{\partial \theta^2} + \frac{1}{Y \sin \varphi} \frac{\partial}{\partial \varphi} \left( \sin \varphi \frac{\partial Y}{\partial \varphi} \right). \quad (\text{B.2})$$

Because  $l$  could be any constant, we can now consider the multiplication of equation (B.2) with  $Y \sin^2 \varphi$  that is given by

$$\frac{\partial^2 Y}{\partial \theta^2} + \sin \varphi \frac{\partial}{\partial \varphi} \left( \sin \varphi \frac{\partial Y}{\partial \varphi} \right).$$

With this notations the eigenvalue equation finally reads

$$\left( \frac{\partial^2}{\partial \varphi} + \frac{\cos \varphi}{\sin \theta} \frac{\partial}{\partial \varphi} + \frac{1}{\sin^2 \varphi} \frac{\partial^2}{\partial \theta^2} \right) Y_{lm}(\varphi, \theta) = -l(l+1) Y_{lm}(\varphi, \theta).$$

## C | Glossary

**actin** Actin is a structure protein found in essentially all eukaryotic cells. It forms microfilaments and participates in many important cellular processes, including cell division and cell movement. It is also involved in the assembly of the cytoskeleton.

**axon** The axon is the long threadlike extension of a nerve cell that conducts nerve impulses from the cell body.

**cytosol** The liquid found inside cells is called cytosol or cytoplasmic matrix. It is separated into compartments by membranes.

**dendrite** Dendrites are any of the short branched threadlike extensions of a nerve cell which conduct impulses towards the cell body.

**depolymerization** Depolymerization is the reverse mechanism of the polymerization and describes the process of converting a polymer into a monomer or a mixture of monomers.

**endoplasmic reticulum** The endoplasmic reticulum which can be found in eukaryotic cells describes a type of organelle. It is a membrane network of tubules, vesicles, and cisternae found throughout the cell.

**endosome** In cell biology, an endosome describes a membrane-bound compartment of the endocytic membrane transport pathway originating from the trans Golgi membrane.

**eukaryotic cell** Eukaryotes are cells that contain a nucleus and other organelles enclosed within membranes. Eukaryotic organisms may be unicellular, or multicellular.

**filament** In biology, a long chain of proteins, such as those found in hair, muscle, or in flagella, is termed filament.

**filopodia** Filopodia are slender cytoplasmic projections that extend beyond the leading edge of lamellipodia in migrating cells.

**formin** Formins are a group of proteins that are involved in the polymerization of actin and associate with the fast-growing end (barbed end) of actin filaments.

**Golgi** The Golgi apparatus or simply the Golgi is an organelle found in most eukaryotic cells. The Golgi apparatus packages proteins into membrane-bound vesicles inside the cell before the vesicles are sent to their destination.

**in vitro** Biological processes that occur in a laboratory vessel or other controlled experimental environment rather than within a living organism or natural setting are called *in vitro*.

**in vivo** *in vivo* describes processes that occur within a living organism or natural setting.

**lipid** A lipid is generally considered to be any molecule that is insoluble in water and soluble in organic solvents. Biological lipids are a group of naturally occurring molecules that include fats, waxes, sterols, and others.

**microtubule** Microtubules are filamentous intracellular structures that together with other protein filaments maintain cell shape by its role in cytoskeletal assembly.

**phosphorylation** In biochemistry phosphorylation describes the reversible addition of a phosphoryl group to a molecule, especially to proteins.

**plasma membrane** The plasma membrane or cell membrane is a biological membrane (separating layer) which separates the interior milieu of a cell from the outside environment.

**polymerization** Polymerization is the process whereby monomer molecules combine chemically to form polymer chains or a large network molecule.

**proliferation** Cell proliferation is the process that results in an increase of the number of cells. It is defined by the balance between cell divisions and cell loss through cell death or differentiation. Cell proliferation is increased in tumours.



**septin** Septins are a group of GTP-binding proteins found primarily in eukaryotic cells.

**vesicle** Vesicles are small structures within a cell. They form naturally during the processes of exocytosis and consists of fluid enclosed by a lipid bilayer.



# D | Notation and symbols

## Abbreviations and Notations

Notation	Description
DOF	degree of freedom
DUNE	Distributed and Unified Numerics Environment
EOC	Experimental Order of Convergence
FEM	Finite Element Method
FVM	Finite Volume Method
GAP	GTPase activating protein
GDI	GTPase dissociation inhibitor
GDP	guanosine diphosphate
GEF	guanine nucleotide exchange factor
GOR	system proposed by GORYACHEV AND POKHILKO [32]
GTP	guanosine triphosphate
LatA	latrunculin A
MOL	method of lines
ODE	ordinary differential equation
PCP	planar cell polarity
PDE	partial differential equation
RR	system proposed by RÄTZ AND RÖGER [72]
SDE	stochastic differential equation
WP	Wave-Pinning system proposed by MORI ET AL. [61]

## Mathematical Symbols

Symbols	Description
$\nabla_{\Gamma}$	Surface gradient

<b>Symbols</b>	<b>Description</b>
$\Delta_\Gamma$	Laplace-Beltrami operator
$[\cdot]$	Jump of a function
$\ \cdot\ $	Operator norm, or Sobolev norm
$E$	Reference element
$F_{T_k}$	Transformation from a reference element to $T_k$
$\Gamma$	Surface, boundary $\partial\Omega$ of a domain $\Omega$
$\Gamma_D$	Dirichlet boundary, part of $\partial\Omega$ of a domain $\Omega$
$\Gamma_N$	Neumann boundary, part of $\partial\Omega$ of a domain $\Omega$
$\mathbf{J}$	Flux function
$L^1_{\text{loc}}$	The set of locally integrable functions
$\vec{n}$	Outward pointing normal unit vector
$\Omega$	Domain $\Omega \subseteq \mathbb{R}^d$
$\partial\Omega$	Boundary of a domain $\Omega$
$\mathcal{P}_k$	Space of polynomial functions of degree $k$
$\mathcal{T}_h$	Triangulation (mesh) of a domain
$T_k$	Element in a mesh

# Bibliography

- [1] S. J. Altschuler, S. B. Angenent, Y. Wang, and L. F. Wu. On the spontaneous emergence of cell polarity. *Nature*, 454(7206):886–889, 2008.
- [2] K. Anguige and R. Matthias. Global existence for a bulk/surface model for active-transport-induced polarisation in biological cells. 2016.
- [3] N. Arimura and K. Kaibuchi. Neuronal Polarity: from extracellular signals to intracellular mechanisms. *Nature Review Neuroscience*, 8(3):194–205, 2007.
- [4] K. E. Atkinson and W. Han. *Spherical harmonics and approximations on the unit sphere*. Springer, Heidelberg, 2012.
- [5] B. Aulbach. *Gewöhnliche Differentialgleichungen*. Springer Spektrum, 2nd edition, 2004.
- [6] K. R. Ayscough. Endocytosis and the development of cell polarity in yeast require a dynamic F-actin cytoskeleton. *Current Biology*, 10(24):1587–1590, 2000.
- [7] K. R. Ayscough, J. Stryker, N. Pokala, M. Sanders, P. Crews, and D. G. Drubin. High Rates of Actin Filament Turnover in Budding Yeast and Roles for Actin in Establishment and Maintenance of Cell Polarity Revealed Using the Actin Inhibitor Latrunculin-A. *The Journal of Cell Biology*, 137(2):399–416, 1997.
- [8] P. Bastian, M. Blatt, A. Dedner, C. Engwer, R. Klökorn, R. Kornhuber, M. Ohlberger, and O. Sander. A Generic Grid Interface for Parallel and Adaptive Scientific Computing. Part II: Implementation and Tests in DUNE. *Computing*, 82(2-3):121–138, 2008.
- [9] P. Bastian, M. Blatt, A. Dedner, C. Engwer, R. Klökorn, M. Ohlberger, and O. Sander. A Generic Grid Interface for Parallel and Adaptive Scientific Computing. Part I: Abstract Framework. *Computing*, 82(2-3):103–119, 2008.

- [10] P. Bastian, M. Blatt, C. Engwer, A. Dedner, R. Klökorn, S. P. Kuttanikkad, M. Ohlberger, and O. Sander. The Distributed and Unified Numerics Environment (DUNE). *In Proc. of the 19th Symposium on Simulation Technique in Hannover*, 2006.
- [11] P. Bastian, F. Heimann, and S. Marnach. Generic implementation of finite element methods in the distributed and unified numerics environment. *Kybernetik*, 46(2):294–315, 2010.
- [12] J. Bey. *Finite-Volumen- und Mehrgitter-Verfahren für elliptische Randwertprobleme*. Springer Fachmedien Wiesbaden, 1998.
- [13] I. Bose, J. E. Irazoqui, J. J. Moskow, and B. E. S. G. Assembly of Scaffold-mediated Complexes Containing Cdc42p, the Exchange Factor Cdc24p, and the Effector Cla4p Required for Cell Cycle-regulated Phosphorylation of Cdc24p. *The Journal of Biological Chemistry*, 276:7176–7186, 2000.
- [14] H. Brézis. *Functional analysis, Sobolev spaces and partial differential equations*. Springer New York, 2011.
- [15] S. M. Buttery, S. Yoshida, and D. Pellman. Yeast formins bni1 and bnr1 utilize different modes of cortical interaction during the assembly of actin cables. *Molecular Biology of the Cell*, 18(5):1826–1838, 2007.
- [16] A.-C. Butty, N. Perrinjaquet, A. Petit, M. Jaquenoud, J. E. Segall, K. Hofmann, C. Zwahlen, and M. Peter. A positive feedback loop stabilizes the guanine-nucleotide exchange factor Cdc24 at sites of polarization. *The EMBO Journal*, 21(7):1565–1576, 2002.
- [17] J. Chant. Cell Polarity in Yeast. *Annual Review of Cell and Developmental Biology*, 15(1):365–391, 1999. PMID: 10611966.
- [18] V. J. Cid, L. Adamikova, M. Sanchez, M. Molina, and C. Nombela. Cell cycle control of septin ring dynamics in the budding yeast. *Microbiology*, 147(6):1437–1450, 2001.
- [19] G. M. Cooper. *The Cell*. Sunderland (MA): Sinauer Associates, 2nd edition, 2000.
- [20] R. R. Daga and F. Chang. Dynamic positioning of the fission yeast cell division plane. *Proceedings of the National Academy of Sciences of the United States of America*, 102(23):8228–8232, 2005.

- 
- [21] G. Dziuk. Finite Elements for the Beltrami operator on arbitrary surfaces. *Partial Differential Equations and Calculus Of Variations (Lecture Notes in Mathematics)*, 1357:142–155, 1988.
- [22] C. Eck, H. Garcke, and K. Peter. *Mathematische Modellierung*. Springer Berlin Heidelberg, 2nd edition, 2011.
- [23] H. Elman, D. J. Silvester, and A. J. Wathen. *Finite Elements and Fast Iterative Solvers : with Applications in Incompressible Fluid Dynamics*. Oxford University Press, 2005.
- [24] S. Etienne-Manneville. Cdc42 - the centre of polarity. *Journal of Cell Science*, 117(8):1291–1300, 2004.
- [25] S. Etienne-Manneville and A. Hall. Rho GTPases in cell biology. *Nature*, 420(6916):629–635, 2002.
- [26] M. Evangelista, D. Pruyne, D. C. Amberg, C. Boone, and A. Bretscher. Formins direct Arp2/3-independent actin filament assembly to polarize cell growth in yeast. *Nature Cell Biology*, 4(1):32–41, 2002.
- [27] L. C. Evans. *Partial Differential Equations*. American Mathematical Society, 2nd edition, 2010.
- [28] T. Freisinger, K. Ben, J. Johnson, N. Müller, G. Pichler, G. Beck, M. Costanzo, C. Boone, R. A. Cerione, E. Frey, and R. Wedlich-Söldner. Establishment of a robust single axis of cell polarity by coupling multiple positive feedback loops. *Nature Communications*, 4(1807), 2002.
- [29] C. Geuzaine and J.-F. Remacle. Gmsh: A 3-D finite element mesh generator with built-in pre- and post-processing facilities. *International Journal for Numerical Methods in Engineering*, 79(11):1309–1331, 2009.
- [30] A. Gierer and H. Meinhardt. A theory of biological pattern formation. *Kybernetik*, 12(1):30–39, 1972.
- [31] W. Giese, M. Eigel, S. Westerheide, C. Engwer, and E. Klipp. Influence of cell shape, inhomogeneities and diffusion barriers in cell polarization models. *Physical Biology*, 12(6), 2015.
- [32] A. B. Goryachev and A. V. Pokhilko. Dynamics of Cdc42 network embodies a Turing-type mechanism of yeast cell polarity. *FEBS Letters*, 582(10):1437–1443, 2008.

- [33] B. Govindan, R. Bowser, and P. Novick. The role of Myo2, a yeast class V myosin, in vesicular transport. *The Journal of Cell Biology*, 128(6):1055–1068, 1995.
- [34] L. Grüne and O. Junge. *Gewöhnliche Differentialgleichungen. Eine Einführung aus der Perspektive der dynamischen Systeme*. Springer Spektrum Wiesbaden, 2nd edition, 2009.
- [35] M.-P. Gulli, M. Jaquenoud, Y. Shimada, G. Niederhäuser, P. Wiget, and M. Peter. Phosphorylation of the Cdc42 Exchange Factor Cdc24 by the PAK-like Kinase Cla4 May Regulate Polarized Growth in Yeast. *Molecular Cell*, 6(5):1155–1167, 2000.
- [36] A. Hall. Rho GTPases and the Actin Cytoskeleton. *Science*, 279(5350):509–514, 1998.
- [37] A. S. Howell, M. Jin, C.-F. Wu, T. R. Zyla, T. C. Elston, and D. J. Lew. Negative Feedback Enhances Robustness in the Yeast Polarity Establishment Circuit. *Cell*, 149(2):322–333, 2012.
- [38] A. S. Howell, N. S. Savage, S. A. Johnson, I. Bose, A. W. Wagner, T. R. Zyla, F. H. Nijhout, M. C. Reed, A. B. Goryachev, and D. J. Lew. Singularity in Polarization: Rewiring Yeast Cells to Make Two Buds. *Cell*, 139(4):731–743, 2009.
- [39] N. Hoze, Z. Schuss, and D. Holcman. Reconstruction of Surface and Stochastic Dynamics from a Planar Projection of Trajectories. *SIAM J IMAGING SCIENCES*, 6(4):2430–2449, 2013.
- [40] W. Hundsdorfer and J. G. Verwer. *Numerical Solution of Time-Dependent Advection-Diffusion-Reaction Equations*. Springer Science & Business Media, 2013.
- [41] J. E. Irazoqui, A. S. Gladfelter, and D. J. Lew. Scaffold-mediated symmetry breaking by Cdc42p. *Nature Cell Biology*, 5(12):1062–1070, 2003.
- [42] J. E. Irazoqui and D. J. Lew. Polarity establishment in yeast. *Journal of Cell Science*, 117(11):2169–2171, 2004.
- [43] C. W. Jacobs, A. E. M. Adams, P. J. Szaniszló, and P. J. R. Functions of microtubules in the *Saccharomyces cerevisiae* cell cycle. *The Journal of Cell Biology*, 107(4):1409–1426, 1988.



- [44] A. Jilkine. *A wave-pinning mechanism for eukaryotic cell polarization based on Rho GTPase dynamics*. PhD thesis, University of British Columbia, 2009.
- [45] J. M. Johnson, M. Jin, and D. J. Lew. Symmetry breaking and the establishment of cell polarity in budding yeast. *Current opinion in genetics & development*, 21(6):740–746, 2011.
- [46] G. C. Johnston, J. A. Prendergast, and R. A. Singer. The *Saccharomyces cerevisiae* MYO2 gene encodes an essential myosin for vectorial transport of vesicles. *The Journal of Cell Biology*, 113(3):539–551, 1991.
- [47] M. Jose, S. Tollis, D. Nair, J.-B. Sibarita, and D. McCusker. Robust polarity establishment occurs via an endocytosis-based cortical corralling mechanism. *The Journal of Cell Biology*, 200(4):407–418, 2013.
- [48] B. Klünder, T. Freisinger, R. Wedlich-Söldner, E. Frey, and J. J. Saucerman. GDI-Mediated Cell Polarization in Yeast Provides Precise Spatial and Temporal Control of Cdc42 Signaling. *PLoS Computational Biology*, 9(12), 2013.
- [49] L. Kozubowski, K. Saito, J. M. Johnson, A. S. Howell, T. R. Zyla, and D. J. Lew. Symmetry-Breaking Polarization Driven by a Cdc42p GEF-PAK Complex. *Current Biology*, 18(22):1719–1726, 2008.
- [50] G. Krauss. *Biochemistry of Signal Transduction and Regulation*. Wiley-VCH Verlag GmbH & Co KGaA, 5th edition, 2014.
- [51] C.-C. Kuo, N. S. Savage, H. Chen, C.-F. Wu, T. R. Zyla, and D. J. Lew. Inhibitory GEF phosphorylation provides negative feedback in the yeast polarity circuit. *Current Biology*, 24(7):753–759, 2014.
- [52] A. T. Layton, N. S. Savage, A. S. Howell, S. Y. Carroll, D. G. Drubin, and D. J. Lew. Modeling vesicle traffic reveals unexpected consequences for Cdc42p-mediated polarity establishment. *Current Biology*, 21(3):184–194, 2011.
- [53] D. J. Lew. Yeast Polarity: Negative Feedback Shifts the Focus. *Current Biology*, 15(24):994–996, 2005.
- [54] W.-C. Lo, H.-O. Park, and C.-S. Chou. Mathematical Analysis of Spontaneous Emergence of Cell Polarity. *Bulletin of Mathematical Biology*, 76(8):1835–1865, 2014.

- [55] G. J. Lord, C. E. Powell, and T. Shardlow. *Introduction to Computational Stochastic Differential Equations*. Cambridge Univ. Press, New York, NY, 2014.
- [56] E. Marco, R. Wedlich-Soldner, R. Li, S. J. Altschuler, and L. F. Wu. Principles for the dynamic maintenance of cortical polarity. *Cell*, 129(2):411–422, 2007.
- [57] J. Mata and N. Paul. *tea1* and the microtubular cytoskeleton are important for generating global spatial order within the fission yeast cell. *Cell*, 89(6):939–949, 1997.
- [58] Z. Mei. *Numerical Bifurcation Analysis for Reaction-Diffusion Equations*. Springer-Verlag Berlin Heidelberg, 1st edition, 2000.
- [59] H. Meinhardt. Orientation of chemotactic cells and growth cones: models and mechanisms. *Journal of Cell Science*, 112(17):2867–2874, 1999.
- [60] H. Meinhardt and A. Gierer. Pattern formation by local self-activation and lateral inhibition. *BioEssays*, 22(8):753–760, 2000.
- [61] Y. Mori, A. Jilkine, and L. Edelstein-Keshet. Wave-Pinning and Cell Polarity from a Bistable Reaction-Diffusion System. *Biophysical Journal*, 94(9):3684–3697, 2008.
- [62] J. D. Murray. *Mathematical Biology - I. An Introduction*. Springer-Verlag New York, 3rd edition, 1989.
- [63] J. D. Murray. *Mathematical Biology - II. Spatial Models and Biomedical Applications*. Springer-Verlag New York, 3rd edition, 1989.
- [64] S. Müthing. *A flexible framework for multi physics and multi domain PDE simulations*. PhD thesis, Institut für Parallele und Verteilte Systeme der Universität Stuttgart, 2015.
- [65] W. J. Nelson. Remodeling Epithelial Cell Organization: Transitions Between Front–Rear and Apical–Basal. *Cold Spring Harbor Perspectives in Biology*, 1(1), 2009.
- [66] E. M. Ozbudak, A. Becskei, and A. Van Oudenaarden. A System of Counter-acting Feedback Loops Regulates Cdc42p Activity during Spontaneous Cell Polarization. *Developmental Cell*, 9(4):565–571, 2005.

- [67] H.-O. Park and E. Bi. Central Roles of Small GTPases in the Development of Cell Polarity in Yeast and Beyond. *Microbiology and Molecular Biology Reviews*, 71(1):48–96, 2007.
- [68] H.-O. Park, E. Bi, J. R. Pringle, and I. Herskowitz. Two active states of the Ras-related Bud1/Rsr1 protein bind to different effectors to determine yeast cell polarity. *Proceedings of the National Academy of Sciences of the United States of America*, 94(9):4463–4468, 1997.
- [69] T. D. Pollard. The cytoskeleton, cellular motility and the reductionist agenda. *Nature*, 422(6933):741–745, 2003.
- [70] D. Pruyne and A. Bretscher. Polarization of cell growth in yeast. I. Establishment and maintenance of polarity states. *Journal of Cell Science*, 113(3):365–375, 2000.
- [71] D. W. Pruyne, D. H. Schott, and A. Bretscher. Tropomyosin-containing Actin Cables Direct the Myo2p-dependent Polarized Delivery of Secretory Vesicles in Budding Yeast. *The Journal of Cell Biology*, 143(7):1931–1945, 1998.
- [72] A. Rätz and M. Röger. Symmetry breaking in a bulk–surface reaction–diffusion model for signalling networks. *Nonlinearity*, 27(8):1805–1827, 2014.
- [73] A. J. Ridley, M. A. Schwartz, K. Burridge, R. A. Firtel, M. H. Ginsberg, G. Borisy, J. T. Parsons, and A. R. Horwitz. Cell Migration: Integrating Signals from Front to Back. *Science*, 302(5651):1704–1709, 2003.
- [74] N. G. G. Robinson, L. Guo, J. Imai, A. Toh-e, Y. Matsui, and F. Tamanoi. Rho3 of *Saccharomyces cerevisiae*, which regulates the actin cytoskeleton and exocytosis, is a GTPase which interacts with Myo2 and Exo70. *Molecular and Cellular Biology*, 19(5):3580–3587, 1999.
- [75] I. Sagot, S. K. Klee, and D. Pellman. Yeast formins regulate cell polarity by controlling the assembly of actin cables. *Nature Cell Biology*, 4(1):42–50, 2002.
- [76] N. S. Savage, A. T. Layton, D. J. Lew, and L. Edelstein-Keshet. Mechanistic mathematical model of polarity in yeast. *Molecular Biology of the Cell*, 23(10):1998–2013, 2012.
- [77] J. Schnakenberg. Simple chemical reaction systems with limit cycle behaviour. *Journal of Theoretical Biology*, 81(3):389 – 400, 1979.

- [78] D. H. Schott, R. N. Collins, and A. Bretscher. Secretory vesicle transport velocity in living cells depends on the myosin-V lever arm length. *The Journal of Cell Biology*, 156(1):35–40, 2002.
- [79] J. D. Shaw, K. B. Cummings, G. Huyer, S. Michaelis, and B. Wendland. Yeast as a Model System for Studying Endocytosis. *Experimental Cell Research*, 271(1):1–9, 2001.
- [80] S. E. Siegrist and C. Q. Doe. Microtubule-induced cortical cell polarity. *Cold Spring Harbor Laboratory Press*, 21:483–496, 2007.
- [81] B. D. Slaughter, A. Das, J. W. Schwartz, B. Rubinstein, and R. Li. Dual Modes of Cdc42 Recycling Fine-Tune Polarized Morphogenesis. *Developmental cell*, 17(6):823–835, 2009.
- [82] B. D. Slaughter and S. E. Smith. Symmetry Breaking in the Life Cycle of the Budding Yeast. *Cold Spring Harbor Perspectives in Biology*, 1(3), 2009.
- [83] B. D. Slaughter, J. R. Unruh, A. Das, S. E. Smith, B. Rubinstein, and R. Li. Non-Uniform Membrane Diffusion Enables Steady-State Cell Polarization via Vesicular Trafficking. *Nature communications*, 4:1380, 2013.
- [84] S. E. Smith, B. Rubinstein, I. Mendes Pinto, B. D. Slaughter, J. R. Unruh, and R. Li. Independence of symmetry breaking on Bem1-mediated autocatalytic activation of Cdc42. *The Journal of Cell Biology*, 202(7):1091–1106, 2013.
- [85] M. Sohrmann and M. Peter. Polarizing without a C(1)ue. *Trends in Cell Biology*, 13(10):526–533, 2003.
- [86] Y. Sun, A. C. Martin, and D. G. Drubin. Endocytic Internalization in Budding Yeast Requires Coordinated Actin Nucleation and Myosin Motor Activity. *Developmental Cell*, 11(1):33–46, 2006.
- [87] M. Symons and N. Rusk. Control of Vesicular Trafficking by Rho GTPases. *Current Biology*, 13(10):R409–R418, 2003.
- [88] M. H. Symons. *Rho GTPases*. Springer US, 1st edition, 2004.
- [89] S. Tahirovic and F. Bradke. Neuronal Polarity. *Cold Spring Harbor Perspectives in Biology*, 1(3), 2009.
- [90] B. Tanos and E. Rodriguez-Boulan. The epithelial polarity program: machineries involved and their hijacking by cancer. *Oncogene*, 27(55):6939–6957, 2008.

- [91] C. Tiedje, I. Sakwa, U. Just, T. Höfken, and D. Lew. The Rho GDI Rdi1 regulates Rho GTPases by distinct mechanisms. *Molecular Biology of the Cell*, 19(7):2885–2896, 2008.
- [92] A. M. Turing. The Chemical Basis of Morphogenesis. *Biological Sciences*, 237(641):37–72, 1952.
- [93] S. C. Wai, S. A. Gerber, R. Li, and N. Hotchin. Multisite phosphorylation of the guanine nucleotide exchange factor Cdc24 during yeast cell polarization. *PLoS One*, 4(8), 2009.
- [94] Y. Wang and X. Lu. Cell Polarity: A Key Defence Mechanism Against Infection and Cancer Cell Invasion? pages 167–186, 2015.
- [95] L. J. Watson, G. Rossi, and P. Brennwald. Quantitative Analysis of Membrane Trafficking in Regulation of Cdc42 Polarity. *Traffic*, 15(12):1330–1343, 2014.
- [96] R. Wedlich-Söldner, S. Altschuler, L. Wu, and R. Li. Spontaneous Cell Polarization Through Actomyosin-Based Delivery of the Cdc42 GTPase. *Science*, 299(5610):1231–1235, 2003.
- [97] R. Wedlich-Söldner and R. Li. Spontaneous cell polarization: undermining determinism. *Nature Cell Biology*, 5(4):267–270, 2003.
- [98] R. Wedlich-Söldner, S. C. Wai, T. Schmidt, and R. Li. Robust cell polarity is a dynamic state established by coupling transport and GTPase signaling. *The Journal of Cell Biology*, 166(6):889–900, 2004.
- [99] L. Werner. Baby Tipps, 6. SSW (Schwangerschaftswoche). <http://www.baby-tipps.com/schwangerschaft-geburt/6-ssw-schwangerschaftswoche/>. Accessed: 2016-09-13.
- [100] S. J. Winder and K. R. Ayscough. Actin-binding proteins. *Journal of Cell Science*, 118(4):651–654, 2005.
- [101] D. Winter, A. V. Podtelejnikov, M. Mann, and R. Li. The complex containing actin-related proteins Arp2 and Arp3 is required for the motility and integrity of yeast actin patches. *Current Biology*, 7(7):519–529, 1997.
- [102] J. Wohlgemuth. Signs of a Happy Baby. <http://www.parents.com/baby/development/social/signs-of-a-happy-baby-/>. Accessed: 2016-09-13.

- 
- [103] B. Woods, C.-C. Kuo, C.-F. Wu, T. R. Zyla, and L. D. J. Polarity establishment requires localized activation of Cdc42. *Journal of Cell Biology*, 211(1):19–26, 2015.
- [104] T. Yoshimura, N. Arimura, and K. Kaibuchi. Signaling Networks in Neuronal Polarization. *The Journal of Neuroscience*, 26(42):10626–10630, 2006.
- [105] J. H. Yu, A. H. Crevenna, M. Bettenbühl, T. Freisinger, and R. Wedlich-Söldner. Cortical actin dynamics driven by formins and myosin V. *Journal of Cell Science*, 124(9):1533–1541, 2011.
- [106] J. A. Zallen. Planar Polarity and Tissue Morphogenesis. *Cell*, 129(6):1051–1063, 2007.

# Natalie Emken

*Curriculum Vitae*

